

# Master of Science Thesis

Optimization of a representative wing  
component using a Genetic Algorithm

by

Etienne BELLANGER

to obtain the degree of Master of Science  
at the Delft University of Technology,  
to be defended publicly on Wednesday October 18, 2023 at 09:30 AM.

Student number: 5628423  
Project duration: December, 2022 - October, 2023  
Thesis committee: Prof. dr. ir. C. Bisagni, TU Delft, supervisor  
Prof. dr. ir. S.G.P. Castro, TU Delft, chair  
Prof. dr. ir. J.A. Pascoe, TU Delft

An electronic version of this thesis is available at <http://repository.tudelft.nl/>.

# Contents

<b>Nomenclature</b>	<b>vii</b>
<b>Acknowledgments</b>	<b>viii</b>
<b>Abstract</b>	<b>ix</b>
<b>1 Introduction</b>	<b>1</b>
1.1 Background and motivation . . . . .	1
1.2 Previous results . . . . .	2
1.3 Objective and research question . . . . .	3
1.4 Structure of the report . . . . .	3
<b>2 Literature Study</b>	<b>4</b>
2.1 Composite wing structure analysis . . . . .	4
2.1.1 Failure criteria . . . . .	4
2.1.2 Composite design guidelines . . . . .	6
2.2 Optimization formulation . . . . .	7
2.2.1 Design variables . . . . .	7
2.2.2 Optimization objectives (Weight, Cost, Buckling, flutter velocity, Drag, Max strain, Aeroelastically tailored, multi-objectives) . . . . .	14
2.2.3 Type of constraints (Strength, Stability, Buckling, Flutter, Geometry, Stiffness, Strain...) . . . . .	15
2.3 Type of optimizations . . . . .	17
2.3.1 Multi-objective . . . . .	17
2.3.2 Multi-level . . . . .	19
2.3.3 Multi-step approach . . . . .	20
2.3.4 Multi-fidelity . . . . .	21
2.3.5 Probabilistic optimization . . . . .	23
2.4 Optimization algorithms . . . . .	27
2.4.1 Most Used Algorithms . . . . .	27
2.4.2 Inspired from real-life behavior . . . . .	29
<b>3 Preliminary Analyses</b>	<b>32</b>
3.1 Coupon geometry . . . . .	32
3.1.1 Model description . . . . .	32
3.1.2 aluminum 6063AT6 . . . . .	34
3.1.3 USN150B composite . . . . .	34
3.2 Failure criteria . . . . .	39
3.2.1 Hashin criteria . . . . .	39
3.2.2 Comparison with other failure criteria . . . . .	41
3.3 Buckling of a plate . . . . .	43
3.3.1 Aluminum Alloy 2024-T4 . . . . .	43
3.3.2 Composite laminate : UD Carbon Prepreg IM7/8552 . . . . .	46
3.4 Buckling of the stiffened panel . . . . .	53
3.4.1 Model description . . . . .	53
3.4.2 Linear Buckling . . . . .	55
3.4.3 Post-buckling analysis with <b>Dynamic, Implicit</b> simulation . . . . .	58
<b>4 Optimization Strategy</b>	<b>60</b>
4.1 Problem statement . . . . .	60
4.1.1 Presentation of the structure . . . . .	60
4.1.2 Optimization Formulation . . . . .	62

---

4.1.3	Baseline configuration . . . . .	63
4.1.4	Cut-out configuration . . . . .	63
4.2	Optimization process using a Genetic Algorithm . . . . .	66
<b>5</b>	<b>Implementation of the Optimization</b>	<b>70</b>
5.1	Fitness function determination . . . . .	70
5.1.1	Weight determination . . . . .	70
5.1.2	Simulation to obtain stiffness and buckling behavior . . . . .	72
5.1.3	Determination of the weighing factors: . . . . .	78
5.2	Genetic Algorithm implementation . . . . .	78
5.2.1	Initialization (Python code) . . . . .	79
5.2.2	Simulations (Abaqus using hpc12) . . . . .	84
5.2.3	Selection (Excel sheet) . . . . .	85
5.2.4	Creation of the next generation (Python code) . . . . .	85
<b>6</b>	<b>Results of the Optimization</b>	<b>88</b>
6.1	Presentation of the Genetic Algorithm results . . . . .	88
6.2	Optimal design obtained . . . . .	89
6.3	Simulations details . . . . .	92
6.3.1	Reduction of the design space . . . . .	92
6.3.2	Termination criteria . . . . .	94
<b>7</b>	<b>Conclusion</b>	<b>96</b>
7.1	Thesis overview . . . . .	96
7.2	Recommandations . . . . .	97
	<b>References</b>	<b>99</b>
<b>A</b>	<b>Appendix A : Genetic Algorithm Results</b>	<b>105</b>

# List of Figures

1.1	Previous results obtained by Bisagni et al. in [1]	2
2.1	Optimization formulation with the design variables to find, the optimization objective to minimize, and the constraints subjected to the problem. Adapted from [13]	7
2.2	Heterogeneous QUAD properties change with tapering, while homogenized Double Double properties remain constant. Adapted from [37]	8
2.3	Outer- and inner-blending comparison. Adapted from [27]	9
2.4	Continuous and discrete design space of the in-plane parameters $V_1^A$ and $V_3^A$ . Adapted from [27]	11
2.5	Typical SpaRibs design in a wing structure. Adapted from [57]	13
2.6	Comparison between Hooke's law and multi-linear behavior	13
2.7	Thickness distribution of the skin (in mm) over the 28 zones. Adapted from [34]	14
2.8	multi-objectives optimization formulation. Adapted from [67]	17
2.9	Conversion from multi-objective functions to single objective function thanks to weighing factors. Adapted from [64].	17
2.10	Illustration of the Pareto optimal front with two objectives functions. Adapted from [61]	18
2.11	Choosing a solution from the Pareto front. Adapted from [14]	19
2.12	Multi-level optimization approach. Adapted from [71]	19
2.13	Multi-step optimization framework. Adapted from [27]	21
2.14	Two level optimization: preliminary design and detailed design. Adapted from [14]	21
2.15	General idea of Multi-fidelity optimization using HFM and LFM. Adapted from [71]	22
2.16	Models with increasing structural fidelity of the NASA CRM wing box. Adapted from [66]	23
2.17	Robust Design Optimization illustration: Probability Density Function (PDF) against the objective function. Adapted from [49]	24
2.18	Robust Design Optimization mathematical formulation. Adapted from [71]	24
2.19	Robust Design Optimization illustration: Probability Density Function (PDF) against Nonlinear Postbuckling Strength (NPS). Adapted from [72]	25
2.20	Reliability-Based Design Optimization illustration. Adapted from [49]	25
2.21	Reliability-Based Design Optimization mathematical formulation. Adapted from [49]	26
2.22	Reliability-Based Design Optimization illustration. Adapted from [49]	26
2.23	Crossover and Mutation selection procedures of the Genetic Algorithm (GA). Adapted from [84]	27
2.24	Typical Genetic Algorithm flowchart. Adapted from [85]	28
2.25	Typical Particle Swarm Optimization flowchart. Adapted from [89]	29
2.26	Typical Black Widow Optimization Algorithm flowchart. Adapted from [90]	30
3.1	Basic coupon geometry. Dimensions : 100mm (x-dir), 10 mm (z-dir), 1 mm (y-dir)	32
3.2	Load case for tension test	33
3.3	Mesh of the coupon geometry	33
3.4	Stress Strain curve obtained	34
3.5	Simulation 1 : $[0/0/0/0]_s$ . (a) Stacking sequence; (b) Stress-Strain Curve obtained	35
3.6	Simulation 2 : $[90/90/90/90]_s$ . (a) Stacking sequence; (b) Stress-Strain Curve obtained	36
3.7	Stacking sequence of the simulation 3: $[0/-45/45/90]_s$	36
3.8	Strains through the thickness for the quasi-isotropic laminate	37
3.9	Stacking sequence of the simulation 4: $[0/30]_4$	38
3.10	Strains through the thickness for the simulation 4: $[0/30]_4$	38
3.11	Different failure modes of the simulations.	40
3.12	Hashin Fiber Tension through the plies in the Quasi-Isotropic laminate	40
3.13	Different failure criteria available with Abaqus	41

3.14	Failure criteria comparison on simulation 1: $[0/0/0/0]_s$ . . . . .	41
3.15	Failure criteria comparison on simulation 2: $[90/90/90/90]_s$ . . . . .	42
3.16	aluminum plate loading case . . . . .	44
3.17	Mesh of the aluminum plate . . . . .	44
3.18	Buckling of the aluminum plate . . . . .	44
3.19	First buckling mode of the aluminum plate, obtained with <b>Dynamic, Implicit</b> analysis .	46
3.20	Load displacement curve of the aluminum plate obtained with <b>Dynamic, Implicit</b> analysis	46
3.21	First two buckling modes of the $[0/0/0/0]_s$ plate, obtained with linear buckling analysis	47
3.22	First buckling mode of the $[0/0/0/0]_s$ plate, obtained with <b>Dynamic, Implicit</b> analysis .	48
3.23	Load displacement curve of the $[0/0/0/0]_s$ plate obtained with <b>Dynamic, Implicit</b> analysis	48
3.24	First two buckling modes of the $[90/90/90/90]_s$ plate, obtained with linear buckling analysis	49
3.25	First buckling mode of the $[90/90/90/90]_s$ plate, obtained with <b>Dynamic, Implicit</b> analysis	49
3.26	Load displacement curve of the $[90/90/90/90]_s$ plate obtained with <b>Dynamic, Implicit</b> analysis . . . . .	50
3.27	First two buckling modes of the $[0/45/-45/90]_s$ plate, obtained with linear buckling analysis . . . . .	50
3.28	First buckling mode of the $[0/45/-45/90]_s$ plate, obtained with <b>Dynamic, Implicit</b> analysis	51
3.29	Load displacement curve of the $[0/45/-45/90]_s$ plate obtained with <b>Dynamic, Implicit</b> analysis . . . . .	51
3.30	First two buckling modes of the $[0/15/30/0]_s$ plate, obtained with linear buckling analysis	52
3.31	First buckling mode of the $[0/15/30/0]_s$ plate, obtained with <b>Dynamic, Implicit</b> analysis	52
3.32	Load displacement curve of the $[0/15/30/0]_s$ plate obtained with <b>Dynamic, Implicit</b> analysis . . . . .	53
3.33	Components of the test panel . . . . .	53
3.34	Dimensions of the components (all values are in mm) . . . . .	54
3.35	Tie constraints between the 5 stiffeners and the top surface of the composite plate . . . .	55
3.36	Mesh of the stiffened panel . . . . .	55
3.37	Displacement and Load driven simulation: apply on each node . . . . .	56
3.38	Displacement and Load driven simulation: apply only on the reference node . . . . .	57
3.39	Constraints available between the reference node and all the other nodes of the edge. . .	57
3.40	First Buckling mode obtained with the 6 different simulations. . . . .	58
3.41	Comparison of the buckling behavior of the stiffened panels using various methods. . .	59
4.1	Representative wing component. Adapted from Bisagni et al. [1] . . . . .	60
4.2	Dimensions of the main part of the wing components (Test panel right and rib panel left). Adapted from Bisagni et al. [1] . . . . .	61
4.3	Previous results obtained by Bisagni et al. in [1] and result obtained this year. . . . .	63
4.4	Comparison between the different load-displacement curves presented in Figure 4.3 . .	63
4.5	Rib dimensions . . . . .	64
4.6	Cut-out configuration . . . . .	65
4.7	Cut-out configuration in the wing component . . . . .	65
4.8	Stress concentration around the holes . . . . .	66
4.9	Comparison of the stress between one design with cut-out and another without cut-out.	66
4.10	Flow chart of the Genetic Algorithm developed. . . . .	67
4.11	Crossover and Mutation selection process of the Genetic Algorithm (GA). Adapted from [84] . . . . .	68
5.1	Finite Element Model . . . . .	73
5.2	Wing component with the loading rig for the 4-point bending test. Taken from [1] . . .	73
5.3	4-point bending test. Taken from [1] . . . . .	74
5.4	Vertical displacement of the first simulation . . . . .	75
5.5	Vertical displacement of the second simulation . . . . .	75
5.6	Vertical displacement of the third simulation . . . . .	75
5.7	Load displacement curves of the three simulations . . . . .	76
5.8	Vertical displacement through the simulation . . . . .	77
5.9	Stiffness and buckling assessment . . . . .	77

---

5.10	Flow chart of the optimization . . . . .	79
5.11	Change in the ply number and ply orientation in the .inp file . . . . .	82
5.12	Lines to change the thickness of the ribs . . . . .	82
5.13	Thickness of the stiffeners = 3mm in this case . . . . .	83
5.14	Change in the ply number and ply orientation in the .inp file . . . . .	83
6.1	First two generations of the Genetic Algorithm. . . . .	88
6.2	Fitness function through the generations, normalized to the final value . . . . .	89
6.3	Load displacement curve of the optimal design obtained . . . . .	90
6.4	Vertical displacement through the simulation . . . . .	90
6.5	Hashin's criteria on the optimized structure . . . . .	91
6.6	Out of plane stress of the bottom test panel . . . . .	91
6.7	Mean value of the fitness function of each individual, per generation. Normalized to the value of the last generation. . . . .	93
6.8	Mean value of the fitness function of the "parents", per generation. Normalized to the value of the last generation. . . . .	94
6.9	Summary of the fitness function evolution. . . . .	95

# List of Tables

3.1	Summary of the simulations done	33
3.2	aluminum 6063AT6 properties	34
3.3	USN150B composite Engineering constants (Part 1)[1]	35
3.4	USN150B composite Engineering constants (Part 2)[1]	35
3.5	Strains through the thickness for the quasi-isotropic laminate	37
3.6	Comparison of strain through the thickness between FEA analysis and CLT	38
3.7	USN150B composite Hashin damage properties [1]	39
3.8	Comparison between various failure criteria	42
3.9	Plate of aluminum Alloy 2024-T4 properties	43
3.10	Boundary conditions of the plate	43
3.11	UD Carbon Prepreg IM7/8552 composite Engineering constants [1]	47
3.12	Summary of the composite plate linear buckling analysis	53
3.13	Test Panel components and their materials	54
3.14	Boundary conditions of the stiffened panel	56
3.15	Summary of linear buckling analysis of the stiffened panel	58
3.16	Summary of the buckling analysis of the stiffened panel	59
4.1	Wing components and their materials	61
4.2	Aluminum 6082AT6 properties	61
4.3	Optimization variables of the wing component	61
4.4	Baseline design studied by Bisagni et al. [1]	63
5.1	Three potential candidates for the optimization.	74
5.2	Stiffness and buckling performance of the three individuals.	78
5.3	Summary of the performance of the three individuals.	78
6.1	Optimal design obtained with the simulation.	89
6.2	Summary of the performance of the optimal design.	90
6.3	Optimized design compared to baseline design	91
6.4	Performance of the optimized design compared to the baseline design	92
6.5	Evaluation of the impact of the structural performance on the fitness function.	94
6.6	5 best designs obtained with the simulation.	95

# Nomenclature

## Abbreviations

Abbreviation	Definition
ACO	Ant Colony Optimization
ANN	Artificial Neural Network
BWB	Blended Wing Body
BWO	Black Widow Optimization
CAD	Computer-Aided Design
CAE	Computer-Aided Engineering
CFD	Computational Fluid Dynamics
CFRP	Carbon Fiber Reinforced Polymer
CMA-ES	Covariance Matrix Adaptation-Evolution Strategy
CRM	Common Research Model
DD	Double-Double
EASA	European Aviation Safety Agency
EFEM	Equivalent Finite Element Model
EPM	Equivalent Plate Methodology
FE	Finite Element
FEA	Finite Element Analysis
GA	Genetic Algorithm
GWO	Grey Wolf Optimization
HFM	High-Fidelity Modeling
LASER	Light Aerobatic Simple Economic Robust
LFM	Low-Fidelity Modeling
LP	Lamination Parameters
MCS	Monte Carlo Simulation
MDO	Multi-Disciplinary Optimization
MTOM	Maximum Take-Off Mass
MZFM	Maximum Zero-Fuel Mass
NASA	National Aeronautics and Space Administration
NSGA-II	Non-Dominated Sorting Genetic Algorithm
OEM	Operating Empty Mass
PSO	Particle Swarm Optimization
RBDO	Reliability Based Design Optimization
RDO	Robust Design Optimization
SM	Surrogate Modelling
SPEA-II	Strength Pareto Evolutionary Algorithm
UAV	Unmanned Air Vehicle
VAT	Variable Angle Tow
WCO	Water Cycle Optimization



# Acknowledgments

This Master's thesis is based upon work from COST Action CA18203 - Optimising Design for Inspection (ODIN), supported by COST (European Cooperation in Science and Technology).

First, I would like to thank my supervisor, Prof. Dr. Chiara Bisagni, for her precious guidance and feedback throughout the Master thesis. I want to thank her for letting me work on this exciting subject: optimizing wing structure. I would like to thank her for suggesting multiple topics to me and for giving me suggestions about picking this specific one based on my profile. Additionally, as a student under the direction of Prof. Dr. Chiara Bisagni, I participated in the Composites Design Workshop XXIV on double-double composite, organized by Prof. Tsai, and visited the Airbus Launchers Assembly in Leiden while working on my thesis. I think these are great opportunities that would not be possible without working with Prof. Dr. Chiara Bisagni.

Then, I would like to thank my flatmates, Grégoire, Robin, and Zhana, for all the hours shared around the table, all working on our topics and struggling to understand and help each other with their work. Together with them, I would like to thank my friends, Guillaume, Kübra, Avyadish, Tanuj, Sovit, Javier, and many more, for their presence in the Master room when I was coming on campus to see them and share some coffee breaks with them.

Finally, I would also like to thank my parents and family for their support and their continuous efforts to understand the nature of my work. Their enduring encouragement has been a pillar of strength throughout my academic pursuits.



# Abstract

This thesis aims to study the design and optimization of composite wing components for aircraft, focusing on the pivotal goal of reducing weight while preserving and enhancing structural performance. This is one of the goals of the COST Action joined in the span of the thesis: CA18203 - Optimising Design for Inspection (ODIN). Within this COST Action, a comparison between different Finite Element modeling predictions of the response of this structure subjected to 4-point loading has been presented by Bisagni et al. [1] before this thesis. The thesis, which corresponds to the optimization of this same structure, is the continuity of this work.

The foundation of this thesis is built upon a literature study that investigates the optimization of composite wing structures. It explores diverse optimization formulations, including design variables, objectives, and constraints. Different methodologies for optimizing wing structures, like multi-objective and probabilistic methods, are studied. Various algorithms used to tackle these challenges are presented, shedding light on their advantages and drawbacks.

Once a solid knowledge of wing structure optimization is built, preliminary analyses (study of coupon geometries, failure criteria, and the buckling behavior of various materials and geometries) form the basis for the upcoming optimization strategy. These preliminary investigations refine our understanding and guide the selection of optimal constraints, such as failure criteria.

Based on these preliminary analyses and the literature study, the optimization strategy has been established. A new configuration with cut-outs is developed to explore new innovative designs. To solve the optimization problem, Genetic Algorithms, inspired by real-life behaviors and processes, emerge as the optimization algorithm of choice. These algorithms contribute to the development of design solutions that are better than traditional designs.

The objective is to achieve weight reduction in the structure while considering its structural performance. Consequently, the fitness function, employed to assess candidate designs within the Genetic Algorithm, is based on three primary factors: weight, stiffness, and buckling behavior. Weight carries the most significant part of the fitness function, accounting for approximately 80% of the total value, whereas the remaining two factors contribute approximately 10% each. To evaluate these aspects, weight is determined through basic calculations, while stiffness and buckling behavior are assessed by simulating a 4-point bending test using Abaqus.

The implementation of the Genetic Algorithm, adapted to our special case, allows us to showcase its effectiveness in achieving optimal designs. These optimal designs achieve remarkable weight reductions while maintaining great structural performance. Following 20 generations, each comprising 10 potential candidates, one of the two termination criteria is triggered: there is no improvement in the best solution for eight consecutive generations. The optimized solution obtained is 16.89 kg lighter compared to the baseline configuration studied by Bisagni et al. [1]. This represents a significant 25% reduction in structure weight. Concerning the structural performance, only a reduction of 1.5% and 0.25% is observed for the stiffness and the buckling performance, respectively, which is acceptable regarding the weight reduction. Nonetheless, achieving such a reduction in wing weight may not be realistic as it was specifically tailored for the test case of this thesis, other loading scenarios need to be studied to assess its applicability.

These outcomes underscore the potential of optimization techniques in aerospace engineering, paving the way for the development of lightweight and high-performing composite wing components.

# Introduction

## 1.1. Background and motivation

Evolving towards the lightest aircraft possible is crucial since the aviation industry accounts for 2.5% of global carbon dioxide ( $CO_2$ ) emissions [2]. Despite the COVID-19 pandemic, which temporarily decreased global air travel, the aviation industry is expected to continue its growth trajectory in the coming years [2]. This growth could lead to a significant increase in  $CO_2$  emissions from aviation, which could have severe consequences for the environment and human health [3]. By reducing the weight of large aircraft, fuel consumption decreases, longer flights are possible, and the payload capacity of aircraft increases [4]. Therefore, the evolution towards lighter solutions, provided in part through the use of composite materials and optimization techniques, to reduce the carbon footprint of aviation is essential.

Once the interest in the lightest aircraft is established, in the dynamic and constantly evolving field of aerospace engineering, the pursuit of lightweight yet robust structural designs stands as a significant challenge. With the demand for enhanced performance, fuel efficiency, and safety driving technological advancements, structural optimization emerges as a critical effort [5]. It embodies a multi-factorial approach that requires a deep understanding of material properties, mechanical behavior, and the complex interaction between various design parameters [6]. This pursuit of an optimal balance between strength, weight, and performance has led scientists to explore innovative techniques and methodologies [6] [7]. This thesis explores structural optimization techniques in depth, focusing on the utilization of genetic algorithms to navigate the complex landscape of design possibilities and discover solutions that push back the limits of structural efficiency in aerospace applications.

In this context, there is a demand for effective and creative optimization techniques for lightweight and high-performance aerospace structures. This need stands as one objective of one COST Action. According to their website [8], COST (European Cooperation in Science and Technology) is "a funding organization for research and innovation networks". Their actions aim to connect collaborative research efforts all around Europe and even extend beyond, providing a platform for researchers and innovators to grow their ideas across diverse scientific and technological domains. COST Actions are four years long, fostering research, innovation, and professional growth [8].

For this thesis, I have joined the following COST Action: CA18203 - Optimising Design for Inspection (ODIN). According to their website [9], this action aims to optimize the utilization of continuous, in-service monitoring for critical aerospace structures by integrating technologies such as ultrasonic wave-based non-destructive evaluation (NDE), energy harvesting, and wireless sensor systems during the initial design stage [9]. This Action is divided into five different Working Groups. In my case, I have joined Working Group 1, composed of Aerospace experts, which has the objective of analyzing the requirements for integrating Structure Health Monitoring systems at the creation of an aerospace design [9].

In the span of this Working Group, Bisagni et al. [1] published a paper in April 2022 showing a comparison of different numerical analyses of a composite wing component subjected to a 4-point

bending test. This paper is the basis of the work developed in the thesis, and the main results are presented hereafter in section 1.2.

## 1.2. Previous results

In a study by Bisagni et al., [1], the results of a collaborative effort involving six partners are presented. These partners were all part of the Working Group 1 activities within the ODIN COST Action. The study involved the construction of finite element (FE) models and subsequent numerical analyses of a representative wing component. Various FE codes were employed by each partner for their analyses. For this collaborative study, a comprehensive CAD model of the structure was provided, including the loading fixture and details of the component materials. This standardized CAD model was distributed to each participating partner. The key aspect of this study was that each partner conducted a "blind prediction" of the structural behavior of the wing component. The outcome of this blind prediction was then compared against the experimental results obtained from physical testing. This comparison aimed to assess the accuracy and reliability of the numerical analyses conducted by the different partners using various FE codes. The study thus highlighted the effectiveness and consistency of the FE modeling techniques employed by the different partners and provided insights into the overall predictive capability of the chosen FE codes in simulating the structural behavior of the wing component.

The results of the comparison revealed that the experimental load-displacement characteristics exhibited a linear trend, consistent with the predictions obtained from the various numerical models [1]. However, it was observed that the experimental setup yielded a lower stiffness compared to the predictions made by the numerical models. Bisagni et al. [1] discussed several potential reasons to account for this disparity, which included possible clearances between mounted components, excessive compliance in the supporting structure, and inaccuracies in the material property data used in the simulations.

Despite these variations, it is noteworthy that the initial stiffness predicted by each of the numerical models remained consistent. This observation is graphically illustrated in Figure 1.1a, which is provided in the work by Bisagni et al. [1]. For a more comprehensive understanding of the diverse numerical models employed in this comparison, as well as detailed insights into the experimental setup, readers are encouraged to refer to the paper authored by Bisagni et al. [1].

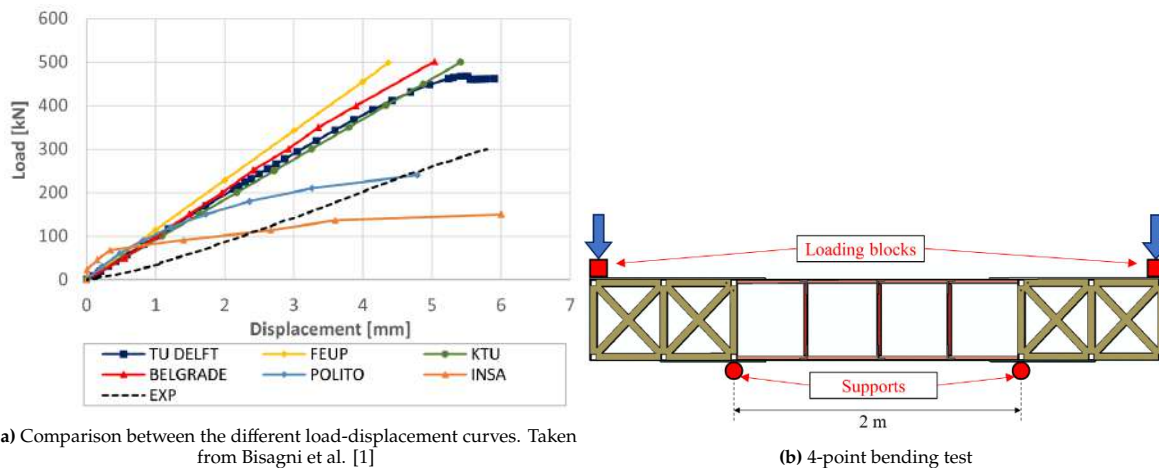


Figure 1.1: Previous results obtained by Bisagni et al. in [1]

### 1.3. Objective and research question

After the publication of the paper presented in section 1.2, the next objective of Working Group 1 concerning this project was to numerically optimize the composite wing component and then manufacture the optimized structure to compare the numerical results with the experiments once more. The optimization of the wing component is the objective of my thesis. Therefore, the main research question to be answered in reaching the project goal is the following:

- **How can optimization using a Genetic Algorithm be used to reduce the weight of a composite wing component, while taking structural performance into account?**

To solve this research question, the following process was undertaken. Firstly, an in-depth review of the literature concerning the optimization of composite structures was conducted. Subsequently, basic cases were analyzed using Abaqus, helping to refine the optimization strategy. Then, based on the literature study, a strategy, using a Genetic Algorithm, was developed and created according to the case of the composite wing component. Once the strategy was established, its subsequent implementation took place. Finally, based on the results obtained and the strategy chosen to minimize the weight of the structure, the research question is solved.

### 1.4. Structure of the report

The first chapter is focused on understanding the field through a literature study. After explaining the basic concepts of failure criteria and design guidelines for composite design, a detailed examination of the design variables, the optimization objectives, and the types of constraints is presented. Various types of optimizations, such as multi-objective, multi-level, multi-step, multi-fidelity, and probabilistic optimizations, as well as different optimization algorithms are finally discussed in this first chapter.

Then, the second chapter embarks on preliminary analyses, including investigations into coupon, plate, and stiffened panel geometry. Failure criteria and buckling behaviors of different materials are investigated in this chapter.

The third chapter introduces the optimization strategy, detailing the problem statement and the optimization formulation.

A detailed presentation of the implementation of the optimization process using a Genetic Algorithm is presented in the fourth chapter, covering aspects like fitness function determination and algorithm implementation.

Finally, the report ends with the fifth chapter, revealing the results of the optimization process. Details of the optimal design obtained, simulation features such as the reduction of the design space, and termination criteria choice are meticulously described, providing an overview of the outcomes achieved through the application of the Genetic Algorithm.

# 2

## Literature Study

This first section aims to introduce the literature study useful in the span of the master thesis. First, general ideas about composite wing structure analysis (such as the failure criteria) will be reminded, and then, an overview of the different optimization formulations that can be found in the literature will be proposed. Finally, a classification of those formulations into different types of optimization and the algorithms often developed to solve them will be presented

### 2.1. Composite wing structure analysis

The 1960s saw the development of the widely used design tool known as Classical Lamination Theory (CLT), which allows for the analysis of complicated processes that may take place in composite laminates. It can predict the strains, and displacements that a laminate would experience under mechanical and thermal loading. As this theory is well known nowadays and can easily be found in many textbooks from the literature (e.g., [10] or [11]), it has been chosen not to report it in this literature study.

#### 2.1.1. Failure criteria

Before starting with the different failure criteria that exist, the failure modes usually recognized are:

- Tension failure along the fibers with strength symbol  $X_T$
- Compression failure along the fibers with strength symbol  $X_C$
- Tension failure transverse to the fibers with strength symbol  $Y_T$
- Compression failure transverse to the fibers with strength symbol  $Y_C$
- Pure shear failure of a ply with strength symbol  $S$
- Delamination.

Five of the main failure criteria will be presented hereafter. Other criteria have been developed, such as the Puck criteria [10], the LaRC03 failure criterion [12], or the global failure criterion [13], but it has been chosen not to explain them here since they are less common than the five following ones.

#### Tsai-Wu failure criterion

The Tsai-Wu failure criterion was developed to provide a mathematical generalization of the Tsai-Hill failure criterion [10]. It was created by fitting a curve based on tensor theory to account for the fact that composites have different strengths in tension and compression [10]. The criterion takes the following form:

$$\frac{\sigma_x^2}{X_T X_C} + \frac{\sigma_y^2}{Y_T Y_C} - \sqrt{\frac{1}{X_T X_C Y_T Y_C}} \sigma_x \sigma_y + \left( \frac{1}{X_T} - \frac{1}{X_C} \right) \sigma_x + \left( \frac{1}{Y_T} - \frac{1}{Y_C} \right) \sigma_y + \frac{\tau_{xy}^2}{S^2} = 1 \quad (2.1)$$

with the tension failure strength along the fibers  $X_T$ , the compression failure strength along the fibers  $X_C$ , the tension failure strength transverse to the fibers  $Y_T$ , the compression failure strength transverse

to the fibers  $Y_C$ , and pure shear failure strength  $S$

Tsai-Wu failure criteria are the most commonly used criteria to assess failure when dealing with the optimization of composite structure [14][15][16][17][18][19][20][21][22].

### Tsai-Hill failure criterion

Hill was among the first to propose a failure criterion with the combination of both strain and stress for composite material [10]. He expressed it first as follows [23]:

$$F_x \sigma_x^2 + F_y \sigma_y^2 + F_S \tau_{xy}^2 + F_{xy} \sigma_y \sigma_x = 1 \quad (2.2)$$

Then, Tsai determined the stress coefficients in Equation 2.2 by considering three simple loading situations: Firstly, only  $\sigma_x$  acts on a ply with corresponding strength  $X$ ; Secondly, only  $\sigma_y$  acts with corresponding strength  $Y$ ; Thirdly, only  $\tau_{xy}$  acts with corresponding strength  $S$ [10]. For example, if only  $\sigma_y$  acts, Equation 2.2 gives:

$$F_y \sigma_y^2 = 1 \quad (2.3)$$

It is also known that if only  $\sigma_y$  acts, which is perpendicular to the fibers, failure will occur when  $\sigma_y^2$  equals  $Y^2$ . Re-injecting it into Equation 2.4 gives directly [10]:

$$F_y = \frac{1}{Y^2} \quad (2.4)$$

Based on the three simple loading cases and one more condition by considering the original three-dimensional form of the Hill yield criterion [23], the final version of the Tsai-Hill criterion is :

$$\frac{\sigma_x^2}{X^2} + \frac{\sigma_y^2}{Y^2} + \frac{\tau_{xy}^2}{S^2} - \frac{\sigma_y \sigma_x}{X^2} = 1 \quad (2.5)$$

However, the Tsai-Wu criterion is often preferred compared to the Tsai-Hill criterion. It has been used fewer times for the optimization of composite structures [24][25].

### Maximum stress failure theory

The maximum stress failure criterion is a simple failure criterion used in the design and analysis of structures. It is based on the assumption that a material will fail when the maximum stress in the material exceeds its allowable stress, which is the corresponding strength values  $X_T$ ,  $X_C$ ,  $Y_T$ ,  $Y_C$  and  $S$ . The mathematical formulation of the maximum stress failure theory is the following [10]:

$$\begin{aligned} \sigma_x &< X_T \text{ or } X_C \quad \text{depending on whether } \sigma_x \text{ is tensile or compressive} \\ \sigma_y &< Y_T \text{ or } Y_C \quad \text{depending on whether } \sigma_y \text{ is tensile or compressive} \\ |\tau_{xy}| &< S \end{aligned} \quad (2.6)$$

This straight-forward criterion has been used in multiple optimizations for composite structures [4][24][15].

### Maximum strain failure theory

Similarly to the maximum stress failure theory, the maximum strain failure criterion is based on the assumption that a material will fail when the maximum strain in the material exceeds its allowable strain. Therefore, it can be expressed as follows:

$$\begin{aligned} \epsilon_x &< \epsilon_{xu}^T \text{ or } \epsilon_{xu}^C \quad \text{depending on whether } x \text{ is tensile or compressive} \\ \epsilon_y &< \epsilon_{yu}^T \text{ or } \epsilon_{yu}^C \quad \text{depending on whether } \epsilon_y \text{ is tensile or compressive} \\ |\gamma_{xy}| &< \gamma_{xyu} \end{aligned} \quad (2.7)$$

where  $\epsilon_x$ ,  $\epsilon_y$  and  $\gamma_{xy}$  are ply strains in the ply coordinate system ( $x$  parallel to fibers and  $y$  perpendicular to fibers). Also,  $\epsilon_{xu}^T, \epsilon_{xu}^C, \epsilon_{yu}^T, \epsilon_{yu}^C$  and  $\gamma_{xyu}$  are allowable strains in the corresponding direction and loading (tensile or compressive). Blair et al. [24] used it to analyze the composite layup of their structure. However, Sinha et al. [26] highlight that this failure criterion may be conservative.

### Hashin criteria

Unlike the other criteria previously explained, the Hashin criterion considers two failure modes: fiber failure and matrix failure. Fiber failure occurs when the tensile or compressive stress in the fibers reaches a critical value, while matrix failure occurs when the shear stress in the matrix exceeds a critical value [10]. Therefore, composite materials have multiple failure modes and the Hashin criterion can identify them and evaluate failure occurrences [13]. The Hashin criterion can be formulated as follows [13]:

$$\begin{aligned}
 \text{Fiber tensile failure: } \phi_{1T} &= \left( \frac{\sigma_{11}}{X_{1T}} \right)^2 + \left( \frac{\tau_{12}}{S_{12}} \right)^2 \geq 1 \\
 \text{Fiber compression failure: } \phi_{1C} &= \left( \frac{\sigma_{11}}{X_{1C}} \right)^2 \geq 1 \\
 \text{Matrix tensile failure: } \phi_{2T} &= \left( \frac{\sigma_{22}}{X_{2T}} \right)^2 + \left( \frac{\tau_{12}}{S_{12}} \right)^2 \geq 1 \\
 \text{Matrix compression failure: } \phi_{2C} &= \left( \frac{\sigma_{22}}{2S_{21}} \right)^2 + \left[ \left( \frac{X_{2C}}{2S_{21}} \right)^2 - 1 \right] \frac{\sigma_{22}}{X_{2C}} + \left( \frac{\tau_{12}}{S_{12}} \right)^2 \geq 1
 \end{aligned} \tag{2.8}$$

where  $\sigma$  and  $\tau$  are respectively the ply normal and shear stresses. In addition,  $X$  and  $S$  are normal and shear strengths of the composite laminate. In subscripts, 1 and 2 represent the ply axis direction, and  $T$  and  $C$  stand for tensile and compressive [13].

### 2.1.2. Composite design guidelines

Analysis of trends, test results, and experience all contribute to the development of design guidelines. There is no justification for strictly adhering to any of the recommendations. Deviations from them are frequently required, as shown by the example of an unbalanced layup in the aeroelastic tailoring of aircraft wings [27]. There is no reason to restrict the designs by adhering to all these standards strictly. However, the basic ones, which are among the most important, will be presented hereafter.

- **Balance:** The layup should be balanced. For every ply angle  $\theta$ , a  $-\theta$  ply should be present in the layup to eliminate both stretching and shearing coupling ( $A_{16} = A_{26} = 0$ ) [10][28] [29] [30][27]. Even if this is beneficial in most designs, unbalanced designs can be advantageous for some designs (e.g., in the aeroelastic tailoring of aircraft wings)[27].
- **Symmetry:** The layup should be symmetric about the mid-ply. As a result, the B matrix is zero, avoiding bending, coupling, warping, and twisting effects [10][28] [29] [30][27].
- **The 10% rule:** The stacking sequence should contain at least 10% of plies with each of the four principal directions:  $0^\circ$ ,  $45^\circ$ ,  $45^\circ$ , and  $90^\circ$  [10] [27]. This protects against unexpected secondary load cases. Indeed, these loads have small load magnitudes, so they are not included in the design process. Since they are not expected, they could lead to premature failure if this rule is not followed [10] [27]. In some cases, other values are chosen instead of 10%. Barkanov et al. [30] decided to require at least 8% of each orientation.
- **$\pm 45^\circ$  plies in the outer layers:** The ply orientations of the outer layers of the stacking sequence should be  $\pm 45^\circ$  plies. It provides better impact resistance by protecting the main load-carrying layers, closer to the middle of the stacking sequence [28] [29] [27].  $\pm 45^\circ$  plies away from the mid-ply limit the amount of fiber splitting [10]. Moreover, buckling resistance is also improved by placing  $\pm 45^\circ$  layers away from the mid-ply [27].
- **Ply Contiguity:** The number of unidirectional ply with the same orientation next to each other should be minimized (not exceeding 2 to 4 plies). Indeed, with multiple plies with the same orientation next to each other, delamination and residual stresses are more likely to happen. As an example, a matrix crack can grow more easily and extend from one end of the identical ply orientation to the other without being arrested. To not exceed 0.6–0.8 mm (corresponding typically to 4–5 plies) [10] [28] [29] [27].

These are the basic composite design guidelines followed by most of the designs. It exists in many more rules, well described with their effects on the design in [10]. Depending on the goal of the design (e.g., for bending, or buckling), some rules need to be followed carefully, while others can be avoided.



## 2.2. Optimization formulation

To reduce the overall weight of a panel structure by optimizing the stacking sequence, taking into account the buckling constraints, or to increase the buckling performance by changing the number of spars and ribs in a wing structure, when considering the optimization of a composite structure in general, the different formulations done in the literature tend to have one similar approach: one, or several, **design variables** are optimized to reach the **optimization objectives** while considering the **constraints** of the problem.

$$\begin{aligned}
 &\text{find } \mathbf{t} = \{t_j\} \\
 &\quad \boldsymbol{\theta} = \{\theta_{ij}\}, \quad i = 1, 2, \dots, m_1 \\
 &\quad j = 1, 2, \dots, m_2 \\
 &\text{min } W = f(\mathbf{t}, \boldsymbol{\theta}) \\
 &\text{subject to } \psi_{i_1}^{\text{static}}(\mathbf{t}, \boldsymbol{\theta}, T) \leq 0, \quad i_1 = 1, 2, \dots, m_3 \\
 &\quad \psi_{i_2}^{\text{fatigue}}(\mathbf{t}, \boldsymbol{\theta}, T) \leq 0, \quad i_2 = 1, 2, \dots, m_4 \\
 &\quad \psi_{i_3}^{\text{damage tolerance}}(\mathbf{t}, \boldsymbol{\theta}, T) \leq 0, \quad i_3 = 1, 2, \dots, m_5 \\
 &\quad m_1, m_2, m_3, m_4, m_5 \in N+
 \end{aligned}$$

**Figure 2.1:** Optimization formulation with the design variables to find, the optimization objective to minimize, and the constraints subjected to the problem. Adapted from [13]

In section 2.2, the different variables available for optimization and their effect on the overall formulation will be presented in subsection 2.2.1. Then, the objectives and the concept of multi-objective optimization will be introduced in subsection 2.2.2. Finally, the constraints mainly observed in the literature for the optimization of composite structures will be shown in subsection 2.2.3.

### 2.2.1. Design variables

When dealing with the optimization of a composite structure, multiple design variables are available. The objective of this section is to understand the perspectives given by the different variables and assess their impact on the overall optimization.

#### Ply orientation

The main design variables often considered in the optimization formulation of composite structures are related to the plies, mainly the number of plies in the stacking sequence, and the orientation of these plies. The general idea when optimization is using thickness and ply orientation as design variables is to find the best laminate that meets the design guidelines summarized in subsection 2.1.2 as best as possible to fulfill the optimization objectives, accounting for the constraints. As an example, Guo et al. in [31] used the thickness of the laminate ply and the orientation of the wing skins as design factors. In the first step of their optimization, they decreased the weight by 44.6%. Bin Kamarudin et al. in [32] studied the impact of different stacking sequences on the critical buckling load of structures with different types of holes. Many other studies take thickness and ply orientation as design variables. [33] [5] [34] [35].

These previous examples use the number of plies in the stacking sequence and their orientation as design variables with the main objective to follow as many design guidelines as possible with the QUAD laminate (with 4 main orientations  $[0, \pm 45, 90]$ ), to fulfill the structural requirements of their structure. However, it is also possible to consider the plies as design variables in other types of configurations.

The first one is the **Double Double composite**, a new family of composites introduced by Tsai et al. in [36] characterized by a specific laminate description  $[\pm\Phi, \pm\Psi]_{rT}$  where  $r$  is the number of repeats and  $T$  is the total number of plies. It promises great advantages for aerospace laminates. Indeed, the traditional QUAD laminates have detailed design guidelines such as the mid-plane symmetry to avoid out-of-plane warping of the laminates, the 10% rule such that each ply angle exists in the laminate, and

the balanced laminates to maintain in-plane isotropy. These basic instructions make ply-drops very difficult and restrict a lot of the available optimization of QUAD laminates. [18] On the contrary, Double Double laminate, thanks to its four plies building block that is repeated to build the laminate, simplifies both laminate manufacturing and laminate optimization. They need only Tsai's modulus to fully characterize the material stiffness. Only one stacking sequence is available instead of thousands when dealing with QUAD laminate. [37] Moreover, Double Double laminate makes tapering easy, whereas it is almost impossible to consider it with QUAD laminates due to the balance and symmetry required for them. [37] As shown in Figure 2.2, homogenization is another important enabling feature of Double Double laminate. It allows a reduction in laminate thickness without changing the laminate properties. This is not possible with QUAD laminate because ply drops do change its laminate properties, and it is too thick to be homogenized [37].

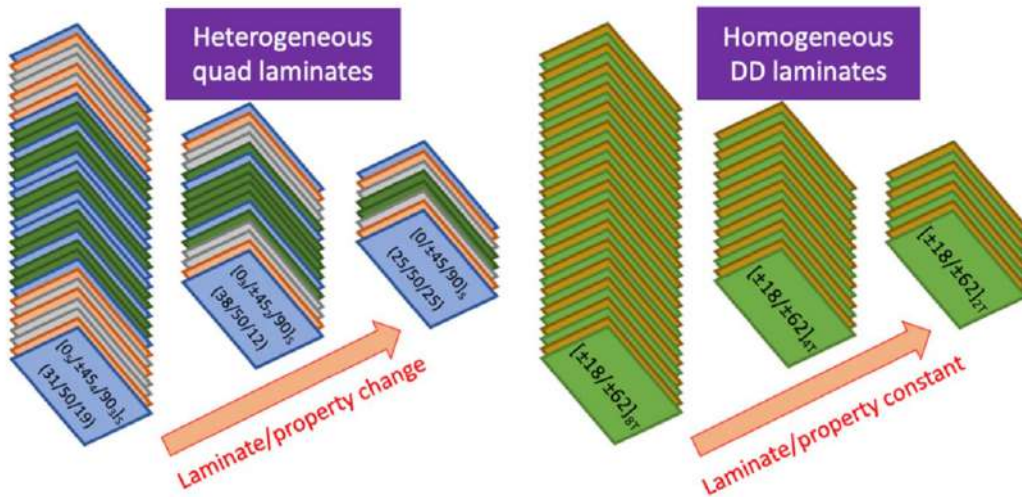


**Figure 2.2:** Heterogeneous QUAD properties change with tapering, while homogenized Double Double properties remain constant. Adapted from [37]

Due to the reasons presented previously, the studies that have been done considering Double Double laminate as design variables offer great expectations for the potential mass reduction offered by Double Double laminate. Shrivastava et al. in [18] presented an optimization algorithm that shows 68–70% mass reduction for a full-length ply wing-box model when replacing Double Double laminates compared to QUAD laminates. Zhang et al. in [38] also used Double Double laminate to compare the ability of multiple machine learning methods to predict the displacement field of a 2D wing-shaped model under three loading conditions (tension, shear, and bending).

The second one is the **Variable Angle Tow (VAT) laminates**. When dealing with tow-steered laminates, the fiber angles vary continuously in the plane of the ply. With a variable stiffness, the buckling loads can be increased by adjusting the stiffness of the plate based on the stress on the plate [39]. It can reduce stress concentrations around structural discontinuities, such as a hole [40]. Multiple improvements in structural performance can be achieved by adopting curved fiber paths and thereby tailoring stress distributions in the structure. [22] Perspectives offered by Variable Angle Tow laminates lead to multiple comparisons between traditional straight-fiber plies and plies with continuously varying fiber orientations [39]. As an example, Wang et al. [22] reached a 10% weight reduction in their optimization using tow-steered laminates.

### Blending

To efficiently design lightweight structures, an equally loaded material mindset is needed. This is achieved by defining regions of different stiffness throughout the structure based on the varying load distribution. Each of these regions can be represented by a stacking sequence, which can be modified by adding or removing plies to accommodate the stiffness layout of the different regions. The variation of these properties along the structures leads to discontinuities in the fiber path, leading to stress concentrations that can contribute to delamination effects. [27] The ply compatibility along the structure also ensures that a laminated composite panel is manufacturable [29]. Therefore, it is necessary to

consider strategies to optimize layer continuity and ply drops in variable stiffness composite laminates [28]. This is usually called "blending" [27].

One of the earliest methods for blending proposed by Liu and Haftka [41] involves the use of a continuity measure between adjacent laminates to control both the fiber continuity at the global level and the stacking sequence at the local level. This method uses minimum continuity constraints in a two-step optimization with a genetic algorithm for stacking sequence retrieval, demonstrating that high fiber continuity can be achieved throughout the structure without a significant increase in weight.

Another approach to blending is the "greater-than-or-equal-to" blending strategy introduced by Kristinsdottir et al. [42] In this method, plies can be progressively dropped depending on the loads, resulting in an efficient structure. However, the achievable structural efficiency is limited as removed ply cannot be re-added, which can result in over-designed low-load regions.

Soremekun et al. [43] proposed a two-step strategy based on sub-laminates, where sub-laminates covering the entire structure are defined in the first step based on the thinnest region, followed by a second step where the remaining sub-laminates are defined for the remaining unassigned thickness regions. These sub-laminates are then optimized by a Genetic Algorithm until a satisfactory solution is retrieved.

Adams et al. [44] proposed a guideline-based strategy for blending composite laminates. This method describes the variable stiffness composite laminates with a guide stacking sequence that matches the thickest region in the structure and subsequent ply drops. This method has the advantage that all solutions are inherently blended, which removes the need for blending constraints in the GA. The guide-based approach introduces two types of blending, outer and inner-blending (see Figure 2.3), which depend on whether the outermost or innermost plies can be dropped.

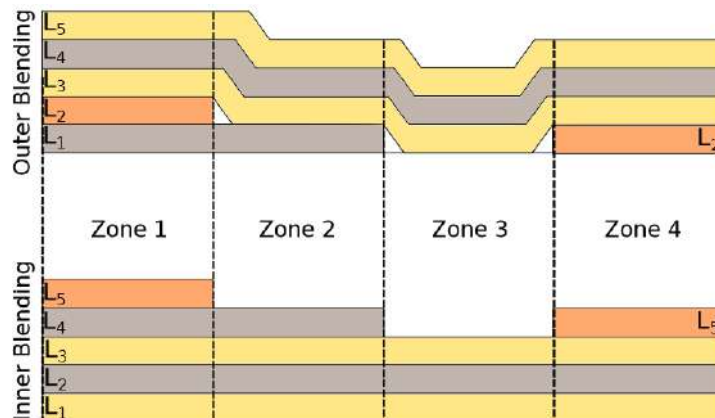


Figure 2.3: Outer- and inner-blending comparison. Adapted from [27]

### Lamination Parameters

A direct correlation between stiffness characteristics and the stacking sequence in terms of layer thicknesses and fiber angles is well known by the development of stiffness matrices using classical lamination theory. Therefore, instead of characterizing the stiffness as a function of the stacking sequence, another option is to represent the laminate stiffness matrices as a function of the **lamination parameters**. [11]

The lamination parameters, which were first established by Tsai et al. in [45], represent an integrated form of the layer angles over the laminate thickness as shown in Equation 2.9

$$\begin{aligned}
(V_1^A, V_2^A, V_3^A, V_4^A) &= \frac{1}{h} \int_{-\frac{h}{2}}^{\frac{h}{2}} (\cos(2\theta), \sin(2\theta), \cos(4\theta), \sin(4\theta)) dz \\
(V_1^B, V_2^B, V_3^B, V_4^B) &= \frac{4}{h^2} \int_{-\frac{h}{2}}^{\frac{h}{2}} z (\cos(2\theta), \sin(2\theta), \cos(4\theta), \sin(4\theta)) dz \\
(V_1^D, V_2^D, V_3^D, V_4^D) &= \frac{12}{h^3} \int_{-\frac{h}{2}}^{\frac{h}{2}} z^2 (\cos(2\theta), \sin(2\theta), \cos(4\theta), \sin(4\theta)) dz
\end{aligned} \tag{2.9}$$

Related to the lamination parameters, the material invariant  $U_i$ , which only depends on material properties and not on the stacking sequence, can be derived from elements of the reduced stiffness matrix, as follows :

$$\begin{aligned}
U_1 &= (3Q_{11} + 3Q_{22} + 2Q_{12} + 4Q_{66})/8 \\
U_2 &= (Q_{11} - Q_{22})/2 \\
U_3 &= (Q_{11} + Q_{22} - 2Q_{12} - 4Q_{66})/8 \\
U_4 &= (Q_{11} + Q_{22} + 6Q_{12} - 4Q_{66})/8 \\
U_5 &= (Q_{11} + Q_{22} - 2Q_{12} + 4Q_{66})/8
\end{aligned} \tag{2.10}$$

From these invariants, Equation 2.10, the material invariant matrices  $\Gamma_i$  can be obtained. Again, because the material invariant  $U_i$  only depends on material properties and not on fiber angle, the material invariant matrices  $\Gamma_i$  only depend on material properties.

$$\begin{aligned}
\Gamma_0 &= \begin{bmatrix} U_1 & U_4 & 0 \\ U_4 & U_1 & 0 \\ 0 & 0 & U_5 \end{bmatrix}, \quad \Gamma_1 = \begin{bmatrix} U_2 & 0 & 0 \\ 0 & -U_2 & 0 \\ 0 & 0 & 0 \end{bmatrix}, \quad \Gamma_2 = \begin{bmatrix} 0 & 0 & U_2/2 \\ 0 & 0 & U_2/2 \\ U_2/2 & U_2/2 & 0 \end{bmatrix} \\
\Gamma_3 &= \begin{bmatrix} U_3 & -U_3 & 0 \\ -U_3 & U_3 & 0 \\ 0 & 0 & -U_3 \end{bmatrix}, \quad \Gamma_4 = \begin{bmatrix} 0 & 0 & U_3 \\ 0 & 0 & -U_3 \\ U_3 & -U_3 & 0 \end{bmatrix}
\end{aligned} \tag{2.11}$$

Thanks to these material invariant matrices  $\Gamma_i$  and the lamination parameters described in Equation 2.9, the material stiffness matrices can be computed as follows: [27]

$$\begin{aligned}
\mathbf{A} &= h \left( \Gamma_0 + \Gamma_1 V_1^A + \Gamma_2 V_2^A + \Gamma_3 V_3^A + \Gamma_4 V_4^A \right) \\
\mathbf{B} &= \frac{h^2}{4} \left( \Gamma_1 V_1^B + \Gamma_2 V_2^B + \Gamma_3 V_3^B + \Gamma_4 V_4^B \right) \\
\mathbf{D} &= \frac{h^3}{12} \left( \Gamma_0 + \Gamma_1 V_1^D + \Gamma_2 V_2^D + \Gamma_3 V_3^D + \Gamma_4 V_4^D \right)
\end{aligned} \tag{2.12}$$

Therefore, the lamination parameters constitute a set of twelve continuous variables that along, with a laminate thickness  $h$ , can describe the material stiffness matrices [11]. Moreover, lamination parameters may, in theory, vary independently, but only within regions that can provide feasible stacking sequences. This suggests that a parameter's range of variation depends on all other parameters. This defines some feasible regions for any combination of lamination parameters. Figure 2.4 depicts the feasible region of the in-plane lamination parameters  $V_1^A$  and  $V_3^A$  for a balanced-symmetric laminates. The continuous design space is the entire region enclosed by the quadratic function. The feasible space is reduced to the triangular area inside the dashed lines, assuming an infinite number of plies, by limiting the permitted ply angles to combinations of  $[0, 90, \pm 45]$  layers in the discrete step. The design space becomes discrete when the number of plies is limited. The only choices for an 8-ply laminate subject to balance and symmetry restrictions are shown by the red dots in Figure 2.4. Thus, to get laminates with realistic stiffness qualities, feasible limitations resulting from the interdependency between lamination

parameters must be addressed. Implementing these limitations on a feasible basis is computationally costly. To deal with this drawback for the lamination parameters, Macquart et al. in [46] showed that, without the use of computationally expensive feasibility restrictions, maps can guarantee lamination parameter feasibility at each step of the optimization process.

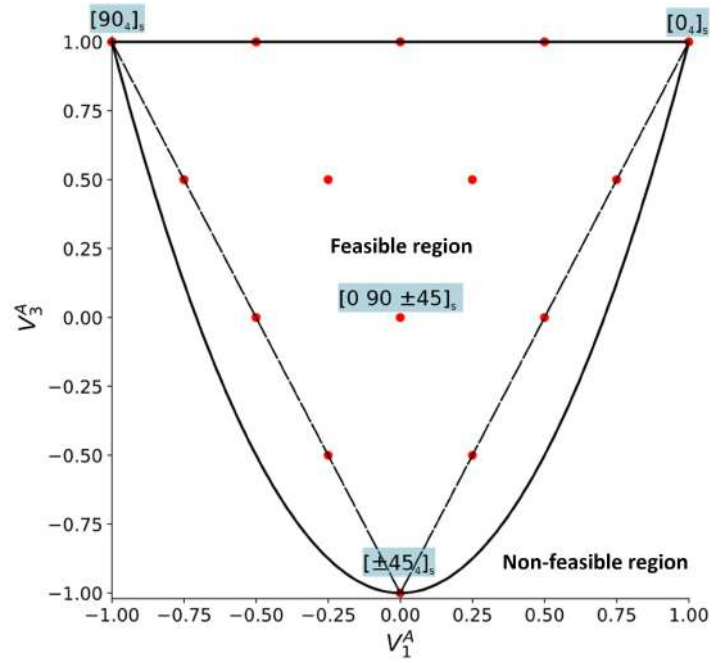


Figure 2.4: Continuous and discrete design space of the in-plane parameters  $V_1^A$  and  $V_3^A$ . Adapted from [27]

As previously said, an arbitrary stacking sequence can be described using the entire set of twelve lamination parameters. In the case of a symmetric laminate, the coupling matrix  $B$  vanishes, so  $V_{iB} = 0$ . Therefore, a symmetric, unbalanced laminate with filled stiffness matrices is what is often specified by the eight remaining lamination parameters for  $A$  and  $D$ . When the laminate is also balanced, the lamination parameters  $V_{2A}$ ,  $V_{4A}$ ,  $V_{2D}$ , and  $V_{4D}$  are zero. As a result, only four lamination parameters can adequately define symmetric and balanced laminates, reaching a simpler and easier optimization [11].

Compared to a representation using layer thicknesses and angles, the description of laminate stiffness qualities using lamination parameters has two major advantages. First, thanks to the formulation of the lamination parameters outlined above, the number of variables representing the stiffness properties is fixed at a maximum of twelve lamination parameters and one thickness. On the other hand, for the stacking sequence description, a specification of  $2n$  variables is necessary, where  $n$  is the number of layers in the laminate. The number of variables needed for a stiffness description substantially exceeds the one needed with the lamination parameter when stacking sequences in industrial applications feature tens or even hundreds of layers within a laminate. [11] [47] [46] [28] Second, the stiffness matrices, when parameterized using layer thicknesses and angles, are connected to the defining variables in a non-linear way, whereas stiffness matrices in the lamination parameter description are a linear function of continuous lamination parameter variables. This makes it possible to employ fast-convergent gradient-based optimization techniques that are effective in locating optimal design points at a relatively cheap computing cost [27]. Since a second step is required to acquire feasible stacking sequences that best match the design variables (i.e., the values of the lamination parameters) obtained in the first optimization step, lamination parameter optimization is typically performed using a multi-step optimization technique [27] [28].

Mainly due to these advantages, lamination parameters have been widely used for the optimization of composite structures. Meddaikar et al. in [48] recently chose lamination parameters as design variables in a continuous optimization step. Optimization trends show areas of the wing box where sandwich composites improve structural performance as well as significant cost savings by requiring fewer stringers. Similarly, Scarth et al. used them to limit the number of design variables to four

random variables regardless of the number of plies in a surrogate model to simplify the overall process in [49]. Mainly because of the advantages of the lamination parameters previously explained, other optimization studies also chose to use lamination parameters instead of stacking sequences as design variables for their formulation. [21] [47] [50] [51] [29]

### **Materials**

When dealing with the optimization of a composite wing structure, the materials chosen for the different parts of the wing have a crucial impact on the overall weight, strength, and stiffness of the wing. By definition, they appear as a critical design variable for the optimization of a composite wing structure. Ricco et al. introduced a choice between carbon fiber and glass fiber for multi-objective optimization of both cost and weight [16]. Other optimizations even introduced a comparison between composite materials and metallic materials. Toffol et al. in [52] compared an aluminum alloy with a symmetric and balanced CFRP stacking sequence, resulting in a lighter design with the CFRP stacking sequence. The same outcome has been found in multiple studies in the literature when comparing a composite wing and a metallic wing [53] [26] [54]. Moreover, some studies presented the optimization of sandwich composites. Indeed, sandwich composites offer a larger bending stiffness compared to a classical composite structure without penalizing structural weight. Based on this greater bending stiffness, there exists the possibility of using a lesser number of stringers in the design, resulting in a lighter design. Fewer stringers in a specific design also reduce manufacturing and maintenance costs over the structure's lifetime. [48] Based on this previous idea, some studies show weight savings of up to 30% using sandwich composites rather than a classical laminated design. [48] [55]

Despite having a great impact on the overall weight, strength, and stiffness of the wing, the materials chosen for the different parts of the wing are often constrained by the manufacturing process when dealing with real-life projects. It will be the case for the future optimization of the master's thesis, therefore, it was chosen not to develop this section further.

### **Spar and Rib**

When considering a full-scale composite wing structure, the optimization of the panels could be done based on the stacking sequence or lamination parameters, as previously explained. However, the location and number of spars and ribs are also important features when a full-scale wing is subject to optimization. Stamatelos et al., in [56] have presented an innovative multispar configuration instead of the conventional two-spar design. It showed that the 4-spar configuration seems to be lighter than the traditional 2-spar, with similar results in terms of compression buckling of the upper skin and lateral displacement of the wing tip, meaning that the two wing configurations keep the same total stiffness [56].

Other work has been done about the spar and rib: Locatelli et al. in [57] has presented the SpaRibs concept: the usage of curvilinear spars and ribs because, unlike in traditional wing design, there is no longer a clear separation between the spars and ribs of the wing box and their structural role in the optimized wing structure (see Figure 2.5). This concept has also been used by Zhao et al. in [17] for the wing box design by optimizing both SpaRibs locations with manufacturing constraints. It has to be noticed that all the optimizations do not have the spar and rib locations as design variables since they are often considered fixed and already defined in the geometry. It will be the case for the future optimization of the master's thesis, therefore, it was chosen not to develop this section further.



Figure 2.5: Typical SpaRibs design in a wing structure. Adapted from [57]

### (Non) Linear stress-strain relation

Apart from other classical design variables previously explained, [58] introduced a new kind of variable by considering a multi-linear relation between strain and stress instead of the classical Hooke's law used for most of the study cases. Figure 2.6 shows a multi-linear behavior between the stresses  $\sigma$  and the strains  $\epsilon$ . These linear relations are defined stepwise with a defined set of points in [58] as follows:

$$\begin{aligned} \sigma_i &= \{0, \sigma_1, \sigma_2, \dots, \sigma_n\} \\ \epsilon_i &= \{0, \epsilon_1, \epsilon_2, \dots, \epsilon_n\} \\ \text{with } E_i &= \frac{\sigma_i - \sigma_{i-1}}{\epsilon_i - \epsilon_{i-1}} \end{aligned} \quad (2.13)$$

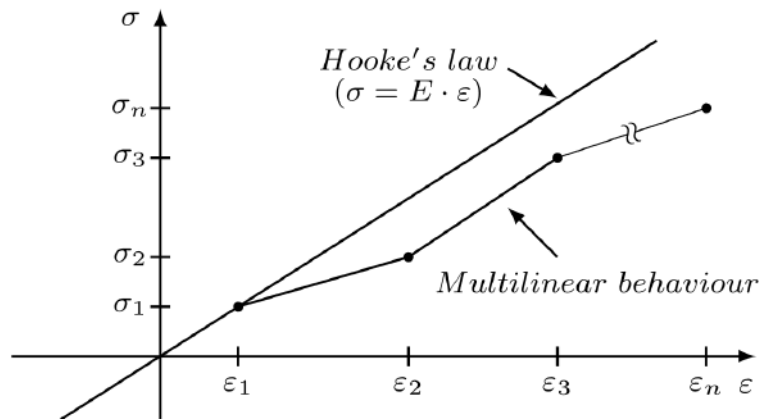


Figure 2.6: Comparison between Hooke's law and multi-linear behavior

Due to this new behavior of the structure, [58] explains that a behavior closer to reality can be obtained. Since this new behavior reduces the bending moment of the wings at the root, it has the potential to significantly lower the loading of design the load cases while maintaining the cruise flight shape.

### Reduce the number of variables

Due to the complexity of the structure that needs optimization, a large number of variables is sometimes necessary to proceed with a realistic optimization. As previously introduced, the lamination parameters allowed us to drastically reduce the number of them compared to classical optimization with the stacking sequence. Especially when dealing with large stacking sequences, for example, in industrial applications

that feature tens or even hundreds of layers within a laminate. Multiple applications of this method have already been presented previously in the Lamination Parameters subsection. Other methods to avoid optimization with high computational costs have been developed. Li and Guo proposed the idea to divide the wing structure into design zones along the span to consider smaller structures to simplify the optimization. This technique has also been used similarly by Ricci et al. in [16] to reduce the weight of multi-laminated composite aerospace structures thanks to multi-objective optimization. In general, dividing the structure into different zones to properly design based on the constraints applied to each zone is a well-developed technique used in multiple optimization. Michaud et al. in [34] divide their skin panel into 28 zones, resulting in a thickness distribution of the skin that is highly dependent on the zones, as shown in Figure 2.7. Finally, Zhang et al. in [55] used a correlation analysis of nine design variables and constraints to avoid a huge amount of computation due to parameter coupling. The correlation between the two variables was measured with the Pearson correlation coefficient. Thanks to this correlation analysis, their optimization could run smoothly by understanding the main factors affecting each step of their optimization.

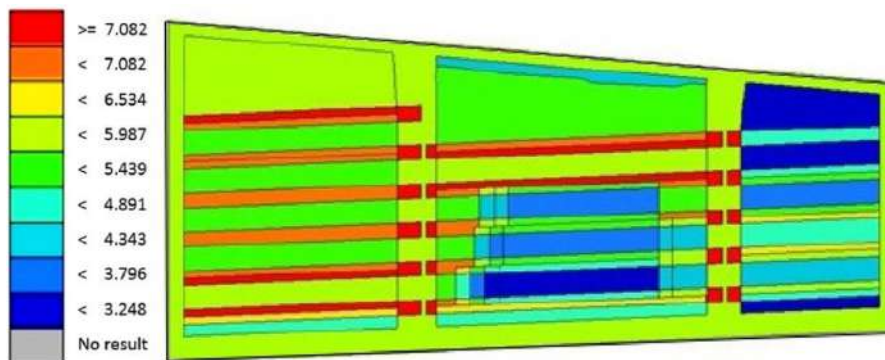


Figure 2.7: Thickness distribution of the skin (in mm) over the 28 zones. Adapted from [34]

### 2.2.2. Optimization objectives (Weight, Cost, Buckling, flutter velocity, Drag, Max strain, Aeroelastically tailored, multi-objectives)

The different design variables previously introduced need to be optimized with specific objectives. This section aims to understand the different optimization objectives available and their impact on the overall optimization.

Optimization objectives play a crucial role in the design of composite structures, which must meet a range of performance criteria to ensure their safety and efficiency. The main objectives of optimization for composite structures typically include weight, cost, buckling performance, flutter velocity, drag, maximum strain, and aeroelastically tailored properties.

**Weight** is often an optimization objective for composite structures. Reducing weight can lead to a range of benefits, including improved fuel efficiency, increased payload capacity, and enhanced performance. Additionally, lightweight structures can be easier to transport, and install, reducing overall costs and increasing efficiency. Reducing weight can also have environmental benefits, as it can result in lower emissions and reduce the carbon footprint of a product or system. By using advanced materials and design techniques, it is possible to optimize the structural layout and thickness of composite components to reduce their weight while maintaining strength and stiffness. Therefore, most of the optimization dealing with structural composition in the literature uses weight as a main objective. [35][59][34][39][60]

**Cost** is another important optimization objective, as composite materials can be expensive to produce and assemble. By optimizing the design and manufacturing processes, engineers can reduce the cost of composite structures while maintaining their performance and reliability. When dealing with real-life projects, cost is often the driving factor due to profitability issues. For this reason, some optimization processes account for this optimization objective. [16] [61]

**Buckling performance** is a key optimization objective for composite structures, as buckling can



cause catastrophic failure if the structure is not designed to withstand the loads it will experience. Mostly by optimizing the geometry and material properties of composite components, an improvement in buckling performance is obtained, which ensures the structural integrity of the structure under a range of loading conditions. Buckling performance is often combined with other optimization objectives, such as reducing the weight, as shown in [18] [35] [22].

**Maximum strain** is an optimization objective that ensures that the composite structure can withstand the maximum loads it will experience without experiencing deformation or failure [62]. By optimizing the thickness and material properties of composite components, engineers can ensure that the structure can withstand the loads it will experience without exceeding its maximum strain limits. [63] has the optimization objective to minimize the maximum strain of the element.

**Lift-to-drag ratio** is another optimization objective for composite structures, as reducing drag can increase their efficiency and reduce fuel consumption. By optimizing the aerodynamic shape and surface finish of composite components, it is possible to minimize drag and improve the overall performance of the structure. [64] [17] [15] are multiple articles dealing with this issue. However, it is more related to the aerodynamic shape of the wing than to its structural composition. That is why it has not been the subject of particular attention for this literature study. Similarly, **Aeroelastically tailored properties** is an optimization objective not closely related to the structural composition of the wing, meaning that it is not of particular attention for this literature study. However, it ensures that composite structures can be designed to meet specific aerodynamic requirements, such as reduced turbulence or increased lift, as it is described in [60] [65] [31].

To conclude, many optimization objectives are closely related to the structural composition of the wing and, therefore, are of strong interest in this literature study. Other optimization objectives, more related to the aerodynamic shape of the wing, were not as well studied and described in this section. It has to be noticed that these optimization objectives can either be taken into account alone or together, leading to multi-objectives optimization, which is a specific type of optimization that will be explained in subsection 2.3.1.

### 2.2.3. Type of constraints (Strength, Stability, Buckling, Flutter, Geometry, Stiffness, Strain...)

The optimization of composite structures involves not only setting optimization objectives but also taking into account a range of constraints that the design must satisfy to ensure its safety, reliability, and functionality. For example, minimizing weight by removing plies weakens the structure. Thus, the structure may no longer meet its structural requirements. This is why it is necessary to add constraints to the optimization problem. The main types of constraints in the optimization of composite structures typically include strength, strain/displacement, stiffness, geometry, and buckling performance.

**Strength** constraints are critical in ensuring that the composite structure can withstand the loads it will experience without critical deformation or failure. Strength constraints typically involve setting limits on the maximum stresses (using the different failure criteria summarized in subsection 2.1.1) that the structure can experience, as well as ensuring that the structure can withstand fatigue loading over its lifetime. For example, Dillinger et al. [50] assess strength with a strain-based failure index. the Tsai-Wu criteria, explained in subsection 2.1.1 is the most common failure index used to assess strength in the composite structure [17] [31] [66]. Another approach has been used by Zhang et al. [55] using the Factor of Safety (FoS), considered to be 1.5, to assess that the tensile, compressive, and shear stresses of the carbon fiber stay within a reasonable range of values.

Moreover, it is also possible to set limits on the maximum strain, referred to in this case as the **strain/displacement** constraints. They are also important in ensuring the structural integrity of composite structures. [66] These constraints involve setting limits on the maximum deformation or displacement that the structure can experience under various loading conditions. This is important in ensuring that the structure maintains its shape and functionality under all operating conditions [62] [28].

Thus, **stiffness** constraints are critical in ensuring that the composite structure maintains its structural integrity and functionality under a range of loading conditions. Indeed, low stiffness brings out large

deformation, which leads to an instantaneous change in the aerodynamic force of the wing, causing the working condition of the aircraft to deviate from the design point. [55] Therefore, it is necessary to constrain the stiffness of the beam. Stiffness constraints typically involve setting limits on the deflection or deformation of the structure. Both the flexural and torsional stiffness can be controlled. The wingtip deflection  $\delta_{tip(z)}$  is kept below 15% in [66] or 10% in [17] [62], of the wing semi-span  $b$  to ensure flexural stiffness, while the twist angle at the wingtip should not exceed 6 to ensure torsional stiffness. Stiffness constraints are often related to flutter since torsional stiffness helps to counteract the twisting of the wing under aerodynamic loads and thus prevents flutter [66].

Despite being sometimes the optimization objective, the **buckling performance** is also considered a constraint in some optimization formulations. This constraint is critical in ensuring that the composite structure can withstand buckling under various loading conditions. Buckling performance constraints typically involve setting limits on the critical buckling load of the structure as well as ensuring that the structure can withstand buckling under a range of loading conditions. Considering buckling load as a constraint can be done by introducing a buckling load factor  $\lambda_b$  into the optimization. [28] This factor is often settled with a lower bound in the optimization, such as 1.15 in [17]. Some studies are performing the buckling analysis based on an idealized buckling model where each wing panel, between two ribs and two stiffeners, is idealized as a simply supported plate under inplane loading. [50] It is also possible to perform both global and local buckling analysis with the classical buckling theory known [62].

Finally, some study cases need simple **geometry** constraints. They are important in ensuring that the composite structure can be manufactured and assembled within specified dimensional tolerances. Geometry constraints typically involve setting limits on the dimensional accuracy of the structure as well as ensuring that the structure can be manufactured and assembled within specified tolerances. For example, Zhang et al. in [55] are optimizing a composite sandwich beam box where the geometrical thickness of the sandwich plate needs to be limited. Otherwise, the area enclosed by the section center line of the sandwich box beam will decrease, leading the torsional shear stress to increase. To make the structure satisfy the thin plate assumption, they kept the ratio of the thickness of the sandwich plate to the external dimension of the wing beam at 10% [55].

All the constraints related to the aerodynamic design of the wing and the aeroelasticity, such as flutter, hinge moment, angle of attack, aeroelastic stability, and gust response... have not been detailed in this section as they are not of interest to this literature study.

In conclusion, the optimization of composite structures involves not only setting optimization objectives and design variables but also taking into account a range of constraints that the design must satisfy to ensure its safety, reliability, and functionality. The main types of constraints in the optimization of composite structures typically include strength, strain/displacement, stiffness, geometry, and buckling performance. By accounting for these different constraints, the overall optimization process is complete.

## 2.3. Type of optimizations

To solve the optimization formulation previously described in 2.2, multiple types of optimization exist, this section aims to summarize them and classify them based on the special features of each one.

### 2.3.1. Multi-objective

A multi-objective optimization is an optimization approach that involves optimizing a design to simultaneously satisfy multiple conflicting objectives. As explained for any kind of optimization, the multi-objective optimization problem may contain several constraints that any feasible solution must satisfy. [14] Due to its complexity, the optimization of a composite wing structure often has multiple objectives. Guo et al. in [31] deal with both strength and aeroelastic stability for example. In multi-objective optimization, the challenge is to find a set of design parameters that simultaneously satisfy all of these objectives. This typically involves using optimization algorithms that can search for the optimal set of design parameters while taking into account the trade-offs between the different objectives [14]. Multiple solutions to deal with the multi-objective problem have been developed. They are deeply detailed in [67]. Those most commonly used when dealing with the optimization of composite structures will be briefly introduced hereafter.

$$\begin{aligned} & \underset{\mathbf{x}}{\text{Minimize}} \mathbf{F}(\mathbf{x}) = [F_1(\mathbf{x}), F_2(\mathbf{x}), \dots, F_k(\mathbf{x})]^T \\ & \text{subject to } g_j(\mathbf{x}) \leq 0, \quad j = 1, 2, \dots, m, \\ & h_l(\mathbf{x}) = 0, \quad l = 1, 2, \dots, e, \end{aligned}$$

Figure 2.8: multi-objectives optimization formulation. Adapted from [67]

where  $k$  is the number of objective functions,  $m$  is the number of inequality constraints, and  $e$  is the number of equality constraints.  $x$  is a vector of design variables.  $F(x)$  is a vector of objective functions  $F_i(x)$ .

### Convert the multi-objective optimization into a single objective form thanks to weighing factors

The basic idea behind converting the multi-objective optimization formulation into a single-objective one is to simplify the problem by combining all the objective functions into a single function. This single function is then easy to optimize with the usual optimization technique based on gradient descent, for example. Molinari et al. in [64] used a linear scalarization to reduce the multi-objective problem to a single objective function, which was then optimized with the Covariance Matrix Adaptation-Evolution Strategy (CMA-ES). The linear scalarization between their two optimization objectives has been done with weighing factors. (See Figure 2.9) It means that both objectives have a different weight in the single objective function, introducing the notion of preference [61] between the different optimization objectives. The preference-based classical methods to convert the multi-objective optimization problem into a single objective form have been used by most of the research in the field of multi-objective optimization of composites [61]. In the case of Molinari et al.[64], the weighing factors have been heuristically chosen to find the best optimum possible. The CMA-ES allowed us to find an optimal that dominates the majority of the Pareto-optimal solutions, which is the other classical solution for multi-objective optimization, explained hereafter [64].

$$\mathbf{f}(\mathbf{x}) = \begin{cases} c_{D0}(\mathbf{x}) + c_{Di}(\mathbf{x}) \\ -c_{\ell}(\mathbf{x}) \end{cases} \Big|_{\alpha=\bar{\alpha}} \quad f(\mathbf{x}) = (k_{c_D} \cdot (c_{D0}(\mathbf{x}) + c_{Di}(\mathbf{x})) - k_{c_{\ell}} \cdot |c_{\ell}(\mathbf{x})|) \Big|_{\alpha=\bar{\alpha}}$$

(a) multi-objective functions                      (b) Single objective function thanks to weighing factors ( $k_{c_i}$  and  $k_{c_D}$ )

Figure 2.9: Conversion from multi-objective functions to single objective function thanks to weighing factors. Adapted from [64].

### Pareto Front

As previously explained, the solution for multi-objective optimization is achieved through the best trade-off possible between the different optimization objectives. Indeed, in contrast to single objective optimization, where there is no single global solution, it is necessary to determine a set of points that all fit a definition of an optimum, called a set of trade-off solutions [67]. A set of trade-off solutions that cannot be improved concerning one objective without hurting another objective is known as a Pareto set. When plotted in the design space, it is referred to as a Pareto optimal front [61](see Figure 2.10).

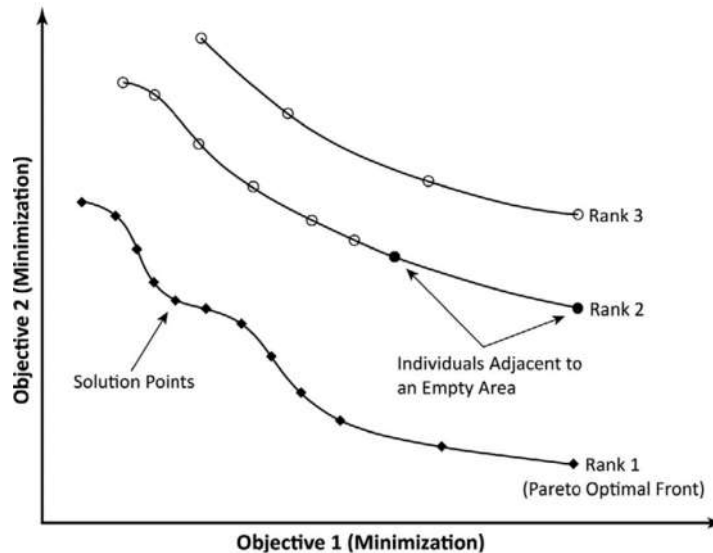


Figure 2.10: Illustration of the Pareto optimal front with two objectives functions. Adapted from [61]

There are multiple algorithms to produce a set of Pareto optimal sets. Strength Pareto evolutionary algorithm (SPEA-II) [68], Pareto archived evolutionary strategies (PAES) [69] and non-dominated sorting genetic algorithm (NSGA-II) [70] are some examples of these algorithms, applied to generate optimal Pareto sets. Amongst these, NSGA-II is the most popular due to its effectiveness and simplicity. Multiple studies are using it to generate Pareto-front [64][14] [61] [71]. This algorithm is based on non-domination and crowding distance sorting and generates populations through the use of genetic operators, hence leading to optimal solutions, in several iterations known as a generation. [61] More algorithms have been developed to produce Pareto fronts, but it has been chosen not to detail more this part since it is a complete topic of research.

Once the Pareto front is obtained with the algorithm, the next step is to choose a solution from the Pareto front. At this point of the designing process, designers rely on their experience and knowledge to choose the best solution. Figure 2.11 is a great illustration from [14] to explain the idea. Based on three different optimization objectives, the designer obtained a complete set of optimal solutions thanks to a Pareto front from which to choose the design. Bacarreza et al. in [14] decided to use a panel with a mass of around 4.53 kilograms. Two possible solutions, illustrated in Figure 2.11, are available, with comparable masses, but solution 1 has a higher reaction force and Tsai-Wu index than solution 2. These solutions are completely different in the design space, one has more stringers and smaller cross-sections, while the other has fewer stringers, but a bigger stringer cross-section. However, they both have the same thickness of the skin and stringers. Each one has its advantages (higher reaction force, or a lower Tsai-Wu index), so it is possible to make a choice based on the advantage desired [14].

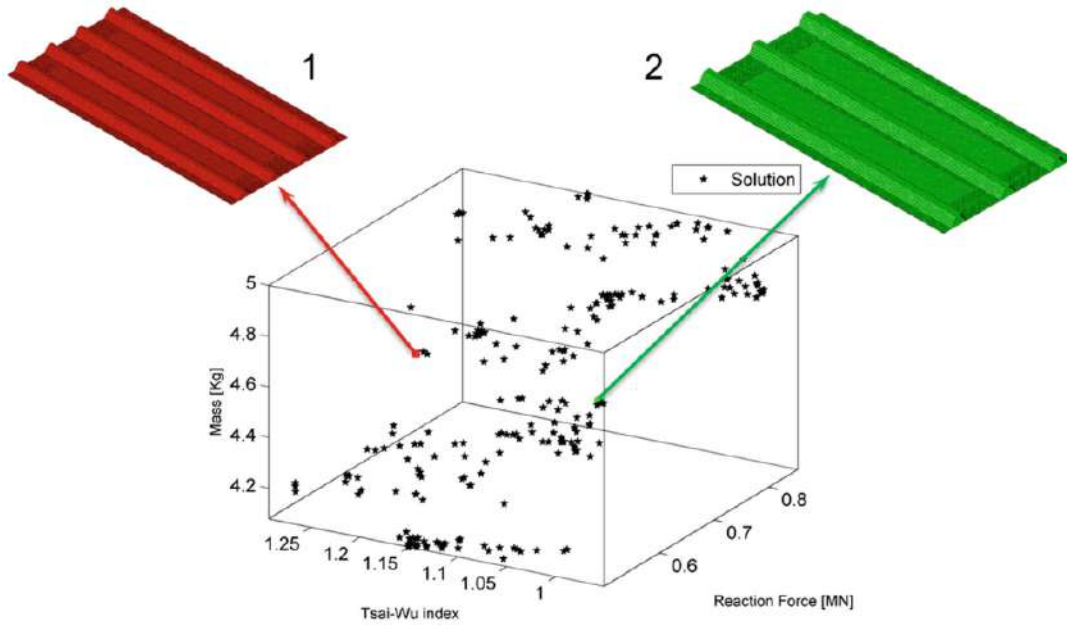


Figure 2.11: Choosing a solution from the Pareto front. Adapted from [14]

### 2.3.2. Multi-level

Multi-level optimization offers significant advantages for large-scale problems in structural engineering, such as enhancing computational efficiency. This approach involves dividing a complex optimization problem into smaller sub-problems, leading to easier optimization at each level [71]. A multi-level optimization approach freezes some parameters at each level to solve the sub-problem more easily [72]. As presented in Figure 2.12, each level has its own sets of design variables, objectives, and constraints.

$$\begin{array}{lll}
 & \text{Level 1} & \\
 \text{minimise/maximise} & f_i(X) & (i = 1, 2, \dots, I) \\
 \text{subject to} & g_j(X) \leq 0 & (j = 1, 2, \dots, J) \\
 & h_k(X) = 0 & (k = 1, 2, \dots, K) \\
 & x_l^{(L)} \leq x_l \leq x_l^{(U)} & (l = 1, 2, \dots, L) \\
 & \vdots & \\
 & \text{Level n} & \\
 \text{minimise/maximise} & f_o(Y) & (o = 1, 2, \dots, O) \\
 \text{subject to} & g_p(Y) \leq 0 & (p = 1, 2, \dots, P) \\
 & h_q(Y) = 0 & (q = 1, 2, \dots, Q) \\
 & y_r^{(L)} \leq y_r \leq y_r^{(U)} & (r = 1, 2, \dots, R)
 \end{array}$$

Figure 2.12: Multi-level optimization approach. Adapted from [71]

Where  $X$  is the design variable,  $f_i$  is the  $i^{th}$  objective function,  $g_j$  is the  $j^{th}$  inequality constraint,  $h_k$  is the  $k^{th}$  equality constraint, and  $x_l^L$  and  $x_l^U$  are the lower and upper bounds for the  $l^{th}$  design variables in Level 1. In the same way,  $Y$  is the design variable,  $f_o$  is the  $o^{th}$  objective function,  $g_p$  is the  $p^{th}$  inequality constraint,  $h_q$  is the  $q^{th}$  equality constraint, and  $y_r^L$  and  $y_r^U$  are the lower and upper bounds for the  $r^{th}$  design variables in Level n. It should be mentioned that some of the objectives from one level can be applied to another [71].

One of the pioneering works in multilevel optimization has been done by Liu et al. [73]. They developed a two-level optimization (bottom and global) procedure for analyzing a composite wing. At the global level, the thicknesses of  $0^\circ$ ,  $90^\circ$ ,  $45^\circ$  and  $-45^\circ$  plies were optimized to reduce weight

while satisfying strain and buckling constraints. At the bottom level, a permutation Genetic Algorithm (GA) was used to optimize the stacking sequence of the plies for a given number of plies and loads to maximize the buckling load [73]. This optimization is compared to a single-level composite optimization by Liu et al. [51]. Similar designs are produced by both approaches. However, the single optimization developed is only useful for simple structures, giving a huge argument in favor of the two-level approach, which can deal with complex composite structures such as stiffened panels [51].

Most of the multilevel optimizations in composite wing optimization are bi-level (or two-level) optimizations with a global level and a local level. Liu et al. [29] presented a comparison between two bi-level optimizations. The first, the material volume is the objective function at the global level, and the stacking optimization to satisfy blending and manufacturing constraints is performed at the local level. For the second, lamination parameters and numbers of plies of the classical 4 predefined angles are the design variables for buckling, strain, and ply percentage constraints at a local level, while minimizing the material volume is still the global level objective. The second optimization with the lamination parameters has also been reused by Liu et al. in [28]. Zhao et al. [74] ran an optimization with a similar distinction between local and global levels. In their optimization, the design requirements are adjusted at the global level (called system level in the paper) according to the structural deformation, while the stacking sequence is optimized at the local level (called subsystem level in the paper) to satisfy the constraints at the global level [74]. Similarly, Grihon et al. [75] used a bi-level global-local optimization for stiffened panels. At a global level, a finite element analysis provides internal loads applied to each stiffener, while at a local level, these loads are used to compute static mechanical criteria [75].

### 2.3.3. Multi-step approach

Multi-step optimization is a process in which an optimization problem is solved in multiple stages or steps, with the solution from one stage used as the starting point for the next stage. One of the advantages of multi-step optimization is that it breaks down a complex problem into smaller, more manageable sub-problems. Indeed, as seen in subsection 2.3.1, optimization of composite structures is often a complex problem with multiple objectives and constraints to deal with. Therefore, dividing it into smaller sub-problems is an efficient way to solve them. It is quite the same idea as multi-level optimization described in subsection 2.3.2.

A multi-step approach allows for dealing with one issue at a time, leading to simpler problems to solve. Multiple types of step-division have been done in the literature. Shrivastava et al. [76] choose to find the limiting values of wing tip deflection and wing twist as flutter constraints based on finite element analysis for the first step of their optimization. The second step of the optimization was then a classical weight optimization of the laminate for strength and stiffness design parameters, based on the flutter constraints previously found in the first step [76]. On the contrary, Guo et al. [31] focused their first stage on minimizing weight, while their second stage was focused on aeroelastic tailoring to reduce the wing gust response and reach the same level as the original value of the preliminary design, accounting for the minimum weight found in the first stage [31]. A similar scheme was used by Ren et al. [13]. However, in their study, the first step is to optimize the thickness of the layers of the laminated composite structure. Then, based on the thickness optimization results, and the angles of the different plies, the stacking sequence is optimized in the second step [13]. Multiple other types of multi-step optimization exist in the literature: Zhang et al. [55] propose a two-stage optimization design methodology for sandwich box beams. Wang et al. [62] propose a three-stage optimization: first, the thickness of the composite skin was optimized, then the structural-efficiency optimization (SEO) for minimum weight was done for each stiffened panel between ribs, and finally, the stiffness of the overall wing was optimized [62].

Moreover, as explained in Figure 2.2.1, lamination parameters are another type of design variable available for the optimization of composite structures, offering promising opportunities. They are often part of a multi-step optimization. Indeed, they allow the use of continuous design space (see Figure 2.4), in which gradient-based optimizers can be used to derive optimal design points [27]. This is typically the first step of an optimization using lamination parameters. Then, the second step of the optimization needs to translate the optimal lamination parameters found in the first step, into stacking sequences with an equivalent stiffness distribution, reaching a discrete design space (see Figure 2.4). Sousa et al. [27] have developed an optimization using this two-step optimization with lamination parameters, with

a first step in the continuous design space, and the second step in a discrete design space, reaching a feasible design. Figure 2.13

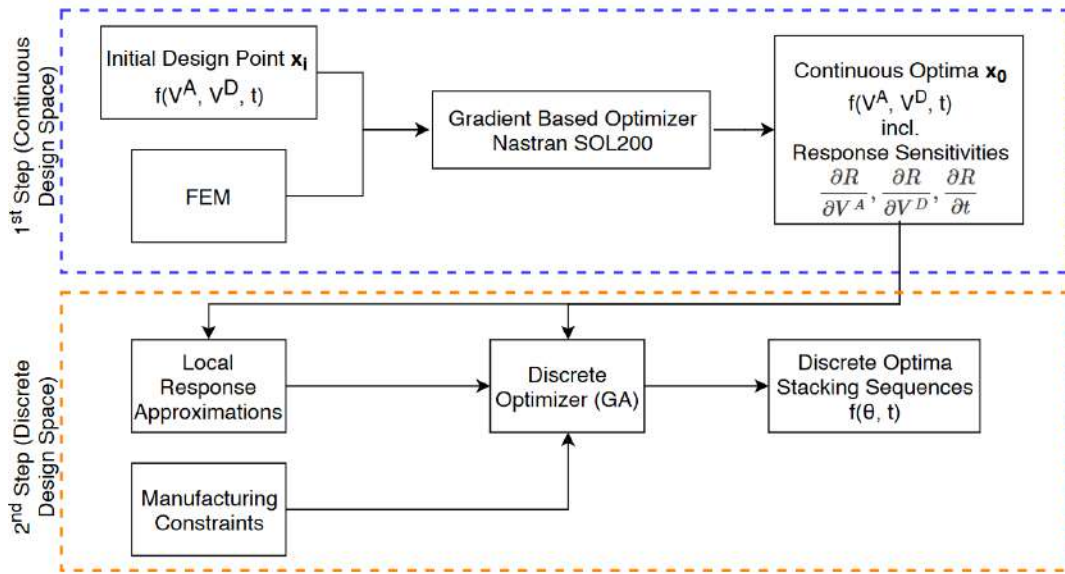


Figure 2.13: Multi-step optimization framework. Adapted from [27]

Another type of multi-step optimization, with a different level of design, is presented by Bacarreza et al. [14]. They are running an optimization described in Figure 2.14 with a preliminary design with a low fidelity model as the first step, and a detailed design with a higher fidelity model as the second step. This introduces the notion of fidelity in the optimization, further explained in subsection 2.3.4. To briefly explain, in [14], the size of the component to be optimized does not change, but the model complexity does, including a failure analysis propagation in the detailed design, for example. The results obtained at the end of the preliminary design stage are used as a basis to explore the solutions at the detailed design stage [14]. This time, each step of the optimization is not focused on a specific objective or constraint but rather on a different level of design complexity. However, similarly, the results obtained in the first step are used in the second one.

$$\begin{array}{lll}
 \text{Preliminary Design} & & \\
 \text{Min./Max.} & f_m(\mathbf{x}) & m = 1, 2, \dots, M; \\
 \text{Subject to} & g_j(\mathbf{x}) \leq 0 & j = 1, 2, \dots, J; \\
 & h_k(\mathbf{x}) = 0 & k = 1, 2, \dots, K; \\
 & x_i^{(L)} \leq x_i \leq x_i^{(U)} & i = 1, 2, \dots, n; \\
 \\
 \text{Detailed Design} & & \\
 \text{Min./Max.} & o_u(\mathbf{y}) & u = 1, 2, \dots, U; \\
 \text{Subject to} & p_s(\mathbf{y}) \leq 0 & s = 1, 2, \dots, S; \\
 & q_t(\mathbf{y}) = 0 & t = 1, 2, \dots, T; \\
 & y_r^{(L)} \leq y_r \leq y_r^{(U)} & r = 1, 2, \dots, v;
 \end{array}$$

Figure 2.14: Two level optimization: preliminary design and detailed design. Adapted from [14]

### 2.3.4. Multi-fidelity

Multi-fidelity optimization is a technique that combines different levels of fidelity in the analysis of the structure to improve the efficiency and accuracy of the optimization process. It can be used to re-

duce the computational cost of the optimization problem while still achieving high-quality solutions [77].

The concept of multi-fidelity optimization is related to High-Fidelity Modeling (HFM) and Low-Fidelity Modeling (LFM). First, with HFM, the structure is analyzed using a high-fidelity analysis method, such as full-scale finite element analysis, that provides accurate results but requires significant computational resources [77]. High-fidelity modeling can rely on large-scale structural optimization problems with thousands of design variables, millions of state variables, and hundreds of load cases [78]. Second, with LFM, the structure is analyzed using a simplified analysis method, such as Equivalent Plate Methodology (EPM)[77], low fidelity aerodynamics [77], that provides approximate results but requires significantly less computational resources than the high-fidelity analysis [77]. Then, in the multi-fidelity optimization, the high-fidelity and low-fidelity analyses are used together in an optimization algorithm that searches the design space for the set of designs that satisfy the optimization objectives. The optimization algorithm may use high-fidelity analysis to evaluate a small number of promising designs while using low-fidelity analysis to evaluate a larger number of less promising designs [71]. Alternatively, the optimization algorithm may use a surrogate model that combines the results of the high-fidelity and low-fidelity analyses to predict the performance of new designs [71]. This concept has been used by Yoo et al. [71] where the High-Fidelity Model and Low-Fidelity Model cover different design spaces (see Figure 2.15). This means that the HFM has only a few design variables, whereas the LFM explores the entire design space during the optimization process.

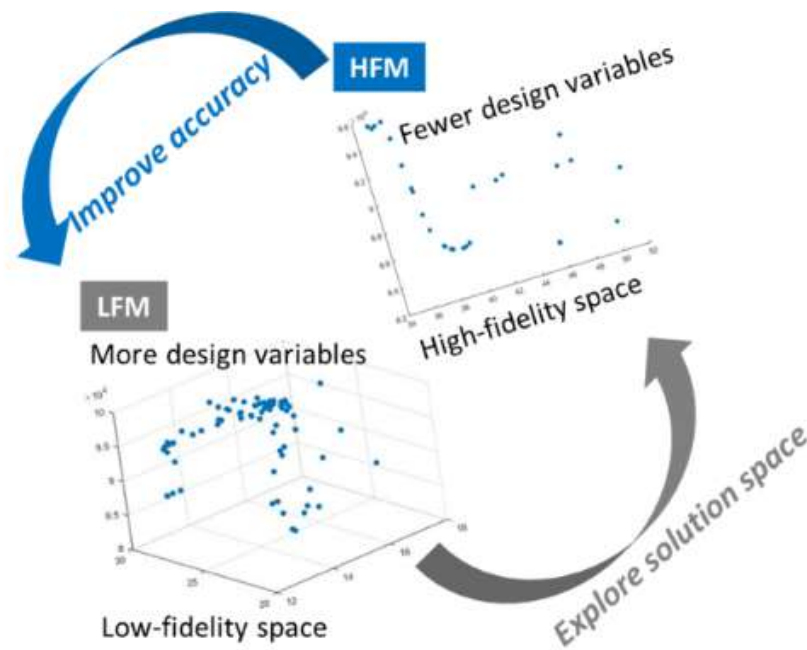


Figure 2.15: General idea of Multi-fidelity optimization using HFM and LFM. Adapted from [71]

Moreover, depending on the accuracy requirements, the introduction of either HFM or LFM into the modelization is of interest. Wang et al. [62] stated that for their static-analysis model, a detailed finite element (FE) should be employed, as a HFM, while for their dynamic-and-aeroelastic-analysis model, the simplified analysis model with the reduced global stiffness and mass properties is adapted, as a LFM [62]. Thus, HFM and LFM concepts allow one to focus the computational power where it is most efficient and useful in the optimization process. Similarly, Yang et al. [79] needed high-fidelity analysis models in the preliminary design stages of wing structures using a specific FEM technique since it makes the design evaluation more accurate, leading to shorter design cycle times and cost savings [79].

Finally, Dababneh et al. [66] developed four different models of the NASA CRM wing box with increasing structural fidelity (see Figure 2.16) to study the necessary and appropriate level of detail that is required to effectively characterize the structural geometry of aircraft wings and predict the mass of the primary load-carrying wing structure with a respectable degree of precision. With increasing structural



fidelity, the number of design variables increases; thus, the design space enlarges. Consequently, the possible design alternatives within the design domain increase, which expands the chances of finding a better local optimal solution [66]. The study concludes that the mass of the metallic CRM wing box can be estimated with an acceptable level of accuracy and reduced computational time with a high degree of confidence by using the second wing box model of structural fidelity [66].

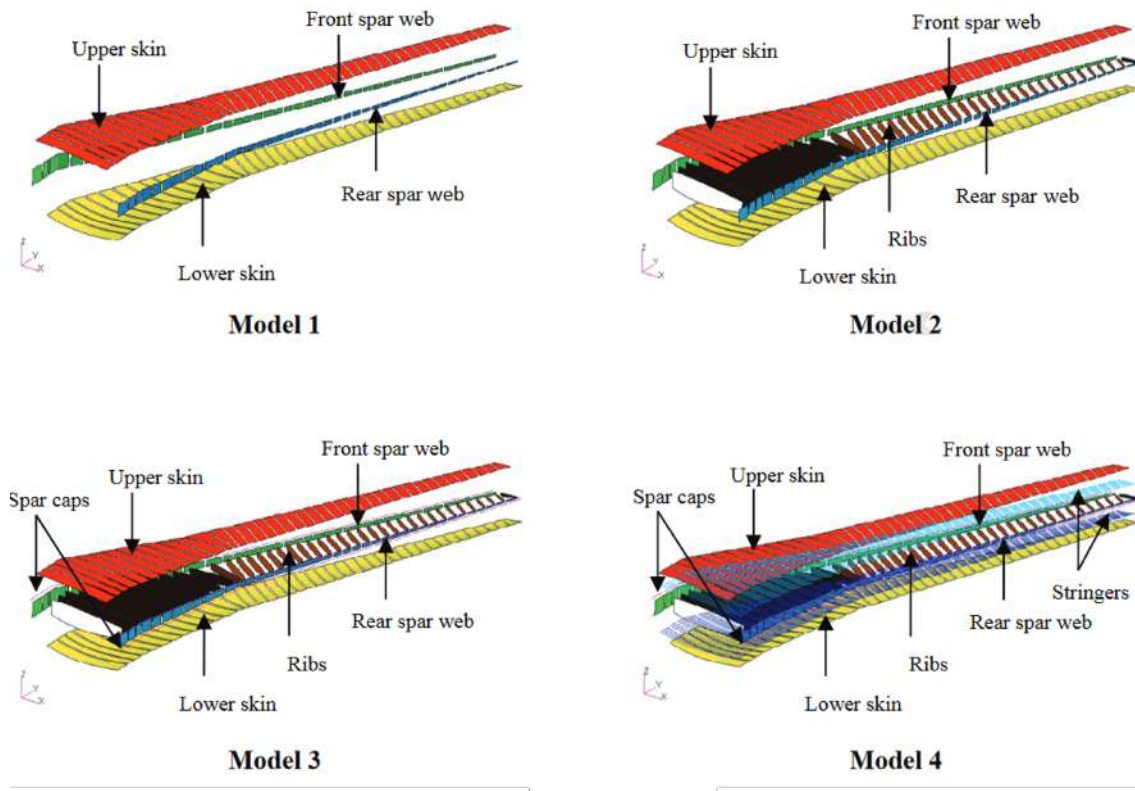


Figure 2.16: Models with increasing structural fidelity of the NASA CRM wing box. Adapted from [66]

### 2.3.5. Probabilistic optimization

Probabilistic optimization is a technique that accounts for the variability and uncertainty in the design variables and the optimization objectives. These variables can depend on the material properties, loading conditions, or any other factors that affect the optimization of the structure [72][80]. Probabilistic optimization is opposed to deterministic optimization, which by definition assumes that all factors of the optimization are known with certainty. They are treated as fixed values, and the optimization algorithm searches for the optimal values of the design variables that maximize or minimize the objectives. [49] To account for the variability and uncertainty in the factors of the optimization, it is possible to model them using probability distributions or statistical models. Monte Carlo simulation (MCS) is the most straightforward technique for modeling uncertainty. It requires a large number of model runs to achieve accurate results, and as such, a large amount of work has focused on using efficient approximation techniques [49]. Once the statistical models, or probability distributions, are found, the optimization algorithm searches for the optimal values of the design variables that fulfill the objectives, subject to probabilistic constraints that ensure the probability of violating the constraints are within acceptable limits [49]. Multiple probabilistic optimization methods have been developed recently; however, two methods are more studied and will be presented afterward: Robust Design Optimization (RDO) and Reliability-Based Design Optimization (RBDO).

#### Robust Design Optimization (RDO)

Robust Design Optimization (RDO) is a methodology that aims to optimize the structure under possible variations of the manufacturing process, environmental aspects, and product life conditions, which could influence the product's quality and performance [71]. The goal of RDO is to find a design that not

only performs well under the expected or nominal operating conditions but also performs well under a range of uncertain or off-nominal conditions. It has the goal of improving product quality by stabilizing the deviations in response behavior as well as minimizing the effect of design uncertainties [14]. RDO prevents the production of highly conservative designs resulting from the consideration of excessive safety factors or worst-case scenarios [71]. With RDO, the quality of a design is justified not only by the mean value but also by the variability of the structural performance [14] [61]. Figure 2.17 shows the concept of robustness in RDO: minimizing variability is part of the optimization, leading to a lower mean value for the objective function [49].

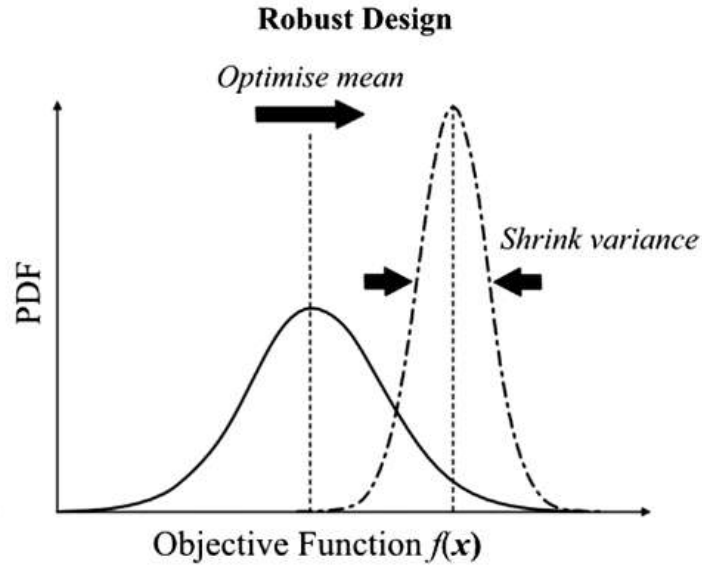


Figure 2.17: Robust Design Optimization illustration: Probability Density Function (PDF) against the objective function. Adapted from [49]

From a mathematical point of view, the RDO final objective function considers both the mean and the standard deviation of the original objective function, leading to a multi-objective optimization (see Figure 2.18) [71] [14].

$$\begin{array}{ll}
 \text{mininise/maximise} & \{\mu(f(X)), \sigma(f(X))\} \\
 \text{subject to} & g_i(X) \leq 0 \quad (i = 1, 2, \dots, I) \\
 & h_j(X) = 0 \quad (j = 1, 2, \dots, J) \\
 & \sigma(f(X)) \leq \sigma_M^+ \quad (k = 1, 2, \dots, K) \\
 & x_l^{(L)} \leq x_l \leq x_l^{(U)} \quad (l = 1, 2, \dots, L)
 \end{array}$$

Figure 2.18: Robust Design Optimization mathematical formulation. Adapted from [71]

where  $X$  is the design variables,  $\mu(f(X))$  and  $\sigma(f(X))$  are the first (mean) and second (standard deviation) statistical moments of the objective function respectively.  $h_j$  is the  $j^{\text{th}}$  equality constraint,  $g_i$  is the  $i^{\text{th}}$  inequality constraint,  $\sigma_M^+$  is the upper limit for the standard deviation,  $x_l^U$  and  $x_l^L$  are the upper and lower bounds for the  $l^{\text{th}}$  design variables.

As an example, Farokhi et al. [72] developed robust design optimizations that considered uncertainties in mechanical properties or geometric parameters. In both cases, compared to deterministic designs, robust designs tend to have a slightly smaller Nonlinear Postbuckling Strength (which was the objective function of the optimization) mean value and a smaller Nonlinear Postbuckling Strength standard deviation. In other words, RDO finds designs that are less sensitive to variations in mechanical properties and geometric parameters, but at the cost of a slightly reduced objective function mean value compared to the deterministic designs [72].

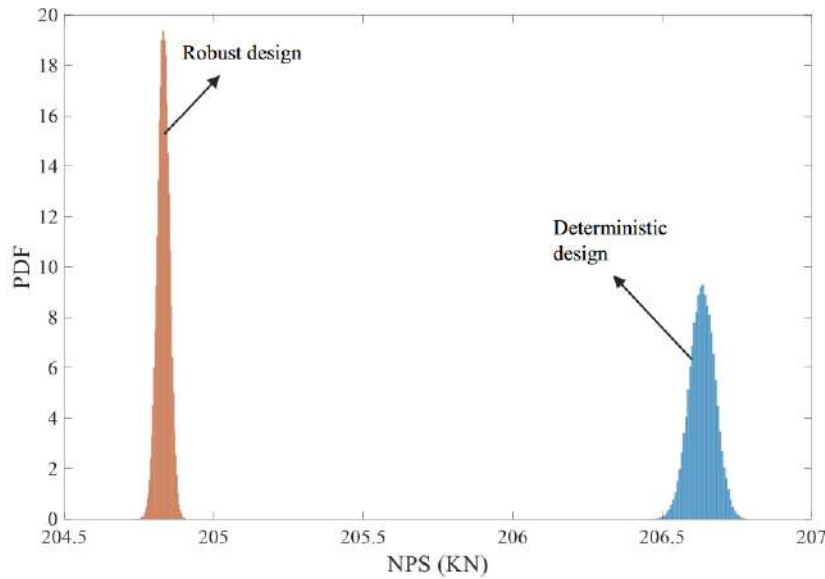


**Figure 2.19:** Robust Design Optimization illustration: Probability Density Function (PDF) against Nonlinear Postbuckling Strength (NPS). Adapted from [72]

### Reliability-Based Design Optimization (RBDO)

Reliability-Based Design Optimization (RBDO) is a method to achieve confidence in product reliability under a prescribed probabilistic constraint [14] [72] [81]. RBDO aims to ensure that constraints are enforced such that the probability of failure does not exceed an acceptable threshold [47] (see Figure 2.20). In the case of RBDO, failure is assessed using a limit-state function, called  $g(x)$  [72]. Multiple methods exist, the most common ones are the first- and second-order reliability methods (FORM and SORM, respectively) [49]. For these methods, the limit state function is approximated using Taylor series expansions about the most probable point upon the failure surface [49].

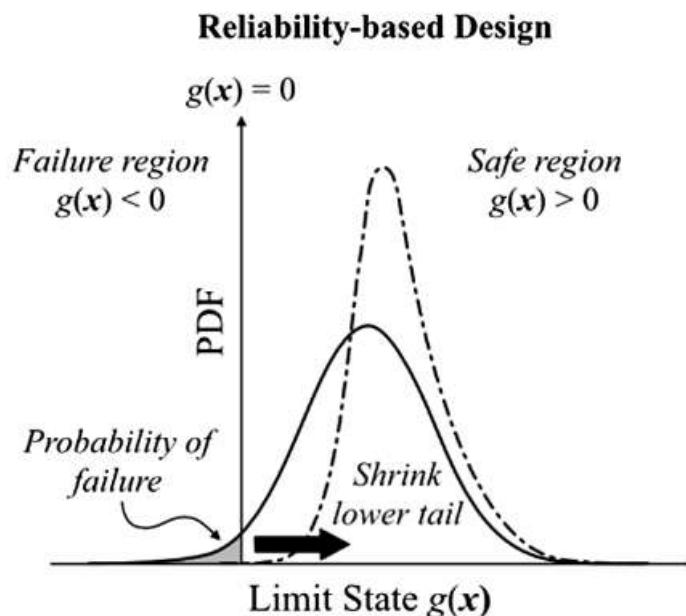


**Figure 2.20:** Reliability-Based Design Optimization illustration. Adapted from [49]

Moreover, as explained previously, reliability is a measure of the probability that failure does not occur within the design envelope. Failure is defined by a limit state function,  $g(x, p)$ . This limit state

function is comparable to the constraints used in deterministic optimization, with the distinction that constraints may be violated with some acceptable probability. Therefore the mathematical formulation of an RBDO can be expressed as follows [47]:

$$\begin{aligned} & \min_{\bar{\mathbf{x}}} f(\bar{\mathbf{x}}, \bar{\mathbf{p}}) \\ & \text{s.t. } P(g(\mathbf{x}, \mathbf{p}) \leq 0) \leq P_f \\ & \quad \bar{\mathbf{x}}_L \leq \bar{\mathbf{x}} \leq \bar{\mathbf{x}}_U \end{aligned}$$

Figure 2.21: Reliability-Based Design Optimization mathematical formulation. Adapted from [49]

where  $P_f$  is the acceptable probability of failure and an over-bar denotes a nominal value. A distinction is made between parameters and variables because the uncertainties need not be limited to the variables over which the designer has control [47].

Scarth et al. [49] developed an RBDO for their aeroelastic model to minimize the probability of instability occurring at different design speeds of 145 and 150 m/s. A 96% reduction in the failure probability is achieved by using the larger design space for a 145 m/s design speed, and 74% is achieved for a 150 m/s design speed. These reductions have been compared to a deterministic optimization, as shown by Figure 2.22

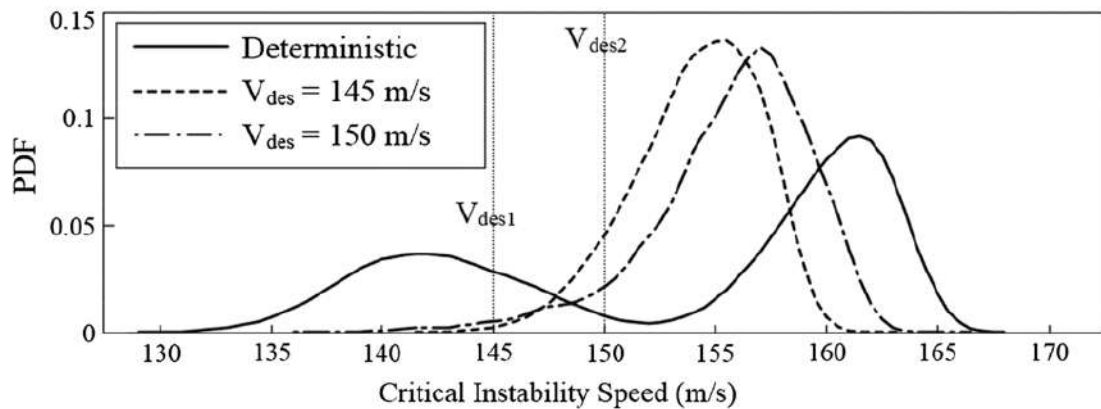


Figure 2.22: Reliability-Based Design Optimization illustration. Adapted from [49]

## 2.4. Optimization algorithms

All the previous types of optimization emerged in various types of algorithms. In this chapter, we will summarize the different types of algorithms that exist and the opportunities they offer.

### 2.4.1. Most Used Algorithms

#### Genetic Algorithms

The most common algorithm used for the optimization of composite structures is the Genetic Algorithm (GA) [82]. It is inspired by the processes of natural selection and evolution, and it looks for the optimal design by generating and evolving a population of potential solutions [11]. Typical GA optimization process involves the following steps [82] :

- Initialization: A population of potential solutions is generated randomly. Each individual in the population represents a candidate design for the composite structure[83] [27].
- Evaluation: Each individual in the population is evaluated by a fitness function that quantifies how well the individual satisfies the design objectives and constraints [83] [84].
- Selection: A subset of the population is selected for reproduction based on their fitness values. This step mimics the natural selection process, where individuals with higher fitness values are more likely to pass on their genetic material to the next generation [84].
- Crossover: The selected individuals are combined through a crossover operator to generate new offspring. This process involves exchanging genetic material between the selected individuals to create new potential designs [83] [27]. This step is described in Figure 2.23.
- Mutation: In some cases, a small number of individuals in the population may undergo a mutation operation that introduces a random change in their genetic material. This step helps to introduce diversity in the population and avoid convergence to a suboptimal solution [83] [27]. This step is described in Figure 2.23.
- Replacement: The new offspring and mutated individuals replace some of the individuals in the previous population to form a new population for the next generation [14].
- Termination: The optimization process continues for a specified number of generations or until a termination criterion is met [14].

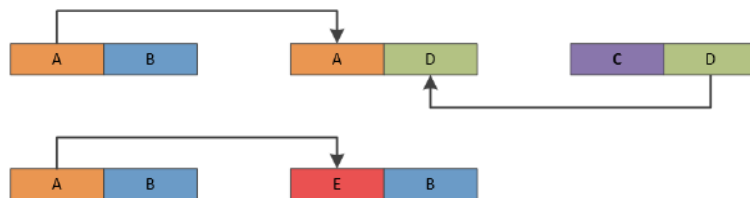


**Figure 2.23:** Crossover and Mutation selection procedures of the Genetic Algorithm (GA). Adapted from [84]

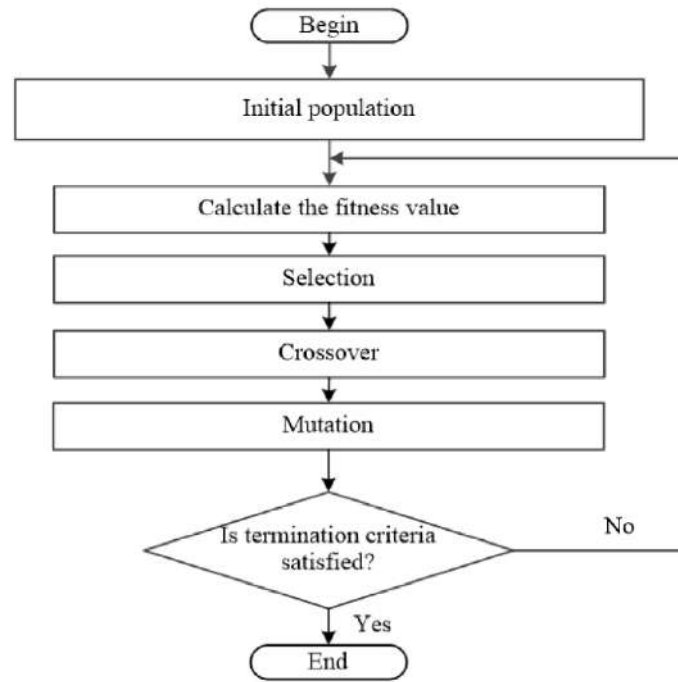


Figure 2.24: Typical Genetic Algorithm flowchart. Adapted from [85]

Being a population-based approach, Genetic Algorithms are well suited to solve complex, multi-objective optimization problems [14]. Thus, it has been explored for every known discipline of engineering and science [83], such as the optimization of composite structure, where it is the most popular meta-heuristic algorithm for the optimization of composite structure [82] [28] [13] [49] [86] [15] [22] [76] [27] [87] [14] [84] [7] [83].

### Gradient-based Algorithms

Gradient-based algorithms rely on the gradient of the objective function to search for the optimal solution. These optimization algorithms tend to converge quite quickly, especially close to the optimum, which is one of their main advantages [84]. The computational cost typically increases linearly as the number of design variables increases [78]. There are multiple specific features related to gradient-based algorithms, and different types of algorithms (such as steepest descent, conjugate gradient, and quasi-Newton methods, etc.) have been developed that differ in their update rules and performance characteristics.

Furthermore, Gradient-based algorithms have a clear termination criterion, as the reduction of the step size by a certain magnitude indicates that a local minimum has been reached [50]. This is considered an advantage [84]. However, these methods can be sensitive to noise in the objective function, which can cause premature termination or oscillations around a specific point. Additionally, there is no assurance that a global minimum will be found. The starting point may also have an impact on the result, as a different initial location may lead the algorithm to a distinct basin of attraction, resulting in a different optimal solution [84].

For these reasons, multiple types of gradient-based algorithms have been developed for the optimization of composite structures, and they are considered the most popular heuristic search algorithms for the optimization of composite structures [82] [17][78][50][88]. However, the presence of nonlinearities, material uncertainties, and manufacturing variations can make the objective function of the optimization non-smooth or non-convex [50]. In this kind of situation, more advanced optimization techniques such as Genetic Algorithms (see subsection 2.4.1) might be needed.

Moreover, one of the common gradient-based algorithms is the Globally Convergent Method of Moving Asymptotes (GCMMA). The GCMMA algorithm works by dividing the feasible region of the optimization problem into subdomains and using a separate asymptote for each subdomain. The

algorithm then iteratively updates the asymptotes and the design variables to converge towards an optimal solution [48]. One of the key features of GCMMA is that it guarantees finding the globally optimal solution. This is accomplished through the use of a series of approximated convex sub-problems, which are solved iteratively to find the original optimization problem [48]. The use of convex subproblems ensures convergence. GCMMA can efficiently solve non-linear and non-convex optimization problems [39].

### 2.4.2. Inspired from real-life behavior

#### Particle Swarm Optimization (PSO)

Particle Swarm Optimization (PSO) is a metaheuristic optimization algorithm that is inspired by the social behavior of bird flocking or fish schooling [15]. The algorithm works by initializing a swarm of particles randomly, similar to the Genetic Algorithm [4], each representing a potential solution to the optimization problem. The particles move through the solution space, and their movement is guided by their own best solution and the best solution found by the swarm so far. Each particle adjusts its position based on its own experience and the experience of other particles in the swarm [89]. By doing so, the space is efficiently explored, and local minimums do not affect the optimization results [15]. The algorithm continues until a stopping criterion is met, such as reaching a certain number of iterations or a certain level of convergence [89].

The advantages of PSO compared to GA and other algorithms are a clear and concise theory; an easy-to-realize algorithm; stable convergence; and highly effective calculation[4]. All these advantages push the use of the PSO algorithm for the optimization of composite structures in multiple studies [4][15][17].

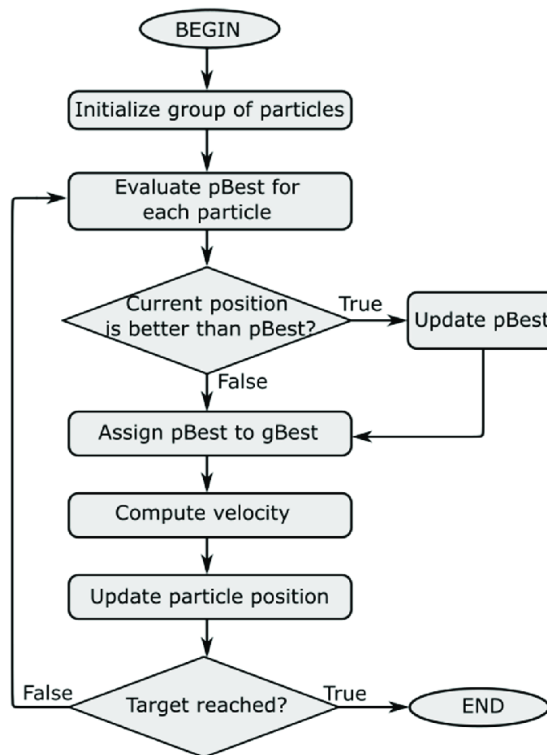


Figure 2.25: Typical Particle Swarm Optimization flowchart. Adapted from [89]

#### Black Widow Optimization Algorithm (BWO)

The Black Widow Optimization (BWO) algorithm is a metaheuristic optimization algorithm inspired by the hunting behavior of black widow spiders, taken from real-life behavior, similar to the Genetic Algorithm [90]. The BWO algorithm is a population-based algorithm that starts with an initial population of candidate solutions. The algorithm iteratively searches for better solutions by updating

the population using a combination of exploration and exploitation strategies. At each iteration, the algorithm evaluates the fitness of each candidate solution and selects the best ones to survive and reproduce[90]. The exploration strategy in BWO is inspired by the hunting behavior of black widow spiders, which use a combination of movement and web-building to capture prey. In the algorithm, this is represented by a random movement of the candidate solutions, which allows them to explore the search space in a non-linear way. In this way, it avoids the optimization to stay on a local minimum; the global one is often found thanks to this randomization of the process [90]. The exploitation strategy in BWO is based on a probabilistic model that allows the algorithm to focus on promising regions of the search space. The algorithm uses a fitness-based probability distribution to select the parent solutions for the next generation[90]. Similarly to the Genetic Algorithm, the mutation operator is applied to generate new offspring solutions.

It is particularly well-suited for problems with a large number of variables and complex, non-linear objective functions. Therefore, it has been used by Bashir et al. [15] and it showed a quicker convergence to the best optimal solution compared to Particle Swarm Optimization (see subsection 2.4.2) and Genetic Algorithm (see subsection 2.4.1) [15].

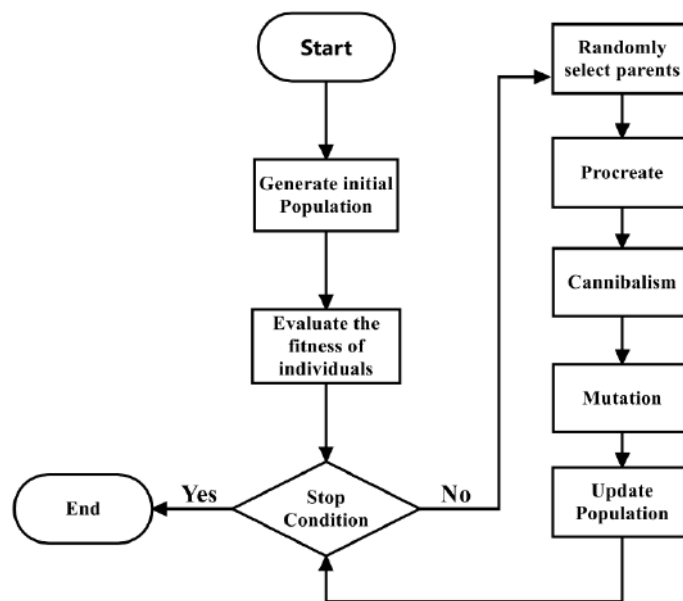


Figure 2.26: Typical Black Widow Optimization Algorithm flowchart. Adapted from [90]

### Ant Colony Optimization (ACO) and MIDACO

Ant Colony Optimization (ACO) is a metaheuristic optimization algorithm inspired by the behavior of ants. The algorithm works by simulating the foraging behavior of ants. Ants deposit pheromone trails as they travel, and other ants follow the trails to find food. In the context of optimization, the pheromone represents the quality of a solution, and the ants represent the optimization process [91]. The algorithm initializes a set of artificial ants, each representing a potential solution to the optimization problem. The ants then move through the solution space, constructing solutions by stochastically selecting components of the solution based on the pheromone levels. The pheromone levels are updated based on the quality of the solutions constructed by the ants[91]. Over time, the pheromone levels guide the ants towards better solutions, as higher-quality solutions have higher pheromone levels. The algorithm continues until a stopping criterion is met [91]. Thanks to this optimization technique, Kafkas et al. [77] developed the Mixed Integer Distributed Ant Colony Optimization (MIDACO), which is used to provide an initial optimized design, that is further optimized after [77].

### Grey-Wolf Optimizer

Grey Wolf Optimization (GWO) is a metaheuristic optimization algorithm inspired by the social behavior of grey wolves. The algorithm simulates the hunting behavior of grey wolves in a pack. The pack



contains alpha, beta, and delta wolves, which represent the best solution, the second-best solution, and the third-best solution, respectively [83]. The algorithm initializes a population of grey wolves, randomly distributed within the search space, similar to Genetic Algorithm[83]. Each grey wolf then updates its position based on the positions of the alpha, beta, and delta wolves. The position update is done using three different equations, one for each wolf, which represent different hunting behaviors (respectively searching, encircling, and attacking). Over time, the positions of the wolves converge towards the optimal solution, as the alpha wolf's position guides the rest of the pack towards better solutions. The algorithm continues until a stopping criterion is met[83].

Grey wolf optimization has been combined, by Kittinan Wansasueb et al. [83], with Genetic Algorithm (see subsection 2.4.1) and Water Cycle Algorithm to investigate a new algorithm for the optimal design of composite wings [83].

#### **Water Cycle Algorithm (WCA)**

Water Cycle Optimization (WCO) is a metaheuristic optimization algorithm inspired by the water cycle in nature. The optimization process is represented as a water cycle, where the water droplets represent the candidate solutions and the precipitation and evaporation processes represent the selection and updating of the candidate solutions. Introduced in 2012 by H. Eskandar et al. [92], the WCO algorithm is designed to handle constrained optimization problems by using a penalty function approach. The algorithm begins by generating an initial population of water droplets, which represent the candidate solutions. The water droplets are then evaluated using the objective function and the penalty function to determine their fitness. The fitness of each water droplet is then used to select the best solutions for the precipitation process, which involves the selection of the best candidate solutions [92]. In the evaporation process, the selected water droplets are updated based on their fitness and their proximity to other water droplets in the population. The evaporation process also ensures that the solutions remain within the feasible region by applying a constraint handling mechanism [92].

Water Cycle Algorithm has been combined, by Kittinan Wansasueb et al. [83], with Genetic Algorithm (see subsection 2.4.1) and Grey-Wolf Optimizer to investigate a new algorithm for the optimal design of composite wing [83].

# 3

## Preliminary Analyses

This chapter aims to introduce fundamental analysis using Abaqus. It begins by modeling a coupon geometry, which facilitates the study of materials intended for the optimized structure ahead – an aluminum alloy and a composite material. Subsequently, a comparison of distinct failure criteria for composites within Abaqus is executed to determine the most suitable criterion for subsequent optimization efforts. Following this, an investigation into buckling phenomena ensues, commencing with plate buckling behavior and extending to the scrutiny of a stiffened panel, mirroring the configuration present within the target wing component for optimization. The resulting numerical results are then compared with analytical outcomes, to confirm these results.

### 3.1. Coupon geometry

#### 3.1.1. Model description

To kick things off, several analyses were performed using a simple coupon geometry. These initial simulations aimed to characterize two distinct types of materials. In total, five different configurations were set up within Abaqus for this purpose.

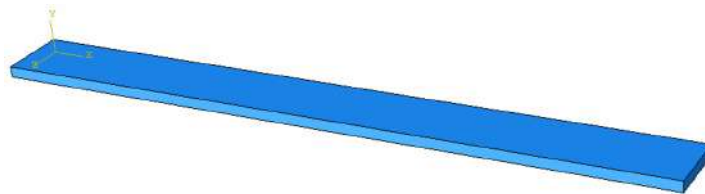


**Figure 3.1:** Basic coupon geometry. Dimensions : 100mm (x-dir), 10 mm (z-dir), 1 mm (y-dir)

For the assessment of both aluminum and composite materials in the design, a range of configurations was investigated, all featuring the same coupon geometry. The subsequent table provides an overview of these various configurations:

Simulation Number	Materials	Ply Orientation (if needed)
1	Al 6063AT6 Aluminum	X
2	USN150B Composite	$[0/0/0/0]_s$
3	USN150B Composite	$[90/90/90/90]_s$
4	USN150B Composite	$[0/-45/45/90]_s$
5	USN150B Composite	$[0/30]_4$

Table 3.1: Summary of the simulations done

For all simulations, a consistent loading scenario was employed: the coupon underwent uniaxial loading along one edge while being fixed along the opposite edge.



Figure 3.2: Load case for tension test

Depending on the material utilized in each simulation, the element type varies: the aluminum simulation employs conventional shell elements (S8R), while the composite simulation employs continuum shell elements (SC8R). The difference between conventional and continuum shell elements is explained in the Abaqus manual [93]. According to [93], "Continuum shells discretize an entire three-dimensional body, unlike conventional shells which discretize a reference surface", therefore, for conventional shells: "the thickness is defined through the section property definition" [93]. Unlike composite simulation, which requires continuum shell elements, the property through the thickness of aluminum simulation is always the same (isotropic material), which is why conventional shell elements are chosen as they lead to simpler simulations.

However, the mesh configuration remains identical for both cases, featuring elements with dimensions of  $5\text{mm} \times 2.5\text{mm} \times t$ , where 't' is the thickness, which varies according to the material. As a result, the model depicted in Figure 3.3 contains a total of 80 elements.

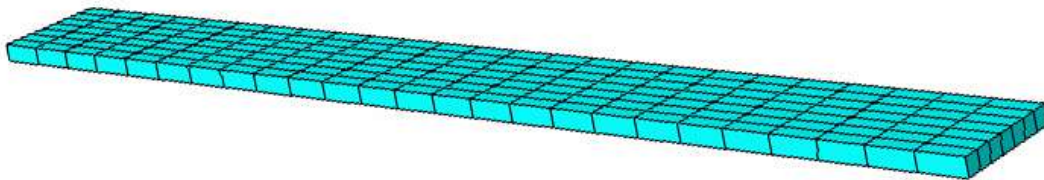


Figure 3.3: Mesh of the coupon geometry

### 3.1.2. aluminum 6063AT6

#### Simulation 0 : Al 6063AT6

Utilizing shell element S8R, the simulation for the Aluminum alloy coupon involved loading, as illustrated in Figure 3.2. This choice was made in alignment with the utilization of aluminum 6063AT6 for ribs, stiffeners, and joints in the representative wing structure (which will be optimized in the subsequent part of the master thesis) [1].

For this first simulation, a straightforward tension test was conducted on the Al6063AT6 Aluminum material. Notably, in this specific loading scenario, the slope of the stress-strain curve directly corresponds to the value of Young's Modulus (E) of the isotropic material.

The material properties are given by Bisagni et al. [1] and are as follows :

Material	E [MPa]	$\sigma_y$	$\nu$	$\rho[g/cm^3]$
Al 6063AT6	70,000	170	0.33	2.7

Table 3.2: aluminum 6063AT6 properties

By requesting field output values throughout the simulation in Abaqus, stress and strain values in the loaded right edge of the coupon are available. Thus, the following stress-strain curve, corresponding to stress and strain in the x direction (the loaded direction), taken at an element of the coupon's loaded right edge, has been obtained :

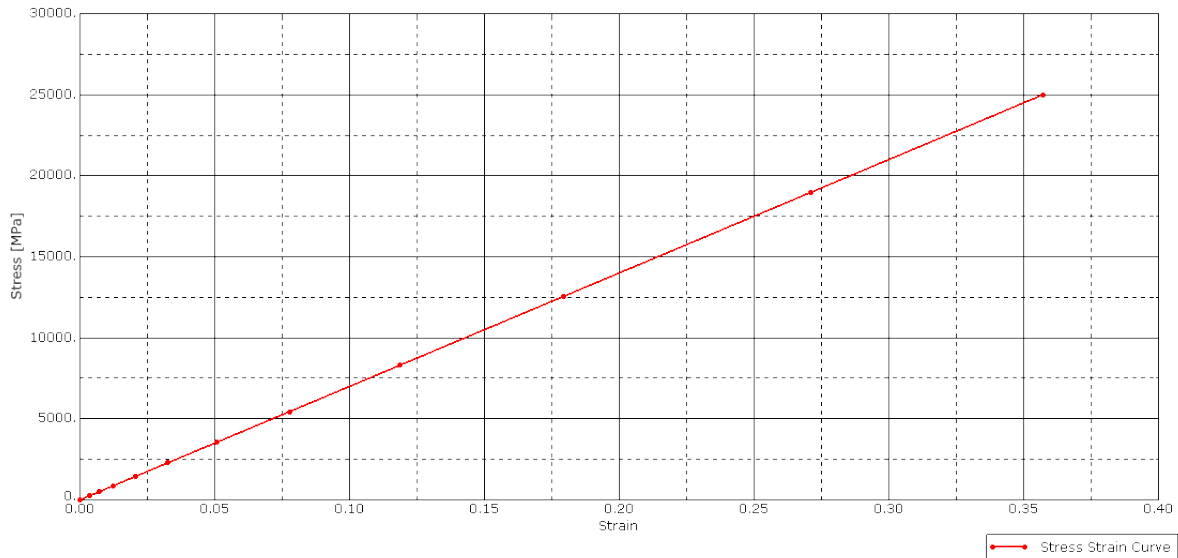


Figure 3.4: Stress Strain curve obtained

To compare the Young Modulus obtained by the simulation with the one given in Table 3.2, the slope of the curve is calculated :

$$E_{simulation} = 25000/0.357143 = 69999.972MPa \quad (3.1)$$

Here,  $E_{simulation}$  represents the slope of the curve and corresponds to Young's Modulus determined through the simulation. The difference observed between both values is negligible.

### 3.1.3. USN150B composite

In contrast to the first simulation, subsequent simulations were conducted to evaluate the USN150B composite material. This material, which is employed in both panels of the representative wing structure that will be optimized in the later stages [1], was subjected to testing through four distinct stacking sequences. The main objective of these simulations is to learn how to implement composites in Abaqus: to understand how to calculate strains, stresses, and ply failure in the composite. Another aim of these

simulations is to understand how Abaqus models the stacking sequence, to avoid errors when dealing with more complicated structures later in the thesis.

Again, the material properties are given by Bisagni et al. in [1] and are as follows :

$E_{11}$ [MPa]	$E_{22}$ [MPa]	$E_{33}$ [MPa]	$\nu_{12}$ [-]	$\nu_{13}$ [-]	$\nu_{23}$ [-]
131,000	8,000	8,000	0.29	0.47	

**Table 3.3:** USN150B composite Engineering constants (Part 1)[1]

$G_{12}$ [MPa]	$G_{13}$ [MPa]	$G_{23}$ [MPa]	$t_{ply}$ [mm]	$\rho$ [g/cm <sup>3</sup> ]
4,500	4,500	3,500	0.194	1.544

**Table 3.4:** USN150B composite Engineering constants (Part 2)[1]

Furthermore, it's important to note that each ply has a thickness of 0.194 mm. As a result, the overall thickness of the coupon has increased slightly. With a total of 8 plies, the coupon's combined thickness now amounts to  $8 \times 0.194$ , mm = 1.552, mm. Importantly, the same loading scenario, illustrated in Figure 3.2, has been selected for all four simulations.

#### **Simulation 1 :** $[0/0/0/0]_s$

This simulation exclusively employs plies oriented at 0 degrees, resulting in the stacking sequence  $[0/0/0/0]_s$ . The simulation allows us to determine the value of  $E_{11}$  as indicated in Table 3.3. This value is obtained through the slope of the stress-strain curve. The process employed in this simulation is analogous to that of the simulation 0.

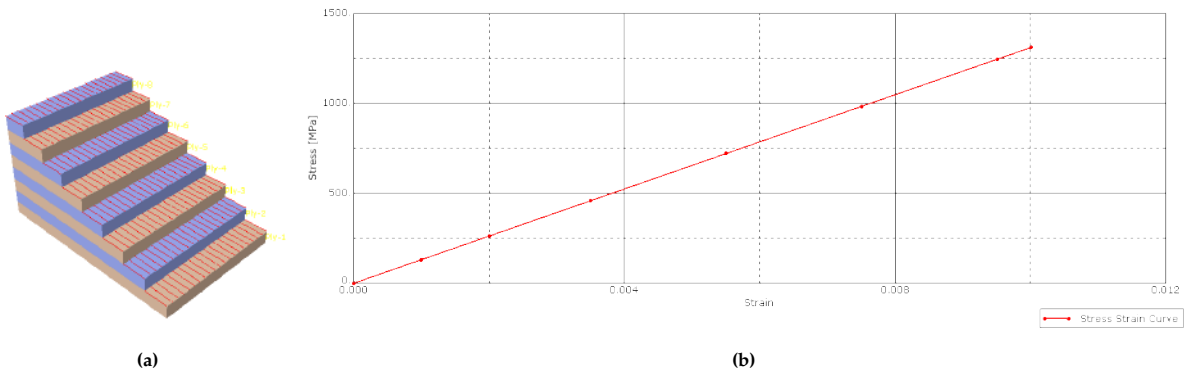


**Figure 3.5:** Simulation 1 :  $[0/0/0/0]_s$ . (a) Stacking sequence; (b) Stress-Strain Curve obtained

Based on Figure 3.5, it is possible to derive  $E_{11,simulation}$  :

$$E_{11,simulation} = 1311.41/0.0100108 = 130999.520518MPa \quad (3.2)$$

Here,  $E_{11,simulation}$  is the longitudinal stiffness of the composite determined through simulation. This value is compared with the known value of  $E_{11} = 131,000$  MPa, as outlined in Table 3.3. Similarly to previous instances, the difference, resulting from numerical approximations within the simulation, is negligible.

#### **Simulation 2 :** $[90/90/90/90]_s$

In this particular simulation, the coupon exclusively consists of 90-degree plies, forming the stacking sequence  $[90,90,90,90]_s$ . Consequently, this simulation allows us to determine the value of  $E_{22}$  as detailed in Table 3.3, which corresponds to the slope of the stress-strain curve.

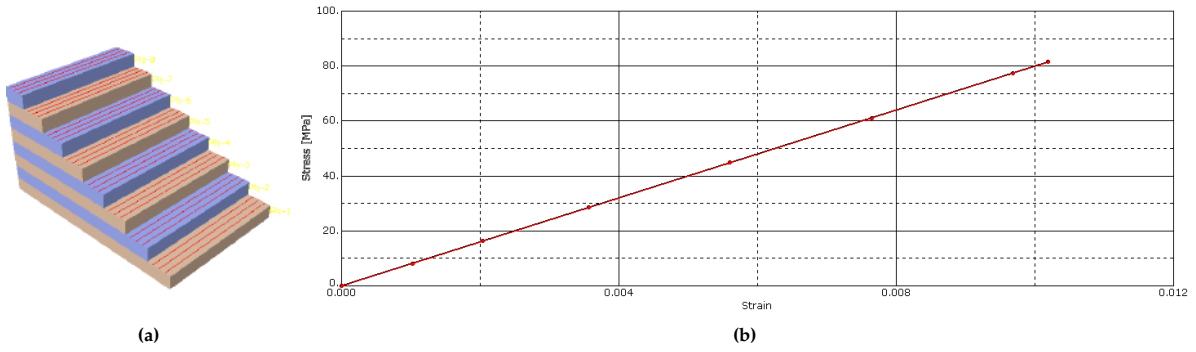


**Figure 3.6:** Simulation 2 :  $[90/90/90/90]_s$ . (a) Stacking sequence; (b) Stress-Strain Curve obtained

Based on Figure 3.6, it is possible to find  $E_{22,simulation}$ :

$$E_{22,simulation} = 81.5167/0.0101896 = 7999.99018607MPa \quad (3.3)$$

Where  $E_{22,simulation}$  is the transverse stiffness of the composite obtained with the simulation. This value needs to be compared with  $E_{22} = 8000$  MPa (see Table 3.3). Again, the difference obtained is negligible.

Following the preceding two simulations, which are renowned notably for their ability to readily determine the values of  $E_{11}$  and  $E_{22}$  for composite materials, attention was turned towards investigating two additional stacking sequences.

### **Simulation 3 :** $[0/-45/45/90]_s$

The selection of this particular stacking sequence was driven by its representation of a quasi-isotropic laminate. The arrangement of these ply orientations effectively contributes to an approximation of isotropic behavior across the coupon.

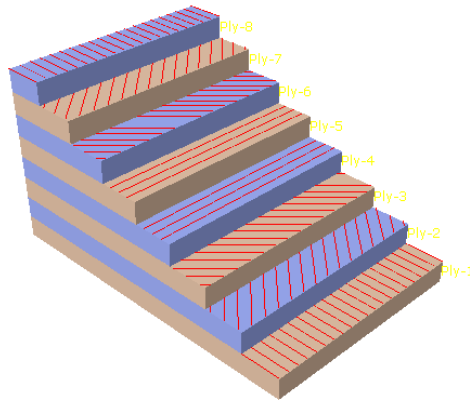


**Figure 3.7:** Stacking sequence of the simulation 3:  $[0/-45/45/90]_s$

This simulation helps to understand the variation in strain throughout the thickness of the coupon between Finite Element Analysis (referred to as FEA) and Classical Lamination Theory (abbreviated as CLT). The CLT offers a method for investigating intricate coupling processes that may occur within composite laminates. This theory is proficient in predicting the strains, displacements, stresses, etc. that would manifest in a laminate subjected to mechanical and thermal loading. Given the widespread familiarity with this theory, which is extensively covered in various textbooks within the literature (such as Kassapoglou's publication [10]), it has been deemed unnecessary to provide a complete explanation within this master thesis. Nonetheless, a Python code was developed to extract the strain evolution throughout the thickness of the quasi-isotropic laminate. The attained results were subsequently compared and visually presented in Figure 3.8.

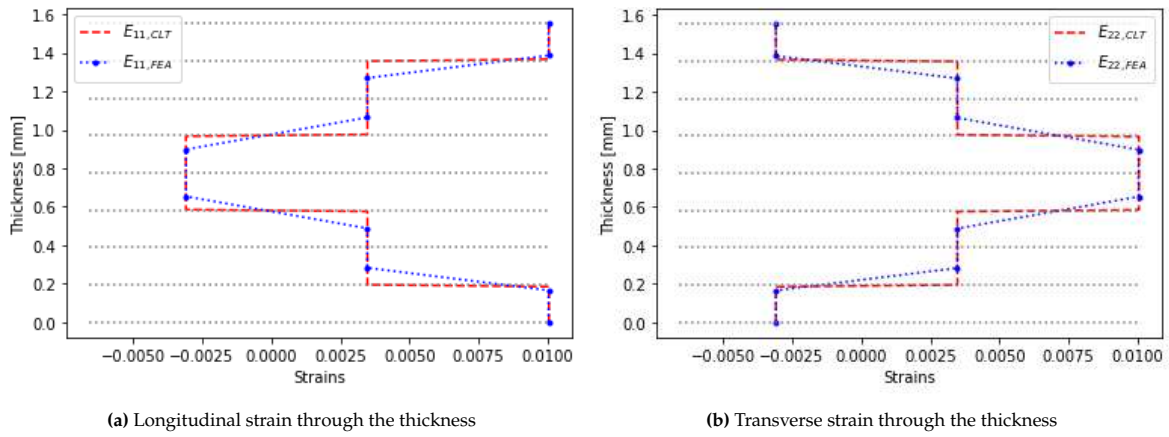


Figure 3.8: Strains through the thickness for the quasi-isotropic laminate

As with previous simulations, the finite element analysis values for plotting these curves were obtained by requesting output field values in Abaqus, such as the strain values through the coupon thickness. The plots above show the values obtained for longitudinal and transverse strains.

Ply $n^\circ$	Ply orientation [°]	$E_{11,FEA}$	$E_{11,CLT}$	$diff_{11}$ [%]	$E_{22,FEA}$	$E_{22,CLT}$	$diff_{22}$ [%]
1	0	0.010033	0.010048	0.150	-0.003082	-0.003086	0.129
2	-45	0.003475	0.003481	0.172	0.003477	0.003481	0.115
3	45	0.003477	0.003481	0.115	0.003475	0.003481	0.172
4	90	-0.003082	-0.003086	0.129	0.010033	0.010048	0.150

Table 3.5: Strains through the thickness for the quasi-isotropic laminate

where  $E_{11,FEA}$  is the longitudinal strain for the FEA,  $E_{11,CLT}$  is the longitudinal strain for the CLT,  $E_{22,FEA}$  is the transverse strain for the FEA,  $E_{22,CLT}$  is the transverse strain for the CLT.  $diff$  is the difference in % between the value obtained in FEA and CLT, obtained with the following formula :

$$diff_i = \frac{|E_{i,FEA} - E_{i,CLT}|}{E_{i,CLT}}, \text{ with } i = 11, 22 \quad (3.4)$$

Table 3.5 presents the precise strain values within the various plies of the quasi-isotropic laminate. It's important to note that due to the limited availability of only 10 points across the thickness in Abaqus, each ply is represented by only one point (except for the outer plies, which have two points). If more points were accessible through the thickness in the Abaqus simulation, the blue line would exhibit closer alignment with the red lines. Notably, the differences remain consistently below 0.2% for both longitudinal and transverse strains across all plies. Additionally, Figure 3.8 showcases only 4 plies since the laminate possesses symmetry, resulting in identical strain values for the symmetric plies.

#### Simulation 4 : $[0/30]_4$

For this last simulation, another stacking sequence has been studied:  $[0/30]_4$ .

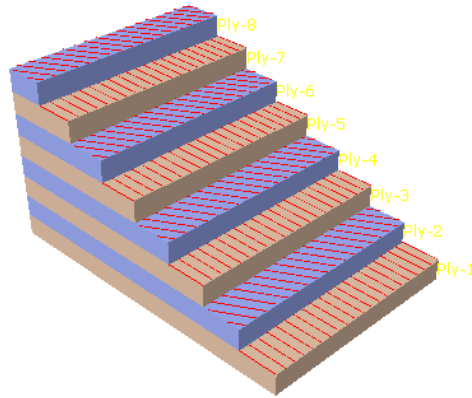


Figure 3.9: Stacking sequence of the simulation 4:  $[0/30]_4$

This stacking sequence lacks symmetry and features four 30-degree ply. Utilizing the CLT framework outlined by Kassapoglou [10], a juxtaposition is drawn between FEA and CLT. Figure 3.10 shows the longitudinal and transverse strains distributed throughout the thickness of the coupon.

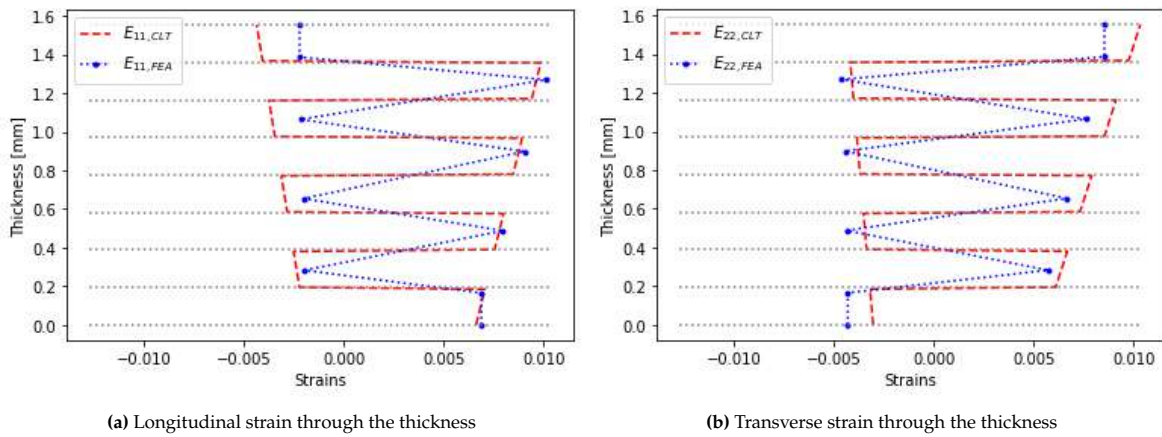


Figure 3.10: Strains through the thickness for the simulation 4:  $[0/30]_4$

Ply $n^\circ$	Ply orientation $[\circ]$	$E_{11,FEA}$	Mean $E_{11,CLT}$	$E_{22,FEA}$	Mean $E_{22,CLT}$
1	0	0.00688	0.00683	-0.0042988	-0.00311
2	30	-0.00197	-0.00235	0.00570717	0.00635
3	0	0.00796	0.00776	-0.00436487	-0.00342
4	30	-0.00202	-0.00295	0.00664911	0.00752
5	0	0.00904	0.00862	-0.00443094	-0.00376
6	30	-0.00217	-0.00359	0.00759106	0.00883
7	0	0.01012	0.00962	-0.00459702	-0.00408
8	30	-0.00221	-0.00421	0.008533	0.00988

Table 3.6: Comparison of strain through the thickness between FEA analysis and CLT

Table 3.6 provides detailed strain values across the distinct plies of the laminate. Notably, larger discrepancies are observed when compared to the quasi-isotropic simulation. However, these discrepancy values are observed within an identical overall behavior exhibited by the coupon in both simulations.



It's worth mentioning that a consistent offset is noticeable for both longitudinal and transverse strains.

Furthermore, an intriguing aspect to note is that, due to the asymmetry of the laminate, the strain variation across a single ply is not constant according to the CLT prediction. Unfortunately, this phenomenon can't be effectively observed within FEA due to the limited number of points, leading to only one value being observed for each ply. Considering the non-constant strain across a ply as predicted by the CLT, the mean strain value across each ply has been included in Table 3.6. This particular characteristic contributes to explaining the observed differences between the CLT and FEA results.

## 3.2. Failure criteria

As elaborated upon in subsection 2.1.1, diverse failure modes are evident in composites, accompanied by a range of failure criteria to assess structural integrity. Certain criteria, such as Hashin criteria, aid in identifying the specific failure mode, while others—Tsai-Wu, Tsai-Hill, Maximum strain, and Maximum stress—offer distinct criteria for assessing failure. The objective of this analysis is to select the most suitable failure criterion for our simulation by conducting a comprehensive comparison of the primary failure criteria available within Abaqus. This evaluation is conducted utilizing the same model employed in the preceding section, retaining the coupon geometry, loading scenario, and mesh configuration.

As outlined in the Abaqus user's manual [93], the manifestation of damage in fiber-reinforced composites is depicted through the degradation of material stiffness. These materials typically demonstrate an elastic-brittle behavior, indicating minimal plastic deformation upon the initiation of damage. Consequently, plasticity is excluded from the modelization of such materials. Further elaboration on the theory underpinning damage initiation in fiber-reinforced composites within the Abaqus framework is available in the user's manual [94].

The main damage properties of the USN150B composite are given by Bisagni et al. [1] and are reported hereafter :

	Tensile Strength [MPa]	Compression Strength [MPa]	Shear Strength [MPa]
Longitudinal	2000	2000	70
Transverse	61	200	40

**Table 3.7:** USN150B composite Hashin damage properties [1]

### 3.2.1. Hashin criteria

Moreover, Abaqus simulations already incorporate Hashin's failure criteria (as discussed in subsection 2.1.1) within the application. Additionally, the simulation allows for the specification of properties related to damage evolution. However, since no delamination is considered in the scope of this thesis, it is not necessary to specify values corresponding to these properties.

The four simulations employing different stacking sequences were evaluated using Hashin's failure criterion. It's crucial to reiterate that Hashin's theory serves to not only assess failure but also identify the critical failure mode. Since composite materials exhibit a variety of failure modes, Hashin's criterion is instrumental in determining the mode that is most critical in a given scenario. Accordingly, various critical failure modes are observed based on the specific stacking sequence. For instance, Figure 3.11a illustrates that the first simulation, comprised solely of 0-degree plies, experiences initial failure due to fiber tension. Similarly, the quasi-isotropic laminate, as shown in Figure 3.11c, also encounters failure due to fiber tension (in the first ply, as explained later). On the contrary, Figure 3.11b demonstrates that the second simulation, featuring solely 90-degree plies, experiences failure primarily due to matrix tension. In the final simulation with the  $[0/30]_4$  stacking sequence, Hashin's criteria for both matrix tension and fiber tension are exhibited. It's noticeable in Figure 3.11d that matrix tension reaches the

critical value of 1, triggering failure, while fiber tension remains below 1, specifically at 0.23 when failure initiates due to matrix tension, as depicted in Figure 3.11e.

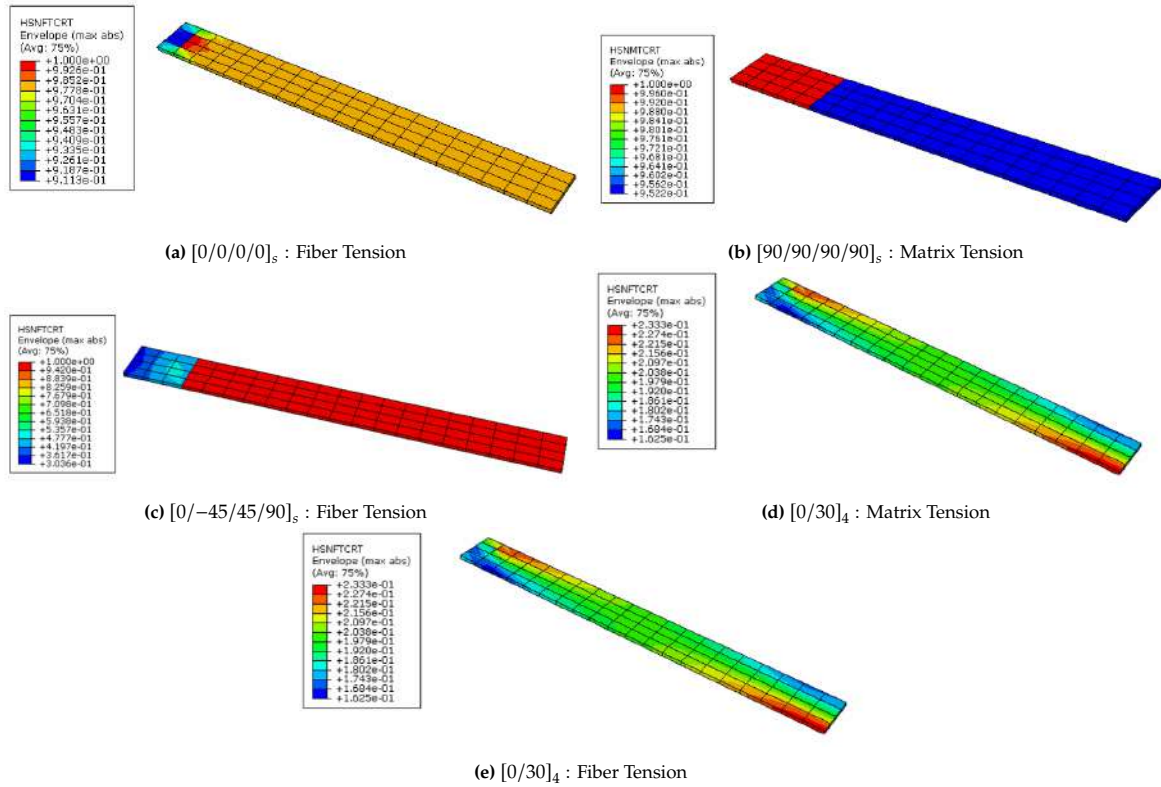


Figure 3.11: Different failure modes of the simulations.

The various contour plots of the failure mode depicted in Figure 3.11 showcase the corresponding failure mode values across the entire laminate. To be specific, these plots display the envelope value, which corresponds to the maximum value of the variable (the respective failure mode in this case) across all plies of the laminate. However, when confronted with complicated stacking sequences, such as the example of the quasi-isotropic laminate, it becomes valuable to discern precisely which ply is experiencing failure. This prompted the creation of Figure 3.12, which specifically illustrates the Fiber tension failure mode across the four plies of the Quasi-Isotropic laminate. From these illustrations, it becomes apparent that the first ply is failing, given that its failure index reaches the critical value of 1. Meanwhile, the remaining three plies do not approach the critical value; they all remain below 0.16. Specifically, both the 45-degree and -45-degree plies exhibit a value of 0.1511, while the 90-degree ply registers a value of 0.1219. Notably, the symmetric plies exhibit analogous behavior.

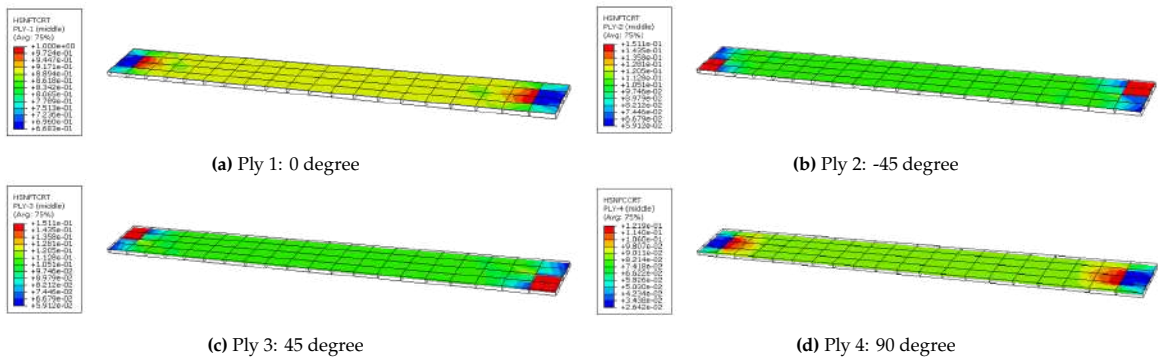


Figure 3.12: Hashin Fiber Tension through the plies in the Quasi-Isotropic laminate

The behavior of the 45° and -45° plies is symmetrical, showcasing a reinforced value of the Hashin criteria in the direction normal to the orientation of the plies (refer to Figure 3.7 for the ply orientation). This observation aligns with expectations, considering that the material exhibits superior properties in the longitudinal direction compared to the transverse direction, according to Table 3.7.

### 3.2.2. Comparison with other failure criteria

Abaqus provides various alternative failure criteria. Utilizing the output field request feature, it's possible to extract the following four failure criteria: Tsai-Hill, Tsai-Wu, Maximum strain, and Maximum stress. These criteria, which have been detailed in subsection 2.1.1, are computed during the simulation utilizing the strain and stress values. Furthermore, the material's damage properties, outlined in Table 3.7, contribute to these calculations. Figure 3.13 portrays the computed values of the diverse failure criteria at the end of the simulation. Notably, all these values exceed 1, which represents the critical threshold for initiating failure. Unlike Hashin's criteria, these four criteria do not provide insight into the specific failure mode of the composite material.

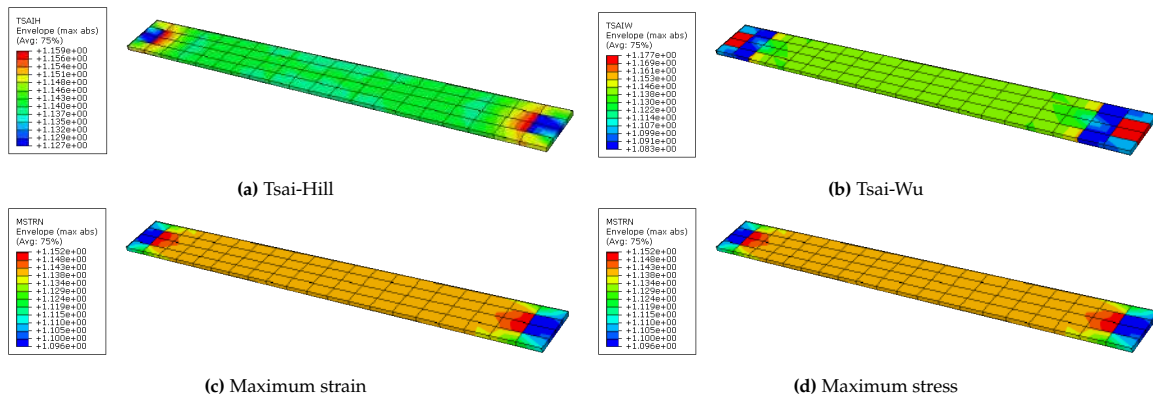


Figure 3.13: Different failure criteria available with Abaqus

Based on Figure 3.13 and Figure 3.12, it becomes evident that the five failure criteria yield comparable contour plots. The failure stress from each criterion can be added to the previously acquired Stress-Strain curves of simulation 1 and simulation 2, with the following stacking sequence  $[0/0/0/0]_s$  and  $[90/90/90/90]_s$  respectively. These curves, complete with the corresponding failure stress values, are presented in Table 3.8.

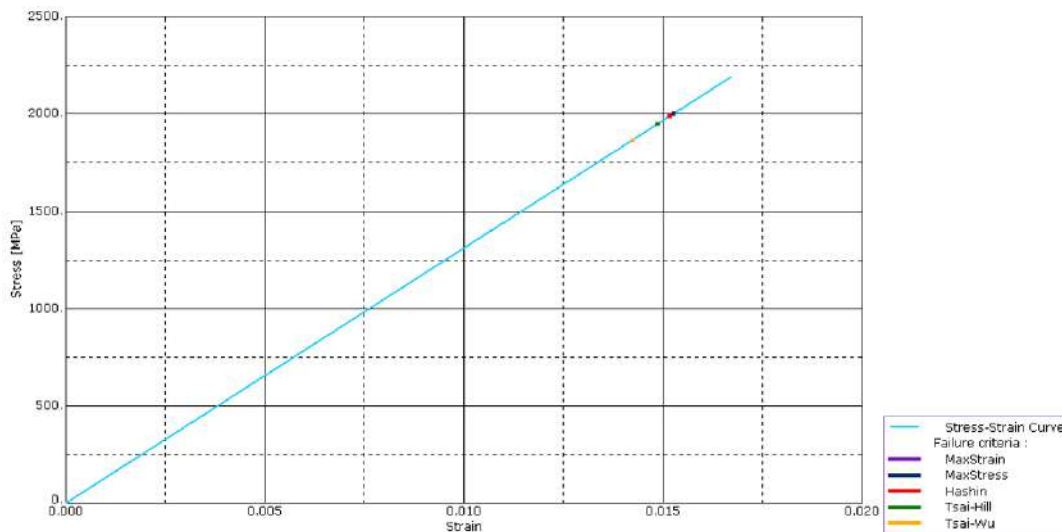


Figure 3.14: Failure criteria comparison on simulation 1:  $[0/0/0/0]_s$

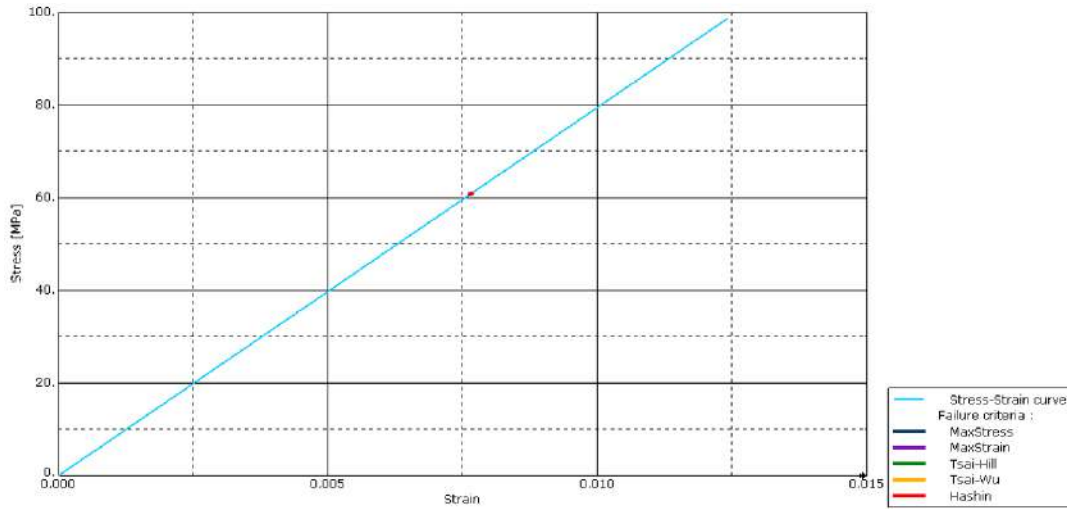


Figure 3.15: Failure criteria comparison on simulation 2:  $[90/90/90/90]_s$

Failure criteria	Failure stress		Failure stress	
	Simulation 1 [MPa]	$diff_1$ [%]	Simulation 2 [MPa]	$diff_2$ [%]
Hashin	1987	X	61.0	X
Tsai-Wu	2002	0.8	60.9	0.2
Tsai-Hill	2000	0.7	61.0	0.0
Maximum Strain	1866	6.1	60.1	1.5
Maximum Stress	1948	2.0	60.1	1.5

Table 3.8: Comparison between various failure criteria

In Table 3.8,  $diff_i$  is the difference in % between the value obtained with Hashin's failure criteria and the other's failure criteria, with  $i = 1$  corresponding to simulation 1:  $[0/0/0/0]_s$  and  $i = 2$  corresponding to simulation 2:  $[90, 90, 90, 90]_s$ .

The data in Table 3.8 underscores the remarkable consistency among the five criteria, as they yield comparable failure stress values (and by extension, similar failure strains, although not explicitly provided in the table due to their linear relationship with stress). Specifically, for Tsai-Wu and Tsai-Hill criteria, both  $diff$  values are less than 1%, highlighting the remarkable similarity. While there is slightly higher variance in the values provided by the maximum strain and maximum stress failure criteria, this observation is expected given the distinct equations governing their definitions (refer to subsection 2.1.1).

To conclude this segment, it's evident that similar outcomes are obtained across different failure criteria. The contour plots consistently exhibit similar patterns, with peak failure criterion values located at both sides of the coupon. However, Hashin's criteria present two distinct advantages over the other criteria.

Firstly, Hashin's criteria provide insights into the specific failure mode, be it Fiber tension, Matrix tension, Fiber compression, or Matrix compression. This valuable information contributes to a deeper understanding of the ongoing damage process within the structure.

Secondly, Hashin's criteria facilitate the plotting of failure criteria across each ply within the composite structure, as demonstrated by Figure 3.12. Such a capability is not offered by the other criteria.

Considering these factors, especially for assessing ply failure in the final structure, Hashin's criteria will be the preferred choice moving forward in the thesis.

### 3.3. Buckling of a plate

#### 3.3.1. Aluminum Alloy 2024-T4

This section focuses on the classic solution for plate buckling. The considered plate possesses dimensions characterized by length "a" width "b" and thickness "t". These specific values, along with the pertinent properties of the Aluminum Alloy 2024-T4, have been outlined in Table 3.2.

$E$ [MPa]	$\nu$ [-]	$\rho$ [kg/m <sup>3</sup> ]	a [mm]	b [mm]	t [mm]
73,100	0.3	2780	900	300	1.1

**Table 3.9:** Plate of aluminum Alloy 2024-T4 properties

Given these particular values, it's appropriate to categorize the plate as thin, where the thickness "t" is considered negligible when compared to the dimensions "a" and "b". Additionally, the transverse shear strains are deemed to be insignificant. For a simply-supported plate, classical textbooks provide the linear buckling solution, as considered in the following part:

$$N_x = \frac{D\pi^2}{b^2} \times \left( \frac{mb}{a} + \frac{a}{mb} \right)^2 \quad (3.5)$$

$N_x$  represents the compression load per unit length. When multiplied by the length of the edge on which the load is applied, it results in the total compression load. The variable "m" corresponds to the number of half-waves in the buckling mode shape along the loading direction. The parameter "D" represents a well-known constant referred to as the bending stiffness of the plate. This constant can be calculated using the expression defined in Equation 3.6. In the case of an isotropic material, such as the aluminum alloy in question, this constant can be expressed as a combination of Young's modulus "E," Poisson's ratio " $\nu$ ," and the thickness "t" of the plate as follows:

$$D = \frac{Et^3}{12(1 - \nu^2)} \quad (3.6)$$

The objective of this section is to juxtapose the analytical solution with numerical results acquired through Abaqus simulations. To achieve this, a plate characterized by the properties outlined in Table 3.9 was modeled. This plate was subjected to uniaxial loading along one edge while being fixed along the opposite edge. The remaining edges were constrained through displacement in the  $U_z$  direction, which is the normal direction of the plate. A detailed account of all the boundary conditions can be found in Table 3.10, which collectively represents a configuration of a simply supported plate. This approach was adopted to validate the accuracy of the analytical solution.

Location	Boundary conditions
Edge $x = 0$	$U_x = 0 ; U_z = 0$
Edge $x = a$	$U_z = 0$
Edges $y = 0$ and $y = b$	$U_z = 0$
Origin $(x,y) = (0,0)$	$U_y = 0$

**Table 3.10:** Boundary conditions of the plate

The displacement  $U_y$  in the direction perpendicular to the applied load was constrained at the origin, which corresponds to the bottom-left corner of the plate. This strategy was pursued after encountering unexpected behavior in the buckling modes when attempting to constrain this displacement for all the fixed edges. According to the thesis written by Zhang [95], by confining the displacement constraint to one corner of the edge, this issue was successfully addressed.

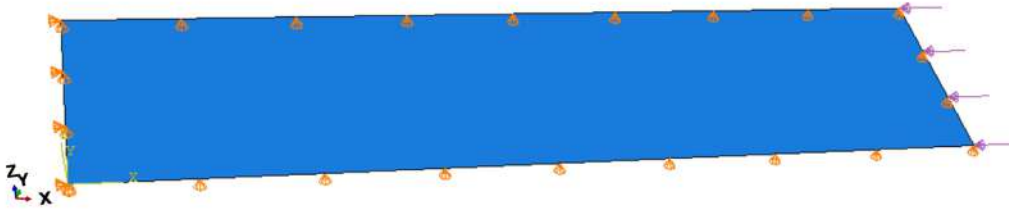


Figure 3.16: aluminum plate loading case

Regarding the meshing of the plate, an element size of 10 mm was adopted. This choice results in a total of 2700 elements, achieved by dividing the plate into a grid of dimensions 90x30 elements. As specified by Zhang in [95], this element size selection ensures convergence towards the anticipated solutions while minimizing significant computational time disparities compared to larger element sizes. The meshing of the aluminum plate is visualized in Figure 3.17.

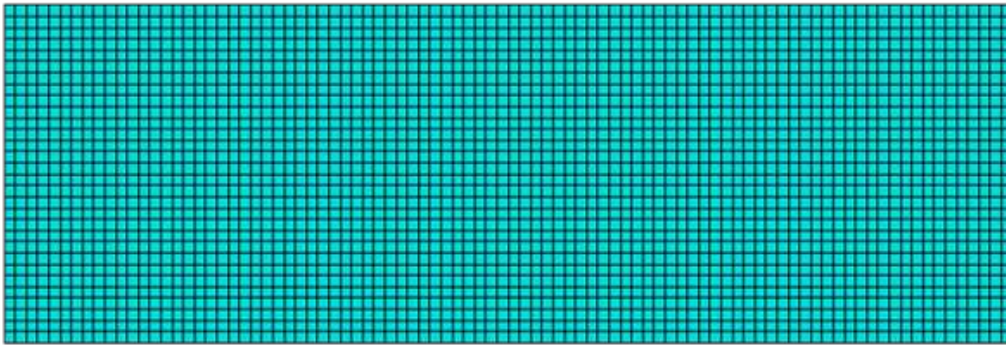


Figure 3.17: Mesh of the aluminum plate

Utilizing Abaqus, an eigenvalue analysis can be performed using the **Buckle** step within the procedure type termed "Linear Perturbation." In this context, the initial focus will be on conducting a standard eigenvalue analysis and subsequently comparing the obtained results with those anticipated from the analytical solution.

Using shell element SC8R, Figure 3.18 shows the first buckling mode obtained with the eigenvalue analysis.

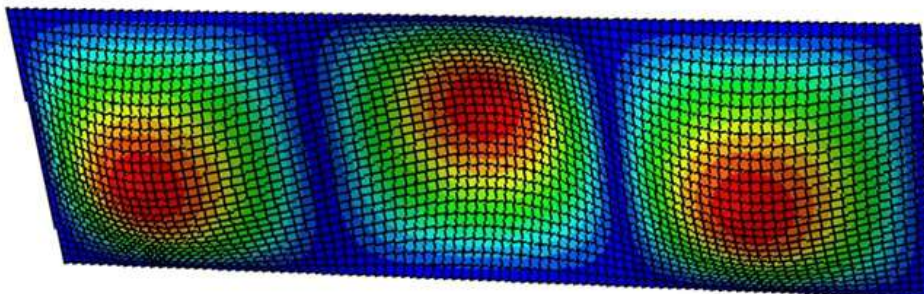


Figure 3.18: Buckling of the aluminum plate

Based on the simulation, the first eigenvalue, which corresponds to the buckling compression load

per unit length, is determined to be  $N_{x,numerical} = 3.9134$ . Consequently, it becomes feasible to calculate the critical buckling load, denoted as  $P_{cr,numerical}$ , using the following relationship:

$$P_{cr,numerical} = N_{x,numerical} \times b = 3.9134 \times 300 = 1174N \quad (3.7)$$

With the numerical buckling load determined, a validation process can be conducted against the analytical buckling load. Referring to Figure 3.18, it's established that the first buckling mode entails three half-waves within the buckling mode shape along the loading direction.

The analytical solution for the aluminum plate can be deduced using Equation 3.5:

$$N_x = \frac{D\pi^2}{b^2} \times \left( \frac{mb}{a} + \frac{a}{mb} \right)^2 \quad (3.8)$$

$$N_x = \frac{\frac{73,100 \cdot 1.1^3}{12(1-0.3^2)} \pi^2}{300^2} \times \left( \frac{m * 300}{900} + \frac{900}{m * 300} \right)^2$$

The value of  $m$ , a positive integer, needs to be found to minimize the value of  $N_x$ . Therefore, it has to minimize the right term, under the square, of  $N_x$ . This means finding the minimum value of the following function:  $f(m) = \frac{3}{m} + \frac{m}{3}$ . Derivation of the previous term gives  $f'(m) = -\frac{3}{m^2} + \frac{1}{3}$ . This is equal to zero for  $m = 3$ . Since  $f'$  is negative for values lower than 3 and positive for values higher than 3, it means that the minimum of  $f$  is reached for  $m = 3$ . As a consequence, to find the analytical solution for the aluminum plate, the value taken by  $m$  in Equation 3.8 is 3, leading to :

$$N_x = \frac{\frac{73,100 \cdot 1.1^3}{12(1-0.3^2)} \pi^2}{300^2} \times \left( \frac{3 * 300}{900} + \frac{900}{3 * 300} \right)^2 \quad (3.9)$$

$$N_x = 3.9088N/mm$$

Therefore, the critical buckling load according to the analytical solution, called  $P_{cr,analytical}$ , as follows:

$$P_{cr,analytical} = N_x \times b = 3.9088 \times 300 = 1173N \quad (3.10)$$

Finally, the difference between both solutions can be calculated as follows :

$$diff = \frac{|P_{cr,numerical} - P_{cr,analytical}|}{P_{cr,analytical}} = 0.085\% \quad (3.11)$$

The small disparity between the two solutions, measuring less than 0.01%, substantiates the conclusion that the numerical model of the plate effectively mirrors the behavior of the plate.

Furthermore, building upon the outcomes derived through the **Buckle** step, it is possible to develop post-buckling analyses. This entails introducing the first mode of the eigenvalue analysis as an imperfection within a **Dynamic, Implicit** analysis. In this context, the imperfection is scaled to a magnitude equal to 0.01 times the plate thickness. The results stemming from the **Dynamic, Implicit** simulation are graphically portrayed in Figure 3.19. This visual representation reveals the emergence of a comparable first buckling mode when juxtaposed with the one garnered through the linear buckling analysis depicted in Figure 3.18.

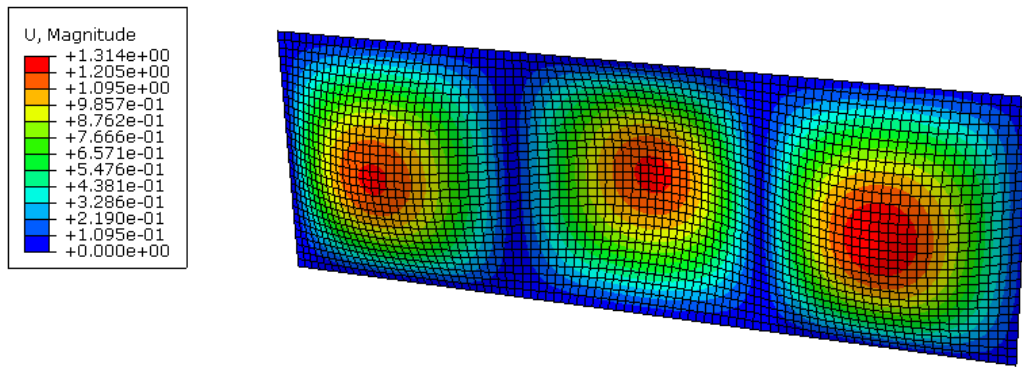


Figure 3.19: First buckling mode of the aluminum plate, obtained with **Dynamic, Implicit** analysis

Moreover, since a post-buckling analysis is conducted, it is possible to plot the load-displacement curve, shown in. From this graph, a change in the slope of the curve is observed exactly at the buckling load (represented by the green dots) calculated analytically and confirmed by the linear buckling analysis. Additionally, given the undertaking of a post-buckling analysis, the opportunity arises to plot the load-displacement curve, as depicted in Figure 3.20. This graphical representation distinctly showcases a discernible change in the slope of the curve precisely at the analytically determined buckling load. This reduction of the stiffness, which is represented by the slope of the curve, is observed beyond the buckling load. This graph confirms the results previously obtained both analytically and with the linear buckling analysis.

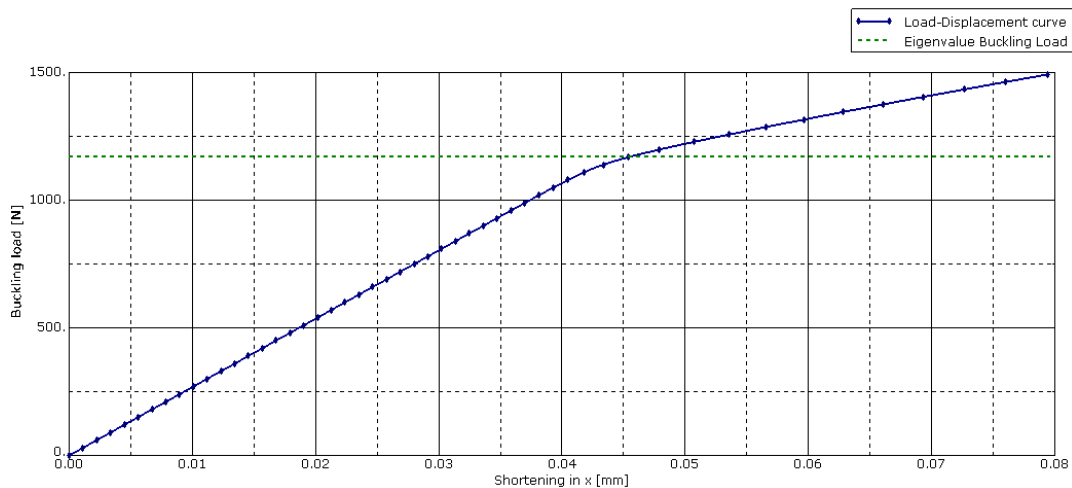


Figure 3.20: Load displacement curve of the aluminum plate obtained with **Dynamic, Implicit** analysis

### 3.3.2. Composite laminate : UD Carbon Prepreg IM7/8552

In addition to the application of aluminum alloy in aircraft components, the utilization of composite laminates to bear primary load structures has increased in contemporary designs. Notably, this includes the representative wing component slated for optimization in subsequent phases of this thesis. To this end, a preliminary examination of the buckling behavior of a composite laminate is subsequently conducted. This analysis serves a dual purpose: first, to evaluate the influence of various layups on the buckling performance, and second, to validate the buckling simulation process within a composite layup.

The analytical solution for buckling of a composite plate is provided by [95]. This solution is derived through Timoshenko's formulation of the equilibrium equations for a thin plate devoid of initial geometric imperfections. The process involves solving the governing equation of the plate using the Fourier series to express the out-of-plane displacement  $w$ . Consequently, the critical buckling load for



an orthotropic laminate can be derived as follows:

$$P_{cr,analytical} = \bar{N}_{cr,analytical} * b = (D_{11}D_{22})^{\frac{1}{2}} * \frac{\pi^2}{b} \left[ \left( \frac{mb}{a} * \frac{1}{\alpha} \right)^2 + \left( \frac{a}{mb} * \alpha \right)^2 + 2\beta \right] \quad (3.12)$$

where  $P_{cr,analytical}$  is the critical buckling load,  $\bar{N}_{cr,analytical}$  is the critical buckling load per unit of length,  $D_{11}$  and  $D_{22}$  are bending stiffness values concerning the x (longitudinal) and y (transverse) directions of the plate, a is the length of the plate, b is the width of the plate, m is the number of half-waves in the buckling mode shape along loading direction, finally,  $\alpha$  and  $\beta$  represent the flexural orthotropy, and are defined as follows:

$$\alpha = \left( \frac{D_{22}}{D_{11}} \right)^{\frac{1}{4}} ; \quad \beta = \frac{D_{12} + 2D_{66}}{(D_{11}D_{22})^{\frac{1}{2}}} \quad (3.13)$$

The plate examined for the composite laminate shares identical dimensions to the one investigated using Aluminum material. This entails equivalent length "a" and width "b". Similarly, both plates feature matching load and boundary conditions, with both being subjected to the scenario of a simply supported plate subjected to uniaxial compression. The specific conditions and constraints can be referenced in Table 3.10 and illustrated visually in Figure 3.16.

For this part, the material is no longer an aluminum alloy but a composite laminate called Unidirectional (UD) Carbon Prepreg IM7/8552, which engineering constants for each ply are precised in Table 3.11.

$E_{11}$ [MPa]	$E_{22}$ [MPa]	$G_{12}$ [MPa]	$\nu$ [-]	$\rho$ [kg/m <sup>3</sup> ]	$t_{ply}$ [mm]
150,000	9080	5290	0.32	1570	0.125

Table 3.11: UD Carbon Prepreg IM7/8552 composite Engineering constants [1]

Similarly to what has been done in the case of the aluminum alloy plate, first a linear buckling analysis will be done with 4 different stacking sequences, to confirm numerically the buckling load calculated by Equation 3.12. In a second step, a post-buckling analysis will be done with **Dynamic, Implicit** simulation. This analysis will allow us to plot the load-displacement curve and observe a reduction of the stiffness after buckling occurs.

#### First stacking sequence: [0/0/0/0]<sub>s</sub>

First, the critical buckling load is calculated analytically, with the element of the matrix **D**. As for the aluminum plate, the value of  $m$ , equal to 2 for this stacking sequence, was chosen to minimize  $P_{cr,analytical}$ . Equation 3.12 gives:

$$P_{cr,analytical} = 314.31N \quad (3.14)$$

Continuing with the linear buckling analysis, the stacking sequence [0/0/0/0]<sub>s</sub> yields a first mode characterized by two half waves, as illustrated in Figure 3.21. In contrast, the second mode displays only one half-wave.

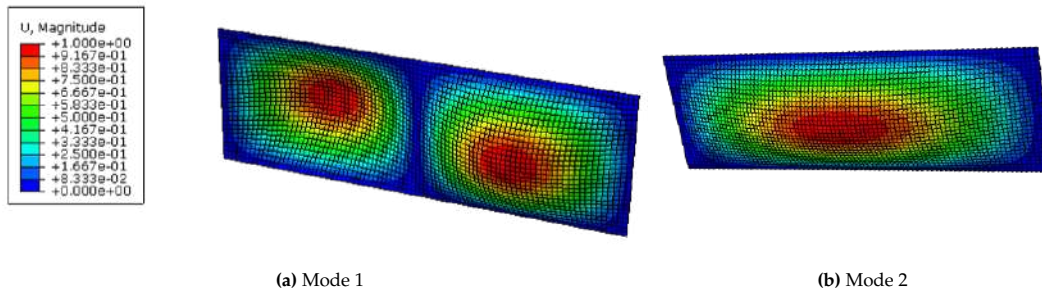


Figure 3.21: First two buckling modes of the [0/0/0/0]<sub>s</sub> plate, obtained with linear buckling analysis

Furthermore, based on the Eigenvalue given by Abaqus, which represents the critical buckling load per unit of length, it becomes feasible to calculate the critical buckling load numerically:

$$P_{cr,numerical} = \bar{N}_{cr,numerical} * b = 1.0488 * 300 = 314.64N \tag{3.15}$$

Therefore, it is possible to derive the difference between numerical and analytical solutions :

$$diff = \frac{|P_{cr,numerical} - P_{cr,analytical}|}{P_{cr,analytical}} = 0.105\% \tag{3.16}$$

This difference is low and confirms the simulations done with Abaqus, as well as the derivation done to obtain the analytical value.

Moreover, similarly to what has been done with the aluminum alloy plate, a post-buckling analysis is done with a **Dynamic, Implicit** simulation. Figure 3.22 shows the first buckling mode obtained with this simulation. The same number of half-waves and buckling behavior is observed.

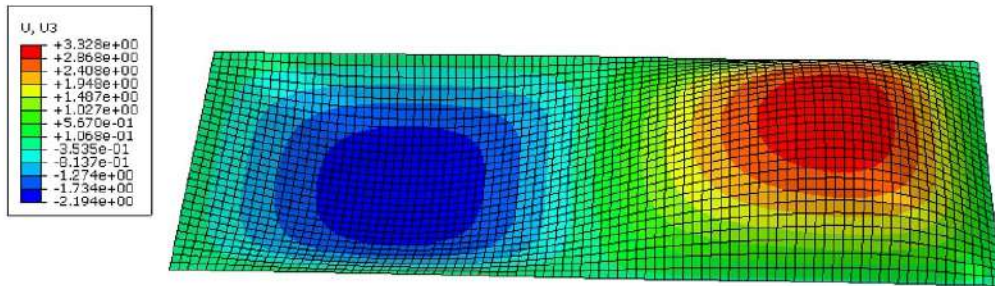


Figure 3.22: First buckling mode of the [0/0/0/0]<sub>s</sub> plate, obtained with **Dynamic, Implicit** analysis

Concluding this analysis, Figure 3.23 portrays the load-displacement curve resulting from the **Dynamic, Implicit** simulation. This graphical representation underscores a discernible change in the curve’s slope precisely at the analytically calculated buckling load. This alignment is further corroborated by the outcomes of the linear buckling analysis, denoted by the green dots in Figure 3.23. This observation aligns with the results previously acquired through both analytical calculations and the linear buckling analysis.

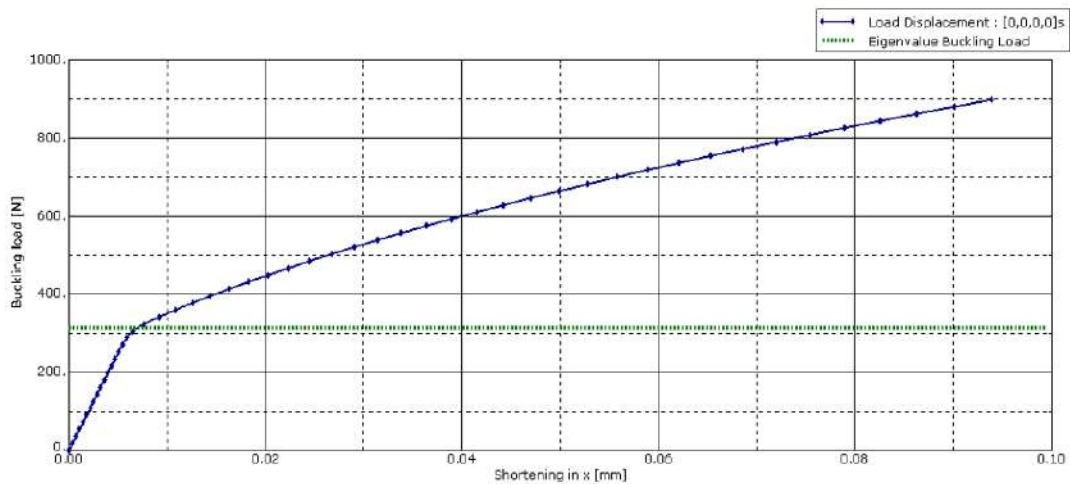


Figure 3.23: Load displacement curve of the [0/0/0/0]<sub>s</sub> plate obtained with **Dynamic, Implicit** analysis

**Second stacking sequence:** [90/90/90/90]<sub>s</sub>

First, the critical buckling load is calculated analytically, called with the element of the matrix **D**. As for the previous simulations, the value of *m*, equal to 6 for this stacking sequence, was chosen to minimize

$P_{cr,analytic}$ . Equation 3.12 gives:

$$P_{cr,analytic} = 277.69N \tag{3.17}$$

Then, the linear buckling analysis, with the following stacking sequence:  $[90/90/90/90]_s$ , gives a first mode with 6 half waves, as shown by Figure 3.21. The second mode presents seven half-waves.

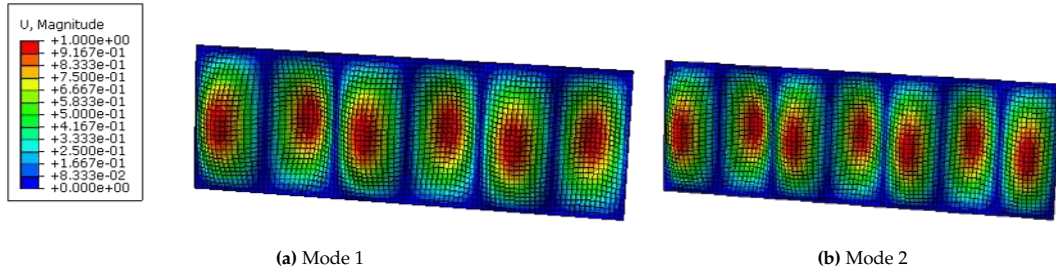


Figure 3.24: First two buckling modes of the  $[90/90/90/90]_s$  plate, obtained with linear buckling analysis

Furthermore, based on the Eigenvalue given by Abaqus, which represents the critical buckling load per unit of length, it is possible to derive the critical buckling load obtained numerically:

$$P_{cr,numerical} = \bar{N}_{cr,numerical} * b = 0.92685 * 300 = 278.06N \tag{3.18}$$

Therefore, it is possible to derive the difference between numerical and analytical solutions :

$$diff = \frac{|P_{cr,numerical} - P_{cr,analytical}|}{P_{cr,analytical}} = 0.14\% \tag{3.19}$$

This difference is low and confirms the simulations done with Abaqus, as well as the derivation done to obtain the analytical value.

Moreover, similarly to what has been done previously, a post-buckling analysis is done with a **Dynamic, Implicit** simulation. Figure 3.25 shows the first buckling mode obtained with this simulation. The same number of half-wave and buckling behavior is observed.

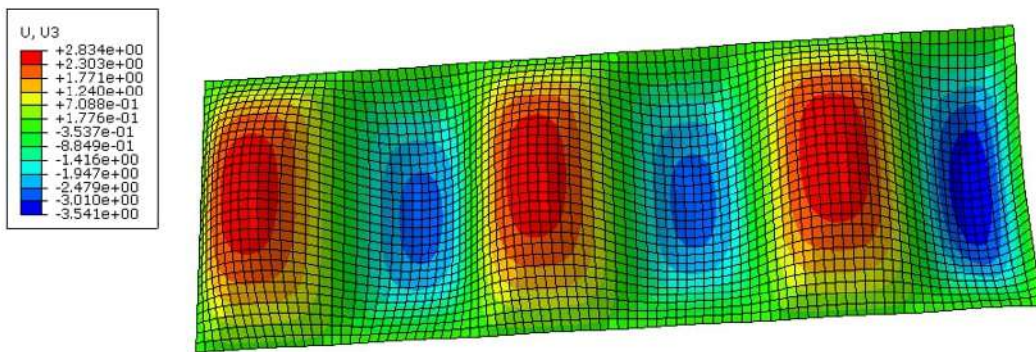


Figure 3.25: First buckling mode of the  $[90/90/90/90]_s$  plate, obtained with **Dynamic, Implicit** analysis

Concluding this analysis, Figure 3.26 portrays the load-displacement curve resulting from the **Dynamic, Implicit** simulation. This graphical representation underscores a discernible change in the curve's slope precisely at the analytically calculated buckling load. This alignment is further corroborated by the outcomes of the linear buckling analysis, denoted by the green dots in Figure 3.26. This observation aligns with the results previously acquired through both analytical calculations and the linear buckling analysis.

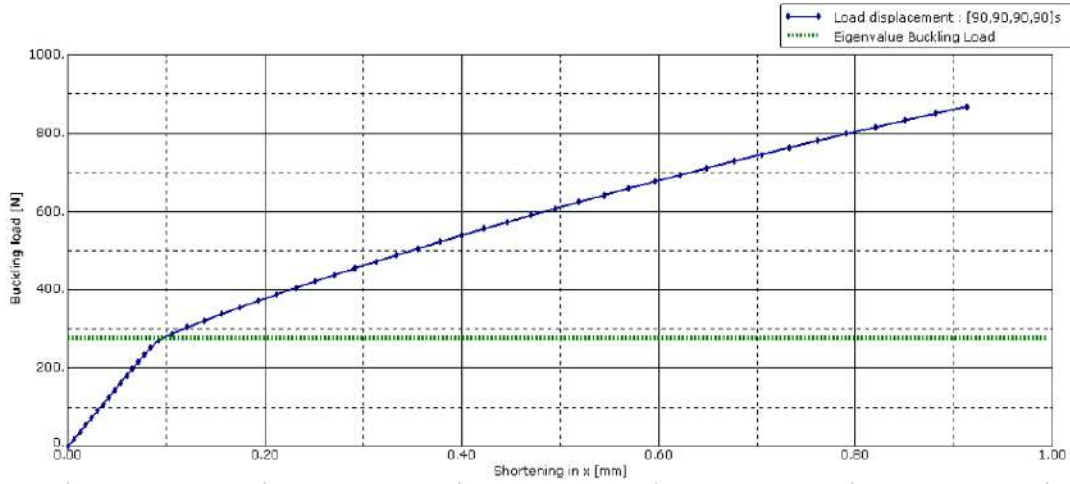


Figure 3.26: Load displacement curve of the  $[90/90/90/90]_s$  plate obtained with **Dynamic, Implicit** analysis

**Third stacking sequence:**  $[0/45/-45/90]_s$

First, the critical buckling load is calculated analytically, with the element of the matrix  $\mathbf{D}$ . As for the previous simulations, the value of  $m$ , equal to 2 for this stacking sequence, was chosen to minimize  $P_{cr,analytic}$ . Equation 3.12 gives:

$$P_{cr,analytical} = 559.04N \quad (3.20)$$

Continuing with the analysis of different stacking sequences, the linear buckling analysis performed with the stacking sequence  $[0/45/-45/90]_s$  yields a first mode characterized by two half waves, as depicted in Figure 3.27. In contrast, the second mode showcases a pattern encompassing three half-waves.

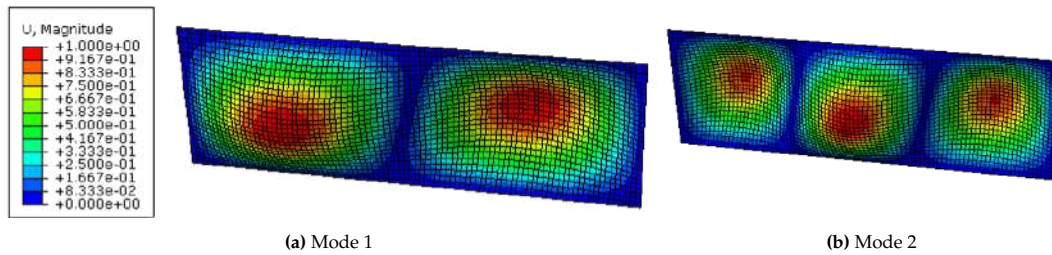


Figure 3.27: First two buckling modes of the  $[0/45/-45/90]_s$  plate, obtained with linear buckling analysis

Furthermore, based on the Eigenvalue obtained from the Abaqus analysis, which represents the critical buckling load per unit length, the critical buckling load obtained numerically is found as follows:

$$P_{cr,numerical} = \bar{N}_{cr,numerical} * b = 1.8921 * 300 = 567.63N \quad (3.21)$$

Therefore, it is possible to derive the difference between numerical and analytical solutions :

$$diff = \frac{|P_{cr,numerical} - P_{cr,analytical}|}{P_{cr,analytical}} = 1.53\% \quad (3.22)$$

While the disparity has somewhat widened in comparison to the first two simulations, it's important to note that this discrepancy remains negligible. This reaffirms the fidelity of the simulations conducted in Abaqus, as well as the accuracy of the analytical value derived. The consistency between these results underscores the reliability of the analysis undertaken.

Moreover, similarly to what has been done previously, a post-buckling analysis is done with a **Dynamic, Implicit** simulation. Figure 3.28 shows the first buckling mode obtained with this simulation. The same number of half-wave and buckling behavior is observed.

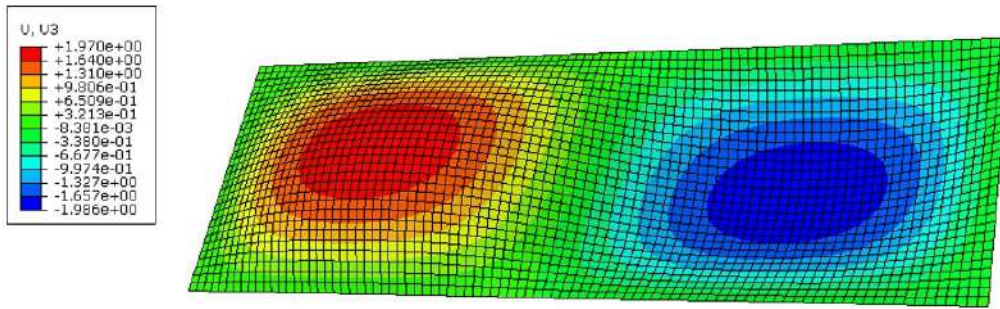


Figure 3.28: First buckling mode of the  $[0/45/-45/90]_s$  plate, obtained with **Dynamic, Implicit** analysis

Finally, Figure 3.29 shows the load-displacement curve. From this graph, a change in the slope of the curve is observed exactly at the buckling load (represented in Figure 3.29 by the green dots) calculated analytically and confirmed by the linear buckling analysis. Again, a reduction of the stiffness is observed beyond the buckling load. This graph confirms the results previously obtained both analytically and with the linear buckling analysis.

Concluding this examination, Figure 3.29 illustrates the load-displacement curve obtained from the **Dynamic, Implicit** simulation corresponding to the stacking sequence  $[0/45/-45/90]_s$ . Within this graph, a discernible shift in the curve's slope is evident precisely at the analytically calculated buckling load, marked by the green dots in Figure 3.29. This graph further reinforces the congruence of results derived through analytical, linear buckling, and dynamic simulations.

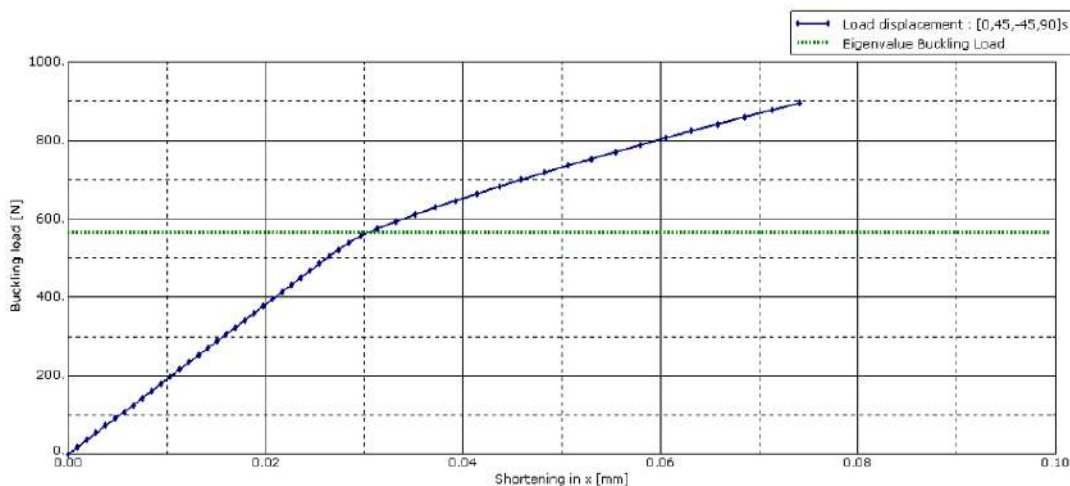


Figure 3.29: Load displacement curve of the  $[0/45/-45/90]_s$  plate obtained with **Dynamic, Implicit** analysis

#### Fourth stacking sequence: $[0/15/30/0]_s$

First, the critical buckling load is calculated analytically, with the element of the matrix  $\mathbf{D}$ . As for the previous simulations, the value of  $m$ , equal to 2 for this stacking sequence, was chosen to minimize  $P_{cr,analytic}$ . Equation 3.12 gives:

$$P_{cr,analytical} = 348.97N \quad (3.23)$$

Continuing the analysis, the linear buckling analysis conducted with the stacking sequence  $[0/15/30/0]_s$  results in a first mode characterized by two half waves, as demonstrated in Figure 3.30. On the other hand, the second mode exhibits a pattern comprising one half-wave.

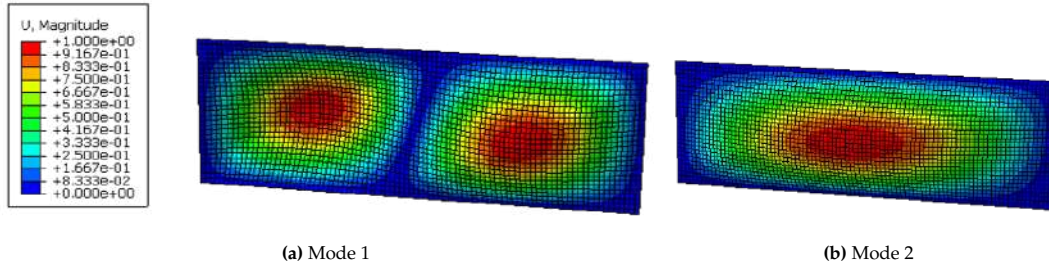


Figure 3.30: First two buckling modes of the  $[0/15/30/0]_s$  plate, obtained with linear buckling analysis

Leveraging the Eigenvalue provided by Abaqus, which corresponds to the critical buckling load per unit length, facilitates the numerical determination of the critical buckling load:

$$P_{cr,numerical} = \bar{N}_{cr,numerical} * b = 1.2317 * 300 = 369.51N \quad (3.24)$$

Therefore, it is possible to derive the difference between numerical and analytical solutions :

$$diff = \frac{|P_{cr,numerical} - P_{cr,analytical}|}{P_{cr,analytical}} = 5.83\% \quad (3.25)$$

While the discrepancy has shown a slight increase compared to the first three simulations, it's important to note that this difference remains within an acceptable range. This alignment reinforces the reliability of the Abaqus simulations and lends credibility to the analytical derivation process.

Moreover, similarly to what has been done previously, a post-buckling analysis is done with a **Dynamic, Implicit** simulation. Figure 3.31 shows the first buckling mode obtained with this simulation. The same number of half-wave and buckling behavior is observed.

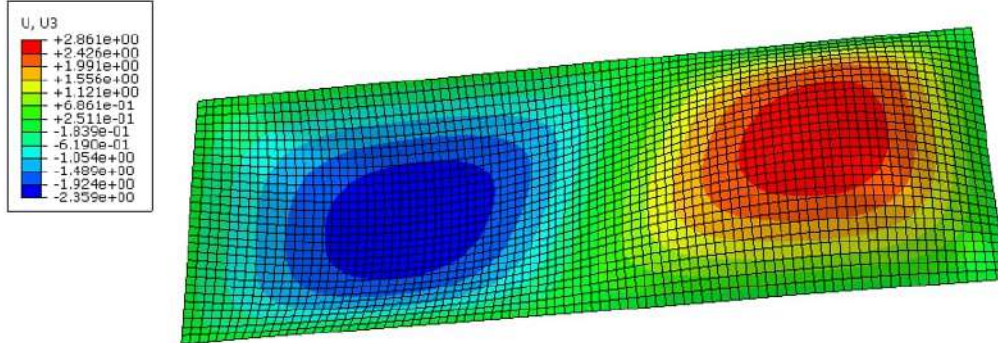


Figure 3.31: First buckling mode of the  $[0/15/30/0]_s$  plate, obtained with **Dynamic, Implicit** analysis

Finally, Figure 3.32 illustrates the load-displacement curve obtained from the **Dynamic, Implicit** simulation corresponding to the stacking sequence  $[0/15/30/0]_s$ . Within this graph, a discernible shift in the curve's slope is evident precisely at the analytically calculated buckling load, marked by the green dots in Figure 3.32. This graph further reinforces the congruence of results derived through analytical, linear buckling, and dynamic simulations.

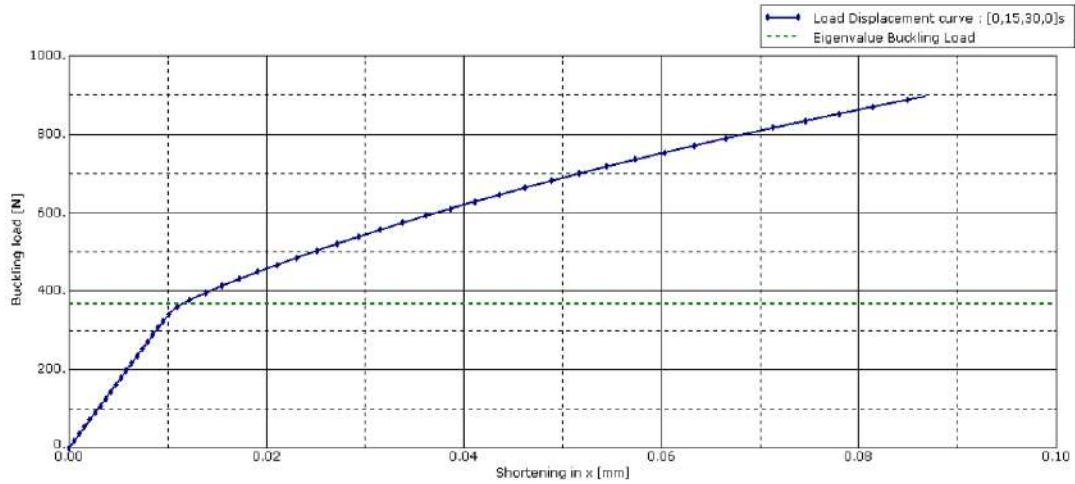


Figure 3.32: Load displacement curve of the  $[0/15/30/0]_s$  plate obtained with **Dynamic, Implicit** analysis

To provide a comprehensive overview, Table 3.12 encapsulates the outcomes acquired through the analysis of the composite laminate for the four distinct stacking sequences.

Composite Layup	$P_{cr,analytical}$ [N]	$P_{cr,numerical}$ [N]	$diff$ [%]	$m_{hw}$ [-]
$[0/0/0/0]_s$	314.31	314.64	0.105	2
$[90/90/90/90]_s$	277.69	278.06	0.14	6
$[0/45/-45/90]_s$	559.04	567.63	1.53	2
$[0/15/30/0]_s$	348.97	369.51	5.83	2

Table 3.12: Summary of the composite plate linear buckling analysis

### 3.4. Buckling of the stiffened panel

Having examined multiple plates with varying stacking sequences for both composite laminates and an aluminum alloy, the focus now shifts to modeling a stiffened panel. It's important to note that this panel mirrors the one embedded within the subsequent optimization model. To comprehensively analyze its behavior, a two-step approach is adopted: a linear buckling analysis followed by a post-buckling analysis utilizing the **Dynamic, Implicit** simulation procedure.

#### 3.4.1. Model description

As earlier elucidated, the work of Bisagni et al. [1] encompassed a comprehensive comparison of various simulations involving a wing component. This structure integrates two distinct test panels, located at the upper and lower sections of the overall structure. Specifically, these test panels consist of a composite panel coupled with five aluminum alloy T-shape stiffeners. Each constituent of the stiffened panel is depicted in Figure 3.33. This schematic illustration provides a clear representation of the individual components comprising the stiffened panel.

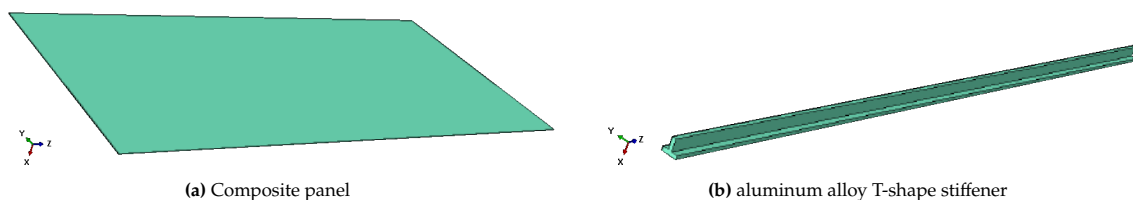


Figure 3.33: Components of the test panel

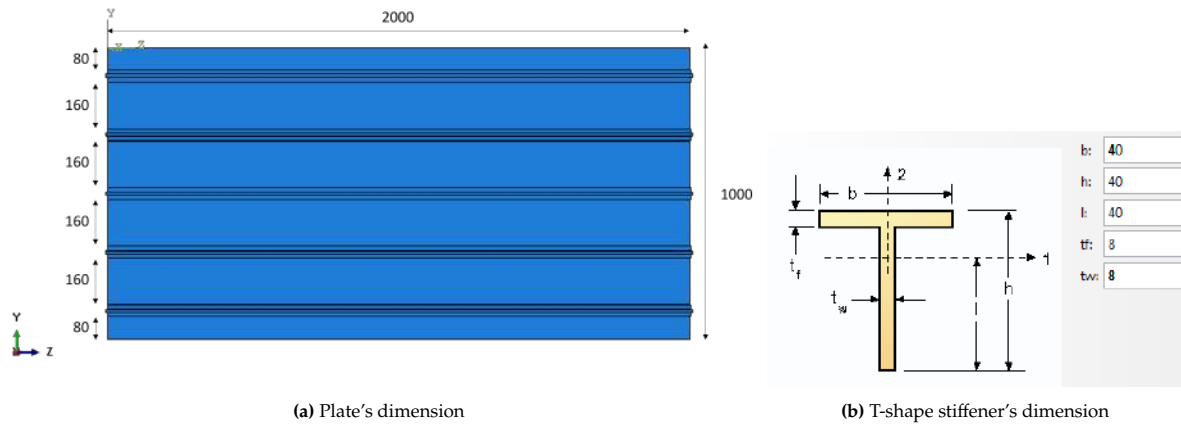
The material properties for both the composite and the aluminum alloy were previously detailed in

Table 3.3 and Table 3.2, respectively. In line with this, Table 3.13 presents a comprehensive breakdown of the various components within the test panel, along with their corresponding material compositions.

Designation	Quantity	Material
Panel	1	18 plies of USN150B: [45/0/45/0/90/0/45/0/45] <sub>s</sub>
Stiffeners	5	Al 6063AT6

**Table 3.13:** Test Panel components and their materials

The five T-shaped stiffeners are arranged in a uniform pattern across the composite plate. As depicted in Figure 3.34b, each T-shaped stiffener measures 40 mm in height and 40 mm in width. These stiffeners span the entire length of the plate, which is 2000 mm, as illustrated in Figure 3.34a. The composite plate itself comprises 18 plies of USN150B, each with a thickness of 0.194 mm, as outlined in Table 3.3. Consequently, the total thickness of the composite plate amounts to 3.492 mm. The width of the composite plate is 1000 mm. To achieve equidistant spacing between the stiffeners, the center points of the stiffeners are aligned at intervals of 100, 300, 500, 700, and 900 mm from the left edge of the plate, respectively. These spacings are designed to ensure the uniform distribution of the stiffeners, as shown in Figure 3.34a.



**Figure 3.34:** Dimensions of the components (all values are in mm)

The distances mentioned along the left side of the plate pertain to the distances between the edges of the panel and the edges of the T-shaped stiffeners, or between two adjacent edges of the stiffeners. The following derivation is only intended to verify that, with this configuration of stiffeners, the panel width is equal to 1000 mm.

$$W_{panel} = 2 * d_{P \rightarrow T} + 4 * d_{T \rightarrow T} + 5 * W_{T-shapestiffeners} = 2 * 80 + 4 * 160 + 5 * 40 = 1000mm \quad (3.26)$$

Where  $W_{panel}$  is the width of the panel,  $d_{P \rightarrow T}$  is the distance between the edge of the panel and the edge of the stiffener, equals to 80mm here,  $d_{T \rightarrow T}$  is the distance between the edge of one stiffener to the edge of another stiffener, equals to 160mm here and  $W_{T-shapestiffeners}$  is the width of one stiffener. With this configuration, the center of the stiffeners is positioned at 100, 300, 500, 700, and 900 mm width respectively.

When skin-stiffener separation is not considered, using tie constraints to attach the stiffeners to the composite panel is a common approach in finite element analysis to simulate the connection between two surfaces. Five tie constraints are used, each located at the intersection of the stiffeners and the composite panel, to ensure that these surfaces behave similarly in all degrees of freedom. Tie constraints are used to model perfect bonding or connection between two surfaces, effectively ensuring that they move together as if they are a single entity. They allow for the transfer of forces and displacements between the surfaces while maintaining their kinematic compatibility. Figure 3.35 shows the locations



of these tie constraints on the stiffened panel, visually indicating how the stiffeners are attached to the composite panel using these constraints.

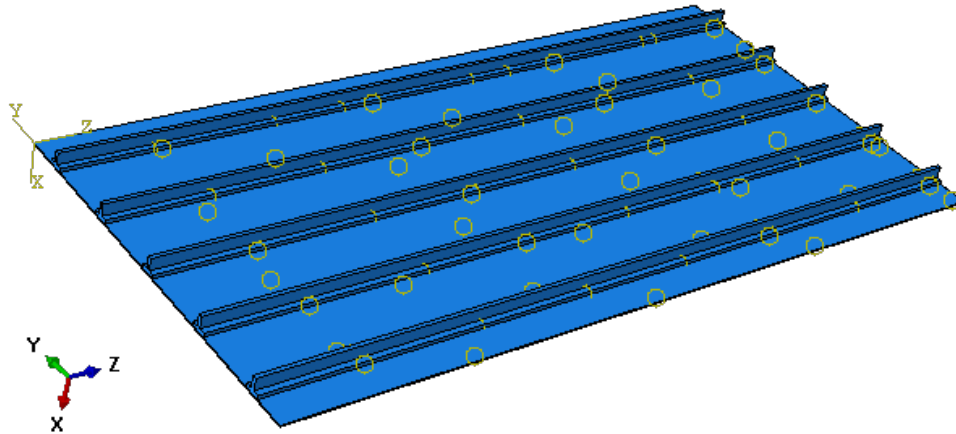


Figure 3.35: Tie constraints between the 5 stiffeners and the top surface of the composite plate

Regarding the meshing strategy for each component, the composite panel is represented using continuum shell elements (SC8R), with each element having a size of 25mm. As a result, a total of 3200 elements (40x80) are required to model the composite panel. On the other hand, the stiffeners are simulated using solid elements (C3D8R). Each solid element takes the form of a cuboid with a 5mm square base and a length of 20mm. Consequently, there are 28 elements per 20mm length (as indicated in Figure 3.36b), leading to a total of 1400 elements per stiffener. Overall, the entire model comprises approximately 10,000 elements (specifically, 3200 for the panel and 5x1400 for the stiffeners, totaling 10200 elements). This configuration strikes a balance between computational efficiency and result accuracy, allowing for reasonable computational times and precise simulation outcomes.

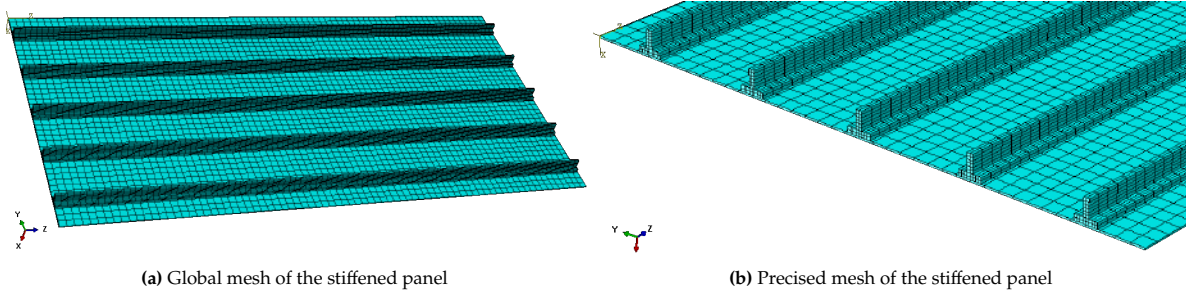


Figure 3.36: Mesh of the stiffened panel

### 3.4.2. Linear Buckling

Now that the model is described, it is possible to run linear buckling analysis, similarly to what has been done previously with the plate geometry in section 3.3.

Indeed, the chosen boundary conditions for the stiffened panel remain consistent with the previously used configuration: simply a supported plate with an uni-axial load. As depicted in Table 3.14, the stiffened panel is situated within the (y,z) plane, with its out-of-plane direction corresponding to the x-axis.

Location	Boundary conditions
Edge $z = 0$	$U_z = 0 ; U_x = 0$
Edge $z = a$	$U_x = 0$
Edges $y = 0$ and $y = b$	$U_x = 0$
Origin $(x,y) = (0,0)$	$U_y = 0$

**Table 3.14:** Boundary conditions of the stiffened panel

In Abaqus, utilizing a **Buckle** step initiates an eigenvalue analysis that enables you to specify the desired number of buckling modes (associated with eigenvalues) for the simulation.

Various approaches are available for modeling the linear buckling of a stiffened panel. Both displacement-driven and load-driven simulations are viable options. In the displacement-driven approach, a displacement boundary condition is imposed on the "loaded" edge, resulting in a linear increase in displacement over the simulation duration. This leads to eigenvalues that can be used to determine the buckling displacement, as demonstrated in Figure 3.37a.

On the contrary, the load-driven approach, similar to the method employed in section 3.3, involves applying an axial load to the "loaded" edge. Consequently, the eigenvalues from the simulation correspond to the critical buckling loads, as illustrated in Figure 3.37b.

Both displacement-driven and load-driven simulations provide insights into either the buckling displacement or the buckling load. Regardless of the chosen method, it's crucial to apply the prescribed displacement or load conditions to all nodes along both the panel and the stiffeners. This ensures a comprehensive simulation that accurately captures the complex behavior of the entire stiffened panel structure.

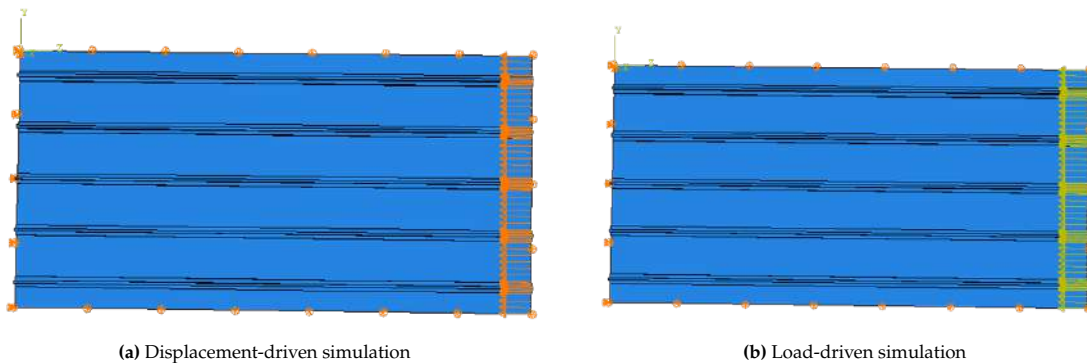


**Figure 3.37:** Displacement and Load driven simulation: apply on each node

Furthermore, considering the scenario depicted in Figure 3.37, the displacement or load is individually applied to all the nodes along the relevant boundary. However, an alternative technique involves connecting all these nodes from the boundary to a single node, termed the "reference node." This approach simplifies the simulation by necessitating the application of displacement or load solely to the reference node, as the constraint enforces corresponding behavior in all the constrained nodes. As illustrated in Figure 3.38, this method used a central node situated on the right edge of the stiffened panel, which constrains all the nodes along that edge.

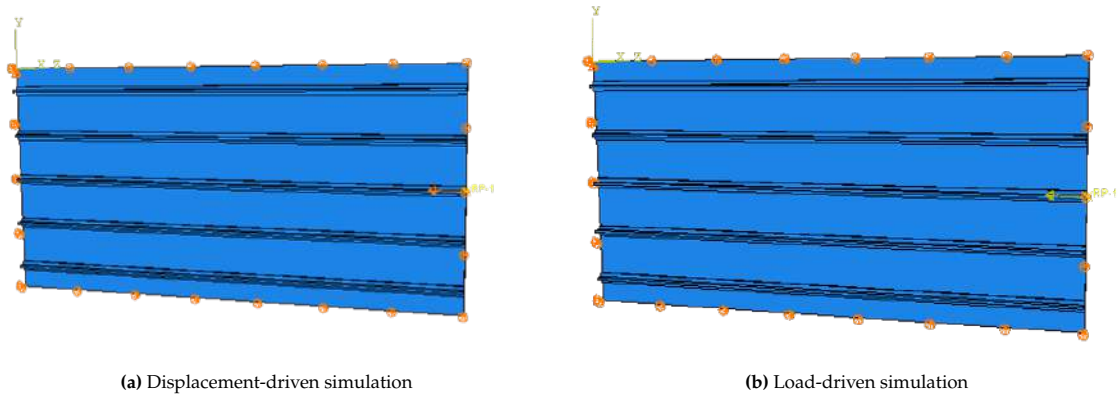


**Figure 3.38:** Displacement and Load driven simulation: apply only on the reference node

Abaqus provides two distinct types of constraints to establish connections between a reference node and other nodes. The reference node, often referred to as the "master" node, can be linked with other nodes, termed "slave" nodes, using either a tie constraint or a coupling constraint. The tie constraint, demonstrated in Figure 3.39a, ensures that all nodes move in the same manner as the reference node. The coupling constraint, as illustrated in Figure 3.39b, follows a similar process. In this approach, a "master" node is coupled with its corresponding "slave" nodes. This coupling can be specified for a specific number of degrees of freedom, which may involve a single direction or all six degrees of freedom for the node. In our particular scenario, the reference node has been coupled with all other nodes along the edge, encompassing all six degrees of freedom, thus enabling their coordinated behavior.

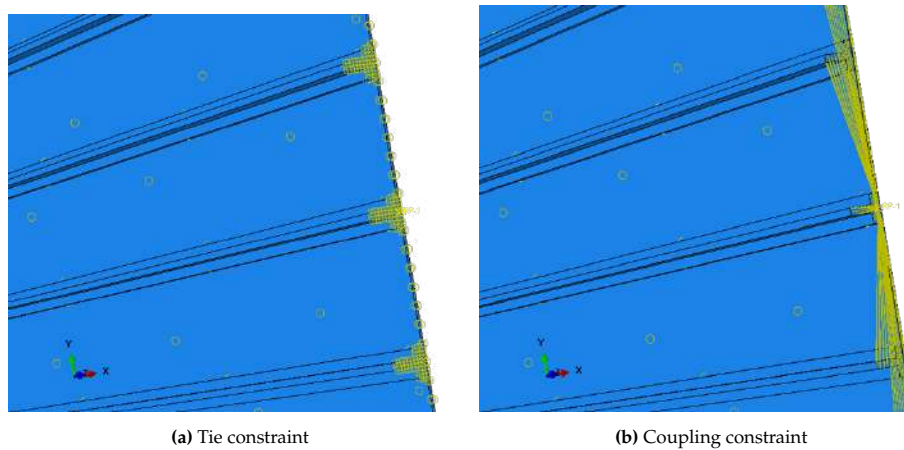


**Figure 3.39:** Constraints available between the reference node and all the other nodes of the edge.

The preceding description encompasses a total of six distinct simulations:

- simulation 1: Displacement-driven simulation applies on all the nodes.
- simulation 2: Load-driven simulation applies on all the nodes.
- simulation 3: Displacement-driven simulation applies only on the reference point, with tie constraint.
- simulation 4: Load-driven simulation applies only on the reference point, with tie constraint.
- simulation 5: Displacement-driven simulation applies only on the reference point, with coupling constraint.
- simulation 6: Load-driven simulation applies only on the reference point, with coupling constraint.

The displacement-driven simulations facilitate the determination of the buckling displacement, whereas the load-driven simulations enable the identification of the buckling load. Nevertheless, all six of these simulations provide insight into the buckling mode of the stiffened panel. As depicted in

Figure 3.40, the first buckling mode of the panel corresponds to a global buckling of the plate. All six simulations yield the same first buckling mode, thus, only one plot is presented here to avoid repetition.

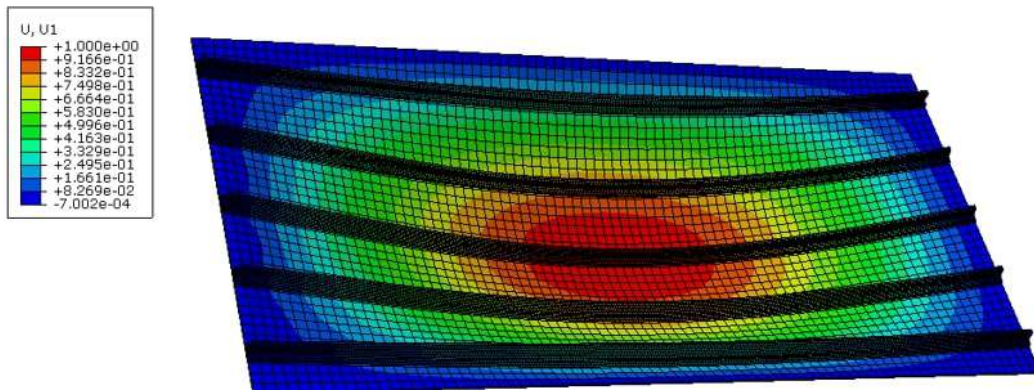


Figure 3.40: First Buckling mode obtained with the 6 different simulations.

The results obtained with these 6 simulations are summarized in Table 3.15 hereafter:

Test case	Buckling displacement [mm]	Buckling load [kN]
Load directly applied on the nodes	0.92 (sim 1)	176 (sim 2)
Reference point : Tie constraint	0.96 (sim 3)	186 (sim 4)
Reference point : coupling constraint	1.06 (sim 5)	203 (sim 6)

Table 3.15: Summary of linear buckling analysis of the stiffened panel

Some differences are observed in the results based on the test case. This is not expected since the different simulations should give similar results as it is expected that they are giving equivalent boundary conditions.

### 3.4.3. Post-buckling analysis with Dynamic, Implicit simulation

Following a similar approach to that used for the aluminum plate, a post-buckling analysis can be conducted using Abaqus' **Dynamic, Implicit** simulation, based on the results of the linear buckling analysis. Once again, the first buckling mode obtained from the linear analysis is introduced as an imperfection in the **Dynamic, Implicit** simulation. This simulation also exhibits the same buckling mode 1, which corresponds to a global buckling of the stiffened panel. The load-displacement curve for this simulation can also be plotted. As shown in Figure 3.41, the curve displays a smoother reduction in stiffness compared to the previous post-buckling analysis.

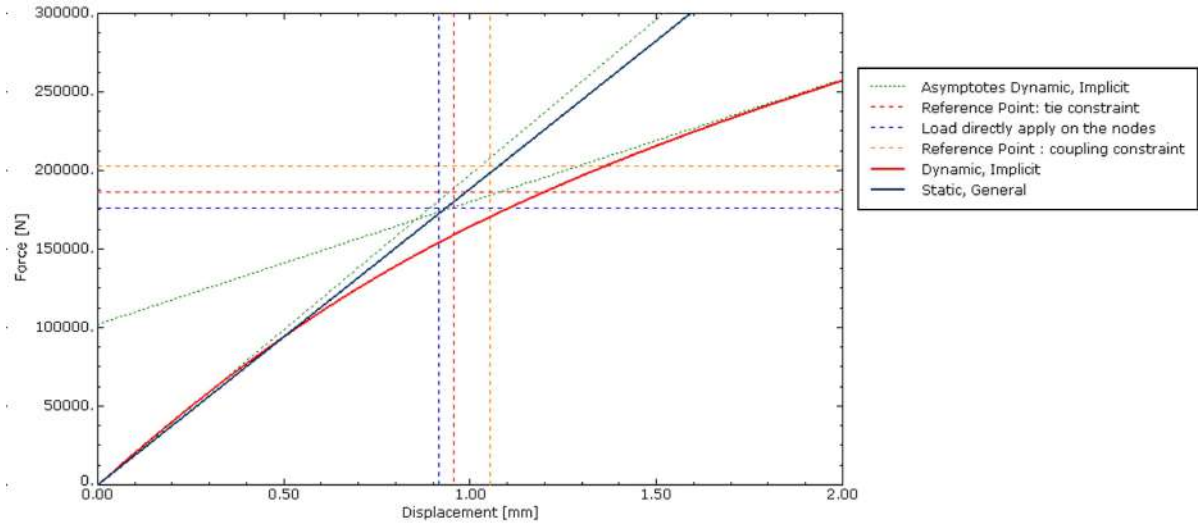


Figure 3.41: Comparison of the buckling behavior of the stiffened panels using various methods.

To determine the buckling load and buckling displacement of the **Dynamic, Implicit** analysis, the asymptotes of the curve are identified. The intersection point of these asymptotes is considered as the buckling load and buckling displacement of the stiffened panel. Regarding the reduction in stiffness, the slope of the load-displacement curve undergoes a decrease from 200 kN/mm to 77.50 kN/mm, indicating a reduction of 61%.

Moreover, the load-displacement curve shown in Figure 3.41 includes the results obtained from a **Static, General** analysis. This type of analysis assumes a linear behavior of the structure under the same loading conditions and boundary constraints (uni-axial compression and simply supported plate). It is evident that while there are slight differences in the results obtained from the four methods, all of them closely adhere to the linear behavior predicted by the **Static, General** analysis. Indeed, the intersection between the buckling displacement and the buckling load of the 3 test cases described in Table 3.15 is located in the linear curve obtained with the **Static, General** analysis.

The values obtained through the **Dynamic, Implicit** method have also been included in the previous table. Additionally, the differences *diff* between each method and the **Dynamic, Implicit** approach have been computed and tabulated.

Test case	Buckling displacement [mm]	<i>diff</i> [%]	Buckling load [kN]	<i>diff</i> [%]
<b>Dynamic, Implicit</b> (obtained with the asymptotes)	0.86	X	168	X
Load directly applied on the nodes	0.92	6.9	176	4.8
Reference point : Tie constraint	0.96	11.6	186	10.7
Reference point : coupling constraint	1.06	23.2	203	20.8

Table 3.16: Summary of the buckling analysis of the stiffened panel

# 4

## Optimization Strategy

This chapter serves to introduce and elucidate the optimization problem concerning the representative wing component. Initially, the structure that requires optimization is outlined. Following that, the problem's formulation is meticulously undertaken. Particular emphasis is placed on a specific cut-out configuration that is explored during the optimization process. Ultimately, a comprehensive overview of the strategy employed to tackle the optimization challenge is provided.

### 4.1. Problem statement

#### 4.1.1. Presentation of the structure

The representative wing component to be optimized, as depicted in Figure 4.1, comprises two test panels, three rib panels, ten panel stiffeners (five for each), fifteen rib stiffeners (five for each), twenty-four panel-to-rib joints, and twelve panel-to-rib half joints. While the test panels are constructed using composite materials, the remaining components are made of aluminum alloys. The aluminum stiffeners are fixed to the composite panels using a two-component epoxy adhesive known as 420 Araldite A/B. Additionally, all the parts are interconnected through bolts that traverse attachment plates.

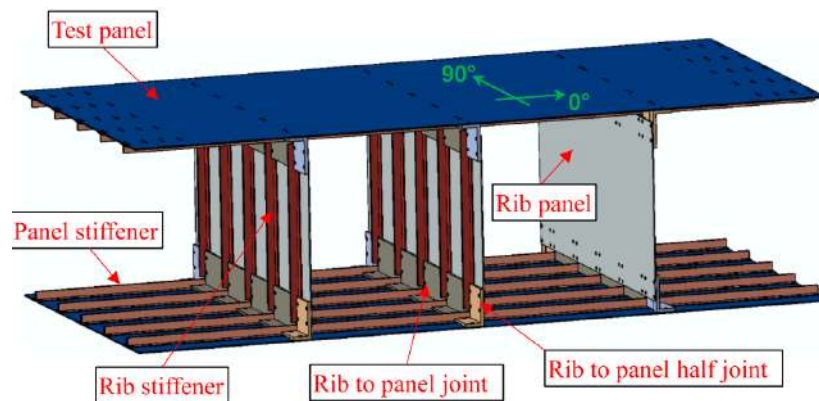


Figure 4.1: Representative wing component. Adapted from Bisagni et al. [1]

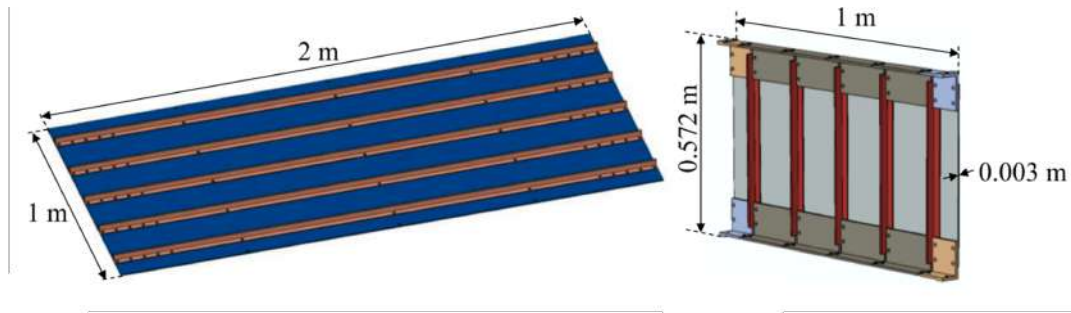


Figure 4.2: Dimensions of the main part of the wing components (Test panel right and rib panel left). Adapted from Bisagni et al. [1]

Designation	Quantity	Material
Panel	2	18 plies of USN150B: [-45/0/45/0/90/0/-45/0/45] <sub>s</sub>
Panel stiffener (T-shape stiffener)	10	Al 6063AT6
Rib panel	3	Al 6082AT6
Rib stiffener (T-shape stiffener)	15	Al 6063AT6
Rib to panel joint	24	Al 6082AT6
Rib to panel half joint	12	Al 6082AT6

Table 4.1: Wing components and their materials

The material properties of the aluminum alloy Al 6063AT6 (as provided in Table 3.2) and the composite material USN150B (as presented in Table 3.3) have been previously outlined. These materials were extensively investigated in chapter 3. On the contrary, the properties of Aluminum 6082AT6 have not yet been introduced or examined. However, the material properties for Aluminum 6082AT6, detailed in Table 4.2, are notably similar to those of Aluminum 6063AT6, except a higher yield strength ( $\sigma_y$ ) in the case of Aluminum 6082AT6.

Material	E [MPa]	$\sigma_y$ [MPa]	$\nu$	$\rho$ [g/cm <sup>3</sup> ]
Al 6082AT6	70,000	260	0.33	2.7

Table 4.2: Aluminum 6082AT6 properties

The optimization variables, which may encompass various types as elaborated in subsection 2.2.1, have been predefined in our context. These variables can be succinctly summarized through the following table:

Designation	Quantity	Optimization variables
Test panel	2	Ply number of the skin panel: between 12 and 18 Ply orientation: [0, 30, 45, 60, 90].
Rib panel	3	Thickness: 1.5, 2, 3 and 4mm. Possibility of cut-out in the three vertical ribs.
T-stiffeners	10 (panel) 15 (rib)	Thickness: 1.59, 3 and 3.18 mm

Table 4.3: Optimization variables of the wing component

The variables detailed in Table 4.3 correspond to changes in the structural design. Nonetheless, these changes have to take into account that the panel skin layup should be kept symmetric, as well

as the overall structure in general. For instance, if the left rib is assigned a certain thickness, the right rib should be assigned an identical thickness. Likewise, any cut-outs within the rib should exhibit uniformity in symmetric ribs. Equally, the number of plies and their orientations must mirror each other for both the top and bottom panels.

#### 4.1.2. Optimization Formulation

This section is intricately tied to section 2.2. Here, a problem formulation is undertaken, drawing inspiration from the formulation approaches commonly found in existing literature as elucidated in section 2.2.

The foremost goal of the optimization is to attain the most lightweight structure feasible while accounting for the stiffness and buckling characteristics of the structure. In light of the information in Table 4.3, the optimization formulation can be succinctly summarized as follows:

$$\begin{aligned}
 &\text{find } N_{ply,i} = \{12, 14, 16, 18\}, \quad i = 1, 2 \\
 &\quad \theta_{ply,i,j} = \{0, 30, 45, 60, 90\}, \quad j = 1, 2, \dots, N_{ply,i} \\
 &\quad t_{rib,k} = \{1.5, 2, 3, 4\}, [mm] \quad k = 1, 2, 3 \\
 &\quad X_{cut-out} = \{0, 1\} \\
 &\quad t_{stiff,rib,l} = \{1.59, 3, 3.18\}, [mm] \quad l = 1, 2, \dots, 15 \\
 &\quad t_{stiff,panel,m} = \{1.59, 3, 3.18\}, \quad m = 1, 2, \dots, 10 \\
 &\text{max } f(N_{ply,i}, \theta_{ply,i,j}, t_{rib,k}, X_{cut-out}, t_{stiff,rib,l}, t_{stiff,panel,m}) = \alpha W + \beta E + \gamma P_{cr} \\
 &\text{Constraints : } \text{No failure (Using Hashin's criteria } < 1) \\
 &\quad \text{Symmetry of the structure}
 \end{aligned} \tag{4.1}$$

where  $N_{ply,i}$  is the number of plies in the top and bottom test panels where  $i$  differentiates these panels, 1 being the top panel and 2 being the bottom panel,  $\theta_{ply,i,j}$  is the ply orientation of the  $j$ -th ply in the  $i$ -th panel, where  $j$  is the ply number, which is between 1 and the number of plies  $N_{ply,i}$ ,  $t_{rib,k}$  is the thickness of the rib panel where  $k$  differentiates these panels, 1 being the left panel, 2 being the middle panel and 3 being the right panel,  $X_{cut-out}$  describes the different types of cut-out configurations: 0 means that no cut-out is present in the structure, 1 stand for one specific cut-out configuration explains in subsection 4.1.4,  $t_{stiff,rib,l}$  is the thickness of the  $l$ -th T-stiffeners presents on the three ribs (5 stiffeners per rib), and  $t_{stiff,panel,m}$  is the thickness of the  $m$ -th T-stiffeners presents on the two panels (5 stiffeners per panel).

Concerning the fitness function to be minimized in this optimization problem,  $W$  represents the total weight of the structure,  $E$  is the equivalent stiffness of the structure,  $P_{cr}$  is the critical buckling load of the structure, and  $\alpha$ ,  $\beta$  and  $\gamma$  are weighting coefficients. More details on this function will be given in section 4.2.

Regarding the constraints, no failures, determined by the Hashin criteria for ply failure, are permissible. The structural symmetry must be upheld as well. As previously elaborated, the structural symmetry imposes certain equalities, such as  $t_{rib,1} = t_{rib,3}$ , for instance. Correspondingly, the number of plies and their orientations must match between both panels, necessitating  $N_{ply,1} = N_{ply,2}$  and  $\theta_{ply,1,j} = \theta_{ply,2,j}$ . Symmetry extends to the stacking sequence as well. In a similar vein, the stiffeners across all three ribs should possess the same thickness. Similarly, the thickness of the stiffeners in the two panels should be uniform, though  $t_{stiff,rib,l}$  and  $t_{stiff,panel,m}$  may differ.

Our optimization formulation is characterized as a multi-objective problem, as delineated in subsection 2.3.1. The primary objective centers on minimizing weight, while the secondary objectives encompass enhancing stiffness and fortifying buckling performance. As shown in subsection 2.2.2, Weight and Buckling frequently constitute the core objectives in optimizing structures of this nature. Stiffness is commonly treated as a constraint in these types of optimizations, as elucidated in subsection 2.2.3.



### 4.1.3. Baseline configuration

The baseline configuration corresponds to the design tested with a 4-point bending test as explained in section 1.2. This particular design has the following values of the variables presented in Equation 4.1:

$N_{ply,i}$	$\theta_{ply,i,j}$	$t_{rib,k}$	$X_{cut-out}$	$t_{stiff,rib,l}$	$t_{stiff,panel,m}$
18	[45/0/45/0/90/0/45/0/45] <sub>s</sub>	3	0	3	3

Table 4.4: Baseline design studied by Bisagni et al. [1]

This baseline design is the one that has to be optimized in the span of this work. But first, it is possible to recreate the simulation done by Bisagni et al. in [1]. Figure 4.3 shows the results obtained by Bisagni et al. in [1] as well as the results obtained this year with my simulation.

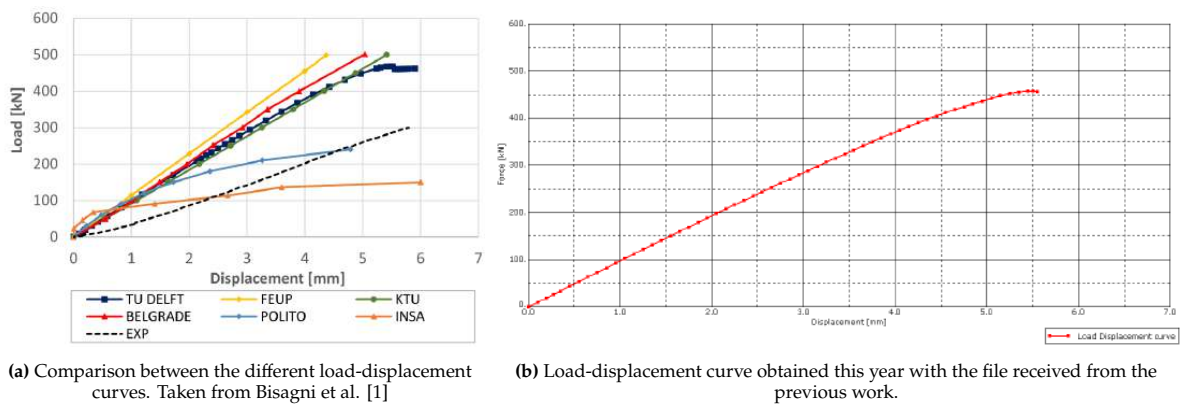


Figure 4.3: Previous results obtained by Bisagni et al. in [1] and result obtained this year.

Superimposed the two previous graphs has been done in Figure 4.4 to show that the results obtained for this master thesis completely match the one obtained last year by TU Delft.

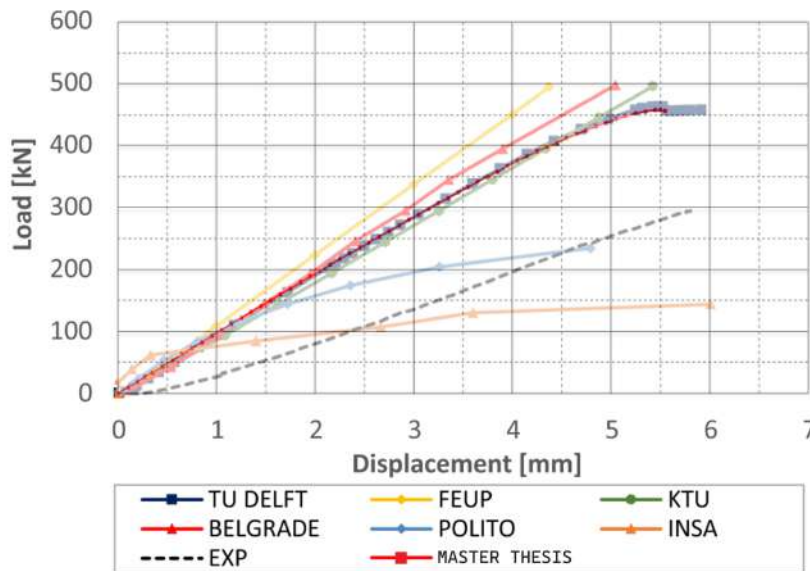


Figure 4.4: Comparison between the different load-displacement curves presented in Figure 4.3

### 4.1.4. Cut-out configuration

Most of the variables outlined in Table 4.3 are self-explanatory: they involve the number of plies and their orientations for the composite panels, the thickness of the aluminum ribs, and the thickness of the

stiffeners for both the panels and ribs. However, the configuration involving the cut-out requires a more in-depth explanation, and this is the focus of the upcoming section.

Cut-outs can be incorporated exclusively into the three aluminum ribs. Aluminum alloy ribs are often designed with cut-outs in wing structures due to their great capacity to endure such modifications [96]. The cut-outs in the ribs are strategically positioned between the stiffeners, denoted as the blue sections in Figure 4.5.

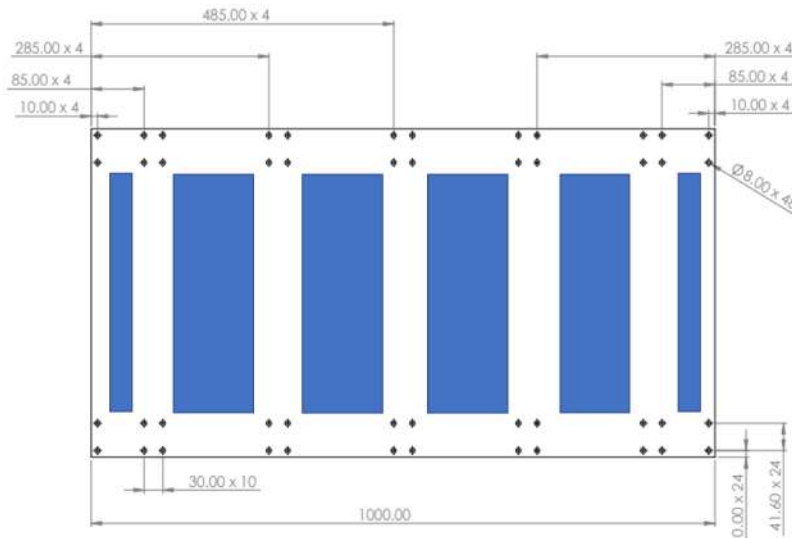


Figure 4.5: Rib dimensions

Furthermore, as demonstrated by Dharmendra et al. in [96], circular holes integrated into wing ribs can potentially enhance the strength of the wing rib when designed with specific configurations, in addition to the reduction of weight. In contrast, Dharmendra et al. [96] found that other cut-out shapes, such as elliptical, rectangular, or triangular, result in inferior structural performance compared to the circular design. This discrepancy is primarily attributed to stress concentrations that arise around corners, a phenomenon prevalent in rectangular or triangular cut-out shapes. As a result, to prevent unnecessary expansion of the design space, the optimization will exclusively explore circular cut-outs, as depicted in Figure 4.6b.

The four larger sections located at the center of the structure, as illustrated in Figure 4.5, are the designated areas for exploring cut-out configurations. These sections possess dimensions of 360mm in height and 150mm in width. Consequently, the following cut-out configuration can be examined (refer to Figure 4.6):

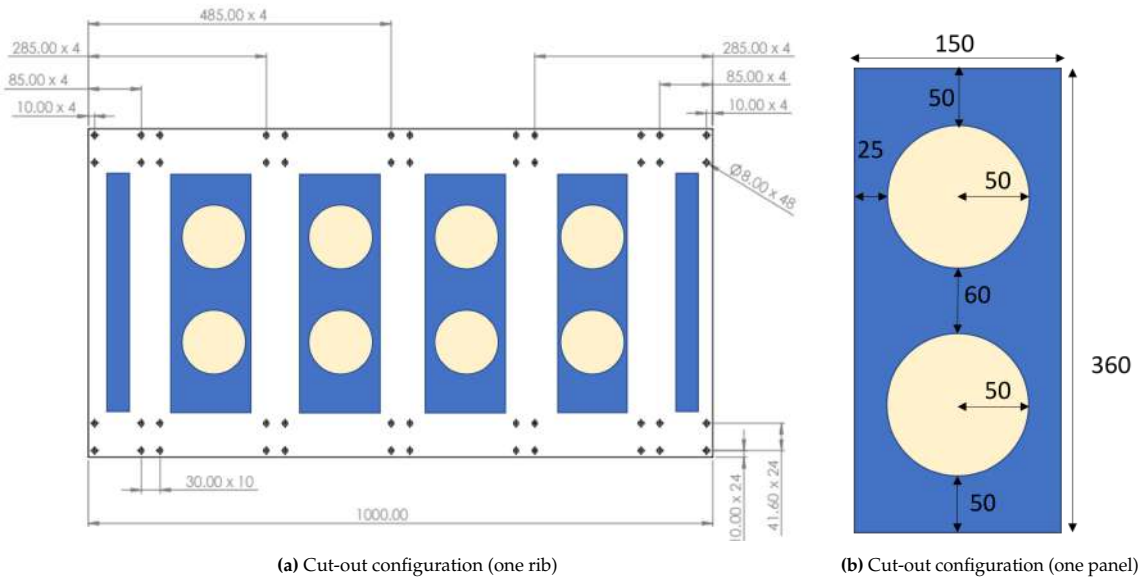


Figure 4.6: Cut-out configuration

In conclusion, the variable associated with the cut-out feature will entail two potential options: either no cut-out across the entire structure or the specific cut-out configuration depicted in Figure 4.6a. It is noteworthy that this chosen cut-out arrangement (illustrated in the complete wing component by Figure 4.7) adheres to the structural symmetry, a crucial requirement within the context of the optimization problem.

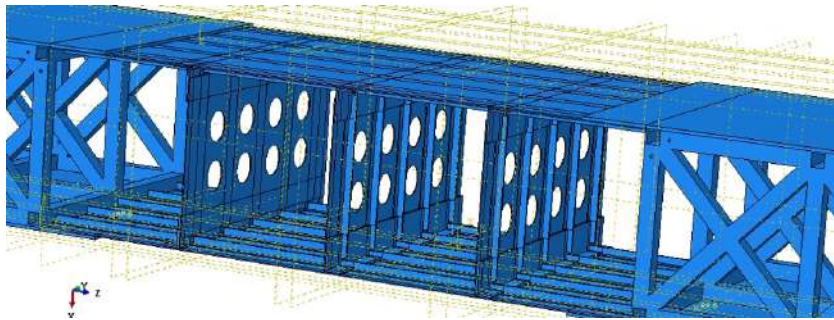


Figure 4.7: Cut-out configuration in the wing component

Examining the stress values within the rib panel featuring the cut-out yields intriguing insights. As illustrated in Figure 4.8, there is a stress concentration around the holes, aligning with expectations. This observation serves as confirmation that a design incorporating cut-outs has the potential to accelerate structural failure or reduce the equivalent stiffness of the structure, among other possible implications.

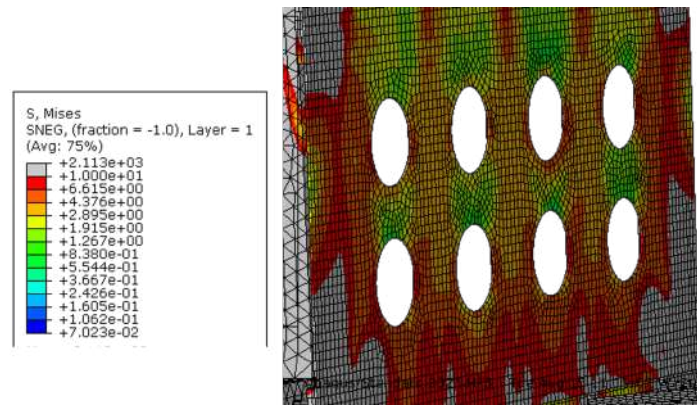


Figure 4.8: Stress concentration around the holes

Additionally, it is possible to plot the stress variation in the rib panel around the hole throughout the simulation. As illustrated in Figure 4.9, it becomes evident that the existence of the holes indeed amplifies the stress levels in comparison to the design without cut-outs, which aligns with the expected behavior.

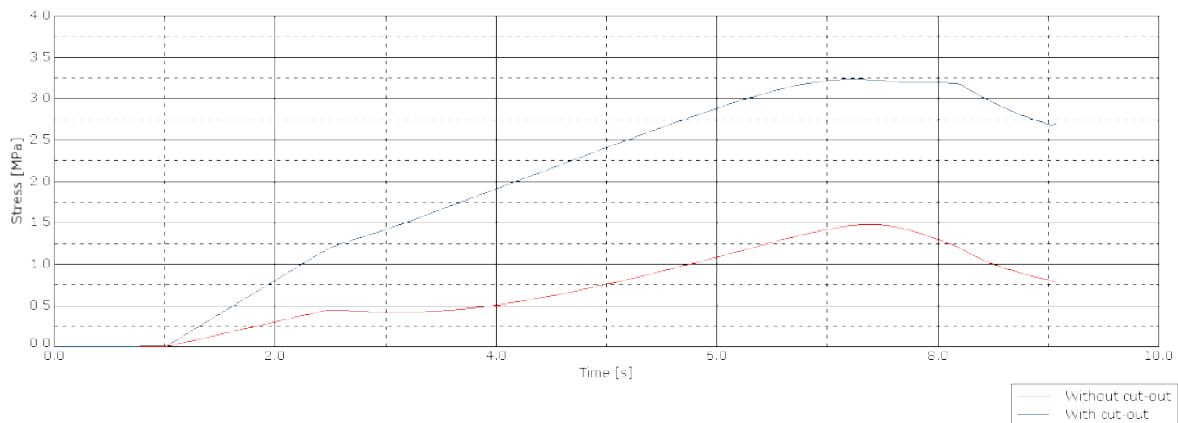


Figure 4.9: Comparison of the stress between one design with cut-out and another without cut-out.

## 4.2. Optimization process using a Genetic Algorithm

Having established the problem by introducing the structure and formulating the optimization objectives, the subsequent step involves devising a solution to address the optimization problem delineated in subsection 4.1.2. The approach described below draws significant inspiration from the methodologies detailed in section 2.4 to identify the optimal and suitable solution for our specific optimization scenario.

Similarly to Morse et al. [97], our optimization task concerns the optimization of a structure composed of three distinct components: the test panels, rib panels, and T-stiffeners. It is important to note that changes in one of the variables can profoundly affect the other variables. Consequently, the optimal values for variables across all three components must be determined concurrently. As illustrated in section 2.4, the prevailing and most effective strategy to tackle such a complex optimization problem (outlined in section 4.1) is through the utilization of a Genetic Algorithm.

As elucidated in subsection 2.4.1, the Genetic Algorithm (called GA hereafter) draws inspiration from natural selection and evolutionary processes. In the context of our optimization challenge, an initial population of potential solutions is generated randomly. Over successive generations, this population evolves and refines to yield improved solutions. The standard GA optimization procedure, as outlined in subsection 2.4.1, has been tailored to our specific case and is succinctly depicted in the flowchart presented in Figure 4.10:

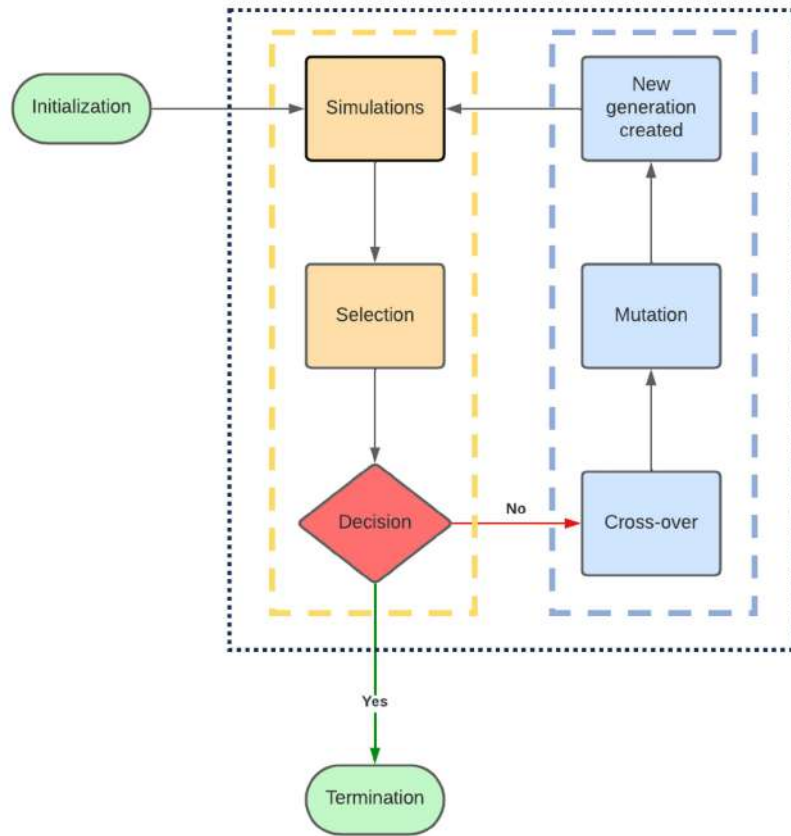


Figure 4.10: Flow chart of the Genetic Algorithm developed.

The process starts with the initialization stage, wherein a population is generated. In a GA, a population comprises a collection of potential optimization solutions. Each potential optimization solution, called individual, possesses a distinct combination of variables within the design space (as detailed in Table 4.3). Consequently, the population of a single generation could be depicted as follows:

$$Population = \begin{pmatrix} N_{ply,i} & \theta_{ply,i,j} & t_{rib,k} & X_{cut-out} & t_{stiff,rib,l} & t_{stiff,panel,m} \\ N_{ply,i} & \theta_{ply,i,j} & t_{rib,k} & X_{cut-out} & t_{stiff,rib,l} & t_{stiff,panel,m} \\ \vdots & \vdots & \vdots & \vdots & \vdots & \vdots \\ N_{ply,i} & \theta_{ply,i,j} & t_{rib,k} & X_{cut-out} & t_{stiff,rib,l} & t_{stiff,panel,m} \end{pmatrix} \quad (4.2)$$

Each row in the matrix represents a candidate design for the structure and corresponds to an individual within the population. The number of columns corresponds to the number of individuals present in the population. This matrix configuration enables the representation of the entire population of a single generation within a single matrix.

With the initialization of the first generation completed, the Genetic Algorithm loop can start. This loop, indicated by the black dotted lines in Figure 4.10, is divided into two distinct parts: the yellow dotted line depicts the evaluation of a generation, while the blue dotted line represents the creation of the next generation. The conclusion of the initial part corresponds to the decision point: if the termination criteria are met, the loop can be exited; otherwise, a new generation is generated through the actions indicated by the blue dotted line.

More precisely, the evaluation of the individuals within a generation starts with the simulation process. This involves performing Finite Element Analysis (FEA) to assess both the stiffness and buckling behavior of each individual. After completing the FEA for all individuals, the selection process takes

place. To determine which individuals will continue to contribute to the creation of the next generation, a fitness function is established to evaluate each candidate. Derived from the optimization formulation in Equation 4.1, the ensuing fitness function is formulated to gauge the quality of a design:

$$f(x) = \alpha W + \beta E + \gamma P_{cr} \quad (4.3)$$

where  $W$  is the total weight of the structure,  $E$  is the equivalent stiffness of the structure,  $P_{cr}$  is the critical buckling load of the structure, and  $\alpha$ ,  $\beta$  and  $\gamma$  are weighting coefficients.

The most important term of the fitness function is the total weight of the structure, which is the objective to be minimized. The incorporation of stiffness and buckling load terms allows for the differentiation of designs that might share the same weight. To ensure that weight takes precedence over the other two terms, appropriate values for  $\alpha$ ,  $\beta$ , and  $\gamma$  will be selected. Importantly, the weight parameter can be evaluated without the need for complex simulations, as straightforward calculations can determine the total weight of the structure. On the contrary, the determination of the critical buckling load and the equivalent stiffness demands the utilization of Finite Element Analysis (FEA) in Abaqus. Integrating considerations of stiffness and buckling performance is indispensable to discerning between designs that exhibit identical weights.

Following the simulations, a selection process ensues to retain only the most promising design, as determined by the aforementioned fitness function. Based on this selection, an evaluation of the termination criteria is carried out. As outlined in the earlier discussions of Genetic Algorithms (GA), termination criteria can take various forms. One possibility is to check for no change in the best fitness function across several generations, which suggests convergence of the algorithm. Alternatively, the algorithm might terminate if a maximum number of generations has been reached [84]. If the termination criteria are met, the algorithm exits the loop, signifying that the optimal design (with the best fitness function) has been identified. On the contrary, if the criteria are not met, the subsequent generation can be generated, initiating the process represented by the blue dotted lines.

The creation of the new generation if the termination criterion is not met starts with evolving the *Parents*, which are the best designs from the previous generation. First, based on the reproduction process, some parents are creating *children* by cross-breeding their characteristics:

Parent 1 with :  $N_{ply,i,1}; \theta_{ply,i,j,1}; t_{rib,k,1}; X_{cut-out,1}; t_{stiff,rib,l,1}; t_{stiff,panel,m,1}$

Parent 2 with :  $N_{ply,i,2}; \theta_{ply,i,j,2}; t_{rib,k,2}; X_{cut-out,2}; t_{stiff,l,2}; t_{stiff,panel,m,2}$

will create Children with a combination of both parent's configurations such as:

$N_{ply,i,1}; \theta_{ply,i,j,1}; t_{rib,k,2}; X_{cut-out,1}; t_{stiff,rib,l,2}; t_{stiff,panel,m,2}$ .

This step is referred to as the crossover step. After a subset of parents has produced children through cross-breeding, these offspring undergo a mutation process. Drawing inspiration from the evolution of species in the natural world, where mutations occur to adapt to the environment, enhance survival, or counter external challenges, this phase introduces changes to the children's characteristics. Thus, the set of children previously generated is as follows:

$N_{ply,i,1}; \theta_{ply,i,j,1}; t_{rib,k,2}; X_{cut-out,1}; t_{stiff,rib,l,2}; t_{stiff,panel,m,1}$

can mutate to

$N_{ply,i,1}; \theta_{ply,i,j,1}; t_{rib,k,3}; X_{cut-out,2}; t_{stiff,rib,l,2}; t_{stiff,panel,m,1}$  where  $t_{rib,k,3}$  corresponds to another value for the thickness of the ribs for example. This mutation process helps to avoid convergence to a suboptimal solution by introducing diversity in the population [83] [27]. Both processes are illustrated by Figure 4.11

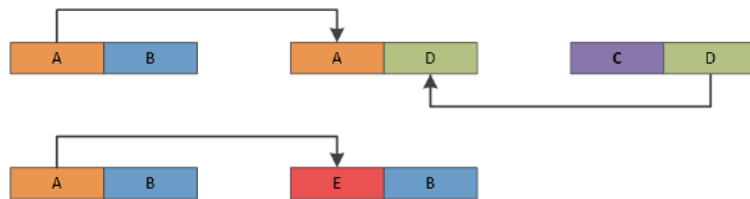


Figure 4.11: Crossover and Mutation selection process of the Genetic Algorithm (GA). Adapted from [84]

With the children generated by parents, it is crucial to introduce random individuals from the design space outlined in Table 4.3. This inclusion of new individuals facilitates continuous exploration of the design space, preventing the algorithm from prematurely converging toward a suboptimal solution. These newcomers are introduced to complete the new generation, which consists of both parents and their offspring. This ensures that the number of individuals remains consistent across generations. With the creation of the new generation completed, the segment denoted by the blue dotted line in Figure 4.10 concludes, allowing the yellow part to start once more.

The loop described above continues until the termination criterion is met. Once this criterion is fulfilled, the Genetic Algorithm concludes, and an optimal solution has been successfully obtained.

# 5

## Implementation of the Optimization

The objective of this chapter is to provide a detailed account of the practical implementation of the optimization process outlined in Section 4.2. This involves explaining the strategies employed to develop and execute the process. The chapter begins by elaborating on how the fitness function, used to evaluate the quality of individual designs, is determined. Subsequently, the concrete realization of the Genetic Algorithm loop is thoroughly elucidated.

### 5.1. Fitness function determination

One of the key parts of the process outlined in Section 4.2 is the establishment of the fitness function. This constitutes the most critical element of the entire process, as it enables the evaluation of individual designs. An incorrect fitness function could result in the selection of an erroneous optimal solution by the Genetic Algorithm. As mentioned earlier, the fitness function is defined as follows:

$$f(x) = \alpha W + \beta E + \gamma P_{cr} \quad (5.1)$$

The weight term  $\alpha W$  is intended to have a stronger influence compared to  $\beta E$  and  $\gamma P_{cr}$ . This emphasis aligns with the primary objective of the optimization, which is to identify the configuration with the lowest weight while also considering stiffness and buckling behavior. Subsequent sections will dive into the process of determining these three terms for each design. Upon establishing the values of these terms, the weighting factors will be adjusted to ensure that the optimization goal is appropriately reflected.

#### 5.1.1. Weight determination

Calculating the weight of a configuration is relatively straightforward. Simple equations involving the relevant variables can be used to determine the weight. The variables that influence the structure's weight include the number of plies in the two panels ( $N_{ply,i}$ ), the thickness of the three ribs ( $t_{rib,k}$ ), the presence of potential cut-outs ( $X_{cut-out}$ ), and the thickness of the stiffeners on both the ribs ( $t_{stiff,rib,l}$ ) and the panels ( $t_{stiff,panel,m}$ ). It's worth noting that the ply orientation ( $\theta_{ply,i,j}$ ) does not impact the weight of the structure, but it plays a critical role in determining stiffness and buckling behavior, as elaborated further.

According to Table 4.1, the total weight of the wing component can be calculated by adding the weight of the different parts of the wing (2 test panels, 10 panel stiffeners, 3 rib panels, 15 rib stiffeners, 24 rib to panel joint and 12 rib to panel half joint) with the following derivation :

$$\begin{aligned} W_{tot} = & \sum_{i=1}^2 W_{panel,i} + \sum_{k=1}^3 W_{rib,k} + \sum_{m=1}^{10} W_{stiff,panel,m} + \sum_{l=1}^{15} W_{stiff,rib,l} \\ & + \sum_{n=1}^{24} W_{joint,n} + \sum_{o=1}^{12} W_{half-joint,o} - X_{cut-out} W_{cut-out} \end{aligned} \quad (5.2)$$



where  $W_{panel,i}$  is the weight of one panel,  $W_{stiff,panel,m}$  is the weight of one stiffener of the panel,  $W_{rib,k}$  is the weight of one rib,  $W_{stiff,rib,l}$  is the weight of one stiffener of the rib,  $W_{joint,n}$  is the weight of one rib to panel joint (referred to Table 4.1),  $W_{half-joint,o}$  is the weight of one rib to panel half joint (referred to Table 4.1), and finally  $W_{cut-out}$  corresponds to the total weight saved by introducing cut-outs in the three ribs.

For the terms related to joints and half-joints (referred to Table 4.1), their weights remain unchanged regardless of the variations in optimization variables. These components are not subject to optimization and remain constant throughout the process. As a result, determining their weights is relatively straightforward:

$$\begin{aligned} W_{joint,n} &= \rho_{Al6082AT6} \times V_{half-joint,n} \\ W_{joint,n} &= 2.7 \times (10.16 \times 9.5 \times 0.63 + 4.45 \times 9.5 \times 0.63) \\ W_{joint,n} &= 422.5 \quad g \end{aligned} \quad (5.3)$$

$$\begin{aligned} W_{half-joint,o} &= \rho_{Al6082AT6} \times V_{half-joint,n} \\ W_{half-joint,o} &= 2.7 \times (10.16 \times 17 \times 0.63 + 4.45 \times 17 \times 0.63) \\ W_{half-joint,o} &= 236.1 \quad g \end{aligned} \quad (5.4)$$

The value of  $\rho_{Al6082AT6}$  is obtained from Table 4.2, and the volume of both the half-joint and the joint components corresponds to the sum of volumes of two rectangular geometries (with the joint having a basic corner-joint geometry).

Having determined these constant terms, the subsequent step involves expressing the remaining terms as functions of the variables in the optimization problem:

$$\begin{aligned} W_{panel,i} &= \rho_{USN150B} \times V_{panel,i} \\ W_{panel,i} &= 1.544 \times 200 \times 100 \times N_{ply,i} \times t_{ply} \\ W_{panel,i} &= 1.544 \times 200 \times 100 \times N_{ply,i} \times 0.0194 \\ W_{panel,i} &= 600 \times N_{ply,i} \quad g \end{aligned} \quad (5.5)$$

The properties of the composite, such as  $\rho_{USN150B}$  and  $t_{ply}$  are precised in Table 3.3.

Similarly, the weight of the rib  $k$  is derived as follows:

$$\begin{aligned} W_{rib,k} &= \rho_{Al6082AT6} \times V_{rib,k} \\ W_{rib,k} &= 0.0027 \times 1000 \times 500 \times t_{rib,k} \\ W_{rib,k} &= 1350 \times t_{rib,k} \quad g \end{aligned} \quad (5.6)$$

The thickness of the ribs  $t_{rib,k}$  should be in millimeters. Using the values specified in Equation 4.1,  $t_{rib,k}$  can take on values of 1.5 mm, 2 mm, 3 mm, or 4 mm.

Then, the weight of the stiffeners is obtained as follows :

$$\begin{aligned} W_{stiff,panel,m} &= \rho_{Al6063AT6} \times V_{stiff,panel,m} \\ W_{stiff,panel,m} &= 0.0027 \times (50 \times t_{stiff,panel,m} \times 2000 + 22 \times 6 \times 2000) \\ W_{stiff,panel,m} &= 712.8 + 270 \times t_{stiff,panel,m} \quad g \end{aligned} \quad (5.7)$$

$$\begin{aligned} W_{stiff,rib,l} &= \rho_{Al6063AT6} \times V_{stiff,rib,l} \\ W_{stiff,rib,l} &= 0.0027 \times (50 \times t_{stiff,rib,l} \times 500 + 22 \times 6 \times 500) \\ W_{stiff,rib,l} &= 178.2.8 + 67.5 \times t_{stiff,rib,l} \quad g \end{aligned} \quad (5.8)$$

The material properties of the aluminum alloy Al 6063AT6 are provided in Table 3.2, and the dimensions of the T-stiffeners are illustrated in Figure 5.13. It's worth noting that due to the differing lengths (2 meters for the panels and 0.5 meters for the ribs), stiffeners on the ribs will be four times lighter than those on the panels if they have the same thickness. However, the rib stiffeners will not necessarily share the same thickness as the panel stiffeners.

Finally, the weight saved by the potential cut-outs is found by the following derivation:

$$\begin{aligned} W_{cut-out} &= \rho_{Al6063AT6} \times V_{cut-out} \\ W_{cut-out} &= 0.0027 \times 3 \times 8 \times (\pi \times 50^2 \times t_{rib,k}) \\ W_{cut-out} &= 508.94 \times t_{rib,k} \quad g \end{aligned} \quad (5.9)$$

$W_{cut-out}$  represents the weight reduction achieved through the presence of the 24 holes in the ribs (8 holes per rib). As a result, this term is also influenced by the thickness of the ribs, which should be expressed in millimeters within the preceding equation.

Before substituting the previously derived expressions into Equation 5.2, it's important to note that the indices presented in Equation 5.2 are unnecessary due to the symmetry of the structure. As explained in the previous chapter, the structure's symmetry significantly constrains the variables of the problem. Consequently, each panel will have the same weight, as will each rib and all the stiffeners. As a result, Equation 5.2 can be simplified as follows:

$$\begin{aligned} W_{tot} &= \sum_{i=1}^2 W_{panel,i} + \sum_{k=1}^3 W_{rib,k} + \sum_{m=1}^{10} W_{stiff,panel,m} + \sum_{l=1}^{15} W_{stiff,rib,l} \\ &+ \sum_{n=1}^{24} W_{joint,n} + \sum_{o=1}^{12} W_{half-joint,o} - X_{cut-out} W_{cut-out} \\ W_{tot} &= 2W_{panel} + 3W_{rib} + 10W_{stiff,panel} + 15W_{stiff,rib} \\ &+ 24W_{joint} + 12W_{half-joint} - X_{cut-out} W_{cut-out} \end{aligned} \quad (5.10)$$

By substituting the derived weight expressions for the different components of the structure, the final weight expression can be formulated as follows:

$$\begin{aligned} W_{tot} &= 2 \times 600 \times N_{ply} + 3 \times 13500 \times t_{rib} + 10 (712.8 + 2700 \times t_{stiff,panel}) + 15 (178.2.8 + 675 \times t_{stiff,rib}) \\ &+ 24 \times 422.5 + 12 \times 236.1 - 5089.4 \times X_{cut-out} \times t_{rib} \end{aligned} \quad (5.11)$$

For example, a random configuration, with the following characteristics:  $N_{ply} = 14$ ;  $X_{cut-out} = 1$ ;  $t_{rib} = 1.5$  mm;  $t_{stiff,panel} = 1.59$  mm and  $t_{stiff,rib} = 3$  mm gives the following weight :

$$W_{tot} = 52,22 \quad kg \quad (5.12)$$

In summary, the weight of the structure can be calculated using the expression provided in Equation 5.11, allowing for a straightforward evaluation of the first term of the fitness function based on a given set of optimization variables.

### 5.1.2. Simulation to obtain stiffness and buckling behavior

Unlike the first term of the fitness function, evaluating the second and third terms is more complex. The stiffness and buckling behavior of a structure cannot be directly calculated through simple formulas; instead, a Finite Element Model (FEM) is required. The FEM used in this context is based on the model developed by TU Delft, as detailed in the paper by Bisagni et al. [1], depicted in Figure 5.1. This model is implemented in the ABAQUS 2019 Finite Element code.

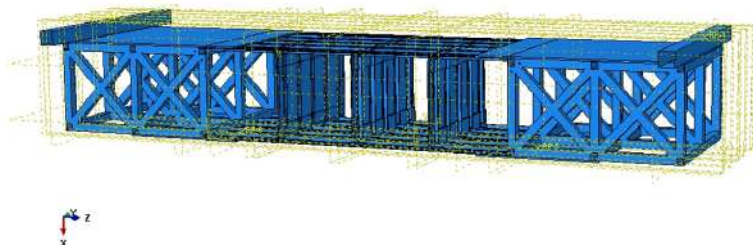


Figure 5.1: Finite Element Model

#### 4-point bending test explanation:

Figure 5.1 illustrates the structure introduced in subsection 4.1.1, accompanied by a loading rig. This rig is designed to apply a 4-point bending test to the wing component.

The various components of the tested structure, as outlined in Table 4.1, are connected using bolts. Instead of directly modeling the holes, tie constraints are employed to simulate the connections between these components. A similar approach is taken for attaching the structure to the loading rigs, where tie constraints are used to represent the link between the attachment plates and the composite panels. The composite panels are modeled using continuum shell elements SC8R, which were discussed in detail in chapter 3. The average element size for these shell elements is set to 10mm. On the other hand, metallic parts are discretized using solid elements C3D8R for the wing components and solid elements C3D10 for the loading rigs. The entire model comprises around 300,000 elements.

The loading rig, as well as the wing components with the loading rig, are shown in Figure 5.2.

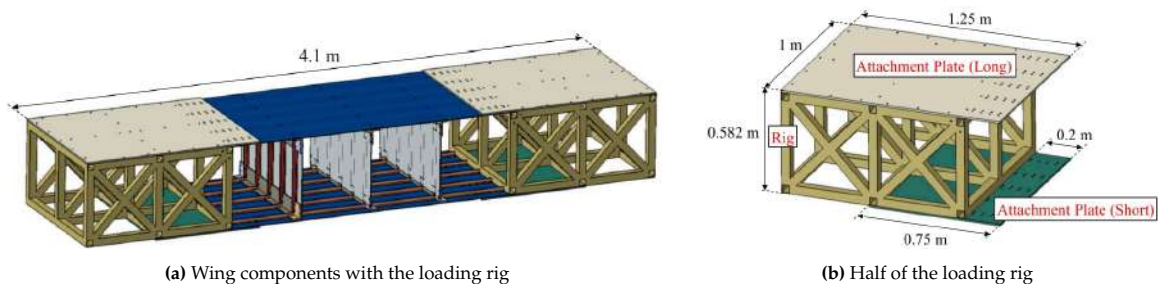


Figure 5.2: Wing component with the loading rig for the 4-point bending test. Taken from [1]

The 4-point bending test, illustrated in Figure 5.3, is designed to evaluate both the stiffness and the buckling behavior of the wing structure. The test involves two rectangular loading blocks featuring rigid surfaces, which introduce the load by causing the loading blocks to undergo a vertical displacement of 10 mm. These loading blocks correspond to the first two points of the four-point bending test. The other two points correspond to supports located at the junction between the bottom composite panel and the attachment rigs. These supports constrain the vertical displacement of the nodes by preventing any vertical movement at these specific locations. The four blocks, comprising two loading blocks and two supports, are modeled as distinct structures. To simulate contact between these blocks and the structure, surface-to-surface contact interactions are employed, utilizing hard contact conditions with frictionless options. This modeling approach prevents interpenetration between the different components. For a visual representation of the boundary conditions and configuration, refer to Figure 5.3.

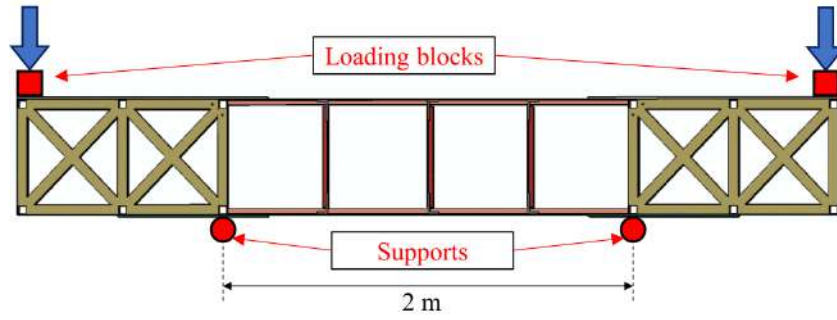


Figure 5.3: 4-point bending test. Taken from [1]

The test depicted in Figure 5.3 is analyzed through a **Dynamic, Implicit** simulation approach, which was covered in detail in chapter 3. In this simulation, a displacement-controlled test is conducted by simulating a vertical displacement of 10 mm for both of the loading blocks situated at the edges of the structure. This displacement-controlled approach ensures that the loading conditions are consistent and controlled, allowing for an accurate assessment of the structure's response to bending forces.

Furthermore, by the findings presented in section 3.2, Hashin's criteria has been selected as the method to identify any potential fiber/matrix damages within the composite laminates. It's important to note that no post-damage degradation of material properties is taken into consideration. However, as indicated by Equation 4.1, the optimization formulation prohibits any form of failure in the composite during the optimization process. This means that all solutions considered must adhere to the constraints that ensure no failure occurs. Therefore, no implementation of any delamination process has been done in the span of the optimization.

### Assessment of the structural properties

The preceding section provides a comprehensive overview of the 4-point bending test conducted using the loading rigs on the wing component. To gain insight into how the structural properties of an individual are obtained, the ensuing three configurations will be examined: (these configurations were chosen arbitrarily while writing the report from the array of configurations generated by the algorithm to serve as illustrative examples for the 4-point bending test results. These three configurations are individual 4 from generation 13, individual 2 from generation 13, and individual 10 from generation 13 (referred to Appendix A))

Simulation number	$N_{ply,i}$	$\theta_{ply,i,j}$	$t_{rib,k}$	$X_{cut-out}$	$t_{stiff,rib,l}$	$t_{stiff,panel,m}$
1	14	$[90/0/30/45/60/30/90]_s$	2	0	3.18	3.18
2	12	$[0/90/0/30/90/45]_s$	1.5	0	3.18	1.59
3	12	$[90/45/0/30/60/45]_s$	3	1	1.59	3.18

Table 5.1: Three potential candidates for the optimization.

Each of these individuals undergoes the 4-point bending test previously elucidated, yielding the subsequent vertical displacements (in the x-direction):

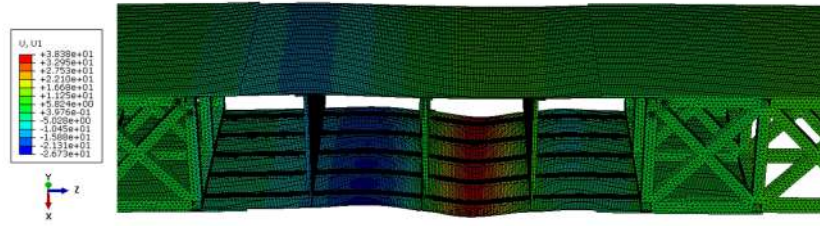


Figure 5.4: Vertical displacement of the first simulation

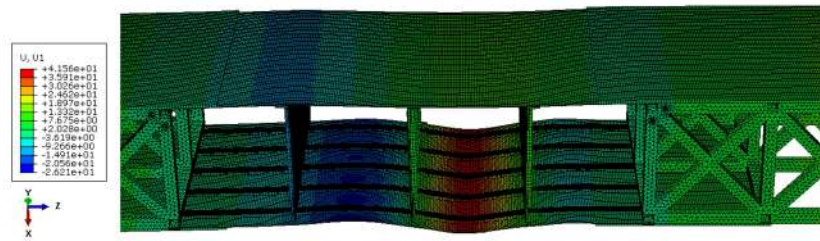


Figure 5.5: Vertical displacement of the second simulation

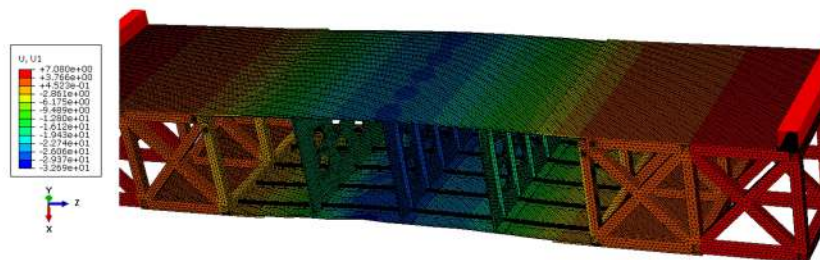


Figure 5.6: Vertical displacement of the third simulation

The first two simulations proceed until the end of the simulation, with the two loading blocks undergoing a vertical displacement of 10 mm each. On the contrary, the third simulation is terminated prematurely. Upon observing Figure 5.4 and Figure 5.5, both simulations 1 and 2 manifest analogous buckling behavior, characterized by the bottom panel experiencing buckling and the occurrence of global buckling. However, as delineated in Figure 5.6, the third simulation does not exhibit any buckling; the simulation stops before its initiation. This discrepancy might be attributed to the presence of cut-outs in this specific configuration ( $X_{cut-out} = 1$ ), whereas the first two simulations do not incorporate any cut-outs ( $X_{cut-out} = 0$ ).

The load-displacement curves of the simulations are depicted in Figure 5.7, utilizing the output data provided by Abaqus. In this context, displacement corresponds to the vertical displacement of the loading blocks, while force signifies the vertical reaction force detected at these blocks.

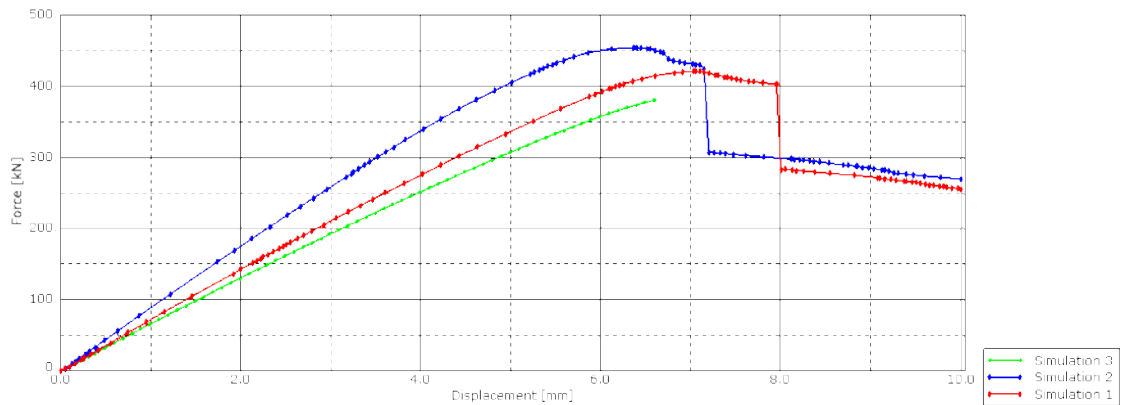


Figure 5.7: Load displacement curves of the three simulations

From Figure 5.7, the fact that simulation 3 stops before the end of the simulation is confirmed. Around 6.6mm vertical displacement of the building block, the simulation stops due to failure that starts to occur in the composite panels. Indeed, in Abaqus, Hashin's criteria reaches the critical value of 1, thus, according to Equation 4.1, the constraint related to failure is no longer respected. This Simulation 3 displays a linear relationship between load and displacement. On the contrary, simulations 1 and 2 proceed through the entire simulation, reaching a displacement of 10mm. Three distinct phases can be identified in the load evolution during the vertical displacement of the loading blocks:

- Phase I: A linear evolution of the load against the displacement is observed. The third simulation is also subjected to this linear evolution. No buckling is observed during this phase. Figure 5.8a shows the vertical displacement of the wing component, for simulation 2, when the displacement of the loading block is 3.25mm, during the linear relation.
- Phase II: a plateau is reached, the beginning of buckling occurs, and the linear relation between load and displacement is no longer true. At this point, for approximately 1mm, the force is almost constant, and local buckling is visible. For simulation 2, this phase starts at (2) (see Figure 5.8b) when the displacement is equal to 6.11mm and finishes at (3) (see Figure 5.8c) when the displacement is equal to 7.15mm. All along this phase, buckling in between the panel stiffeners is observed in the bottom panel of the wing.
- Phase III: buckling of the panel between two ribs occurs suddenly (see Figure 5.8d) and the load drops by losing a bit more than 100 kN. The buckling of the panel between two ribs stays until the displacement finally reached the 10mm, which corresponds to the end of the simulation, as shown by Figure 5.5.

Hereafter, the vertical displacement through the second simulation can be found to visually represent the distinct phases explained earlier.

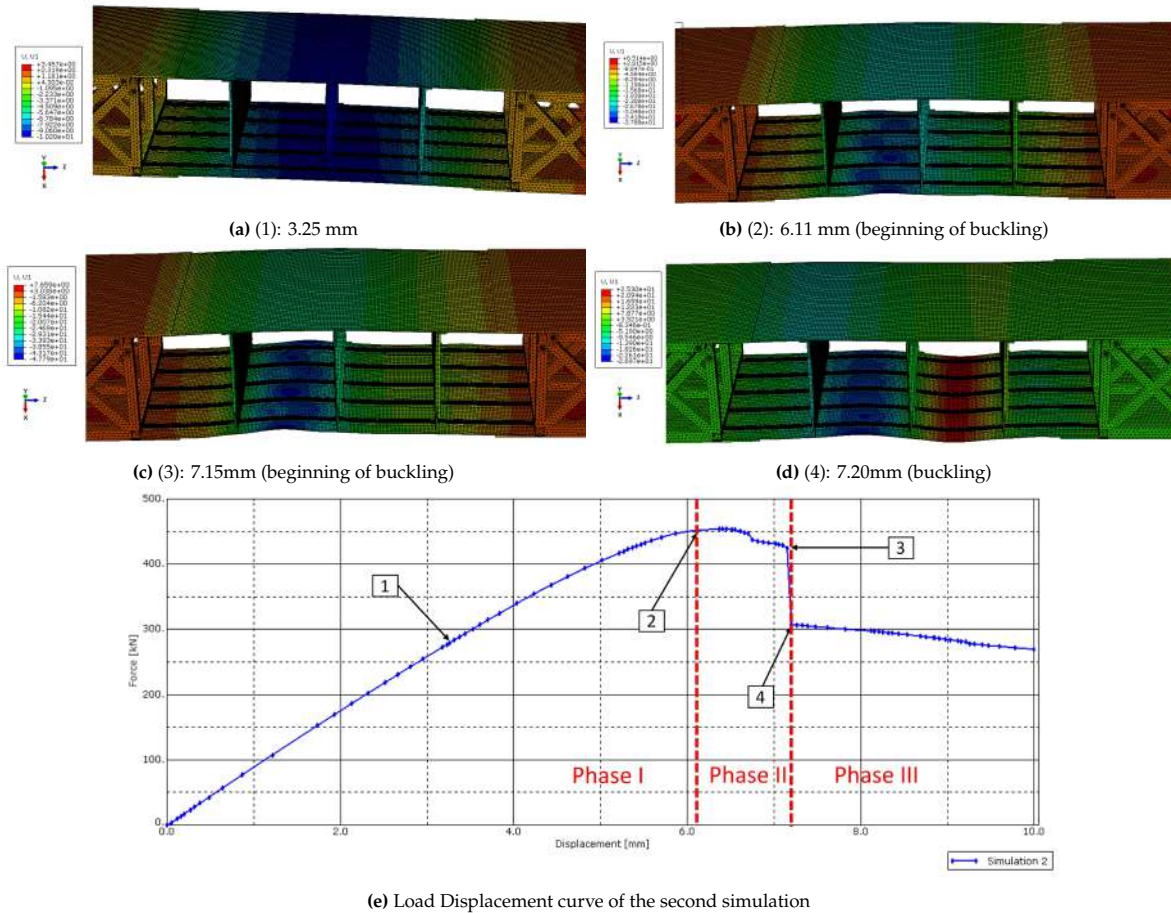


Figure 5.8: Vertical displacement through the simulation

The load-displacement curves of the various simulations provide insights into both the stiffness and buckling behavior of the structure. The linear relationship between the load and displacement during the initial phase directly yields the equivalent stiffness of the structure, expressed in [N/mm]. This stiffness value corresponds to the slope of the curve during this initial phase, which is outlined by the green rectangle in Figure 5.9. Regarding buckling behavior, since phase II corresponds to the onset of buckling, the maximum value on the plateau—depicted by the red ellipsoid in Figure 5.9—indicates the structure’s buckling characteristics. A higher buckling load value signifies better buckling resistance in the structure.

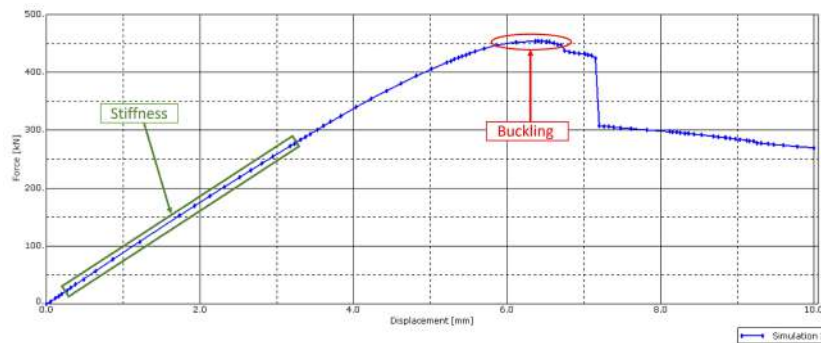


Figure 5.9: Stiffness and buckling assessment

Using these criteria and the load-displacement curves illustrated in Figure 5.7, the values of these criteria can be determined for the three simulations. In the case of simulation 3, where buckling doesn’t

occur, the maximum load value serves as the buckling criterion (albeit lower than a potential buckling load, given that no buckling takes place):

Simulation number	Stiffness criteria [N/mm]	Buckling criteria [N]
1	65930	422770.9
2	75924	460270.4
3	59152	382266.6

**Table 5.2:** Stiffness and buckling performance of the three individuals.

In conclusion, Figure 5.9 outlines the criteria for evaluating both the stiffness (slope of the linear relationship during phase I) and buckling behavior (maximum load value during phase II) of the structure. Thus, the other two terms of the fitness function are assessed through a 4-point bending simulation using Abaqus. The next step involves determining the appropriate values for each weighting factor to finalize the fitness function.

### 5.1.3. Determination of the weighing factors:

Having established the criteria for the three simulations in previous sections, the next step is to evaluate the quality of each individual using the fitness function (as shown in Equation 5.1). For this purpose, the weighting factors  $\alpha$ ,  $\beta$ , and  $\gamma$  need to be calibrated in such a way that weight is the primary criterion, accounting for 80% of the final value, while stiffness and buckling are secondary criteria, each contributing approximately 10% to the final value. The following values for  $\alpha$ ,  $\beta$ , and  $\gamma$  are established:

$$\alpha = 1,8kg^{-1} \quad ; \quad \beta = 1.43 * 10^{-4}mm/N \quad ; \quad \gamma = 2.33 * 10^{-5}N^{-1} \quad (5.13)$$

These values have been selected arbitrarily at the beginning of the Genetic Algorithm (with the results of the first generation shown in Appendix A) to achieve an approximate distribution of 80/10/10 for the weight, stiffness, and buckling criteria, respectively.

Simulation number	Weight [kg]	Stiffness [N/mm]	Buckling [N]	fitness function [-]	W% %	S% %	B% %
1	59.45	75930	422771.0	<b>93,69</b>	77,90	11,59	10,51
2	50.74	88928	460270.4	<b>112,11</b>	79,09	11,34	9,57
3	57.97	69152	382266.6	<b>94,45</b>	80,10	10,47	9,43

**Table 5.3:** Summary of the performance of the three individuals.

Where W%, S%, and B% represent the percentages of the fitness function attributed to the weight term, the stiffness term, and the buckling term, respectively.

In conclusion, this section has outlined the process of calculating the weight, assessing stiffness, and evaluating buckling performance, leading to the final formulation of the fitness function.

## 5.2. Genetic Algorithm implementation

This section aims to detail the practical implementation of the procedure outlined in section 4.2 and to present the diverse strategies devised for executing the optimization process. The flow chart depicted in Figure 5.10 divides the optimization process into three distinct phases, categorized according to the tools employed for each step: Python scripts for the green steps, an Excel sheet for the blue step (selection), and Abaqus simulations executed on the TU Delft hpc12 cluster for the orange steps (simulations).



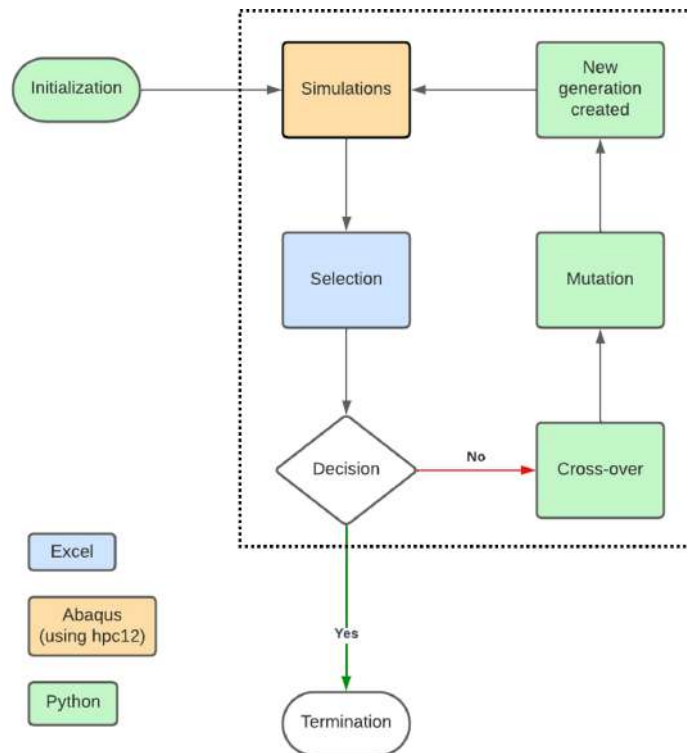


Figure 5.10: Flow chart of the optimization

Unlike typical Genetic Algorithm implementations that operate as standalone programs, generating new generations autonomously until meeting termination criteria, the nature of this optimization problem necessitates a more complex approach. This is because the assessment of the fitness function relies on Finite Element Analysis. Although there are Python codes capable of executing Abaqus simulations directly, it was determined that a step-by-step approach was more efficient than developing a single comprehensive code to fully automate the process. This decision was based on the complexity of the optimization problem and the need to carefully manage different aspects of the process.

### 5.2.1. Initialization (Python code)

The Python code plays a central role in the overall process, his goal is to generate populations of potential candidates for the optimization. This involves creating the various variables of the problem in the following manner:

```

1 Nb_ply=[12, 14, 16, 18]
2 thickness_rib=['1.5', '2.', '3.', '4.']
3 cutout=[0, 1]
4 thickness_stiffpanel=[0, 1, 2]
5 Nb_indiv=10
  
```

The variable *thicknessstiffpanel* takes on the values [0, 1, 2], which correspond respectively to the thicknesses [1.59, 3, 3.18]. This choice simplifies the coding process by using straightforward values. The number of individuals within a single population is set to 10. This decision is primarily influenced by the computational aspects of the simulations, as detailed in subsection 5.2.2. Due to computational constraints, only 10 simulations can be run concurrently on the cluster, which drives the choice of population size. Further explanations about this computational limitation can be found in the subsequent section.

With the variables introduced earlier, the population of the first generation can be initialized using the following function, called **Initiate pop**.

```

1 def Initiate_pop(Nb_indiv, Nb_ply, thickness_rib, cutout, thickness_stiffpanel):
2     Config=[]
  
```

```

3     for j in range(Nb_indiv):
4         X_ply=random.choice(Nb_ply)
5         Orientation_ply=[0,0,0,0,30,30,30,30,45,45,45,45,60,60,60,60,90,90,90,90]
6         X_orientation=stacking_sequence(X_ply,Orientation_ply)
7         X_cutout=random.choice(cutout)
8         X_thickrib=random.choice(thickness_rib)
9         X_thickstiffpanel=random.choice(thickness_stiffpanel)
10        X_thickstiffrib=random.choice(thickness_stiffpanel)
11        X=[X_ply,X_orientation,X_cutout,X_thickrib,X_thickstiffpanel,X_thickstiffrib]
12        Y=CreateInp(X,j)
13        Config.append(Y)
14    return Config

```

Basically, for each individual and each variable within them, a random choice is made within the design space. Regarding the ply orientation, a function named **stacking sequence** is employed to generate a random stacking sequence. This function utilizes the previously randomly selected ply number as a variable.

```

1 def stacking_sequence(NbPly,OrientationPossible):
2     Seq=[]
3     Angle=22
4     for i in range(NbPly//2):
5         Angle1=random.choice(OrientationPossible)
6         while Angle1 == Angle :
7             Angle1=random.choice(OrientationPossible)
8             OrientationPossible.remove(Angle1)
9             Seq.append(Angle1)
10            Angle=Angle1
11        Seq1=Seq
12        for i in range(len(Seq1)):
13            Seq=Seq+[int(Seq1[-(i+1)])]
14    return Seq

```

The first loop aims to create the stacking sequence. Only the orientation of half of the number of plies is necessary since the stacking sequence is always symmetric in the optimization. Following the advice provided in subsection 2.1.2, it was decided to prevent two plies with the same orientation from being adjacent. This is achieved through the while condition, which aims to avoid repeating the same angle consecutively. Furthermore, the orientation of each ply is randomly selected from the variable called *OrientationPossible* which is generated within the function **Initiate pop**. This variable contains four instances of each of the five possible orientations. As a ply adopts a certain orientation, one of the four instances of that orientation is removed from *OrientationPossible*. Consequently, the likelihood of selecting the same orientation for subsequent plies decreases. This approach facilitates the creation of stacking sequences that exhibit a balanced distribution of different angles, in line with the guidelines outlined in subsection 2.1.2. Finally, the second loop generates the symmetric portion of the stacking sequence.

After establishing each variable randomly, an individual is created (represented by the list X in the code). Subsequently, the corresponding .inp file for the individual is generated using a significant python function named **CreateInp**. This function holds huge importance since it is responsible for creating the .inp file associated with the individual. The .inp file serves as the input file for the Abaqus simulation for a given individual. By employing the 4-point bending test explained in subsection 5.1.2, the fitness function is determined.

```

1 def CreateInp(X,j):
2     if X[2] == 0 :
3         fichier=open('temoin.inp', "r")
4     elif X[2] == 1:
5         fichier=open('temoinCutOut.txt', "r")
6     contenu = fichier.read()
7     lignes_contenu = contenu.split("\n")
8
9     #Change 1 : Ply number and ply orientation
10    Ply=[]
11    for i in range (int(X[0])):
12        Ply.append("0.194,3,USN150B," +str(X[1][i])+".,Ply-"+str(i+1))
13

```

```

14 #Change 2 : thickness of the ribs
15 fichier_cutout=open('cut-out'+str(X[2])+'.txt', "r")
16 contenu_cutout = fichier_cutout.read()
17 lignes_contenu_cutout = contenu_cutout.split("\n")
18 compt=1
19 while lignes_contenu_cutout[compt]!='*Element,type=C3D8R':
20     if int(lignes_contenu_cutout[compt][47])==3:
21         if X[3]=='1.5':
22             lignes_contenu_cutout[compt]=lignes_contenu_cutout[compt][:46]+str(X[3])
23         else:
24             lignes_contenu_cutout[compt]=lignes_contenu_cutout[compt][:47]+str(X[3])
25     compt+=1
26
27 #Change 3 : thickness of the ribs
28 fichier_stiffpanel=open('stiffenerspanel'+str(X[4])+'.txt', "r")
29 contenu_stiffpanel = fichier_stiffpanel.read()
30 lignes_contenu_stiffpanel = contenu_stiffpanel.split("\n")
31 fichier_stiffrib=open('stiffenersrib'+str(X[5])+'.txt', "r")
32 contenu_stiffrib = fichier_stiffrib.read()
33 lignes_contenu_stiffrib = contenu_stiffrib.split("\n")
34
35 #Adding the missing part of the .inp file
36 for i in range(len(lignes_contenu)):
37     if lignes_contenu[i] == '*Shell,elset="Test_Panel-1",composite,orientation
38         =Ori-1,stack_direction=3,layup="Test_Panel"':
39         lignes_contenu=lignes_contenu[:i+1]+Ply+lignes_contenu[i+1:]
40     if lignes_contenu[i] == '*Part,name=Cut-Extrude2_1':
41         lignes_contenu=lignes_contenu[:i+1]+lignes_contenu_cutout+lignes_contenu[i+1:]
42     if lignes_contenu[i] == '*Part,name=Mirror2':
43         lignes_contenu=lignes_contenu[:i+1]+lignes_contenu_stiffpanel+lignes_contenu[i
44             +1:]
45     if lignes_contenu[i] == '*Part,name=Cut-Extrude1':
46         lignes_contenu=lignes_contenu[:i+1]+lignes_contenu_stiffrib+lignes_contenu[i+1:]
47 contenu = "\n".join(lignes_contenu)
48 fichier_cutout.close()
49 fichier_stiffpanel.close()
50 fichier_stiffrib.close()
51
52 #Creation of the .inp file
53 fichier = open('Pop_inter'+str(j+1)+'.inp', "x")
54 fichier.write(contenu)
55 fichier.close()
56 return X

```

To generate all the necessary .inp files (a total of 10, one for each individual), two templates have been established: one for configurations without cut-outs and another for configurations with cut-outs. These templates are complete .inp files with the entire structure, with the specific lines pertaining to variable changes left vacant. These lines will be filled in using the subsequent parts of the function to recreate fully formed .inp files. For example, lines corresponding to the stacking sequence of the composite panel are initially removed, along with lines defining the ribs, etc. Then, utilizing the code, the sections influenced by variable changes are reintegrated to reconstruct the comprehensive .inp file. These sections of the .inp file, impacted by the variables, have been studied for one variable after another to understand the impact of a change of this variable in the .inp file with preliminary analyses. Therefore, based on the set of variables, the complete .inp file is recreated.

To provide further clarity, the aforementioned code has been divided into five distinct segments, each serving a distinct purpose, explained below.

**Change 1: Ply number and ply orientation**

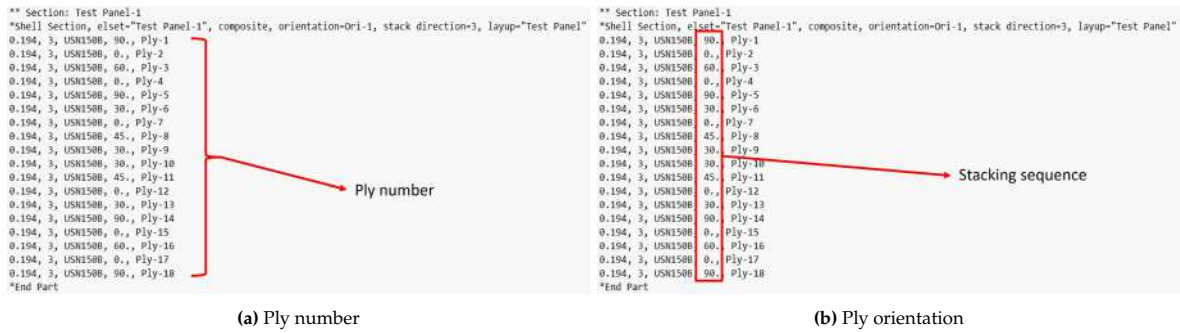


Figure 5.11: Change in the ply number and ply orientation in the .inp file

The locations where the ply number and ply orientation can be altered are illustrated in Figure 5.11. Consequently, in both templates, the lines corresponding to the stacking sequence definition have been omitted. The initial loop of the **CreateInp** function generates these lines, based on both the ply number and ply orientation of the present candidate.

**Change 2 : Thickness of the ribs**

Concerning the change of rib thickness, the thickness of the ribs is altered based on the presence or absence of cut-outs on the ribs. The designation "cut-out0" signifies ribs without cut-outs, while "cut-out1" corresponds to ribs with cut-outs. These configurations, set at a 3mm thickness, are modified according to the value of *thicknessrib*, as shown by Figure 5.13. Notably, .inp files are defined with a column width of only 50 characters. Consequently, if a thickness changes from '3.' mm (two characters) to '1.5' mm (three characters), it needs to start in the preceding column: column 48 rather than 49, to prevent the row from surpassing the 50-column limit. This accounts for the condition "if" within the "while" loop and the slight difference in the code when the thickness is 1.5mm.

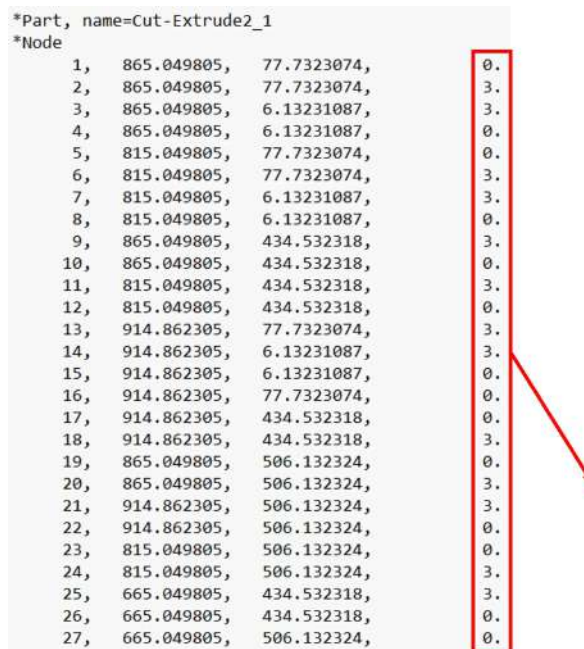


Figure 5.12: Lines to change the thickness of the ribs

Figure 5.13 shows only the first lines of the part, however, all the lines corresponding to this part are changed.

**Change 3 : Thickness of the stiffeners**

Regarding the modification of stiffener thickness, Figure 5.13 demonstrates that it is the y-coordinate of the bottom of the stiffeners that requires adjustment to accurately alter the thickness of the stiffeners.

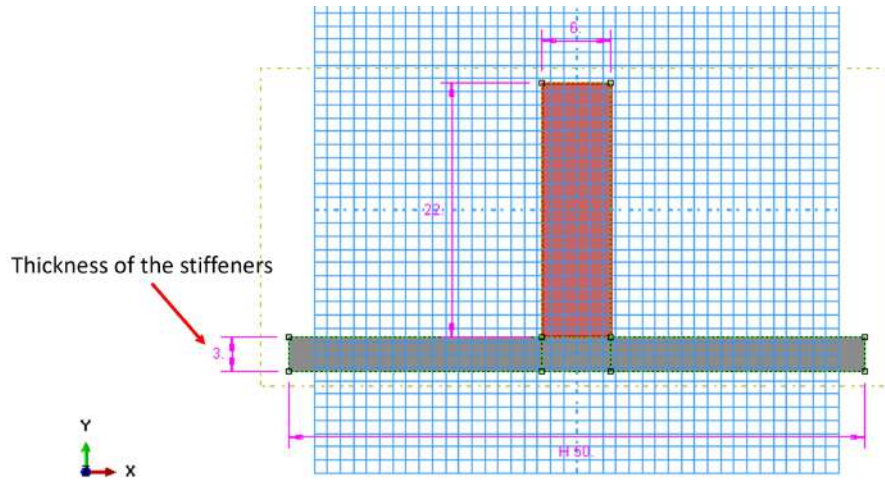


Figure 5.13: Thickness of the stiffeners = 3mm in this case

The stiffeners of the panels are distinct from the stiffeners of the ribs; therefore, modifying them involves altering different parts, as illustrated in Figure 5.14.

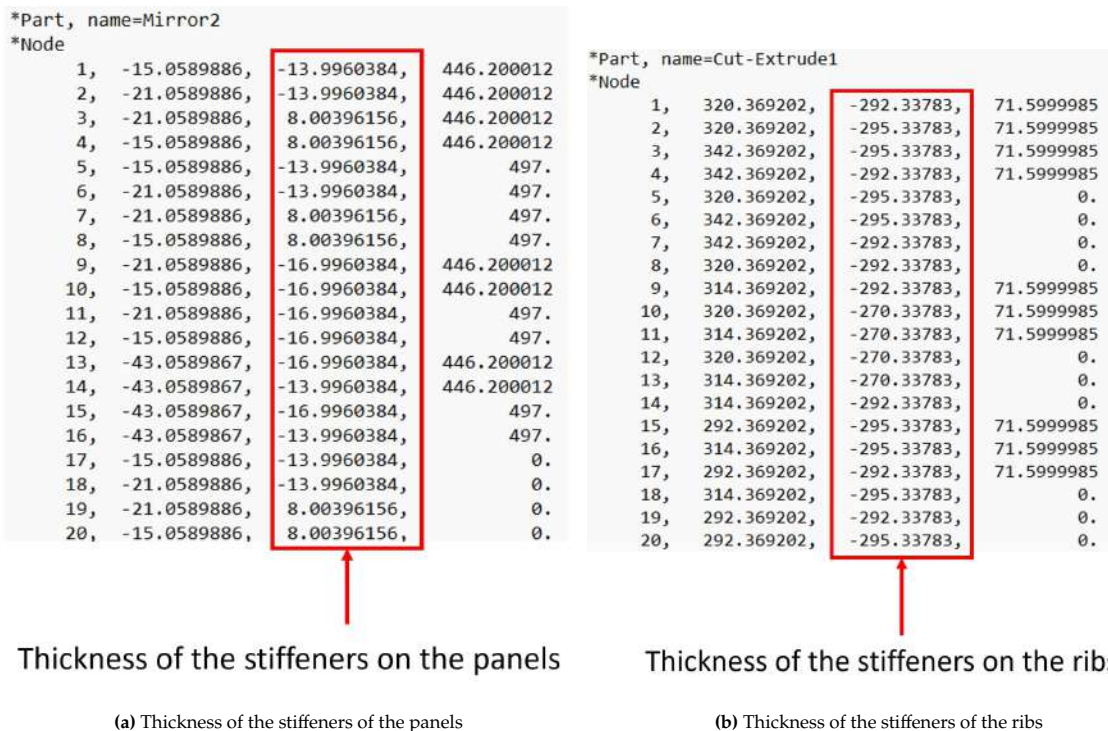


Figure 5.14: Change in the ply number and ply orientation in the .inp file

From Figure 5.14, it can be observed that the y-coordinate values of both stiffeners are not centered around 0. According to Figure 5.13, the thickness of the stiffeners that needs to be adjusted corresponds to the difference between the two lowest values of the y-coordinate (-13.99 and -16.99 for the panels and -292.3 and -295.3 for the ribs). Indeed, the T-stiffeners are oriented in the y-direction (see Figure 5.13). Therefore, changing the thickness of the stiffeners corresponds to changing the lower value of the

y-coordinate, according to the value of *thicknessStiffPanel*.

To address this change, a decision was made to directly generate the .inp files corresponding to the six possible configurations: three for the panel stiffeners (referred to as stiffenerspanel0, stiffenerspanel1, and stiffenerspanel2) and three for the rib stiffeners (referred to as stiffenersrib0, stiffenersrib1, and stiffenersrib2), each configuration corresponding to a distinct thickness. Consequently, based on the variables provided, the appropriate configuration is selected and integrated into the overall .inp file.

### Adding the missing part of the .inp file

As described earlier, two template .inp files were established: one without cut-outs and another with cut-outs. The preceding sections of the code are responsible for generating the lines related to the variables for creating a new comprehensive .inp file. This section of the code is designed to properly integrate these generated lines into the appropriate positions within the template .inp file. For instance, the definition of the vertical metallic ribs is positioned after a line denoted as "\*Part, name=Cut-Extrude2 1" in the .inp file. Consequently, the lines about the ribs must be inserted after this line. Similarly, the stacking sequence is defined after "\*Shell Section, elset = "Test Panel -1", composite, orientation =Ori -1, stack direction =3, layup = "Test Panel", ". The stiffeners of the panels are positioned after "\*Part, name=Mirror2", and the stiffeners of the ribs follow after "\*Part, name=Cut - Extrude1".

### Creation of the .inp file

Consequently, the **CreateInp(X, j)** function generates the actual .inp files using the three simple lines provided at the end of the function. These files are named "Pop inter" followed by the number corresponding to each individual, ranging from 1 to 10 to match the 10 individuals within the population.

## 5.2.2. Simulations (Abaqus using hpc12)

Once the initial .inp files are generated, the first generation of the algorithm is ready for the simulations. As explained in subsection 5.1.2, these simulations involve a 4-point bending test to evaluate the stiffness and buckling behavior of the structure. Access to Abaqus is obtained through a remote desktop connection from TU Delft. On this computer, Abaqus can utilize up to 4 processors simultaneously. This information is indicated when creating a Job from a Model on the "Parallelization" tab. By utilizing this configuration, running the 10-second 4-point bending test took approximately 40 hours to complete. Consequently, for a given population of 10 individuals, running the entire test requires a minimum of 400 hours, equivalent to over 16 days. Consequently, achieving the termination criteria of the algorithm would be excessively time-consuming. Thus, the utilization of the hpc12 cluster from TU Delft is necessary.

The hpc12 cluster, managed by ICT TU Delft, serves both the Aerospace Structure and Materials (ASM) and Flow Physics and Technology (FPT) Departments. hpc12 is specifically designed for executing complex computational tasks, including computational simulations and data analysis. This cluster provides the advantage of utilizing more cores concurrently than a typical computer, resulting in reduced computational time. To execute simulations, users are required to submit jobs to the queuing system. Additional comprehensive information about the cluster is available in [98].

To run Abaqus simulations on this cluster, the following code is required:

```

1 #Job for Torque PBS 4.2.10
2 #
3 # PBS parameters (see: man qsub)
4 # -----
5 #PBS -j oe
6 #PBS -l nodes=1:ppn=20
7 #PBS -M
8 #PBS -m abe
9 #PBS -N pop1
10 #PBS -o pop1.LOG
11 #PBS -q asm-small
12 #PBS -rn
13 #PBS -S /bin/csh
14 # -----
15 #
16 cd ${PBS_O_WORKDIR}

```

```

17 #
18 module load abaqus/2021
19 #
20 abaqus job=Pop1 cpus=20
21 exit 0

```

By utilizing the line "abaqus job=Pop1 cpus=20," the Abaqus job named 'Pop1.inp' is submitted and executed on 20 cores, which is typically the maximum allowed for most nodes available to ASM users [98]. The cluster operates under certain rules and constraints. For instance, the asm-small queue permits the usage of only 1 node per job and allows a maximum of 10 concurrent jobs for a single user. Additionally, there's the asm-medium queue which enables the utilization of multiple nodes per simulation, although only 3 simulations can run concurrently. Consequently, the decision to maintain a population of 10 individuals for each generation stems from the fact that it aligns with the maximum number of simulations that can be executed simultaneously within the constraints of the asm-small queue.

Employing the cluster for simulations, with a significantly higher number of cores available compared to running simulations on a regular TU Delft computer, has resulted in a substantial reduction in computational time, facilitating the development of the Genetic Algorithm. The usage of the cluster has brought about significant efficiency improvements. A single simulation, when executed on the cluster, now takes under 10 hours to complete. This is almost a 5-times reduction in simulation time compared to running simulations on an individual computer from TU Delft.

Furthermore, a key advantage of the cluster is its capacity to handle multiple simulations simultaneously. With the cluster, up to 10 simulations can run concurrently. As a result, if all simulations are initiated simultaneously, it takes only around 10 hours to complete the simulations for an entire generation (comprising 10 individuals). This achievement marks a substantial advancement from the initial estimate of 16 days for the same task. Moreover, since a total of 20 generations of 10 individuals (for a total of 200 simulations) were needed, the use of the hpc12 cluster was mandatory.

Upon completion of the simulations, the hpc12 cluster generates the .odb file, which contains all the requested outputs from the simulation. This .odb file serves as the foundation for the subsequent stages of the Genetic Algorithm.

### 5.2.3. Selection (Excel sheet)

As depicted in Figure 5.10, the next stage after the simulations is the selection process. In this step, the fitness function for each individual is calculated, and based on these evaluations, the selection procedure is executed to retain only the most promising candidates.

An Excel sheet has been developed to automate this process, which is detailed in Appendix A. In this sheet, the variables corresponding to each individual are inputted, and the calculations outlined in subsection 5.1.1 are automatically performed to derive the total weight of the structure. Additionally, using the .odb files generated from the simulations, the assessment of stiffness and buckling behavior, as described in subsection 5.1.2, is conducted. The resulting values are recorded in the Excel sheet, allowing for the computation of each individual's fitness function. From the initial pool of 10 individuals, the 5 individuals with the highest fitness function values are selected to form the basis for the next generation. With the selection phase now complete, the next step of the optimization process—the creation of the subsequent generation—can start using the chosen 5 parent individuals.

### 5.2.4. Creation of the next generation (Python code)

Using the five parent individuals obtained through the selection step, the next generation is generated using a Python function called `next_gen`. This function is responsible for creating the offspring individuals through processes such as crossover and mutation. The new individuals are formed by combining the characteristics of the parents and introducing variations to encourage exploration of the design space. This iterative process aims to evolve the population towards better-performing solutions over successive generations.

```

1 def next_gen(Parents, Nb_indiv, Nb_ply, thickness_rib, cutout, thickness_stiffpanel):
2     #Cross-over

```

```

3   parent1=random.choice(Parents)
4   index1=Parents.index(parent1)
5   parent2=parent1
6   while parent2 == parent1 :
7       parent2=random.choice(Parents)
8   index2=Parents.index(parent2)
9   CrossParents=crossover(parent1, parent2)
10  Parents[index1]=CrossParents[0]
11  Parents[index2]=CrossParents[1]
12
13  #Mutation
14  Parents[index1]=mutation(Parents[index1],Nb_ply,thickness_rib,cutout,thickness_stiffpanel
15  )
16  Parents[index2]=mutation(Parents[index2],Nb_ply,thickness_rib,cutout,thickness_stiffpanel
17  )
18  #Generation of the new population
19  Child=Initiate_pop(Nb_indiv-len(Parents),Nb_ply,thickness_rib,cutout,thickness_stiffpanel
20  )
21  NextGen=Child+Parents
22  CreateInp(Parents[index1],index1+len(Child))
23  CreateInp(Parents[index2],index2+len(Child))
24  return NextGen, Parents, index1, index2

```

This function can be divided into three distinct parts: first, the crossover; then, the mutation; and finally, the generation of the new population. The first two steps primarily involve the parents from the previous generation. The last step involves the introduction of new children, which are created from scratch.

### Cross-over

First, among the 5 parents obtained from the previous generation, two are randomly selected to create new individuals by combining their sets of variables. This process involves subjecting these two parents to the following function, referred to as **crossover** at the beginning of the **next gen** function:

```

1 def crossover(m1, m2):
2     mate1 = []
3     mate2 = []
4     k = np.random.randint(1, len(m1))
5     for val in m1:
6         mate1.append(val)
7     for vals in m2:
8         mate2.append(vals)
9     for i in range(k, len(mate1)):
10        mate1[i], mate2[i] = m2[i], m1[i]
11    return mate1, mate2

```

This function serves to implement the crossover step of the Genetic Algorithm. By utilizing two solutions retained from the previous generation, these two solutions exchange a portion of their configurations. This exchange generates two new individuals that represent a combination of the characteristics of the two previous solutions.

### Mutation

The subsequent stage of the process involves introducing the possibility of mutation, exclusively for the two parents that underwent the crossover step. This task is performed within the next gen function, utilizing the **mutation** function as depicted below:

```

1 def mutation (m1,Nb_ply,thickness_rib,cutout,thickness_stiffpanel):
2     for i in range (len(m1)):
3         compt=np.random.randint(100)
4         if compt<17:
5             if i==0:
6                 m1[i]=random.choice(Nb_ply)
7                 #issue here if the number of ply change -> ply orientation should also
8             if i==1:
9                 Orientation_ply=[0,0,0,0,30,30,30,30,45,45,45,45,60,60,60,60,90,90,90,90]
10                m1[i]=stacking_sequence(m1[0],Orientation_ply)
11            if i==2:
12                m1[i]=random.choice(cutout)

```



```
13         if i==3:
14             m1[i]=random.choice(thickness_rib)
15         if i==4:
16             m1[i]=random.choice(thickness_stiffpanel)
17         if i==5:
18             m1[i]=random.choice(thickness_stiffpanel)
19     return m1
```

According to the literature (refer to subsection 2.4.1), the average number of mutations per mutating candidate is typically set to one. Therefore, considering that our individuals have six different variables, each variable should have a probability of mutation of  $\frac{1}{6}$ . This probability has been adopted in our case.

The two aforementioned processes prevent the optimization process from converging towards a local solution. They enable the exploration of the design space beyond the current locations of the solutions. However, when evaluating the quality of the new generation, if a new solution is found to be worse than the previous solution, the previous solution is retained among the Parents for the next Generation. This approach is implemented to prevent a decrease in the overall solution quality. Further details about this process will be elaborated on in chapter 6.

### Generation of the new population

Following the creation of 2 new solutions through cross-over and mutation of 2 Parents from the previous generation, the need arises to generate 5 new individuals from scratch to introduce potentially improved solutions. This is achieved by employing the **Initiate pop** function, previously described during the initialization step. In this case, only 5 new individuals are necessary to complete the generation and form a population of 10 individuals.

It's worth noting that among the 10 individuals in the new generation, 3 of them are identical to those from the previous generation (specifically the 3 Parents that were not involved in cross-over and mutation). Consequently, there is no need to conduct new Finite Element Analyses for these cases, and the results from the previous generation can be reused to avoid unnecessary simulations. Therefore, only 2 Parents (out of the 5) that underwent cross-over and mutation are required to generate their new .inp files. This approach helps conserve computational resources. Certainly, the utilization of the cluster resources can vary due to the shared nature of the infrastructure among TU Delft students. When all nodes are occupied, the simulations are placed in a queue, which can significantly extend the overall computational time. This uncertainty in execution time, influenced by the concurrent demands on the cluster, has inevitably affected the algorithm's speed.

Once the 7 new .inp files are prepared, the Genetic Algorithm loop (as depicted in Figure 5.10) returns to the Simulations step, using Abaqus on hpc12, and the process begins anew. This loop continues until the termination criterion is met: if there is no improvement in the best solutions found by a generation for 8 consecutive generations or after a total of 50 generations. The outcomes obtained through this process will be elaborated upon in the subsequent and final chapter of this report.

# Results of the Optimization

The progression of the Genetic Algorithm using a generation-by-generation approach is presented hereafter. The results of the first two generations of the algorithm with the fitness terms and the fitness function determination are presented in section 6.1, offering an overview of the evaluations carried out throughout the optimization process.

## 6.1. Presentation of the Genetic Algorithm results

Figure 6.1 shows the first two generations of the Genetic Algorithm. First, at the left of the first grey column, the variables (Ply number, ply orientation, cut-out, thickness of the ribs, thickness of the stiffeners of the panel and the ribs) of each individual are precised. Then, in between the two vertical grey columns, the weight, the buckling performance and the stiffness of each individual are given. They have been found accordingly to the method presented in section 5.1. Finally, at the right of the second grey column, the fitness function value of each individuals is given.

Then, as explained in subsection 5.2.4, based to the ten values of the fitness function of the first generations, the five best one are kept. These five best are highlighted in green in the fitness function column. These five individuals are the Parents of the next generation. Two of them, chosen randomly, are subjected to cross-over and mutation, has explained in subsection 5.2.4. These 2 Parents are highlighted in blue where the variables of each individuals are precised. Again, after assessing the fitness function with the weight, the buckling performance and the stiffness of each individual, the five best are kept to move on to the next generation.

	Nb Ply	Ply Orientation	Cut-out	T_rib mm	t_stiff-panel mm	t_stiff-rib mm	Weight kg	Relative Weight kg	Stiffness N/mm	Buckling N	Fitness Function	
1st Gen	indiv1	12	[0, 45, 30, 90, 60, 0, 0, 60, 90, 30, 45, 0]	0	3	1,59	1,59	55,20	44,80	82997,18	452771,84	103,05
	indiv2	12	[90, 60, 90, 60, 0, 45, 45, 0, 60, 90, 60, 90]	1	4	1,59	1,59	57,22	42,78	62893,47	394785,03	95,20
	indiv3	16	[60, 90, 0, 45, 90, 0, 60, 90, 90, 60, 0, 90, 45, 0, 90, 60]	0	2	1,59	1,59	55,95	44,05	63923,74	427051,46	98,39
	indiv4	14	[45, 90, 0, 90, 0, 45, 30, 30, 45, 0, 90, 0, 90, 45]	0	1,5	3	3,18	56,94	43,06	77187,40	441477,47	98,83
	indiv5	18	[0, 30, 90, 30, 90, 60, 90, 0, 45, 45, 0, 90, 60, 90, 30, 90, 30, 0]	0	4	1,59	1,59	66,44	33,56	63199,24	442727,00	79,75
	indiv6	16	[45, 60, 30, 60, 90, 60, 45, 0, 0, 45, 60, 90, 60, 30, 60, 45]	1	3	1,59	1,59	58,47	41,53	20773,47	423910,09	87,60
	indiv7	12	[60, 90, 60, 0, 30, 45, 45, 30, 0, 60, 90, 60]	0	2	1,59	3,18	52,76	47,24	64363,62	412758,72	103,84
	indiv8	12	[45, 30, 60, 45, 60, 90, 90, 60, 45, 60, 30, 45]	0	2	1,59	3,18	52,76	47,24	48324,58	360640,94	100,34
	indiv9	12	[90, 0, 60, 90, 0, 45, 45, 0, 90, 60, 0, 90]	0	1,5	1,59	3	50,56	49,44	0,00	0,00	89,00
	indiv10	12	[45, 0, 60, 45, 60, 0, 0, 60, 45, 60, 0, 45]	0	2	1,59	3,18	52,76	47,24	79551,54	414302,63	106,05
2nd Gen	indiv1	12	[0, 45, 30, 90, 60, 0, 0, 60, 90, 30, 45, 0]	0	3	1,59	1,59	55,20	44,80	82997,18	452771,84	103,05
	indiv2	16	[45, 60, 30, 45, 30, 90, 0, 60, 60, 0, 90, 30, 45, 30, 60, 45]	0	1,5	3	3	59,16	40,84	0,00	0,00	73,52
	indiv3	16	[45, 0, 60, 30, 60, 30, 0, 60, 60, 0, 30, 60, 30, 60, 0, 45]	0	1,5	3	3,18	59,34	40,66	76250,23	426887,78	94,04
	indiv4	14	[45, 90, 0, 90, 0, 45, 30, 30, 45, 0, 90, 0, 90, 45]	0	1,5	3	3,18	56,94	43,06	77187,40	441477,47	98,83
	indiv5	12	[60, 90, 60, 30, 45, 0, 0, 45, 30, 60, 90, 60]	0	3	3,18	3	60,93	39,07	63739,13	409346,81	88,99
	indiv6	16	[90, 45, 90, 30, 0, 45, 90, 0, 0, 90, 45, 0, 30, 90, 45, 90]	0	1,5	3,18	3	59,64	40,36	0,00	0,00	72,64
	indiv7	16	[45, 0, 60, 45, 30, 60, 45, 30, 30, 45, 60, 30, 45, 60, 0, 45]	1	4	3	3	67,25	32,75	68509,59	399791,78	78,07
	indiv8	12	[60, 90, 60, 0, 30, 45, 45, 30, 0, 60, 90, 60]	0	2	1,59	3,18	52,76	47,24	64363,62	412758,72	103,84
	indiv9	12	[90, 0, 60, 45, 90, 30, 30, 90, 45, 60, 0, 90]	1	2	1,59	3	51,56	48,44	21971,81	408356,06	99,84
	indiv10	12	[45, 0, 60, 45, 60, 0, 0, 60, 45, 60, 0, 45]	0	2	1,59	3,18	52,76	47,24	79551,54	414302,63	106,05

Figure 6.1: First two generations of the Genetic Algorithm.

Appendix A presents the results of all the simulations done throughout the optimization process. In

Appendix A, the process explained above is repeated until the termination criteria is met, leading to the convergence of the algorithm.

## 6.2. Optimal design obtained

The convergence of the optimization has been achieved at the 20<sup>th</sup> generation. It means that a total of 143 individuals (10 for the first generation and then 7 per generation) were studied. This represents 1430 hours (2 months) of simulation on Abaqus. The following termination criterion has been met:

- **Termination criterion met: No improvement of the fitness function for 8 generations.**
- A total of 50 generations

Indeed, observing the data from Figure 6.2, the optimization process converged. The fitness value of the best design in each generation remained unchanged for eight consecutive generations. This stability in the best solution over successive generations indicated convergence and marked the end of the optimization process (Further context on the significance of the red dotted lines can be found in subsection 6.3.1).

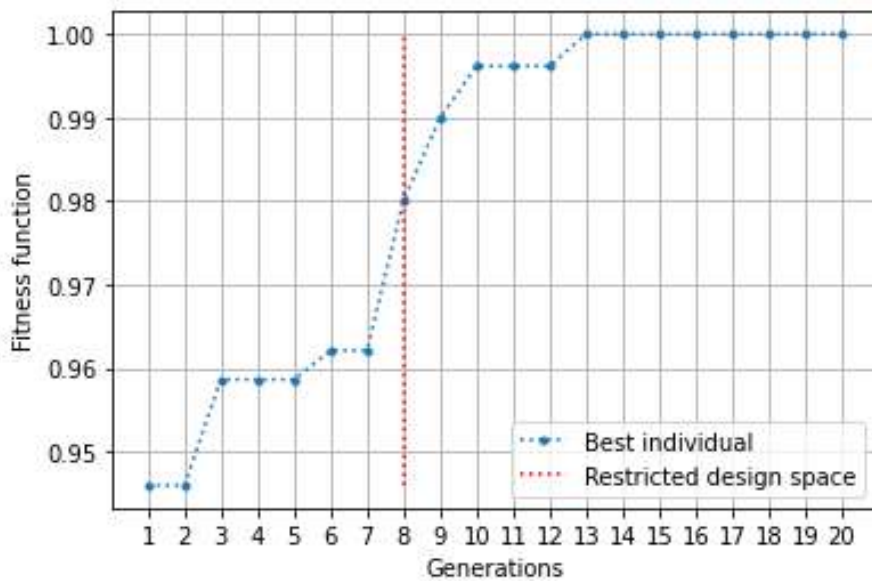


Figure 6.2: Fitness function through the generations, normalized to the final value

The optimal solution obtained upon meeting the termination criterion is as follows:

$N_{ply,i}$	$\theta_{ply,i,j}$	$t_{rib,k}$	$X_{cut-out}$	$t_{stiff,rib,l}$	$t_{stiff,panel,m}$
12	$[0/90/0/30/90/45]_s$	1,5	0	3,18	1,59

Table 6.1: Optimal design obtained with the simulation.

This configuration corresponds to simulation 2 presented in Table 5.3. As explained in Figure 5.1.2, while writing the report, three actual configurations were arbitrarily chosen from the array of configurations generated by the algorithm to serve as illustrative examples for the 4-point bending test results. These three configurations are individual 4 from generation 13 (simulation 1 in Table 5.3), individual 2 from generation 13 (simulation 2 in Table 5.3), and individual 10 from generation 13 (simulation 3 in Table 5.3). Later in the process, individual 2 from generation 13 emerged as the most optimal solution obtained, and remarkably, it maintained this status for a continuous span of eight generations, ultimately triggering the termination of the simulation. Consequently, this particular candidate has already been examined in subsection 5.1.2.

The load-displacement curve corresponding to the optimized solution obtained is depicted in Figure 6.3.

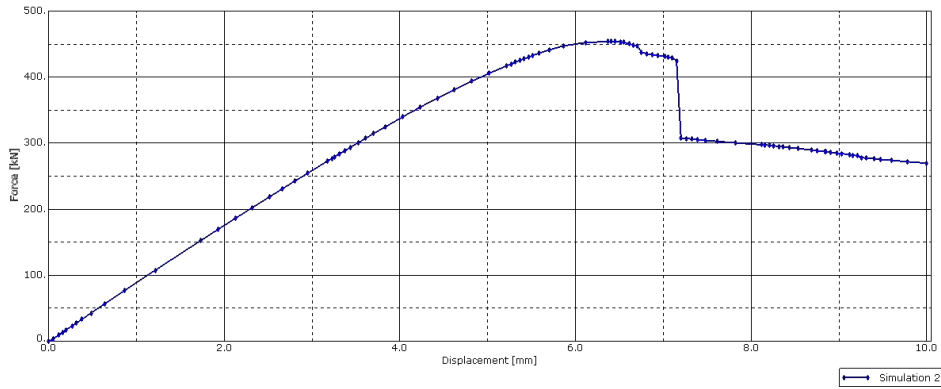


Figure 6.3: Load displacement curve of the optimal design obtained

Thanks to Figure 6.3, the buckling performance and the stiffness of the optimized design are found. In all the optimization process, the best fitness function value obtained is 112,11:

Weight [kg]	Stiffness [N/mm]	Buckling [N]	fitness function [-]	W% %	S% %	B% %
50.74	88928.0	460270.4	<b>112,11</b>	79.09	11,34	9,57

Table 6.2: Summary of the performance of the optimal design.

It exhibits the three phases as previously outlined in subsection 5.1.2: an initial linear relationship between load and displacement, followed by the appearance of buckling between the stiffeners in the bottom panel which leads to a plateau in the load, and ultimately, a sharp drop in load attributed to buckling in between the ribs of the structure. These three phases were previously illustrated with four distinct steps, and are once again visualized in Figure 6.4 below.

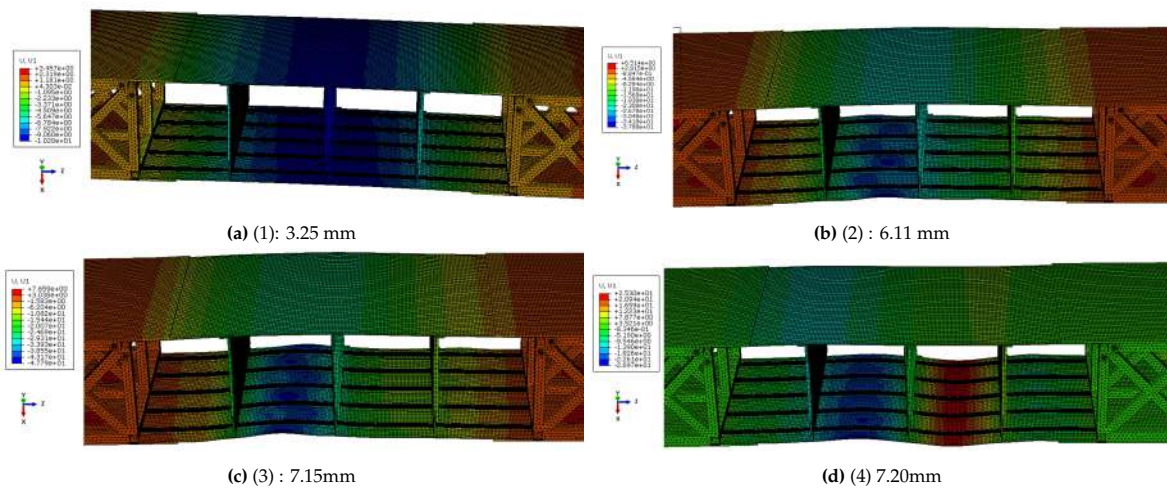


Figure 6.4: Vertical displacement through the simulation

Furthermore, as elaborated upon in Equation 4.1, one of the constraints is to prevent failure in the composite material. Therefore, it is imperative to verify this constraint using Hashin’s criteria, which have been integrated into Abaqus for this purpose. The selection of these criteria was made after section 3.2, following a thorough comparison with other available criteria within Abaqus. In Figure 6.5,

the various Hashin criteria for the optimized design are presented, focusing on the bottom test panel where the most critical values are observed.

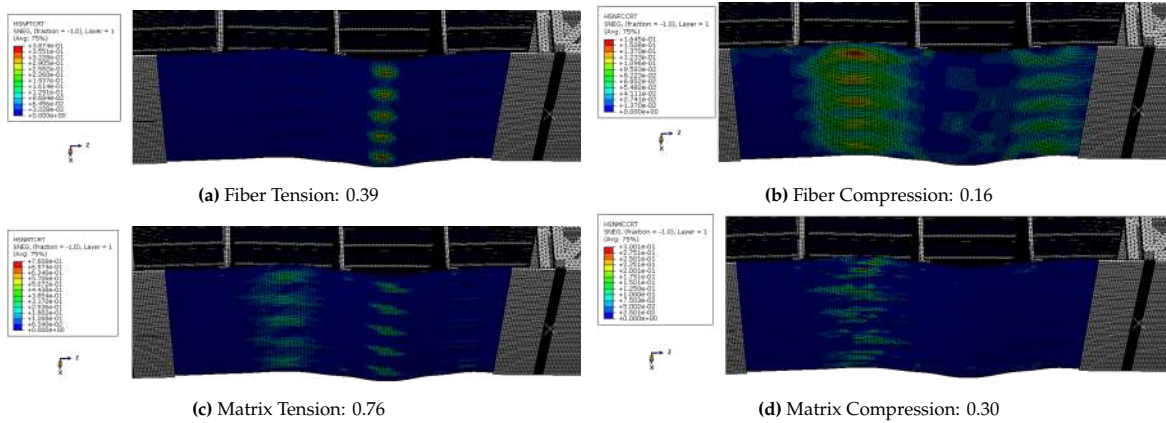


Figure 6.5: Hashin's criteria on the optimized structure

As demonstrated in Figure 6.5, none of the four Hashin's criteria surpass the critical value of 1. This indicates the absence of structural failure in the design, confirming that the constraint outlined in Equation 4.1 is indeed satisfied.

Figure 6.6 presents the out-of-plane stress distribution for the optimized structure. This visual representation highlights the buckling behavior of the structure, occurring between the stiffeners and the ribs, as illustrated in Figure 6.6. Furthermore, the maximum stress values are located in the bottom test panel.

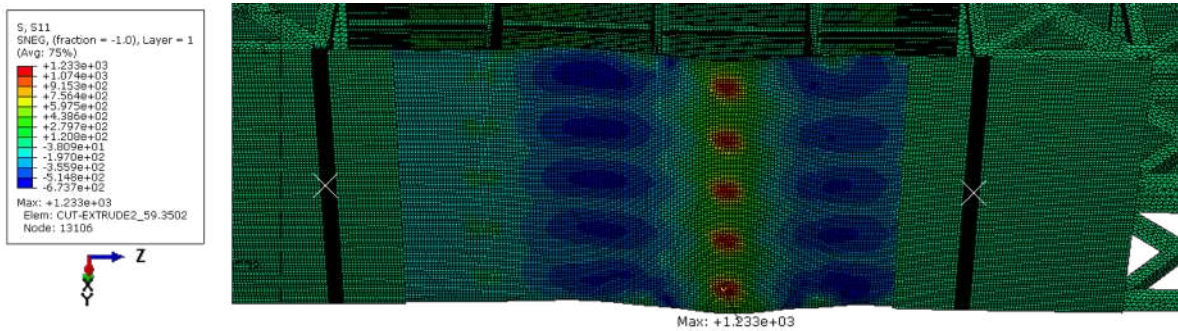


Figure 6.6: Out of plane stress of the bottom test panel

Moreover, the optimized solution and the baseline one introduced in subsection 4.1.3 and studied by Bisagni et al. in [1] are compared hereafter:

Configuration	$N_{ply,i}$	$\theta_{ply,i,j}$	$t_{rib,k}$	$X_{cut-out}$	$t_{stiff,rib,l}$	$t_{stiff,panel,m}$
Optimized	12	[0/90/0/30/90/45] <sub>s</sub>	1,5	0	3,18	1,59
Baseline	18	[45/0/45/0/90/0/45/0/45] <sub>s</sub>	3	0	3	3

Table 6.3: Optimized design compared to baseline design

Design	Weight [kg]	Stiffness [N/mm]	Buckling [N]	fitness function [-]	W% %	S% %	B% %
Optimized	50.74	88928.0	460270.4	<b>112,11</b>	79,09	11,34	9,57
Baseline	67.63	90328.6	472079.4	<b>82,19</b>	70,90	15,72	13,38

**Table 6.4:** Performance of the optimized design compared to the baseline design

The baseline design is too heavy compared to the optimized one. This is not surprising since his test panels have 18 plies, and his ribs, stiffeners of both panel and rib are too thick (equal to 3mm). The optimized solution is 16.89 kg lighter compared to the baseline configuration. This represents a significant 25% reduction in structure weight. Concerning the structural performance, the optimized solution is still close to the baseline configuration: a reduction of 14 kN/mm and 12 kN is observed for respectively the stiffness and the buckling performance. These reductions represent only 1.5% and 0.25% of the baseline value respectively.

### 6.3. Simulations details

An advantage of the generation-by-generation process utilized in running the Genetic Algorithm is the continuous access to the results of each generation while the algorithm is in progress. Unlike a single-code approach that generates generations in sequence until the termination criteria are satisfied, in the current method, each generation's quality can be assessed as it is produced. This allows for potential adjustments to the optimization rules, particularly for the termination criteria, which could be modified during the algorithm's runtime. Taking advantage of this flexibility, the termination criteria were decided while the algorithm was running, as detailed in subsection 6.3.2.

Furthermore, the ability to swiftly analyze the outcomes of each generation, made possible by the generation-by-generation process facilitated a refinement of the design space for quicker convergence. A more comprehensive explanation of this modification is provided below in subsection 6.3.1.

#### 6.3.1. Reduction of the design space

Running the algorithm for 8 generations took longer than anticipated. The congestion on the hpc12 cluster contributed to extended queue times. Despite utilizing nodes from asm-small and asm-medium queues with minimal queuing, there were instances where waiting times in the queue lasted for several days, as other users were also utilizing the resources.

Additionally, based on the results from the initial generations, it became evident that certain designs were inherently too heavy to perform well and achieve a favorable fitness function. While an increase in weight might occasionally lead to improvements in structural performance, such as stiffness and buckling performance, the gains from these factors were outweighed by the negative impact of increased weight on the fitness function. This situation can be observed in the excel sheet (refer to Appendix A). As an illustrative case, individual seven from the third generation can be examined: despite demonstrating excellent structural performance, this individual's fitness function remained low due to the design's excessive weight.

Considering the two aforementioned observations – the significant time spent waiting in the simulation queue on the cluster and the presence of a portion of the design space yielding overly heavy designs – a strategic adjustment was made to the optimization process following the seventh generation: narrowing down the range of variables under consideration in the design space. An analysis revealed that an increase of 2 ply in the panel configuration contributed to an additional 2.6 kg of weight, while a 1 mm increase in rib thickness resulted in a substantial 4.05 kg weight increase. Moreover, as shown by the comparison between the optimized and the baseline designs, weight is the most important factor of the optimization. Consequently, a decision was taken to refine the design space by excluding configurations involving 16 and 18 plies in the panels, as well as ribs with a thickness of 4 mm. The updated design space can be expressed as follows:

$$\begin{aligned}
\text{find } N_{ply,i} &= \{12, 14\}, \quad i = 1, 2 \\
\theta_{ply,i,j} &= \{0, 30, 45, 60, 90\}, \quad j = 1, 2, \dots, N_{ply,i} \\
t_{rib,k} &= \{1.5, 2, 3\}, [mm] \quad k = 1, 2, 3 \\
X_{cut-out} &= \{0, 1\} \\
t_{stiff,rib,l} &= \{1.59, 3, 3.18\}, [mm] \quad l = 1, 2, \dots, 15 \\
t_{stiff,panel,m} &= \{1.59, 3, 3.18\}, \quad m = 1, 2, \dots, 10
\end{aligned} \tag{6.1}$$

The design space refinement had a substantial impact on the optimization's convergence speed. Illustrated in Figure 6.2, the quality of the top candidate improved significantly after the 8<sup>th</sup> generation, indicating accelerated convergence toward the final solution. A more revealing insight can be gained from the evolution of the mean fitness function values across generations, as depicted in Figure 6.7. Post the 8<sup>th</sup> generation, the average fitness value exhibited a remarkable enhancement, consistently surpassing 96% of the final value. This enhancement can be attributed to the refined design space. By eliminating designs prone to excessive weight and inadequate fitness, the overall quality of each generation was uplifted. Notably, the lack of convergence in this context is expected due to the introduction of five new random candidates per generation. This dramatic shift in generation quality reinforces the choice made to reduce the design space.

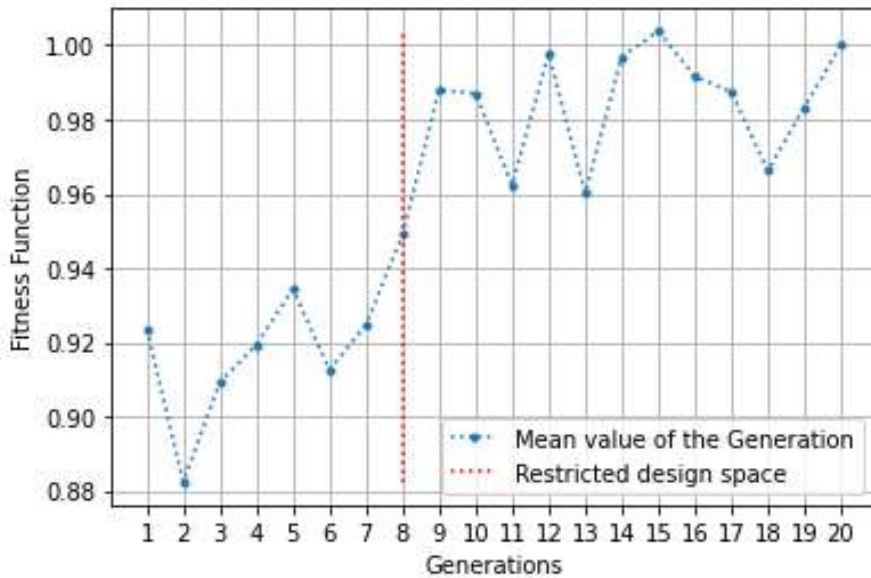


Figure 6.7: Mean value of the fitness function of each individual, per generation. Normalized to the value of the last generation.

To conclude this part, while one might argue that the reduction of the design space has limited the exploration and led to a local optimal solution, a closer look at the Appendix A dispels this notion. Notably, the highest observed stiffness value of 105038.00 N/mm (individual 4 in generation 10) and the top buckling performance of 484053.38 N (individual 1 in generation 17), both occurred after the reduction of the design space. This reduction did not prevent the discovery of solutions with great structural performance.

Moreover, when comparing these values to those of the optimized design, it becomes evident that the structural performance improvements are not significantly greater. In the case of stiffness, there is an increase of 15.1 kN/mm (equivalent to a 2.16 increment in the fitness function) compared to the optimized solution. As for buckling performance, the increase is 24 kN (equivalent to a 0.56 increment in the fitness function) relative to the optimized solution.

It is worth noting that these fitness function equivalents are substantial: a 2.16 increase in fitness function translates to a weight reduction of 1.2 kg, while a 0.56 increase corresponds to a 0.31 kg weight reduction. This underscores the lower priority of structural performance in the optimization process compared to

weight. As previously explained, adding just two more plies results in a substantial 2.6 kg increase (equivalent to a fitness function increase of 4.68), and a 1 mm increase in rib thickness leads to a heavier 4.05 kg gain (equivalent to a fitness function increase of 7.29). Hence, restricting the algorithm from exploring heavier solutions does not risk missing the optimal solution within the design space.

Terms	Optimized	Best solution	Difference in fitness function	Difference in weight
Stiffness	88928.0 N/mm	105038.0 N/mm	2.16	1.2 kg
Buckling	460270.4 N	484053,38 N	0.56	0.31 kg

Table 6.5: Evaluation of the impact of the structural performance on the fitness function.

### 6.3.2. Termination criteria

The generation-by-generation process provided the flexibility to adapt the termination criteria while the simulation was in progress. This criterion was determined based on the observed evolution of the fitness function as depicted in Figure 6.2, along with insights from various papers in the literature (e.g., Wang et al.[22], Shrivastava et al. [76], Albadr et al. [85], and those discussed in subsection 2.4.1). The fitness function initially demonstrates a gradual increase, and the reduction of the design space accelerates this progress. Subsequently, the fitness function remains the same for 8 consecutive generations, which represents 40% of the total number of generations. When focusing on the 5 selected "parents" retained between generations, this convergence phenomenon is even more evident. The evolution of the mean value of these 5 "parents" over generations is illustrated in Figure 6.8.

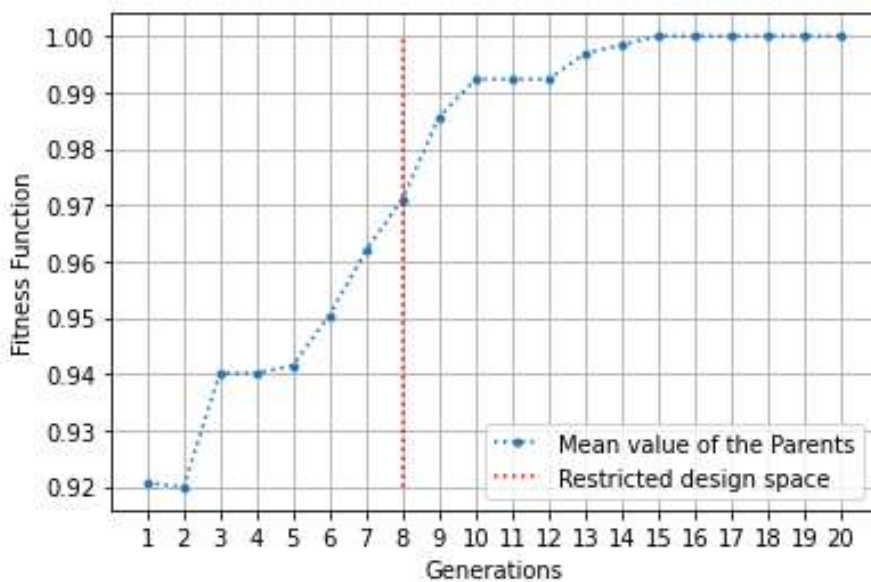


Figure 6.8: Mean value of the fitness function of the "parents", per generation. Normalized to the value of the last generation.

According to Figure 6.8, it becomes apparent that during the last 6 generations, no better "parents" were identified in comparison to those obtained from the 15<sup>th</sup> generation. This implies that none of the cross-overs, mutations, or introductions of new random individuals managed to produce a solution superior to the top 5 individuals obtained in the 15<sup>th</sup> generation. This signifies a definitive convergence achieved by the algorithm, characterized by the persistence of not just the best individual, but rather the consistent presence of the same top 5 individuals. This observation eliminates the possibility of a local optimal solution. The persistent failure of cross-over, mutations, or the introduction of new random individuals to generate superior solutions over several generations strongly suggests that no alternative solutions exist that could surpass the performance of those identified herein. The five "parents" along with their respective fitness values, are succinctly summarized below:



Fitness function	$N_{ply,i}$	$\theta_{ply,i,j}$	$t_{rib,k}$	$X_{cut-out}$	$t_{stiff,rib,l}$	$t_{stiff,panel,m}$
<b>112.11</b>	<b>12</b>	$[0/90/0/30/90/45]_s$	<b>1,5</b>	<b>0</b>	<b>3,18</b>	<b>1,59</b>
111.68	12	$[45/60/0/30/45/0]_s$	1,5	0	3,18	1,59
110.98	12	$[0/30/45/90/0/45]_s$	1,5	0	3,18	1,59
110.74	12	$[30/90/30/45/0/60]_s$	2	1	1.59	1,59
110.67	12	$[90/30/90/30/0/90]_s$	2	1	1.59	1,59

Table 6.6: 5 best designs obtained with the simulation.

These solutions fall into two distinct categories: one with no cut-outs, a rib thickness of 1.5mm, stiffeners of the ribs with a thickness of 3.18mm, and stiffeners of the panels with a thickness of 1.59mm. The other category involves solutions with cut-outs, resulting in slightly thicker ribs (2mm), but a consistent stiffener thickness of 1.59mm for both the ribs and the panels. All the solutions feature a composite panel with only 12 plies, however, the ply orientations of these laminates differ among the solutions. This observation strongly supports the idea that a globally optimal solution has been achieved. The presence of two distinct "types" of solutions within the top five indicates that alternative solutions get worse performances compared to these superior variants.

The three distinct plots presented previously have been gathered in Figure 6.9 to present the disparities in quality between the optimal solution, the parents, and the entire generation. This figure underscores the fact that the "Parents" consistently remain closely aligned with the best solution within each generation.

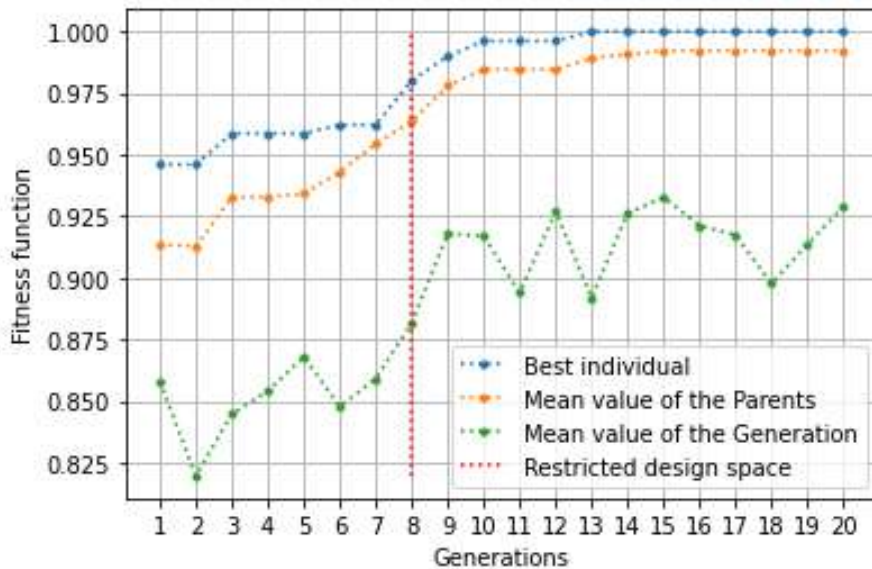


Figure 6.9: Summary of the fitness function evolution.

# 7

## Conclusion

### 7.1. Thesis overview

The primary objective of this thesis is the optimization of a composite wing component within the field of aerospace engineering. In pursuit of this goal, the central research question that guides the entire project is as follows:

**How can optimization using a Genetic Algorithm be used to reduce the weight of a composite wing component, while taking structural performance into account?.**

To address this research question, a detailed process has been executed and presented in this thesis. This process is succinctly summarized hereafter:

- **Chapter 2: Literature Study**

This chapter conducts an extensive literature study on composite wing structure analysis. It explores critical aspects such as failure criteria and design guidelines, laying the foundation for understanding the challenges faced in structural optimization. Additionally, the chapter examines the formulation of optimization problems, encompassing design variables, objectives, and constraints. It provides insights into various optimization types, including multi-objective, multi-level, multi-step, multi-fidelity, and probabilistic optimization, along with an analysis of frequently used optimization algorithms.

- **Chapter 3: Preliminary Analyses**

Chapter 3 focuses on preliminary analyses essential for the optimization process. It begins by examining coupon geometry and describes the materials used in the research, Aluminum 6063AT6 and USN150B Composite. Furthermore, it evaluates failure criteria, particularly Hashin's criteria, and compares them with other criteria available in Abaqus, helping to choose Hashin's criteria for the optimization. The chapter also investigates buckling behavior in plates and stiffened panels, offering crucial insights into structural responses under load.

- **Chapter 4: Optimization Strategy**

This chapter articulates the optimization strategy employed in the thesis. It starts by presenting the problem statement and introducing the structure under consideration. The optimization formulation is discussed, highlighting key design variables and the exploration of a cut-out configuration. The configuration studied by Bisagni et al. [1] is also presented as a baseline configuration for the optimization. Then, the Genetic Algorithm is introduced as the chosen optimization approach, paving the way for its implementation in subsequent chapters.

- **Chapter 5: Implementation of the Optimization**

Chapter 5 dives into the practical implementation of the optimization strategy. It details the determination of fitness functions, including weight, stiffness, and buckling behavior, critical for evaluating structural performance. The chapter outlines the process of conducting simulations to obtain structural data and explains the methodology behind determining weighing factors. It provides an in-depth look at the implementation of the Genetic Algorithm, covering initialization, simulations, and the selection process.

- **Chapter 6: Results of the Optimization**

The final chapter presents the results of the optimization efforts. First, it presents the different simulations developed to reach the convergence of the algorithm. Then, it showcases the optimal design achieved through the implemented methodology. A reduction of 16.89 kg has been achieved while maintaining great structural performance. The chapter provides specific insights into the simulations conducted, emphasizing the reduction of the design space and the termination criteria applied. By presenting these results, the chapter concludes the thesis.

A few major conclusions can be drawn from the detailed process described above.

First, according to the results obtained, the application of a Genetic Algorithm has demonstrated its effectiveness. While other optimization methods could yield favorable results, opting for the Genetic Algorithm (the most popular method in the literature, as discussed in Section subsection 2.4.1) has once again proven its merit.

Then, the inclusion of both stiffness and buckling behavior performance in the fitness function has been justified by the results obtained. This approach has resulted in a weight reduction of 16.89 kg (25% of the baseline value), offset by a marginal decrease of 14 kN/mm (1.5% of the baseline value) in stiffness and 12 kN (0.25% of the baseline value) in buckling performance. This outcome aligns with the intended goal of significantly reducing weight while preserving structural integrity. It's worth noting that such a substantial reduction may not always be realistic and should be validated across various testing cases to ensure its applicability.

Furthermore, exploring a cut-out configuration has unveiled new design possibilities. As depicted in Table 6.6, one of the two observed "types" of solutions incorporates cut-outs. While the optimized solution itself does not have cut-outs, this suggests that designs featuring cut-outs hold significant potential for weight reduction. Unfortunately, within the scope of this study, the introduction of cut-outs led to a decline in structural performance compared to the optimized solution. Nevertheless, for further weight reduction, configurations with cut-outs could be more investigated.

Finally, computational time constraints were encountered during the thesis. Given the extensive number of Abaqus simulations required, the utilization of the TU Delft hpc12 cluster was necessary for achieving convergence within the project timeline. Nevertheless, the process extended beyond expectations, taking over two months, primarily due to the restricted amount of computational power on the hpc12 cluster, computational power that is shared between all the users, leading to an unexpected delay in the project. This experience has underscored the importance of prudent planning in optimization endeavors, taking deadlines into account for a given project, and the necessity of efficient computational resource allocation.

## 7.2. Recommendations

To conclude this thesis, it is imperative to consider potential recommendations that can further enhance the field of aerospace structural optimization.

Firstly, it is recommended to explore more optimization algorithms and methodologies. While this thesis focused on a Genetic Algorithm, there are numerous emerging techniques such as machine learning-based optimization, hybrid algorithms, and surrogate modeling that could offer improved efficiency and accuracy. Some of these techniques have been presented in the literature study chapter (such as the probabilistic optimizations in subsection 2.3.5 and need a deeper focus to understand their potential in structural optimization.

Secondly, expanding the optimization problem's complexity could be beneficial. This could involve incorporating additional design variables, constraints, or objectives, reflecting the intricate nature of real-world aerospace projects. As an example, the number of ribs was not a variable considered in this study. However, considering a design with only two ribs leads to a reduction in the structure's weight. Nevertheless, an examination of the implications of such a reduction on factors like stiffness, buckling resistance, and overall structural integrity needs to be conducted. Future research could delve into optimizing rib placement and quantity while considering these critical performance factors. Exploring the incorporation of Double-Double composite stacking sequences among the available possibilities is another intriguing idea for research (see subsection 2.2.1). This idea warrants further investigation to assess its potential impact on the optimization process and the resulting structural performance of

aerospace components.

Additionally, the incorporation of Multi-Disciplinary Optimization (MDO) approaches should be considered. This would involve optimizing not only the structural aspects but also considering aerodynamics, propulsion, and other critical factors simultaneously. During the literature study phase of this thesis, plenty of articles focused on multidisciplinary optimization approaches. These articles highlighted the potential of combining objectives from various disciplines to achieve optimal structural designs. This integrated approach enables the simultaneous consideration of multiple objectives from multiple disciplines.

In conclusion, by implementing these recommendations, future research in aerospace structural optimization can contribute to the development of even more efficient and lighter aircraft designs.

# References

- [1] C. Bisagni, A. Raimondo, I. Atanasovska, *et al.*, "Comparison of numerical analyses of a composite wing component subjected to 4-point bending," *Composites Part C: Open Access*, vol. 8, p. 100264, Jul. 1, 2022, issn: 2666-6820. doi: 10.1016/j.jcomc.2022.100264.
- [2] Eurocontrol, a european civil-military organisation dedicated to supporting European aviation. "Aviation outlook 2050." (2022), [Online]. Available: <https://www.eurocontrol.int/forecasting>.
- [3] "The contribution of global aviation to anthropogenic climate forcing for 2000 to 2018," *Atmospheric Environment*, vol. 244, p. 117834, Jan. 1, 2021, Publisher: Pergamon, issn: 1352-2310. doi: 10.1016/j.atmosenv.2020.117834.
- [4] D.-G. Choi, S.-Y. Lee, J.-H. Roh, and J.-S. Bae, "Optimal design of a spar cross-section for fabric-covered wind turbine blades," *International Journal of Aeronautical and Space Sciences*, vol. 21, no. 3, pp. 647–656, Sep. 1, 2020, issn: 2093-2480. doi: 10.1007/s42405-019-00240-y.
- [5] N. Gupta, K. Nair, and K. Sekar, "STRUCTURAL ANALYSIS OF AIRCRAFTS WING MADE UP OF COMPOSITE USING FINITE ELEMENT MODELLING," Ph. D., Department of Mechanical Engineering NATIONAL INSTITUTE OF TECHNOLOGY CALICUT, May 1, 2018. doi: 10.13140/RG.2.2.33089.28003.
- [6] S. Dutton, D. Kelly, and A. Baker, "Composite materials for aircraft structures, second edition," *AIAA Journal*, 2004.
- [7] L. Lanzi and C. Bisagni, "Minimum weight optimization of composite stiffened panels using neural networks," *44th AIAA/ASME/ASCE/AHS/ASC Structures, Structural Dynamics, and Materials Conference*, 2003. doi: 10.2514/6.2003-1698.
- [8] "Cost website." (2023), [Online]. Available: <https://www.cost.eu/> (visited on 08/30/2023).
- [9] "Odin cost action website." (2023), [Online]. Available: <https://odin-cost.com/> (visited on 08/31/2023).
- [10] C. Kassapoglou, *DESIGN AND ANALYSIS OF COMPOSITE STRUCTURES : WITH APPLICATIONS TO AEROSPACE STRUCTURES*, second edition. Jan. 1, 2013.
- [11] J. K. S. Dillinger, "Static aeroelastic optimization of composite wings with variable stiffness laminates," Ph. D., DLR–Institute of Aeroelasticity, Delft University of Technology, 2014.
- [12] C. Kassapoglou, "7 - stiffness & strength of composite structural elements," in *Polymer Composites in the Aerospace Industry (Second Edition)*, ser. Woodhead Publishing Series in Composites Science and Engineering, P. Irving and C. Soutis, Eds., Woodhead Publishing, Jan. 1, 2020, pp. 147–193, isbn: 978-0-08-102679-3. doi: 10.1016/B978-0-08-102679-3.00007-1.
- [13] Q. Ren, X. Wang, S. Shi, Y. Ma, J. Wang, and X. Ding, "Structural static/fatigue/damage tolerance comprehensive design optimization of composite laminate," *AIAA Journal*, vol. 60, no. 2, pp. 998–1012, Feb. 2022, issn: 0001-1452, 1533-385X. doi: 10.2514/1.J060020.
- [14] O. Bacarreza, M. Aliabadi, and A. Apicella, "Robust design and optimization of composite stiffened panels in post-buckling," *Structural and Multidisciplinary Optimization*, vol. 51, Jul. 30, 2014. doi: 10.1007/s00158-014-1136-5.
- [15] M. Bashir, S. Longtin-Martel, N. Zonzini, R. M. Botez, A. Ceruti, and T. Wong, "Optimization and design of a flexible droop nose leading edge morphing wing based on a novel black widow optimization (b.w.o.) algorithm—part II," *Designs*, vol. 6, no. 6, p. 102, Dec. 2022, Number: 6 Publisher: Multidisciplinary Digital Publishing Institute, issn: 2411-9660. doi: 10.3390/designs6060102.

- [16] J. T. Ricco, R. F. F. Coimbra, and G. F. Gomes, "Multiobjective optimization of the LASER aircraft wing's composite structural design," *Aircraft Engineering and Aerospace Technology*, vol. 93, no. 6, pp. 995–1010, Aug. 12, 2021, ISSN: 1748-8842, 1748-8842. DOI: 10.1108/AEAT-06-2020-0113.
- [17] W. Zhao, M. Jrad, R. Gupta, and R. K. Kapania, "Multidisciplinary design analysis and optimization of performance adaptive aeroelastic wings," in *AIAA Atmospheric Flight Mechanics Conference*, Grapevine, Texas: American Institute of Aeronautics and Astronautics, Jan. 9, 2017, ISBN: 978-1-62410-448-0. DOI: 10.2514/6.2017-1392.
- [18] S. Shrivastava, N. Sharma, S. W. Tsai, and P. M. Mohite, "D and DD-drop layup optimization of aircraft wing panels under multi-load case design environment," *Composite Structures*, vol. 248, p. 112518, Sep. 15, 2020, ISSN: 0263-8223. DOI: 10.1016/j.compstruct.2020.112518.
- [19] E. I. Basri, M. T. H. Sultan, A. A. Basri, F. Mustapha, and K. A. Ahmad, "Consideration of lamination structural analysis in a multi-layered composite and failure analysis on wing design application," *Materials*, vol. 14, no. 13, p. 3705, Jan. 2021, Number: 13 Publisher: Multidisciplinary Digital Publishing Institute, ISSN: 1996-1944. DOI: 10.3390/ma14133705.
- [20] F. Li, S. Zhang, and W. Cheng, "Application and optimization of wing structure design of DF-2 light sports aircraft based on composite material characteristics," *Journal of Nanomaterials*, vol. 2022, 2022, ISSN: 1687-4110. DOI: 10.1155/2022/6967016.
- [21] D. Rajpal, C. Kassapoglou, and R. De Breuker, "Aeroelastic optimization of composite wings including fatigue loading requirements," *Composite Structures*, vol. 227, p. 111 248, Nov. 1, 2019, ISSN: 0263-8223. DOI: 10.1016/j.compstruct.2019.111248.
- [22] Z. Wang, Z. Wan, R. Groh, and X. Wang, "Aeroelastic and local buckling optimisation of a variable-angle-tow composite wing-box structure," *Composite Structures*, vol. 258, 2021, ISSN: 0263-8223. DOI: 10.1016/j.compstruct.2020.113201.
- [23] R. Hill and R. Hill, *The Mathematical Theory of Plasticity* (Oxford Classic Texts in the Physical Sciences). Oxford, New York: Oxford University Press, Aug. 6, 1998, 368 pp., ISBN: 978-0-19-850367-5.
- [24] M. C. Blair and T. T. Takahashi, "Optimal composite structural design of unmanned aerial system wings," in *AIAA AVIATION 2022 Forum*, Chicago, IL & Virtual: American Institute of Aeronautics and Astronautics, Jun. 27, 2022, ISBN: 978-1-62410-635-4. DOI: 10.2514/6.2022-4009.
- [25] K. Bramsiepe, A. Voß, and T. Klimmek, "Design and sizing of an aeroelastic composite model for a flying wing configuration with maneuver, gust, and landing loads," *CEAS Aeronautical Journal*, vol. 11, no. 3, pp. 677–691, Sep. 1, 2020, ISSN: 1869-5590. DOI: 10.1007/s13272-020-00446-x.
- [26] K. Sinha, T. Klimmek, M. Schulze, and V. Handoyo, "Loads analysis and structural optimization of a high aspect ratio, composite wing aircraft," *CEAS Aeronautical Journal*, vol. 12, Feb. 7, 2021. DOI: 10.1007/s13272-021-00494-x.
- [27] F. Sousa Vicente, "Stacking sequence retrieval of large composite structures in bi-step optimization strategies using mechanical constraints," Ph.D. dissertation, 2019.
- [28] D. Liu, V. V. Toropov, D. C. Barton, and O. M. Querin, "Weight and mechanical performance optimization of blended composite wing panels using lamination parameters," *Structural and Multidisciplinary Optimization*, vol. 52, no. 3, pp. 549–562, Sep. 1, 2015, ISSN: 1615-1488. DOI: 10.1007/s00158-015-1244-x.
- [29] D. Liu, V. V. Toropov, O. M. Querin, and D. C. Barton, "Bilevel optimization of blended composite wing panels," *Journal of Aircraft*, vol. 48, no. 1, pp. 107–118, Jan. 2011, ISSN: 0021-8669, 1533-3868. DOI: 10.2514/1.C000261.
- [30] E. Barkanov, E. Eglitis, F. Almeida, M. C. Bowering, and G. Watson, "Weight optimal design of lateral wing upper covers made of composite materials," *Engineering Optimization*, vol. 48, no. 9, pp. 1618–1637, Sep. 1, 2016, ISSN: 0305-215X, 1029-0273. DOI: 10.1080/0305215X.2015.1128422.
- [31] S. Guo, D. Li, and Y. Liu, "Multi-objective optimization of a composite wing subject to strength and aeroelastic constraints," *Proceedings of the Institution of Mechanical Engineers, Part G: Journal of Aerospace Engineering*, vol. 226, no. 9, pp. 1095–1106, Sep. 1, 2012, Publisher: IMECHE, ISSN: 0954-4100. DOI: 10.1177/0954410011417789.

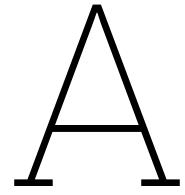
- [32] M. Bin Kamarudin, J. Mohamed Ali, A. Aabid, and Y. Ibrahim, "Buckling analysis of a thin-walled structure using finite element method and design of experiments," *Aerospace*, vol. 9, no. 10, 2022, issn: 2226-4310. doi: 10.3390/aerospace9100541.
- [33] F. Lima and W. Amorim Jr, "Structural analysis of a composite wing spar for a light sporting aircraft," Ph. D. UNIVERSIDADE FEDERAL DE CAMPINA GRANDE, May 10, 2019.
- [34] F. Michaud, H. Dalir, and S. Joncas, "Structural design and optimization of an aircraft morphing wing: Composite skin," *Journal of Aircraft*, vol. 55, no. 1, pp. 195–211, Jan. 2018, issn: 0021-8669, 1533-3868. doi: 10.2514/1.C034340.
- [35] R. R. dos Santos, T. G. d. P. Machado, and S. G. P. Castro, "Support vector machine applied to the optimal design of composite wing panels," *Aerospace*, vol. 8, no. 11, p. 328, Nov. 2021, Number: 11 Publisher: Multidisciplinary Digital Publishing Institute, issn: 2226-4310. doi: 10.3390/aerospace8110328.
- [36] S. Tsai, J. Melo, S. Sihn, A. Arteiro, and R. Rainsberger, *Composite Laminates: Theory and Practice of Analysis, Design and Automated Layout*. Stanford Aeronautics & Astronautics, 2017, isbn: 978-0-9860845-3-9.
- [37] S. W. Tsai, "Double-double: New family of composite laminates," *AIAA Journal*, vol. 59, no. 11, pp. 4293–4305, Nov. 2021, issn: 0001-1452, 1533-385X. doi: 10.2514/1.J060659.
- [38] Z. Zhang, Z. Zhang, F. Di Caprio, and G. X. Gu, "Machine learning for accelerating the design process of double-double composite structures," *Composite Structures*, vol. 285, p. 115233, Apr. 1, 2022, issn: 0263-8223. doi: 10.1016/j.compstruct.2022.115233.
- [39] O. Stodieck, J. E. Cooper, P. M. Weaver, and P. Kealy, "Aeroelastic tailoring of a representative wing box using tow-steered composites," *AIAA Journal*, vol. 55, no. 4, pp. 1425–1439, Apr. 2017, Publisher: American Institute of Aeronautics and Astronautics, issn: 0001-1452. doi: 10.2514/1.J055364.
- [40] E. Cestino, G. Frulla, P. Piana, and R. Duella, "Numerical/experimental validation of thin-walled composite box beam optimal design," *Aerospace*, vol. 7, no. 8, p. 111, Aug. 2020, Number: 8 Publisher: Multidisciplinary Digital Publishing Institute, issn: 2226-4310. doi: 10.3390/aerospace7080111.
- [41] B. Liu and R. Haftka, "Composite wing structural design optimization with continuity constraints," in *19th AIAA Applied Aerodynamics Conference*, ser. Fluid Dynamics and Co-located Conferences, American Institute of Aeronautics and Astronautics, Jun. 11, 2001. doi: 10.2514/6.2001-1205.
- [42] B. Kristinsdottir, Z. Zabinsky, M. Tuttle, and S. Neogi, "Optimal design of large composite panels with varying loads," *Composite Structures*, vol. 51, pp. 93–102, Jan. 31, 2001. doi: 10.1016/S0263-8223(00)00128-8.
- [43] G. Soremekun, Z. Gürdal, C. Kassapoglou, and D. Toni, "Stacking sequence blending of multiple composite laminates using genetic algorithms," *Composite Structures*, vol. 56, no. 1, pp. 53–62, Apr. 1, 2002, issn: 0263-8223. doi: 10.1016/S0263-8223(01)00185-4.
- [44] D. Adams, L. Watson, Z. Gurdal, and C. Anderson-Cook, "Genetic algorithm optimization and blending of composite laminates by locally reducing laminate thickness," *Advances in Engineering Software*, vol. 35, pp. 35–43, Jan. 31, 2004. doi: 10.1016/j.advengsoft.2003.09.001.
- [45] N. J. W. Tsai Stephen W.; Pagano, "AD. 668 761 INVARIANT PROPERTIES OF COMPOSITE MATERIALS," *Air Force Materials Laboratory*,
- [46] T. Macquart, V. Maes, M. T. Bordogna, A. Pirrera, and P. M. Weaver, "Optimisation of composite structures – enforcing the feasibility of lamination parameter constraints with computationally-efficient maps," *Composite Structures*, vol. 192, pp. 605–615, May 15, 2018, issn: 0263-8223. doi: 10.1016/j.compstruct.2018.03.049.
- [47] C. Scarth and J. Cooper, "Reliability-based aeroelastic design of composite plate wings using a stability margin," *Structural and Multidisciplinary Optimization*, vol. 57, no. 4, pp. 1695–1709, 2018, issn: 1615-147X. doi: 10.1007/s00158-017-1838-6.
- [48] Y. Meddaikar, J. Dillinger, G. Silva, and R. De Breuker, "Skin panel optimization of the common research model wing using sandwich composites," *Journal of Aircraft*, vol. 59, no. 2, pp. 386–399, 2022, issn: 0021-8669. doi: 10.2514/1.C036551.

- [49] C. Scarth, P. N. Sartor, J. E. Cooper, P. M. Weaver, and G. H. C. Silva, "Robust and reliability-based aeroelastic design of composite plate wings," *AIAA Journal*, vol. 55, no. 10, pp. 3539–3552, Oct. 2017, ISSN: 0001-1452, 1533-385X. DOI: 10.2514/1.J055829.
- [50] J. K. S. Dillinger, T. Klimmek, M. M. Abdalla, and Z. Gürdal, "Stiffness optimization of composite wings with aeroelastic constraints," *Journal of Aircraft*, vol. 50, no. 4, pp. 1159–1168, Jul. 2013, ISSN: 0021-8669, 1533-3868. DOI: 10.2514/1.C032084.
- [51] B. Liu and R. Haftka, "Single-level composite wing optimization based on flexural lamination parameters," *Structural and Multidisciplinary Optimization*, vol. 26, no. 1, pp. 111–120, Jan. 1, 2004, ISSN: 1615-1488. DOI: 10.1007/s00158-003-0315-6.
- [52] F. Toffol and S. Ricci, "A meta-model for composite wingbox sizing in aircraft conceptual design," *Composite Structures*, vol. 306, p. 116 557, Feb. 15, 2023, ISSN: 0263-8223. DOI: 10.1016/j.compstruct.2022.116557.
- [53] R. Kirubakaran, L. Dhakshinamurthy, S. Rajkumar, and A. Rajendran, "Aircraft wing weight optimization by composite material structure design configuration," *IOSR Journal of Mechanical and Civil Engineering*, vol. 14, pp. 71–80, Dec. 5, 2017. DOI: 10.9790/1684-1406027180.
- [54] S. Kumar, N. Hunsur, and S. Kumar, "Structural design and FE analysis of fixed wing for improved strength and weight characteristics," *Huazhong Keji Daxue Xuebao (Ziran Kexue Ban)/Journal of Huazhong University of Science and Technology (Natural Science Edition)*, vol. 20, p. 10, Jun. 21, 2021.
- [55] L. Zhang, D. Ma, M. Yang, X. Xia, and Y. Yao, "Optimization and analysis of composite sandwich box beam for solar drones," *Chinese Journal of Aeronautics*, vol. 34, no. 10, pp. 148–165, Oct. 1, 2021, ISSN: 1000-9361. DOI: 10.1016/j.cja.2020.10.023.
- [56] D. Stamatelos and G. Labeas, "Towards the design of a multispar composite wing," *Computation*, vol. 8, p. 24, Apr. 9, 2020. DOI: 10.3390/computation8020024.
- [57] D. Locatelli, S. Mulani, and R. Kapania, "Supersonic wing box weight optimization using curvilinear spars and ribs," in *51st AIAA/ASME/ASCE/AHS/ASC Structures, Structural Dynamics, and Materials Conference & 18th AIAA/ASME/AHS Adaptive Structures Conference & 12th*, Orlando, Florida: American Institute of Aeronautics and Astronautics, Apr. 12, 2010, ISBN: 978-1-60086-961-7. DOI: 10.2514/6.2010-2673.
- [58] K. Bramsiepe, T. Klimmek, W.-R. Krüger, and L. Tichy, "Aeroelastic method to investigate nonlinear elastic wing structures," *CEAS Aeronautical Journal*, vol. 13, Aug. 29, 2022. DOI: 10.1007/s13272-022-00596-0.
- [59] P. W. Aung, O. Tatarnikov, and N. L. Aung, "Structural optimization of a light aircraft composite wing," *IOP Conference Series: Materials Science and Engineering*, vol. 709, no. 4, p. 044 094, Jan. 1, 2020, ISSN: 1757-8981, 1757-899X. DOI: 10.1088/1757-899X/709/4/044094.
- [60] J. Sodja, N. P. M. Werter, and R. De Breuker, "Aeroelastic demonstrator wing design for maneuver load alleviation under cruise shape constraint," *Journal of Aircraft*, vol. 58, no. 3, pp. 448–466, May 2021, ISSN: 1533-3868. DOI: 10.2514/1.C035955.
- [61] M. Kalantari, C. Dong, and I. J. Davies, "Multi-objective robust optimisation of unidirectional carbon/glass fibre reinforced hybrid composites under flexural loading," *Composite Structures*, vol. 138, pp. 264–275, Mar. 15, 2016, ISSN: 0263-8223. DOI: 10.1016/j.compstruct.2015.11.034.
- [62] Y. Wang, X. Ouyang, H. Yin, and X. Yu, "Structural-optimization strategy for composite wing based on equivalent finite element model," *Journal of Aircraft*, vol. 53, no. 2, pp. 351–359, Mar. 2016, ISSN: 0021-8669, 1533-3868. DOI: 10.2514/1.C033469.
- [63] Z. Chen, S. Zhu, C. Feng, and C. Liu, "Multi-objective optimization design and analysis of large deformation composite material," *Journal of Physics: Conference Series*, vol. 2383, no. 1, p. 012 110, Dec. 1, 2022, ISSN: 1742-6588, 1742-6596. DOI: 10.1088/1742-6596/2383/1/012110.
- [64] G. Molinari, A. F. Arrieta, and P. Ermanni, "Aero-structural optimization of three-dimensional adaptive wings with embedded smart actuators," *AIAA Journal*, vol. 52, no. 9, pp. 1940–1951, Sep. 2014, ISSN: 0001-1452, 1533-385X. DOI: 10.2514/1.J052715.
- [65] S. Guo, "Aeroelastic optimization of an aerobatic aircraft wing structure," *Aerospace Science and Technology*, vol. 11, no. 5, pp. 396–404, Jun. 1, 2007, ISSN: 1270-9638. DOI: 10.1016/j.ast.2007.01.003.



- [66] O. Dababneh and T. Kipouros, "Influence of high fidelity structural models on the predicted mass of aircraft wing using design optimization," *Aerospace Science and Technology*, vol. 79, pp. 164–173, 2018, ISSN: 1270-9638. DOI: 10.1016/j.ast.2018.05.043.
- [67] R. Marler and J. Arora, "Survey of multi-objective optimization methods for engineering," *Structural and Multidisciplinary Optimization*, vol. 26, no. 6, pp. 369–395, Apr. 1, 2004, ISSN: 1615-147X, 1615-1488. DOI: 10.1007/s00158-003-0368-6.
- [68] E. Zitzler, M. Laumanns, and L. Thiele, "SPEA2: Improving the strength pareto evolutionary algorithm," ETH Zurich, Report, May 2001, Accepted: 2022-08-12T12:06:45Z Publication Title: TIK Report Volume: 103. DOI: 10.3929/ethz-a-004284029.
- [69] J. Knowles and D. Corne, *The Pareto Archived Evolution Strategy: A New Baseline Algorithm for Pareto Multiobjective Optimisation*. Jan. 1, 1999, vol. 1, Journal Abbreviation: Proceedings of the 1999 Congress on Evolutionary Computation, CEC 1999 Publication Title: Proceedings of the 1999 Congress on Evolutionary Computation, CEC 1999. DOI: 10.1109/CEC.1999.781913.
- [70] K. Deb, A. Pratap, S. Agarwal, and T. Meyarivan, "A fast and elitist multiobjective genetic algorithm: NSGA-II," *IEEE Transactions on Evolutionary Computation*, vol. 6, no. 2, pp. 182–197, Apr. 2002, Conference Name: IEEE Transactions on Evolutionary Computation, ISSN: 1941-0026. DOI: 10.1109/4235.996017.
- [71] K. A. Yoo, O. Bacarreza, and M. Aliabadi, "Multi-fidelity robust design optimisation for composite structures based on low-fidelity models using successive high-fidelity corrections," *Composite Structures*, vol. 259, p. 113477, Dec. 1, 2020. DOI: 10.1016/j.compstruct.2020.113477.
- [72] H. Farokhi, O. Bacarreza, and M. Aliabadi, "Probabilistic optimisation of mono-stringer composite stiffened panels in post-buckling regime," *Structural and Multidisciplinary Optimization*, vol. 62, Sep. 1, 2020. DOI: 10.1007/s00158-020-02565-9.
- [73] B. Liu, R. Haftka, and M. Akgun, "Two-level composite wing structural optimization using response surfaces," *Structural and Multidisciplinary Optimization*, vol. 20, pp. 87–96, Oct. 1, 2000. DOI: 10.1007/s001580050140.
- [74] Q. Zhao, Y. Ding, and H. Jin, "A layout optimization method of composite wing structures based on carrying efficiency criterion," *Chinese Journal of Aeronautics - CHIN J AERONAUT*, vol. 24, pp. 425–433, Aug. 1, 2011. DOI: 10.1016/S1000-9361(11)60050-2.
- [75] S. Grihon, E. Burnaev, M. Belyaev, and P. Prikhodko, "Surrogate modeling of stability constraints for optimization of composite structures," in *Surrogate-Based Modeling and Optimization: Applications in Engineering*, S. Koziel and L. Leifsson, Eds., New York, NY: Springer, 2013, pp. 359–391, ISBN: 978-1-4614-7551-4. DOI: 10.1007/978-1-4614-7551-4\_15.
- [76] S. Shrivastava, H. Tilala, P. M. Mohite, and M. D. Limaye, "Weight optimization of a composite wing-panel with flutter stability constraints by ply-drop," *Structural and Multidisciplinary Optimization*, vol. 62, no. 4, pp. 2181–2195, Oct. 2020, ISSN: 1615-147X, 1615-1488. DOI: 10.1007/s00158-020-02569-5.
- [77] A. Kafkas, S. Kilimtzidis, A. Kotzakolios, V. Kostopoulos, and G. Lampeas, "Multi-fidelity optimization of a composite airliner wing subject to structural and aeroelastic constraints," *Aerospace*, vol. 8, no. 12, p. 398, Dec. 2021, Number: 12 Publisher: Multidisciplinary Digital Publishing Institute, ISSN: 2226-4310. DOI: 10.3390/aerospace8120398.
- [78] G. J. Kennedy and J. R. R. A. Martins, "A parallel finite-element framework for large-scale gradient-based design optimization of high-performance structures," *Finite Elements in Analysis and Design*, vol. 87, pp. 56–73, Sep. 15, 2014, ISSN: 0168-874X. DOI: 10.1016/j.finel.2014.04.011.
- [79] W. Yang, Z. Yue, L. Li, and P. Wang, "Aircraft wing structural design optimization based on automated finite element modelling and ground structure approach," *Engineering Optimization*, vol. 48, pp. 1–21, Jan. 9, 2015. DOI: 10.1080/0305215X.2014.995175.
- [80] C. Bisagni and M. Alfano, "A probabilistic approach for buckling analysis of sandwich composite cylindrical shells," *23rd Conference of the Italian Association of Aeronautics and Astronautics (AIDAA 2015)At: Torino, Italy*, Jan. 2015.

- [81] S. Winyangkul, S. Slesongsom, and S. Bureerat, "Reliability-based design of an aircraft wing using a fuzzy-based metaheuristic," *Applied Sciences*, vol. 11, no. 14, p. 6463, Jan. 2021, Number: 14 Publisher: Multidisciplinary Digital Publishing Institute, issn: 2076-3417. doi: 10.3390/app11146463.
- [82] S. Nikbakt, S. Kamarian, and M. Shakeri, "A review on optimization of composite structures part i: Laminated composites," *Composite Structures*, vol. 195, pp. 158–185, Jul. 2018, issn: 02638223. doi: 10.1016/j.compstruct.2018.03.063.
- [83] K. Wansasueb, S. Bureerat, and S. Kumar, "Ensemble of four metaheuristic using a weighted sum technique for aircraft wing design," *Engineering and Applied Science Research*, vol. 48, p. 385 396, 2021, Publisher: Faculty of Engineering, Khon Kaen University. doi: 10.14456/EASR.2021.41.
- [84] P. T. Vasseur, "Optimization strategy for conceptual airplane design," Ph. D., faculty of Aerospace Engineering, Delft University of Technology, 2014.
- [85] M. A. Albadr, S. Tiun, M. Ayob, and F. AL-Dhief, "Genetic algorithm based on natural selection theory for optimization problems," *Symmetry*, vol. 12, no. 11, p. 1758, Nov. 2020, Number: 11 Publisher: Multidisciplinary Digital Publishing Institute, issn: 2073-8994. doi: 10.3390/sym12111758.
- [86] C. Bisagni and R. Vescovini, "Fast tool for buckling analysis and optimization of stiffened panels," *Journal of aircraft*, vol. 46, no. 6, 2009. doi: 10.2514/1.43396.
- [87] R. Vescovini and C. Bisagni, "Buckling analysis and optimization of stiffened composite flat and curved panels," *AIAA journal*, vol. 50, no. 4, 2012. doi: 10.2514/1.J051356.
- [88] M. J. Kalinowski, "Structural optimization of box wing aircraft," *Archive of Mechanical Engineering*, vol. 62, no. 1, pp. 45–60, Mar. 1, 2015, issn: 2300-1895. doi: 10.1515/meceng-2015-0003.
- [89] L. Le, H.-B. Ly, B. Pham, *et al.*, "Hybrid artificial intelligence approaches for predicting buckling damage of steel columns under axial compression," *Materials*, vol. 12, p. 1670, May 22, 2019. doi: 10.3390/ma12101670.
- [90] V. Hayyolalam and A. A. Pourhaji Kazem, "Black widow optimization algorithm: A novel metaheuristic approach for solving engineering optimization problems," *Engineering Applications of Artificial Intelligence*, vol. 87, p. 103 249, Jan. 1, 2020, issn: 0952-1976. doi: 10.1016/j.engappai.2019.103249.
- [91] M. Schlüter, J. A. Egea, and J. R. Banga, "Extended ant colony optimization for non-convex mixed integer nonlinear programming," *Computers & Operations Research*, vol. 36, no. 7, pp. 2217–2229, Jul. 1, 2009, issn: 0305-0548. doi: 10.1016/j.cor.2008.08.015.
- [92] H. Eskandar, A. Sadollah, A. Bahreininejad, and M. Hamdi, "Water cycle algorithm – a novel metaheuristic optimization method for solving constrained engineering optimization problems," *Computers & Structures*, vol. 110-111, p. 151, 2012, issn: 0045-7949.
- [93] "Abaqus manual." (2023), [Online]. Available: <http://130.149.89.49:2080/v6.11/books/usb/default.htm?startat=pt05ch23s03abm45.html> (visited on 08/15/2023).
- [94] "Abaqus manual: Damage initiation." (2023), [Online]. Available: <http://130.149.89.49:2080/v6.11/books/usb/default.htm?startat=pt05ch23s03abm44.html#usb-mat-cdamagein itfibercomposite> (visited on 08/15/2023).
- [95] J. Zhang, "Numerical investigation of buckling-driven mechanisms for shape morphing of composite wings," Master Thesis, faculty of Aerospace Engineering, Delft University of Technology, 2020.
- [96] C. K. J. Dharmendra P, "Design and analysis of an aircraft wing rib for different configurations," *International Research Journal of Engineering and Technology*, vol. 7, 2020.
- [97] L. Morse, L. Cartabia, and V. Mallardo, "Reliability-based bottom-up manufacturing cost optimisation for composite aircraft structures," *Structural and Multidisciplinary Optimization*, vol. 65, no. 5, p. 159, May 12, 2022, issn: 1615-1488. doi: 10.1007/s00158-022-03250-9.
- [98] "Hpc12 cluster guide." (2023), [Online]. Available: <https://gitlab.tudelft.nl/hpc12/training/-/blob/main/sections/Getting-started.md> (visited on 08/14/2023).



# Appendix A : Genetic Algorithm Results

	Nb Ply	Ply Orientation	Cut-out	T_rib mm	t_stiff-panel mm	t_stiff-rib mm	Weight kg	Relative Weight kg	Stiffness N/mm	Buckling N	Fitness Function	Keep previous	
1st Gen	indiv1	12	[0, 45, 30, 90, 60, 0, 0, 60, 90, 30, 45, 0]	0	3	1,59	1,59	55,20	44,80	82997,18	452771,84	103,05	
	indiv2	12	[90, 60, 90, 60, 0, 45, 45, 0, 60, 90, 60, 90]	1	4	1,59	1,59	57,22	42,78	62893,47	394785,03	95,20	
	indiv3	16	[60, 90, 0, 45, 90, 0, 60, 90, 90, 60, 0, 90, 45, 0, 90, 60]	0	2	1,59	1,59	55,95	44,05	63923,74	427051,46	98,39	
	indiv4	14	[45, 90, 0, 90, 0, 45, 30, 30, 45, 0, 90, 0, 90, 45]	0	1,5	3	3,18	56,94	43,06	77187,40	441477,47	98,83	
	indiv5	18	[0, 30, 90, 30, 90, 60, 90, 0, 45, 45, 0, 90, 60, 90, 30, 90, 30, 0]	0	4	1,59	1,59	66,44	33,56	63199,24	442727,00	79,75	
	indiv6	16	[45, 60, 30, 60, 90, 60, 45, 0, 0, 45, 60, 90, 60, 30, 60, 45]	1	3	1,59	1,59	58,47	41,53	20773,47	423910,09	87,60	
	indiv7	12	[60, 90, 60, 0, 30, 45, 45, 30, 0, 60, 90, 60]	0	2	1,59	3,18	52,76	47,24	64363,62	412758,72	103,84	
	indiv8	12	[45, 30, 60, 45, 60, 90, 90, 60, 45, 60, 30, 45]	0	2	1,59	3,18	52,76	47,24	48324,58	360640,94	100,34	
	indiv9	12	[90, 0, 60, 90, 0, 45, 45, 0, 90, 60, 0, 90]	0	1,5	1,59	3	50,56	49,44	0,00	0,00	89,00	
	indiv10	12	[45, 0, 60, 45, 60, 0, 0, 60, 45, 60, 0, 45]	0	2	1,59	3,18	52,76	47,24	79551,54	414302,63	106,05	
2nd Gen	indiv1	12	[0, 45, 30, 90, 60, 0, 0, 60, 90, 30, 45, 0]	0	3	1,59	1,59	55,20	44,80	82997,18	452771,84	103,05	
	indiv2	16	[45, 60, 30, 45, 30, 90, 0, 60, 60, 0, 90, 30, 45, 30, 60, 45]	0	1,5	3	3	59,16	40,84	0,00	0,00	73,52	
	indiv3	16	[45, 0, 60, 30, 60, 30, 0, 60, 60, 0, 30, 60, 30, 60, 0, 45]	0	1,5	3	3,18	59,34	40,66	76250,23	426887,78	94,04	
	indiv4	14	[45, 90, 0, 90, 0, 45, 30, 30, 45, 0, 90, 0, 90, 45]	0	1,5	3	3,18	56,94	43,06	77187,40	441477,47	98,83	
	indiv5	12	[60, 90, 60, 30, 45, 0, 0, 45, 30, 60, 90, 60]	0	3	3,18	3	60,93	39,07	63739,13	409346,81	88,99	
	indiv6	16	[90, 45, 90, 30, 0, 45, 90, 0, 0, 90, 45, 0, 30, 90, 45, 90]	0	1,5	3,18	3	59,64	40,36	0,00	0,00	72,64	
	indiv7	16	[45, 0, 60, 45, 30, 60, 45, 30, 30, 45, 60, 30, 45, 60, 0, 45]	1	4	3	3	67,25	32,75	68509,59	399791,78	78,07	
	indiv8	12	[60, 90, 60, 0, 30, 45, 45, 30, 0, 60, 90, 60]	0	2	1,59	3,18	52,76	47,24	64363,62	412758,72	103,84	
	indiv9	12	[90, 0, 60, 45, 90, 30, 30, 90, 45, 60, 0, 90]	1	2	1,59	3	51,56	48,44	21971,81	408356,06	99,84	
	indiv10	12	[45, 0, 60, 45, 60, 0, 0, 60, 45, 60, 0, 45]	0	2	1,59	3,18	52,76	47,24	79551,54	414302,63	106,05	
3rd Gen	indiv1	12	[0, 60, 0, 30, 45, 90, 90, 45, 30, 0, 60, 0]	0	2	1,59	1,59	51,15	48,85	71457,63	400517,09	107,47	
	indiv2	16	[30, 60, 90, 45, 60, 90, 30, 0, 0, 30, 90, 60, 45, 90, 60, 30]	0	1,5	3	3	59,16	40,84	0,00	0,00	73,52	
	indiv3	14	[0, 30, 45, 90, 0, 45, 90, 90, 45, 0, 90, 45, 30, 0]	0	1,5	1,59	3,18	53,14	46,86	77874,01	437187,56	105,68	
	indiv4	14	[45, 90, 0, 90, 0, 45, 30, 30, 45, 0, 90, 0, 90, 45]	0	1,5	3	3,18	56,94	43,06	77187,40	441477,47	98,83	
	indiv5	18	[60, 30, 60, 45, 30, 45, 0, 30, 90, 90, 30, 0, 45, 30, 45, 60, 30, 60]	1	4	3	3	69,64	30,36	68769,04	408471,91	73,99	
	indiv6	16	[60, 0, 90, 0, 45, 30, 45, 90, 90, 45, 30, 45, 0, 90, 0, 60]	1	1,5	1,59	3	54,59	45,41	0,00	0,00	81,74	
	indiv7	16	[0, 90, 45, 0, 30, 60, 30, 0, 0, 30, 60, 30, 0, 45, 90, 0]	1	3	1,59	3,18	60,08	39,92	94145,46	459980,56	96,04	
	indiv8	12	[60, 90, 60, 0, 30, 45, 45, 30, 0, 60, 90, 60]	0	2	1,59	3,18	52,76	47,24	64363,62	412758,72	103,84	
	indiv9	12	[90, 0, 60, 45, 90, 30, 30, 90, 45, 60, 0, 90]	1	2	1,59	3	51,56	48,44	21971,81	408356,06	99,84	
	indiv10	12	[45, 30, 90, 0, 45, 0, 0, 45, 0, 90, 30, 45]	0	3	1,59	1,59	55,20	44,80	71511,59	468011,56	101,76	106,5
4th Gen	indiv1	12	[0, 60, 0, 30, 45, 90, 90, 45, 30, 0, 60, 0]	0	2	1,59	1,59	51,15	48,85	71457,63	400517,09	107,47	
	indiv2	12	[90, 60, 30, 60, 90, 0, 0, 90, 60, 30, 60, 90]	0	3	3,18	3,18	61,11	38,89	58101,91	411283,13	87,90	
	indiv3	14	[0, 30, 45, 90, 0, 45, 90, 90, 45, 0, 90, 45, 30, 0]	0	3	1,59	1,59	57,60	42,40	79490,60	441692,03	97,98	105,68
	indiv4	16	[30, 45, 90, 60, 0, 45, 30, 60, 60, 30, 45, 0, 60, 90, 45, 30]	1	4	3,18	3	67,73	32,27	63299,60	412569,00	76,75	
	indiv5	18	[0, 90, 30, 0, 90, 0, 45, 90, 30, 30, 90, 45, 0, 90, 0, 30, 90, 0]	1	2	3	3,18	62,74	37,26	87887,63	464445,66	90,45	
	indiv6	14	[30, 45, 30, 45, 30, 90, 60, 60, 90, 30, 45, 30, 45, 30]	1	4	1,59	3,18	61,23	38,77	58337,65	375918,59	86,90	

indiv7	14	[30, 0, 45, 0, 30, 90, 60, 60, 90, 30, 0, 45, 0, 30]	1	4	1,59	3	61,04	38,96	86104,84	435584,66	92,58	
indiv8	12	[60, 90, 60, 0, 30, 45, 45, 30, 0, 60, 90, 60]	0	2	1,59	3,18	52,76	47,24	64363,62	412758,72	103,84	
indiv9	12	[90, 0, 60, 45, 90, 30, 30, 90, 45, 60, 0, 90]	1	2	1,59	3	51,56	48,44	21971,81	408356,06	99,84	
indiv10	12	[45, 0, 60, 45, 60, 0, 0, 60, 45, 60, 0, 45]	0	3	1,59	3,18	56,81	43,19	71511,59	468011,56	98,86	106,5

5th Gen

indiv1	12	[0, 60, 0, 30, 45, 90, 90, 45, 30, 0, 60, 0]	0	3	3,18	1,59	59,50	40,50	86174,81	449165,59	95,69	107,47
indiv2	18	[0, 30, 60, 45, 0, 30, 60, 30, 90, 90, 30, 60, 30, 0, 45, 60, 30, 0]	1	3	3	3,18	66,28	33,72	80079,28	430659,81	82,17	
indiv3	14	[0, 30, 45, 90, 0, 45, 90, 90, 45, 0, 90, 45, 30, 0]	0	1,5	1,59	3,18	53,14	46,86	77874,01	437187,56	105,68	
indiv4	14	[60, 30, 0, 60, 0, 45, 90, 90, 45, 0, 60, 0, 30, 60]	1	3	1,59	1,59	56,07	43,93	81175,28	426074,59	100,60	
indiv5	14	[45, 30, 45, 0, 60, 0, 45, 45, 0, 60, 0, 45, 30, 45]	0	3	1,59	3	59,03	40,97	76476,08	421059,94	94,50	
indiv6	16	[45, 0, 90, 30, 0, 45, 60, 90, 90, 60, 45, 0, 30, 90, 0, 45]	1	2	3	3	60,16	39,84	34339,90	440092,41	86,87	
indiv7	14	[30, 0, 60, 30, 0, 45, 90, 90, 45, 0, 30, 60, 0, 30]	1	1,5	1,59	3	52,19	47,81	0,00	0,00	86,06	
indiv8	12	[60, 90, 60, 0, 30, 45, 45, 30, 0, 60, 90, 60]	0	2	1,59	3,18	52,76	47,24	64363,62	412758,72	103,84	
indiv9	12	[90, 0, 60, 45, 90, 30, 30, 90, 45, 60, 0, 90]	1	2	1,59	3	51,56	48,44	21971,81	408356,06	99,84	
indiv10	12	[30, 60, 90, 0, 60, 90, 90, 60, 0, 90, 60, 30]	0	2	1,59	1,59	51,15	48,85			87,92	post pone next Gen

6th Gen

indiv1	12	[0, 90, 0, 30, 90, 45, 45, 90, 30, 0, 90, 0]	0	2	1,59	3,18	52,76	47,24	84409,47	424247,72	106,98	107,47
indiv2	18	[45, 30, 0, 60, 45, 0, 30, 0, 45, 45, 0, 30, 0, 45, 60, 0, 30, 45]	0	3	3,18	3,18	68,30	31,70	86552,91	435567,72	79,59	
indiv3	14	[0, 30, 45, 90, 0, 45, 90, 90, 45, 0, 90, 45, 30, 0]	0	1,5	1,59	3,18	53,14	46,86	77874,01	437187,56	105,68	
indiv4	14	[60, 30, 0, 60, 0, 45, 90, 90, 45, 0, 60, 0, 30, 60]	1	3	1,59	1,59	56,07	43,93	81175,28	426074,59	100,60	
indiv5	16	[60, 0, 30, 60, 30, 90, 60, 30, 30, 60, 90, 30, 60, 30, 0, 60]	1	2	1,59	3,18	56,54	43,46	0,00	0,00	78,23	
indiv6	12	[90, 30, 45, 90, 45, 0, 0, 45, 90, 45, 30, 90]	1	1,5	3,18	1,59	52,66	47,34	0,00	0,00	85,21	
indiv7	18	[30, 45, 30, 45, 30, 90, 0, 45, 30, 30, 45, 0, 90, 30, 45, 30, 45, 30]	0	1,5	3	3,18	61,74	38,26	69790,12	399601,88	88,17	
indiv8	12	[60, 90, 60, 0, 30, 45, 45, 30, 0, 60, 90, 60]	0	2	1,59	1,59	51,15	48,85	67405,84	405153,44	107,00	
indiv9	14	[45, 60, 30, 60, 90, 30, 0, 0, 30, 90, 60, 30, 60, 45]	0	3	1,59	3	59,03	40,97	50766,97	413838,69	90,65	
indiv10	12	[30, 60, 90, 0, 60, 90, 90, 60, 0, 90, 60, 30]	0	2	1,59	1,59	51,15	48,85	68803,94	433374,91	107,86	

7th Gen

indiv1	12	[0, 60, 0, 30, 45, 90, 90, 45, 30, 0, 60, 0]	0	2	1,59	1,59	51,15	48,85	71457,63	400517,09	107,47	
indiv2	12	[0, 90, 0, 30, 90, 45, 45, 90, 30, 0, 90, 0]	0	2	1,59	3,18	52,76	47,24	84409,47	424247,72	106,98	
indiv3	14	[0, 30, 45, 90, 0, 45, 90, 90, 45, 0, 90, 45, 30, 0]	0	1,5	1,59	3,18	53,14	46,86	77874,01	437187,56	105,68	
indiv4	18	[30, 90, 60, 45, 0, 45, 30, 0, 30, 30, 0, 30, 45, 0, 45, 60, 90, 30]	1	2	3	1,59	61,13	38,87	0,00	0,00	69,96	
indiv5	12	[45, 90, 30, 60, 90, 45, 45, 90, 60, 30, 90, 45]	0	2	3,18	1,59	55,45	44,55	50340,46	359147,56	95,76	
indiv6	14	[90, 0, 60, 90, 30, 90, 45, 45, 90, 30, 90, 60, 0, 90]	1	4	1,59	3,18	61,23	38,77	61151,42	415830,56	88,23	
indiv7	14	[45, 30, 60, 30, 90, 30, 45, 45, 30, 90, 30, 60, 30, 45]	1	1,5	3	3,18	56,18	43,82	25073,29	374658,38	91,19	
indiv8	12	[30, 60, 90, 0, 60, 90, 90, 60, 0, 90, 60, 30]	0	2	1,59	1,59	51,15	48,85	68803,94	433374,91	107,86	107
indiv9	16	[90, 60, 45, 60, 90, 45, 0, 45, 45, 0, 45, 90, 60, 45, 60, 90]	0	1,5	1,59	1,59	53,92	46,08	0,00	0,00	82,94	
indiv10	12	[60, 90, 60, 0, 30, 45, 45, 30, 0, 60, 90, 60]	0	1,5	1,59	1,59	49,13	50,87	0,00	0,00	91,57	107,86

range in the code

8th Gen	indiv1	12	[0, 60, 0, 30, 45, 90, 90, 45, 30, 0, 60, 0]	0	2	1,59	1,59	51,15	48,85	80457,63	448517,09	109,88	
---------	--------	----	--	---	---	------	------	-------	-------	----------	-----------	--------	--

indiv2	12	[0, 90, 0, 30, 90, 45, 45, 90, 30, 0, 90, 0]	0	2	1,59	1,59	51,15	48,85	83474,00	415567,72	109,54
indiv3	14	[0, 30, 45, 90, 0, 45, 90, 90, 45, 0, 90, 45, 30, 0]	0	1,5	1,59	3,18	53,14	46,86	78874,01	437187,56	105,82
indiv4	12	[0, 30, 90, 45, 60, 90, 90, 60, 45, 90, 30, 0]	1	2	3	1,59	53,94	46,06	84711,56	415850,38	104,70
indiv5	14	[30, 90, 30, 0, 30, 0, 45, 45, 0, 30, 0, 30, 90, 30]	0	3	3,18	1,59	61,89	38,11	0,00	0,00	68,59
indiv6	14	[0, 60, 90, 30, 0, 30, 0, 0, 30, 0, 30, 90, 60, 0]	0	2	3	1,59	57,36	42,64	73272,00	415830,56	96,92
indiv7	14	[45, 60, 90, 45, 30, 60, 0, 0, 60, 30, 45, 90, 60, 45]	1	2	1,59	3	53,96	46,04	62079,55	374658,38	100,48
indiv8	12	[60, 90, 60, 0, 30, 45, 45, 30, 0, 60, 90, 60]	0	2	1,59	1,59	51,15	48,85	67405,84	405153,44	107,00
indiv9	12	[30, 90, 45, 60, 0, 60, 60, 0, 60, 45, 90, 30]	0	2	3,18	3	56,88	43,12	0,00	0,00	77,62
indiv10	12	[30, 60, 90, 0, 60, 90, 90, 60, 0, 90, 60, 30]	0	2	1,59	3,18	52,76	47,24	0,00	0,00	85,02

107,86

9th Gen

indiv1	12	[0, 60, 0, 30, 45, 90, 90, 45, 30, 0, 60, 0]	0	2	1,59	1,59	51,15	48,85	80457,63	448517,09	109,88
indiv2	12	[0, 90, 0, 30, 90, 45, 45, 90, 30, 0, 90, 0]	0	2	1,59	1,59	51,15	48,85	83474,00	415567,72	109,54
indiv3	12	[60, 0, 60, 90, 45, 0, 0, 45, 90, 60, 0, 60]	0	2	1,59	1,59	51,15	48,85	79050,00	459128,94	109,92
indiv4	12	[45, 90, 45, 60, 90, 0, 0, 90, 60, 45, 90, 45]	1	1,5	1,59	1,59	48,37	51,63	0,00	0,00	92,94
indiv5	14	[0, 45, 60, 30, 90, 30, 90, 90, 30, 90, 30, 60, 45, 0]	1	1,5	1,59	3	52,19	47,81	0,00	0,00	86,06
indiv6	14	[90, 60, 45, 60, 30, 0, 45, 45, 0, 30, 60, 45, 60, 90]	1	3	1,59	3	57,50	42,50	81286,00	427994,94	98,09
indiv7	14	[90, 30, 60, 30, 90, 60, 45, 45, 60, 90, 30, 60, 30, 90]	1	1,5	1,59	3,18	52,37	47,63	70522,00	409659,06	105,36
indiv8	12	[0, 30, 45, 90, 0, 45, 45, 0, 90, 45, 30, 0]	0	1,5	1,59	3,18	50,74	49,26	90392,00	402803,25	110,98
indiv9	12	[30, 45, 90, 60, 0, 45, 45, 0, 60, 90, 45, 30]	1	2	1,59	3,18	51,75	48,25	74250,00	409951,00	107,03
indiv10	12	[30, 60, 90, 0, 60, 90, 90, 60, 0, 90, 60, 30]	0	2	1,59	1,59	51,15	48,85	68803,94	433374,91	107,86

10th Gen

indiv1	12	[0, 60, 0, 30, 45, 90, 90, 45, 30, 0, 60, 0]	0	2	1,59	1,59	51,15	48,85	80457,63	448517,09	109,88
indiv2	12	[0, 90, 0, 30, 90, 45, 45, 90, 30, 0, 90, 0]	0	2	1,59	1,59	51,15	48,85	87474,00	435567,72	110,58
indiv3	12	[45, 60, 0, 30, 45, 0, 0, 45, 30, 0, 60, 45]	0	1,5	1,59	3,18	50,74	49,26	90072,00	434890,09	111,68
indiv4	14	[90, 0, 30, 0, 60, 0, 60, 60, 0, 60, 0, 30, 0, 90]	1	3	1,59	1,59	56,07	43,93	105038,00	431862,50	104,15
indiv5	14	[30, 0, 30, 60, 90, 60, 0, 0, 60, 90, 60, 30, 0, 30]	1	3	1,59	3,18	57,68	42,32	83768,00	425462,44	98,06
indiv6	12	[45, 0, 30, 0, 60, 90, 90, 60, 0, 30, 0, 45]	1	2	1,59	3,18	51,75	48,25	90744,00	429236,50	109,83
indiv7	14	[30, 45, 60, 30, 45, 0, 90, 90, 0, 45, 30, 60, 45, 30]	1	1,5	1,59	1,59	50,76	49,24	0,00	0,00	88,63
indiv8	12	[60, 0, 45, 0, 90, 45, 45, 90, 0, 45, 0, 60]	0	2	1,59	1,59	51,15	48,85	79540,00	440620,81	109,56
indiv9	14	[30, 45, 30, 90, 60, 0, 45, 45, 0, 60, 90, 30, 45, 30]	1	1,5	1,59	3	52,19	47,81	0,00	0,00	86,06
indiv10	12	[30, 60, 90, 0, 60, 90, 90, 60, 0, 90, 60, 30]	0	2	1,59	1,59	51,15	48,85	68803,94	433374,91	107,86

110,98

11th Gen

indiv1	12	[0, 60, 0, 30, 45, 90, 90, 45, 30, 0, 60, 0]	0	2	1,59	1,59	51,15	48,85	80457,63	448517,09	109,88
indiv2	12	[0, 90, 0, 30, 90, 45, 45, 90, 30, 0, 90, 0]	0	2	1,59	3,18	52,76	47,24	86882,00	464247,72	108,26
indiv3	12	[45, 60, 0, 30, 45, 0, 0, 45, 30, 0, 60, 45]	0	1,5	1,59	3,18	50,74	49,26	90072,00	434890,09	111,68
indiv4	14	[45, 60, 0, 45, 0, 90, 30, 30, 90, 0, 45, 0, 60, 45]	1	3	1,59	1,59	56,07	43,93	86562,00	433351,94	101,54
indiv5	12	[90, 30, 60, 30, 45, 0, 0, 45, 30, 60, 30, 90]	1	1,5	3	3	53,60	46,40	0,00	0,00	83,52
indiv6	12	[90, 0, 60, 0, 90, 60, 60, 90, 0, 60, 0, 90]	1	2	3	1,59	53,94	46,06	83612,00	43079,14	95,86
indiv7	12	[60, 45, 90, 30, 90, 60, 60, 90, 30, 90, 45, 60]	1	3	3,18	1,59	57,97	42,03	55000,00	323282,84	91,05
indiv8	12	[0, 30, 45, 90, 0, 45, 45, 0, 90, 45, 30, 0]	0	1,5	1,59	3,18	50,74	49,26	90392,00	402803,25	110,98
indiv9	12	[30, 0, 45, 60, 90, 45, 45, 90, 60, 45, 0, 30]	0	1,5	1,59	3	50,56	49,44	0,00	0,00	89,00

110,58

109,83

indiv10	14	[90, 30, 0, 60, 45, 60, 0, 0, 60, 45, 60, 0, 30, 90]	1	2	1,59	1,59	52,53	47,47	85428,00	15707,06	98,02
---------	----	--	---	---	------	------	-------	-------	----------	----------	-------

12th Gen	indiv1	12	[0, 60, 0, 30, 45, 90, 90, 45, 30, 0, 60, 0]	1	2	1,59	3,18	51,75	48,25	90970,00	134202,44	102,99	109,88
	indiv2	12	[0, 90, 0, 30, 90, 45, 45, 90, 30, 0, 90, 0]	0	2	1,59	1,59	51,15	48,85	87474,00	435567,72	110,58	
	indiv3	12	[45, 60, 0, 30, 45, 0, 0, 45, 30, 0, 60, 45]	0	1,5	1,59	3,18	50,74	49,26	90072,00	434890,09	111,68	
	indiv4	14	[0, 90, 30, 45, 60, 0, 45, 45, 0, 60, 45, 30, 90, 0]	0	2	3	3,18	58,97	41,03	77780,00	457484,09	95,64	
	indiv5	14	[30, 0, 90, 45, 30, 60, 45, 45, 60, 30, 45, 90, 0, 30]	1	2	1,59	3,18	54,14	45,86	91812,00	454745,16	106,27	
	indiv6	12	[45, 0, 30, 0, 60, 90, 90, 60, 0, 30, 0, 45]	1	2	1,59	3,18	51,75	48,25	90744,00	429236,50	109,83	
	indiv7	14	[45, 60, 0, 90, 0, 45, 60, 60, 45, 0, 90, 0, 60, 45]	0	1,5	1,59	1,59	51,53	48,47	0,00	0,00	87,25	110,98
	indiv8	12	[0, 30, 45, 90, 0, 45, 45, 0, 90, 45, 30, 0]	0	3	1,59	1,59	55,20	44,80	79540,00	440620,81	102,27	
	indiv9	12	[90, 45, 60, 0, 90, 30, 30, 90, 0, 60, 45, 90]	1	3	1,59	1,59	53,68	46,32	74274,00	412223,03	103,61	
	indiv10	12	[90, 45, 0, 30, 60, 45, 45, 60, 30, 0, 45, 90]	1	3	3,18	1,59	57,97	42,03	69152,00	382266,59	94,45	

13th Gen	indiv1	12	[0, 60, 0, 30, 45, 90, 90, 45, 30, 0, 60, 0]	0	2	1,59	1,59	51,15	48,85	80457,63	448517,09	109,88	110,98
	indiv2	12	[0, 90, 0, 30, 90, 45, 45, 90, 30, 0, 90, 0]	0	1,5	1,59	3,18	50,74	49,26	88928,00	460270,41	112,11	
	indiv3	12	[45, 60, 0, 30, 45, 0, 0, 45, 30, 0, 60, 45]	0	1,5	1,59	3,18	50,74	49,26	90072,00	434890,09	111,68	
	indiv4	14	[90, 0, 30, 45, 60, 30, 90, 90, 30, 60, 45, 30, 0, 90]	0	2	3,18	3,18	59,45	40,55	75930,00	422771,00	93,69	
	indiv5	14	[45, 60, 30, 90, 30, 60, 45, 45, 60, 30, 90, 30, 60, 45]	1	2	1,59	1,59	52,53	47,47	57840,00	12417,58	94,00	
	indiv6	12	[45, 0, 30, 0, 60, 90, 90, 60, 0, 30, 0, 45]	1	2	1,59	3,18	51,75	48,25	90744,00	429236,50	109,83	
	indiv7	12	[0, 60, 45, 60, 30, 45, 45, 30, 60, 45, 60, 0]	1	1,5	1,59	3	49,79	50,21	0,00	0,00	90,37	
	indiv8	12	[0, 30, 45, 90, 0, 45, 45, 0, 90, 45, 30, 0]	0	2	1,59	3,18	52,76	47,24	87780,00	446047,53	107,97	
	indiv9	14	[30, 0, 45, 60, 90, 0, 60, 60, 0, 90, 60, 45, 0, 30]	0	2	3,18	3,18	59,45	40,55	0,00	0,00	72,98	
	indiv10	12	[90, 0, 60, 45, 90, 30, 30, 90, 45, 60, 0, 90]	1	1,5	1,59	1,59	48,37	51,63	0,00	0,00	92,94	

14th Gen	indiv1	12	[0, 60, 0, 30, 45, 90, 90, 45, 30, 0, 60, 0]	0	2	1,59	1,59	51,15	48,85	80457,63	448517,09	109,88	110,98
	indiv2	12	[0, 90, 0, 30, 90, 45, 45, 90, 30, 0, 90, 0]	0	1,5	1,59	3,18	50,74	49,26	88928,00	460270,41	112,11	
	indiv3	12	[45, 60, 0, 30, 45, 0, 0, 45, 30, 0, 60, 45]	0	1,5	1,59	3,18	50,74	49,26	90072,00	434890,09	111,68	
	indiv4	12	[60, 30, 60, 0, 90, 45, 45, 90, 0, 60, 30, 60]	1	2	1,59	1,59	50,14	49,86	73282,00	371464,34	108,89	
	indiv5	12	[0, 90, 45, 0, 60, 30, 30, 60, 0, 45, 90, 0]	0	1,5	1,59	3	50,56	49,44	0,00	0,00	89,00	
	indiv6	12	[45, 0, 30, 0, 60, 90, 90, 60, 0, 30, 0, 45]	1	2	1,59	1,59	50,14	49,86	0,00	0,00	89,75	
	indiv7	14	[60, 45, 0, 30, 45, 90, 60, 60, 90, 45, 30, 0, 45, 60]	1	1,5	1,59	1,59	50,76	49,24	0,00	0,00	88,63	
	indiv8	12	[45, 60, 0, 60, 45, 60, 60, 45, 60, 0, 60, 45]	0	1,5	1,59	1,59	49,13	50,87	0,00	0,00	91,57	
	indiv9	12	[90, 30, 90, 30, 0, 90, 90, 0, 30, 90, 30, 90]	1	2	1,59	1,59	50,14	49,86	77058,00	424690,13	110,67	
	indiv10	14	[45, 0, 90, 30, 45, 30, 90, 90, 30, 45, 30, 90, 0, 45]	1	1,5	1,59	3,18	52,37	47,63	75270,00	439872,91	106,74	

15th Gen	indiv1	12	[0, 60, 0, 30, 45, 90, 90, 45, 30, 0, 60, 0]	0	2	1,59	1,59	51,15	48,85	80457,63	448517,09	109,88	111,68
	indiv2	12	[0, 90, 0, 30, 90, 45, 45, 90, 30, 0, 90, 0]	0	1,5	1,59	3,18	50,74	49,26	88928,00	460270,41	112,11	
	indiv3	12	[45, 60, 0, 30, 45, 0, 0, 45, 30, 0, 60, 45]	1	1,5	1,59	1,59	48,37	51,63	0,00	0,00	92,94	
	indiv4	12	[30, 90, 30, 45, 0, 60, 60, 0, 45, 30, 90, 30]	1	2	1,59	1,59	50,14	49,86	78330,00	420045,19	110,74	

indiv5	12	[45, 60, 30, 60, 45, 60, 60, 45, 60, 30, 60, 45]	1	1,5	3	1,59	52,17	47,83	0,00	0,00	86,09
indiv6	14	[45, 60, 30, 90, 60, 0, 60, 60, 0, 60, 90, 30, 60, 45]	1	1,5	1,59	3,18	52,37	47,63	69050,00	401622,41	104,96
indiv7	12	[45, 90, 0, 60, 0, 60, 60, 0, 60, 0, 90, 45]	1	1,5	3,18	1,59	52,66	47,34	0,00	0,00	85,21
indiv8	12	[0, 30, 45, 90, 0, 45, 45, 0, 90, 45, 30, 0]	0	1,5	1,59	3,18	50,74	49,26	90392,00	402803,25	110,98
indiv9	12	[90, 30, 90, 30, 0, 90, 90, 0, 30, 90, 30, 90]	1	2	1,59	3,18	51,75	48,25	55148,00	6682,77	94,90
indiv10	14	[0, 30, 45, 30, 45, 90, 45, 45, 90, 45, 30, 45, 30, 0]	0	2	1,59	1,59	53,55	46,45	73000,00	395000,00	103,25

16th Gen	indiv1	14	[0, 45, 30, 60, 90, 0, 30, 30, 0, 90, 60, 30, 45, 0]	1	3	3	3	61,31	38,69	90382,00	445784,47	92,96
	indiv2	12	[0, 90, 0, 30, 90, 45, 45, 90, 30, 0, 90, 0]	0	1,5	1,59	3,18	50,74	49,26	88928,00	460270,41	112,11
	indiv3	12	[45, 60, 0, 30, 45, 0, 0, 45, 30, 0, 60, 45]	0	2	1,59	1,59	51,15	48,85	85964,00	433908,22	110,32
	indiv4	12	[30, 90, 30, 45, 0, 60, 60, 0, 45, 30, 90, 30]	0	2	1,59	3,18	52,76	47,24	72442,00	428696,22	105,37
	indiv5	12	[0, 45, 90, 45, 60, 90, 90, 60, 45, 90, 45, 0]	0	1,5	3,18	3	54,85	45,15	0,00	0,00	81,27
	indiv6	14	[30, 0, 30, 45, 90, 45, 60, 60, 45, 90, 45, 30, 0, 30]	1	1,5	3,18	3,18	56,67	43,33	75124,00	406517,13	98,22
	indiv7	14	[30, 45, 30, 45, 90, 60, 90, 90, 60, 90, 45, 30, 45, 30]	1	2	1,59	3	53,96	46,04	58536,00	373829,56	99,95
	indiv8	12	[0, 30, 45, 90, 0, 45, 45, 0, 90, 45, 30, 0]	0	1,5	1,59	3,18	50,74	49,26	90392,00	402803,25	110,98
	indiv9	12	[90, 30, 90, 30, 0, 90, 90, 0, 30, 90, 30, 90]	1	2	1,59	1,59	50,14	49,86	77058,00	424690,13	110,67
	indiv10	12	[60, 30, 45, 60, 45, 90, 90, 45, 60, 45, 30, 60]	0	1,5	1,59	3,18	50,74	49,26	50706,00	357473,28	104,25

17th Gen	indiv1	12	[0, 90, 0, 60, 30, 45, 45, 30, 60, 0, 90, 0]	1	2	3	3,18	55,55	44,45	90940,00	484053,38	104,29
	indiv2	12	[0, 90, 0, 30, 90, 45, 45, 90, 30, 0, 90, 0]	0	1,5	1,59	3,18	50,74	49,26	88928,00	460270,41	112,11
	indiv3	12	[45, 60, 0, 30, 45, 0, 0, 45, 30, 0, 60, 45]	0	1,5	1,59	3,18	50,74	49,26	90072,00	434890,09	111,68
	indiv4	12	[30, 90, 30, 45, 0, 60, 60, 0, 45, 30, 90, 30]	1	2	1,59	3,18	51,75	48,25	0,00	0,00	86,86
	indiv5	12	[45, 30, 60, 45, 90, 30, 30, 90, 45, 60, 30, 45]	1	1,5	1,59	1,59	48,37	51,63	0,00	0,00	92,94
	indiv6	12	[60, 45, 60, 0, 90, 0, 0, 90, 0, 60, 45, 60]	1	1,5	1,59	3,18	49,98	50,02	85880,00	308332,72	109,51
	indiv7	12	[45, 60, 90, 30, 60, 0, 0, 60, 30, 90, 60, 45]	0	1,5	3,18	1,59	53,42	46,58	0,00	0,00	83,84
	indiv8	12	[0, 30, 45, 90, 0, 45, 45, 0, 90, 45, 30, 0]	0	1,5	1,59	1,59	49,13	50,87	0,00	0,00	91,57
	indiv9	12	[90, 30, 90, 30, 0, 90, 90, 0, 30, 90, 30, 90]	1	2	1,59	1,59	50,14	49,86	77058,00	424690,13	110,67
	indiv10	12	[45, 30, 60, 30, 45, 60, 60, 45, 30, 60, 30, 45]	1	2	3,18	3,18	56,04	43,96	50706,00	357473,28	94,71

18th Gen	indiv1	12	[60, 45, 0, 30, 60, 45, 45, 60, 30, 0, 45, 60]	0	2	1,59	3,18	52,76	47,24	70140,00	409712,00	104,60
	indiv2	12	[0, 90, 0, 30, 90, 45, 45, 90, 30, 0, 90, 0]	0	1,5	1,59	3,18	50,74	49,26	88928,00	460270,41	112,11
	indiv3	12	[45, 60, 0, 30, 45, 0, 0, 45, 30, 0, 60, 45]	0	1,5	1,59	3	50,56	49,44	0,00	0,00	89,00
	indiv4	12	[30, 90, 30, 45, 0, 60, 60, 0, 45, 30, 90, 30]	1	2	1,59	1,59	50,14	49,86	78330,00	420045,19	110,74
	indiv5	12	[30, 45, 60, 0, 30, 45, 45, 30, 0, 60, 45, 30]	1	1,5	1,59	3	49,79	50,21	0,00	0,00	90,37
	indiv6	12	[0, 30, 45, 0, 30, 0, 0, 30, 0, 45, 30, 0]	0	2	1,59	3,18	52,76	47,24	0,00	0,00	85,02
	indiv7	14	[45, 0, 60, 45, 30, 90, 60, 60, 90, 30, 45, 60, 0, 45]	1	3	3,18	3,18	61,98	38,02	69138,00	408755,69	87,85
	indiv8	12	[0, 30, 45, 90, 0, 45, 45, 0, 90, 45, 30, 0]	0	1,5	3,18	3,18	55,03	44,97	93792,00	473803,25	105,39
	indiv9	12	[90, 30, 90, 30, 0, 90, 90, 0, 30, 90, 30, 90]	1	2	1,59	1,59	50,14	49,86	77058,00	424690,13	110,67
	indiv10	12	[60, 90, 30, 0, 30, 60, 60, 30, 0, 30, 90, 60]	1	1,5	3,18	3,18	54,27	45,73	0,00	0,00	82,32



19th Gen

indiv1	14	[30, 90, 60, 0, 30, 60, 45, 45, 60, 30, 0, 60, 90, 30]	1	1,5	1,59	1,59
indiv2	12	[0, 90, 0, 30, 90, 45, 45, 90, 30, 0, 90, 0]	0	1,5	1,59	3,18
indiv3	12	[45, 60, 0, 30, 45, 0, 0, 45, 30, 0, 60, 45]	0	1,5	1,59	3,18
indiv4	12	[30, 90, 30, 45, 0, 60, 60, 0, 45, 30, 90, 30]	1	2	1,59	1,59
indiv5	14	[30, 90, 0, 90, 0, 90, 0, 0, 90, 0, 90, 0, 90, 30]	0	1,5	1,59	1,59
indiv6	12	[60, 45, 90, 0, 45, 0, 0, 45, 0, 90, 45, 60]	1	1,5	3,18	1,59
indiv7	14	[60, 45, 60, 30, 90, 0, 90, 90, 0, 90, 30, 60, 45, 60]	1	1,5	1,59	3
indiv8	12	[90, 30, 90, 30, 0, 90, 90, 0, 30, 90, 30, 90]	1	2	1,59	1,59
indiv9	12	[0, 30, 45, 90, 0, 45, 45, 0, 90, 45, 30, 0]	0	1,5	1,59	3,18
indiv10	12	[90, 30, 0, 60, 45, 0, 0, 45, 60, 0, 30, 90]	1	2	1,59	3

50,76	49,24	0,00	0,00	88,63
50,74	49,26	88928,00	460270,41	112,11
50,74	49,26	90072,00	434890,09	111,68
50,14	49,86	78330,00	420045,19	110,74
51,53	48,47	0,00	0,00	87,25
52,66	47,34	77188,00	308332,00	103,44
52,19	47,81	0,00	0,00	86,06
50,14	49,86	0,00	0,00	89,75
50,74	49,26	90392,00	402803,25	110,98
51,56	48,44	50706,00	353172,00	102,66

20th Gen

indiv1	12	[90, 60, 90, 60, 0, 45, 45, 0, 60, 90, 60, 90]	1	1,5	3	1,59
indiv2	12	[0, 90, 0, 30, 90, 45, 45, 90, 30, 0, 90, 0]	1	1,5	1,59	1,59
indiv3	12	[45, 60, 0, 30, 45, 0, 0, 45, 30, 0, 60, 45]	0	1,5	1,59	3,18
indiv4	12	[30, 90, 30, 45, 0, 60, 60, 0, 45, 30, 90, 30]	1	2	1,59	1,59
indiv5	12	[30, 60, 45, 0, 90, 45, 45, 90, 0, 45, 60, 30]	1	1,5	1,59	3,18
indiv6	12	[90, 60, 0, 45, 30, 60, 60, 30, 45, 0, 60, 90]	1	3	1,59	1,59
indiv7	12	[60, 30, 90, 30, 60, 45, 45, 60, 30, 90, 30, 60]	1	2	1,59	3,18
indiv8	12	[0, 30, 45, 90, 0, 45, 45, 0, 90, 45, 30, 0]	0	1,5	3	3,18
indiv9	12	[90, 30, 90, 30, 0, 90, 90, 0, 30, 90, 30, 90]	1	2	1,59	1,59
indiv10	12	[60, 90, 30, 0, 45, 90, 90, 45, 0, 30, 90, 60]	1	3	3,18	1,59

52,17	47,83	0,00	0,00	86,09
48,37	51,63	0,00	0,00	92,94
50,74	49,26	90072,00	434890,09	111,68
50,14	49,86	78330,00	420045,19	110,74
49,98	50,02	73088,00	368392,00	109,08
53,68	46,32	0,00	0,00	83,38
51,75	48,25	80390,00	431396,49	108,40
54,55	45,45	0,00	0,00	81,82
50,14	49,86	77058,00	424690,13	110,67
57,97	42,03	86706,00	445473,28	98,43

TERMINATION CRITERION MET, optimal solution:

Nb Ply	Ply Orientation	Cut-out	T_rib	t_stiff-panel	t_stiff-rib
12	[0, 90, 0, 30, 90, 45, 45, 90, 30, 0, 90, 0]	0	1,5	1,59	3,18